

AD 739578

PL
Bulletin 42
(Part 5 of 5 Parts)

THE SHOCK AND VIBRATION BULLETIN

C

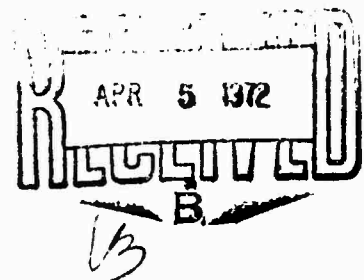
Part 5
Shock, Vibration, Structural Analysis

JANUARY 1972

**A Publication of
THE SHOCK AND VIBRATION
INFORMATION CENTER
Naval Research Laboratory, Washington, D.C.**



Doc ID 739577

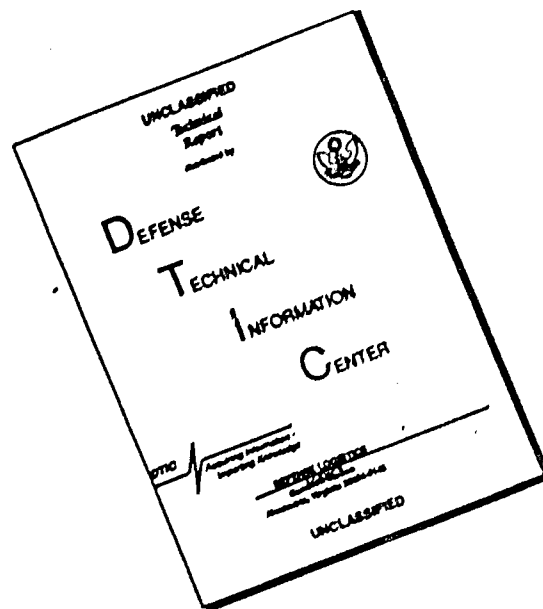


**Office of
The Director of Defense
Research and Engineering**

**Reproduced by
NATIONAL TECHNICAL
INFORMATION SERVICE
Springfield, Va. 22151**

241

DISCLAIMER NOTICE



THIS DOCUMENT IS BEST QUALITY AVAILABLE. THE COPY FURNISHED TO DTIC CONTAINED A SIGNIFICANT NUMBER OF PAGES WHICH DO NOT REPRODUCE LEGIBLY.

SYMPOSIUM MANAGEMENT

THE SHOCK AND VIBRATION INFORMATION CENTER

William W. Mutch. Director
Henry C. Pusey. Coordinator
Rudolph H. Volin. Coordinator
Edward H. Schell. Coordinator

Bulletin Production

Graphic Arts Branch. Technical Information Division.
Naval Research Laboratory

SECTION for		
STI	WHITE SECTION	<input checked="" type="checkbox"/>
DC	DIFF SECTION	<input type="checkbox"/>
ANNOUNCED		<input type="checkbox"/>
JUSTIFICATION		
<i>Kuh</i>		
DISTRIBUTION/AVAILABILITY CODES		
DIST.	AVAIL. and/or SPECIAL	
<i>A</i>	<i>21</i>	

Bulletin 42
(Part 5 of 5 Parts)

THE SHOCK AND VIBRATION BULLETIN

JANUARY 1972

*Details of illustrations in
this document may be better
studied on microfiche*

**A Publication of
THE SHOCK AND VIBRATION
INFORMATION CENTER
Naval Research Laboratory, Washington, D.C.**

The 42nd Symposium on Shock and Vibration was held at the U.S. Naval Station, Key West, Florida, on 2-4 November 1971. The U.S. Navy was host.

**Office of
The Director of Defense
Research and Engineering**

CONTENTS

PAPERS APPEARING IN PART 5

Shock and Vibration Analysis

BANDWIDTH-TIME CONSIDERATIONS IN AUTOMATIC EQUALIZATION	1
C. T. Morrow, Advanced Technology Center, Inc., Dallas, Texas	
A REGRESSION STUDY OF THE VIBRATION RESPONSE OF AN EXTERNAL STORE	9
C. A. Golube, Air Force Flight Dynamics Laboratory, Wright-Patterson Air Force Base, Ohio	
FACTOR ANALYSIS OF VIBRATION SPECTRAL DATA FROM MULTI-LOCATION MEASUREMENT	17
R. G. Merkle, Air Force Flight Dynamics Laboratory, Wright-Patterson Air Force Base, Ohio	
RESPONSES OF A MULTI-LAYER PLATE TO RANDOM EXCITATION	27
H. Saunders, General Electric Company, Aircraft Engine Group, Cincinnati, Ohio	
RESPONSE OF HELICOPTER ROTOR BLADES TO RANDOM LOADS NEAR HOVER	37
C. Lakshmikantham and C. V. Joga Rao, Army Materials and Mechanics Research Center, Watertown, Massachusetts	
INSTRUMENTATION TECHNIQUES AND THE APPLICATION OF SPECTRAL ANALYSIS AND LABORATORY SIMULATION TO GUN SHOCK PROBLEMS	47
D. W. Culbertson, Naval Weapons Laboratory, Dahlgren, Virginia, and V. F. DeVost, Naval Ordnance Laboratory, White Oak, Silver Spring, Maryland	
THE EFFECT OF "Q" VARIATIONS IN SHOCK SPECTRUM ANALYSIS	61
M. B. McGrath, Martin Marietta Corporation, Denver, Colorado, and W. F. Bangs, National Aeronautics and Space Administration, Goddard Space Flight Center, Maryland	
RAPID FREQUENCY AND CORRELATION ANALYSIS USING AN ANALOG COMPUTER	69
J. G. Parks, Research, Development and Engineering Directorate, U.S. Army Tank- Automotive Command, Warren, Michigan	
INVESTIGATION OF LAUNCH TOWER MOTION DURING AEROBEE 350 LAUNCH	77
R. L. Kinsley and W. R. Case, NASA, Goddard Space Flight Center, Greenbelt, Maryland	
ON THE USE OF FOURIER TRANSFORMS OF MECHANICAL SHOCK DATA	87
H. A. Gaberson and D. Pal, Naval Civil Engineering Laboratory, Port Hueneme, California	
WAVE ANALYSIS OF SHOCK EFFECTS IN COMPOSITE ARMOR	97
G. L. Filbey, Jr., USAARDC Ballistic Research Laboratories, Aberdeen Proving Ground, Maryland	
STATISTICAL LOADS ANALYSIS TECHNIQUE FOR SHOCK AND HIGH-FREQUENCY EXCITED ELASTODYNAMIC CONFIGURATIONS	101
K. J. Saczalski and K. C. Park, Clarkson College of Technology, Potsdam, New York	

Structural Analysis

NASTRAN OVERVIEW: DEVELOPMENT, DYNAMICS APPLICATION, MAINTENANCE, ACCEPTANCE	109
J. P. Ramey, Head, NASTRAN Systems Management Office and D. J. Weidman, Aerospace Engineer, NASA Langley Research Center, Hampton, Virginia	
EXPERIENCE WITH NASTRAN AT THE NAVAL SHIP R&D CENTER AND OTHER NAVY LABORATORIES	129
P. Matula, Naval Ship Research & Development Center, Bethesda, Maryland	
RESULTS OF COMPARATIVE STUDIES ON REDUCTION OF SIZE PROBLEM	135
R. M. Mains, Department of Civil and Environmental Engineering, Washington University, St. Louis, Missouri	
STRUCTURAL DYNAMICS OF FLEXIBLE RIB DEPLOYABLE SPACECRAFT ANTENNAS	143
B. G. Wrenn, W. B. Halls, Jr. and J. F. Hedges, Lockheed Missiles and Space Company, Sunnyvale, California	
INFLUENCE OF ASCENT HEATING ON THE SEPARATION DYNAMICS OF A SPACECRAFT FAIRING	155
C. W. Coale, T. J. Kertesz, Lockheed Missiles & Space Company, Inc., Sunnyvale, California	
DYNAMIC WAVE PROPAGATION IN TRANSVERSE LAYERED COMPOSITES	167
C. A. Ross, J. E. Cunningham, and R. L. Sierakowski, Aerospace Engineering Department University of Florida, Gainesville, Florida	
R-W PLANE ANALYSIS FOR VULNERABILITY OF TARGETS TO AIR BLAST	173
P. S. Westine, Southwest Research Institute, San Antonio, Texas	
PERFORM: A COMPUTER PROGRAM TO DETERMINE THE LIMITING PERFORMANCE OF PHYSICAL SYSTEMS SUBJECT TO TRANSIENT INPUTS	185
W. D. Pilkey and Bo Ping Wang, Department of Aerospace Engineering and Engineering Physics, University of Virginia, Charlottesville, Virginia	
STRUCTURAL DYNAMIC ANALYSIS AND TESTING OF A SPACECRAFT DUAL TRACKING ANTENNA	191
D. D. Walters, R. F. Heidenreich, A. A. Woods and B. G. Wrenn, Lockheed Missiles and Space Company, Sunnyvale, California	

Ship's Problems

DETERMINATION OF FIXED-BASE NATURAL FREQUENCIES OF A COMPOSITE STRUCTURE OR SUBSTRUCTURES	203
C. Ni, R. Skop, and J. P. Layher, Naval Research Laboratory, Washington, D.C.	
EQUIVALENT SPRING-MASS SYSTEM: A PHYSICAL INTERPRETATION	215
B. K. Wada, R. Bamford, and J. A. Garba, Jet Propulsion Laboratory, Pasadena, California	
LONGITUDINAL VIBRATION OF COMPOSITE BODIES OF VARYING AREA	227
D. J. Guzy, J.C.S. Yang, and W. H. Walston, Jr., Mechanical Engineering Department, University of Maryland, College Park, Maryland	
SIMPLIFIED METHOD FOR THE EVALUATION OF STRUCTUREBORNE VIBRATION TRANSMISSION THROUGH COMPLEX SHIP STRUCTURES	235
M. Chernjowski and C. Arcidiacona, Gibbs & Cox, Inc., New York, New York	

PAPERS APPEARING IN PART 1

Invited Papers

SMALL SHIPS-HIGH PERFORMANCE

Rear Admiral H. C. Mason, Commander, Naval Ship Engineering Center, Washington, D.C.

Specifications

SURVEY OF VIBRATION TEST PROCEDURES IN USE BY THE AIR FORCE

W. B. Yarcho, Air Force Flight Dynamics Laboratory, Wright-Patterson Air Force Base, Ohio

SPECIFICATIONS -- A PANEL SESSION

SOME ADMINISTRATIVE FACTORS WHICH INFLUENCE TECHNICAL APPROACHES TO SHIP SHOCK HARDENING

D. M. Lund, Naval Ship Engineering Center, Hyattsville, Maryland

Measurement and Application of Mechanical Impedance

FORCE TRANSDUCER CALIBRATIONS RELATED TO MECHANICAL IMPEDANCE MEASUREMENTS

E. F. Ludwig, Assistant Project Engineer, and N.D. Taylor, Senior Engineer, Pratt & Whitney Aircraft, Florida Research & Development Center, West Palm Beach, Florida

THE MEASUREMENT OF MECHANICAL IMPEDANCE AND ITS USE IN VIBRATION TESTING

N. F. Hunter, Jr., and J. V. Otts, Sandia Corporation, Albuquerque, New Mexico

TRANSIENT TEST TECHNIQUES FOR MECHANICAL IMPEDANCE AND MODAL SURVEY TESTING

J. D. Favour, M. C. Mitchell, N. L. Olson, The Boeing Company, Seattle, Washington

PREDICTION OF FORCE SPECTRA BY MECHANICAL IMPEDANCE AND ACOUSTIC MOBILITY MEASUREMENT TECHNIQUES

R. W. Schock, NASA/Marshall Space Flight Center, Huntsville, Alabama and G. C. Kao, Wyle Laboratories, Huntsville, Alabama

DYNAMIC DESIGN ANALYSIS VIA THE BUILDING BLOCK APPROACH

A. L. Klosterman, Ph.D. and J. R. Lemon, Ph.D., Structural Dynamics Research Corporation Cincinnati, Ohio

MOBILITY MEASUREMENTS FOR THE VIBRATION ANALYSIS OF CONNECTED STRUCTURES

D. J. Ewins and M. G. Sainsbury, Imperial College of Science and Technology, London, England

LIQUID-STRUCTURE COUPLING IN CURVED PIPES -- II

L. C. Davidson and D. R. Samsury, Machinery Dynamics Division, Naval Ship Research and Development Center, Annapolis, Maryland

Transportation and Packaging

A SURVEY OF THE TRANSPORTATION SHOCK AND VIBRATION INPUT TO CARGO

F. E. Ostrem, General American Research Division, General American Transportation Corporation, Niles, Illinois

THE DYNAMIC ENVIRONMENT OF SELECTED MILITARY HELICOPTERS

M. B. Gens, Sandia Laboratories, Albuquerque, New Mexico

HIGHWAY SHOCK INDEX

R. Kennedy, U. S. Army Transportation Engineering Agency, Military Traffic Management and Terminal Service, Newport News, Virginia

DEVELOPMENT OF A ROUGH ROAD SIMULATOR AND SPECIFICATION FOR TESTING OF EQUIPMENT TRANSPORTED IN WHEELED VEHICLES

H. M. Forkols and E. W. Clements, Naval Research Laboratory, Washington, D.C.

LABORATORY CONTROL OF DYNAMIC VEHICLE TESTING

J. W. Grant, U. S. Army Tank-Automotive Command, Warren, Michigan

IMPACT VULNERABILITY OF TANK CAR HEADS

J. C. Shang and J. E. Everett, General American Research Division, General American Transportation Corporation, Niles, Illinois

A STUDY OF IMPACT TEST EFFECTS UPON FOAMED PLASTIC CONTAINERS

D. McDaniel, Ground Equipment and Materials Directorate, Directorate for Research, Development, Engineering and Missile Systems Laboratory, U. S. Army Missile Command Redstone Arsenal, Alabama, and R. M. Wyskida, Industrial and Systems Engineering Department, The University of Alabama in Huntsville, Huntsville, Alabama

DEVELOPMENT OF A PRODUCT PROTECTION SYSTEM

D. E. Yound, IBM General Systems Division, Rochester, Minnesota, and S. R. Pierce, Michigan State University, East Lansing, Michigan

MOTION OF FREELY SUSPENDED LOADS DUE TO HORIZONTAL SHIP MOTION IN RANDOM HEAD SEAS

H. S. Zwibel, Naval Civil Engineering Laboratory, Port Hueneme, California

PAPERS APPEARING IN PART 2

Ground Motion

SINE BEAT VIBRATION TESTING RELATED TO EARTHQUAKE RESPONSE SPECTRA

E. G. Fischer, Westinghouse Research Laboratories, Pittsburgh, Pennsylvania

SEISMIC EVALUATION OF ELECTRICAL EQUIPMENT FOR NUCLEAR POWER STATIONS

R. H. Prause and D. R. Ahlbeck, BATTELLE, Columbus Laboratories, Columbus, Ohio

SHOCK INPUT FOR EARTHQUAKE STUDIES USING GROUND MOTION FROM UNDERGROUND NUCLEAR EXPLOSIONS

D. L. Bernreuter, D. M. Norris, Jr., and F. J. Tokarz, Lawrence Livermore Laboratory, University of California, Livermore, California

ROCKING OF A RIGID, UNDERWATER BOTTOM-FOUNDED STRUCTURE SUBJECTED TO SEISMIC SEAFLOOR EXCITATION

J. G. Hammer and H. S. Zwibel, Naval Civil Engineering Laboratory, Port Hueneme, California

DEVELOPMENT OF A WAVEFORM SYNTHESIS TECHNIQUE-A SUPPLEMENT TO RESPONSE SPECTRUM AS A DEFINITION OF SHOCK ENVIRONMENT

R. C. Yang and H. R. Saffell, The Ralph M. Parsons Company, Los Angeles, California

**THE RESPONSE OF AN ISOLATED FLOOR SLAB--RESULTS OF AN EXPERIMENT IN
EVENT DIAL PACK**

J. M. Ferritto, Naval Civil Engineering Laboratory, Port Hueneme, California

A SHOCK-ISOLATION SYSTEM FOR 22 FEET OF VERTICAL GROUND MOTION

**E. C. Jackson, A. B. Miller and D. L. Bernreuter, Lawrence Livermore Laboratory,
University of California, Livermore, California**

**THE COMPARISON OF THE RESPONSE OF A HIGHWAY BRIDGE TO UNIFORM GROUND
SHOCK AND MOVING GROUND EXCITATION**

N. E. Johnson and R. D. Galletly, Mechanics Research, Inc., Los Angeles, California

**DEFORMATION AND FRACTURE OF TANK BOTTOM HULL PLATES SUBJECTED
TO MINE BLAST**

**D. F. Haskell, Vulnerability Laboratory, U.S. Army Ballistic Research
Laboratories, Aberdeen Proving Ground, Md.**

**THE IMPULSE IMPARTED TO TARGETS BY THE DETONATION OF
LAND MINES**

P. S. Westline, Southwest Research Institute, San Antonio, Texas

CIRCULAR CANTILEVER BEAM ELASTIC RESPONSE TO AN EXPLOSION

**Y. S. Kim and P. R. Ukrainetz, Department of Mechanical Engineering, University
of Saskatchewan, Saskatoon, Canada**

MEASUREMENT OF IMPULSE FROM SCALED BURIED EXPLOSIVES

**B. L. Morris, U.S. Army Mobility Equipment Research and Development Center,
Fort Belvoir, Virginia**

Dynamic Analysis

**THE EFFECTS OF MOMENTUM WHEELS ON THE FREQUENCY RESPONSE
CHARACTERISTICS OF LARGE FLEXIBLE STRUCTURES**

F. D. Day III and S. R. Tomer, Martin Marietta Corporation, Denver, Colorado

**INTEGRATED DYNAMIC ANALYSIS OF A SPACE STATION WITH CONTROLLABLE
SOLAR ARRAYS**

**J. A. Heinrichs and A. L. Weinberger, Fairchild Industries, Inc., Germantown, Maryland,
and M. D. Rhodes, NASA Langley Research Center, Hampton, Virginia**

**PARAMETRICALLY EXCITED COLUMN WITH HYSTERETIC MATERIAL
PROPERTIES**

**D. T. Mozer, IBM Corporation, East Fishkill, New York, and R. M. Evan-Iwanowski,
Professor, Syracuse University, Syracuse, New York**

**DYNAMIC INTERACTION BETWEEN VIBRATING CONVEYORS AND
SUPPORTING STRUCTURE**

**M. Paz, Professor, Civil Engineering Department, University of Louisville,
Louisville, Kentucky, and O. Mathis, Design Engineer, Rex Chainbelt Inc.,
Louisville, Kentucky**

**RESPONSE OF A SIMPLY SUPPORTED CIRCULAR PLATE EXPOSED TO THERMAL
AND PRESSURE LOADING**

**J. E. Koch, North Eastern Research Associates, Upper Montclair, N.J., and M. L. Cohen,
North Eastern Research Associates, Upper Montclair, N.J., and Stevens Institute of
Technology, Hoboken, N.J.**

**WHIRL FLUTTER ANALYSIS OF PROPELLER-NACELLE-PYLON SYSTEM ON LARGE
SURFACE EFFECT VEHICLES**

Yuan-Ning Liu, Naval Ship Research and Development Center, Washington, D.C.

**THE DYNAMIC RESPONSE OF STRUCTURES SUBJECTED TO TIME-DEPENDENT
BOUNDARY CONDITIONS USING THE FINITE ELEMENT METHOD**

G. H. Workman, Battelle, Columbus Laboratories, Columbus, Ohio

**VIBRATION ANALYSIS AND TEST OF THE EARTH RESOURCES
TECHNOLOGY SATELLITE**

T. J. Cokonis and G. Sardella, General Electric Company, Space Division,
Philadelphia, Pennsylvania

FINITE AMPLITUDE SHOCK WAVES IN INTERVERTEBRAL DISCS

W. F. Hartman, The Johns Hopkins University, Baltimore, Maryland

ACCELERATION RESPONSE OF A BLAST-LOADED PLATE

L. W. Fagel, Bell Telephone Laboratories, Inc., Whippany, New Jersey

**EFFECT OF CORRELATION IN HIGH-INTENSITY NOISE TESTING AS INDICATED
BY THE RESPONSE OF AN INFINITE STRIP**

C. T. Morrow, Advanced Technology Center, Inc., Dallas, Texas

PAPERS APPEARING IN PART 3

Test Control

ON THE PERFORMANCE OF TDM AVERAGERS IN RANDOM VIBRATION TESTS

A. J. Curtis, Hughes Aircraft Company, Culver City, California

**A MULTIPLE DRIVER ADMITTANCE TECHNIQUE FOR VIBRATION TESTING OF
COMPLEX STRUCTURES**

S. Smith, Lockheed Missiles & Space Company, Palo Alto Research Laboratory,
Palo Alto, California, and A. A. Woods, Jr., Lockheed Missiles & Space Company,
Sunnyvale, California

EQUIPMENT CONSIDERATIONS FOR ULTRA LOW FREQUENCY MODAL TESTS

R. G. Shoulberg and R. H. Tuft, General Electric Company, Valley Forge,
Pennsylvania

COMBINED-AXIS VIBRATION TESTING OF THE SRAM MISSILE

W. D. Trotter and D. V. Muth, The Boeing Company, Aerospace Group,
Seattle, Washington

SHOCK TESTING UTILIZING A TIME SHARING DIGITAL COMPUTER

R. W. Canon, Naval Missile Center, Point Mugu, California

**A TECHNIQUE FOR CLOSED-LOOP COMPUTER-CONTROLLED REVERSED-
BENDING FATIGUE TESTS OF ACOUSTIC TREATMENT MATERIAL**

C. E. Rucker and R. E. Grandle, NASA Langley Research Center,
Hampton, Virginia

**PROGRAMMING AND CONTROL OF LARGE VIBRATION TABLES IN UNIAXIAL
AND BIAxIAL MOTIONS**

R. L. Larson, MTS Systems Corporation, Minneapolis, Minnesota

A DATA AMPLIFIER GAIN-CODE RECORDING SYSTEM

J. R. Olbert and T. H. Hammond, Hughes Aircraft Company, Culver
City, California

STABILITY OF AN AUTOMATIC NOTCH CONTROL SYSTEM IN SPACECRAFT TESTING

B. N. Agrawal, COMSAT Laboratories, Clarksburg, Maryland

Test Facilities and Techniques

SINUSOIDAL VIBRATION OF POSEIDON SOLID PROPELLANT MOTORS

L. R. Pendleton, Research Specialist, Lockheed Missiles & Space Company, Sunnyvale, California

CONFIDENCE IN PRODUCTION UNITS BASED ON QUALIFICATION VIBRATION

R. E. Deitrick, Hughes Aircraft Company, Space and Communications Group, El Segundo, California

SIMULATION TECHNIQUES IN DEVELOPMENT TESTING

A. Hammer, Weapons Laboratory, U. S. Army Weapons Command, Rock Island, Illinois

A ROTATIONAL SHOCK AND VIBRATION FACILITY

R. T. Fandrich, Jr., Radiation Incorporated, Melbourne, Florida

THE EFFECTS OF VARIOUS PARAMETERS ON SPACECRAFT SEPARATION SHOCK

W. B. Keegan and W. F. Bangs, NASA, Goddard Space Flight Center, Greenbelt, Maryland

NON-DESTRUCTIVE TESTING OF WEAPONS EFFECTS ON COMBAT AND LOGISTICAL VEHICLES

R. L. Johnson, J. H. Leete, and J. D. O'Keefe, TRW Systems Group, Redondo Beach, California, and A. N. Tedesco, Advanced Research Projects Agency, Department of Defense, Washington, D.C.

THE EFFECT OF THE FIN-OPENING SHOCK ENVIRONMENT ON GUIDED MODULAR DISPENSER WEAPONS.

K. D. Denton and K. A. Herzing, Honeywell Inc., Government and Aeronautical Products Division Hopkins, Minnesota

DEVELOPMENT OF A FLUIDIC HIGH-INTENSITY SOUND GENERATOR

H. F. Wolfe, Air Force Flight Dynamics Laboratory, Wright-Patterson Air Force Base, Ohio

DEVELOPMENT OF A LIGHTWEIGHT, LINEAR MECHANICAL SPRING ELEMENT

R. E. Keffe, Kaman Sciences Corporation, Colorado Springs, Colorado

TECHNIQUES FOR IMPULSE AND SHOCK TUBE TESTING OF SIMULATED REENTRY VEHICLES

N. K. Jamison, McDonnell Douglas Astronautics Company, Huntington Beach, California

VIBRATION FIXTURING - NEW CELLULAR DESIGN, SATURN AND ORBITAL WORKSHOP PROGRAMS

R. L. Stafford, McDonnell Douglas Astronautics Company, Huntington Beach, California

WALL FLOW NOISE IN A SUBSONIC DIFFUSER

E. F. Timpke, California State College, Long Beach, California, and R. C. Binder, University of Southern California, Los Angeles, California

PAPERS APPEARING IN PART 4

Isolation and Damping

TRANSIENT RESPONSE OF REAL DISSIPATIVE STRUCTURES

R. Plunkett, University of Minnesota, Minneapolis, Minnesota

DYNAMIC RESPONSE OF A RING SPRING

W. L. Eshleman, IIT Research Institute, Chicago, Illinois

SHOCK MOUNTING SYSTEM FOR ELECTRONIC CABINETS

W. D. Delany, Admiralty Surface Weapons Establishment, Portsmouth, U.K.

METHODS OF ATTENUATING PYROTECHNIC SHOCK

S. Barrett and W. J. Kacena, Martin Marietta Corporation, Denver, Colorado

ENERGY ABSORPTION CAPACITY OF A SANDWICH PLATE WITH CRUSHABLE CORE

D. Krajcinovic, Argonne National Laboratory, Argonne, Illinois

ON THE DAMPING OF TRANSVERSE MOTION OF FREE-FREE BEAMS IN DENSE, STAGNANT FLUIDS

W. K. Blake, Naval Ship Research and Development Center, Bethesda, Maryland

OPTIMUM DAMPING DISTRIBUTION FOR STRUCTURAL VIBRATION

R. Plunkett, University of Minnesota, Minneapolis, Minnesota

A LAYERED VISCOELASTIC EPOXY RIGID FOAM MATERIAL FOR VIBRATION CONTROL

C. V. Stahle and Dr. A. T. Tweedie, General Electric Company, Space Division, Valley Forge, Pa.

OPTIMIZATION OF A COMBINED RUZICKA AND SNOWDON VIBRATION ISOLATION SYSTEM

D. E. Zeidler, Medtronic, Inc., Minneapolis, Minnesota, and D. A. Frohrib, University of Minnesota, Minneapolis, Minnesota

TRANSIENT RESPONSE OF PASSIVE PNEUMATIC ISOLATORS

G. L. Fox, and E. Steiner, Barry Division of Barry Wright Corporation, Burbank, California

EXPERIMENTAL DETERMINATION OF STRUCTURAL AND STILL WATER DAMPING AND VIRTUAL MASS OF CONTROL SURFACES

R. C. Leibowitz and A. Kilcullen, Naval Ship Research and Development Center, Washington, D.C.

DAMPING OF A CIRCULAR RING SEGMENT BY A CONSTRAINED VISCOELASTIC LAYER

Cpt. C. R. Almy, U.S. Army Electronics Command, Ft. Monmouth, New Jersey, and F. C. Nelson, Department of Mechanical Engineering, Tufts University, Medford, Mass.

DYNAMIC ANALYSIS OF THE RUNAWAY ESCAPEMENT MECHANISM

G. W. Hemp, Department of Engineering, Science and Mechanics, University of Florida, Gainesville, Florida

Prediction and Experimental Techniques

A METHOD FOR PREDICTING BLAST LOADS DURING THE DIFFRACTION PHASE

W. J. Taylor, Ballistic Research Laboratories, Aberdeen Proving Ground, Maryland

DRAG MEASUREMENTS ON CYLINDERS IN EVENT DIAL PACK

S. B. Mellsen, Defence Research Establishment Suffield, Ralston, Alberta, Canada

DIAL PACK BLAST DIRECTING EXPERIMENT

L. E. Fugelso, S. F. Fields, and W. J. Byrne, General American Research Division, Niles, Illinois

BLAST FIELDS ABOUT ROCKETS AND RECOILLESS RIFLES

W. E. Baker, P. S. Westine, and R. L. Bessey, Southwest Research Institute, San Antonio, Texas

TRANSONIC ROCKET-SLED STUDY OF FLUCTUATING SURFACE-PRESSURES AND PANEL RESPONSES

E. E. Ungar, Bolt Beranek and Newman Inc., Cambridge, Massachusetts, and H. J. Bandgren, Jr. and R. Erwin, National Aeronautics and Space Administration, George C. Marshall Space Flight Center Huntsville, Alabama

SUPPRESSION OF FLOW-INDUCED VIBRATIONS BY MEANS OF BODY SURFACE MODIFICATIONS

D. W. Sallet and J. Berezow, Naval Ordnance Laboratory, Silver Spring, Maryland

AN EXPERIMENTAL TECHNIQUE FOR DETERMINING VIBRATION MODES OF STRUCTURES WITH A QUASI-STATIONARY RANDOM FORCING FUNCTION

R. G. Christiansen and W. W. Parmenter, Naval Weapons Center, China Lake, California

RESPONSE OF AIR FILTERS TO BLAST

E. F. Witt, C. J. Arroyo, and W. N. Butler, Bell Laboratories, Whippany, N.J.

SHOCK AND VIBRATION ANALYSIS

BANDWIDTH-TIME CONSIDERATIONS IN AUTOMATIC EQUALIZATION

Charles T. Morrow
Advanced Technology Center, Inc.
Dallas, Texas

(U) It has sometimes been claimed that close control of output level in an automatic equalizer is possible only when sample time is long enough to provide close estimates of power spectral density. The actual behaviour of an automatic equalizer, if it does not encounter instability problems, tends to be exactly opposite. However, stability and preservation of a Gaussian narrow band distribution ordinarily require a large time-bandwidth product. For this reason, it is unlikely that any pseudo-random signals, however ingeniously devised, will permit a significant speeding up of the equalizing operation.

INTRODUCTION

(U) In recent years, many papers have appeared on automatic equalization of random shaker systems, with particular emphasis on possible methods of speeding up the equalization. A number of these papers have been based on an assumption that for precise control of the level of excitation in a narrow band it is necessary to average over a time sample long enough to provide a close estimate of the mean square of the narrow band random signal as if time bandwidth product considerations were being applied to ordinary data reduction. This assumption would be correct if the equalizer functioned by analyzing only one time sample in each frequency band and setting the attenuators for the remainder of the test. Most equalizers actually function by repeated or even continuous correction. Accordingly, the statistical quantity to be estimated from any one sample is not an average over infinite time but the average over the duration of the next sample.

(U) Some of the papers also involve an assumption that although the excitation should be Gaussian on a broad band basis, the narrow band distribution does not matter. When a test item is subject to random excitation, the actual objective is to make the vibration Gaussian at each failure point, except insofar as nonlinearities in the vicinity of a failure point and possibly associated with the failure mechanism alter a distribution. Failures are usually associated with mechanical resonance and therefore with narrow band random vibration. Ordinarily, vibration that is not Gaussian on a wide band basis rapidly becomes Gaussian as the band is narrowed. However,

when equalization is very rapid or some pseudo-random signals are used as the input to a shaker, the opposite is more likely to be true.

(U) In addition, each narrow band channel in a automatic equalizer is subject to the instability problems of a control system.

(U) The objective of this paper is to show as simply and vividly as possible how these considerations can affect the design of an automatic equalizer.

AN EQUALIZER WITHOUT FEEDBACK

(U) To visualize some of the effects of sampling and estimating, consider the hypothetical equalizer shown in Fig. 1. It is not a practical system, but it will help us to understand what might happen if equalization could be accomplished without any likelihood of instability. Two identical test items and shaker systems are required. All mechanical elements are assumed to be linear. There are two identical comb filters. One is used in performing a spectral analysis of the vibration of shaker A. The operation is performed in real time with no delay except in the filter and averager. The other is used in conjunction with an attenuator bank to equalize the random input to shaker B. An accurate computer, responding to the spectral analysis, adjusts the attenuators so that the excitation applied to test item B is according to specification. As there is no feedback, there can be no control system instability in the usual sense.

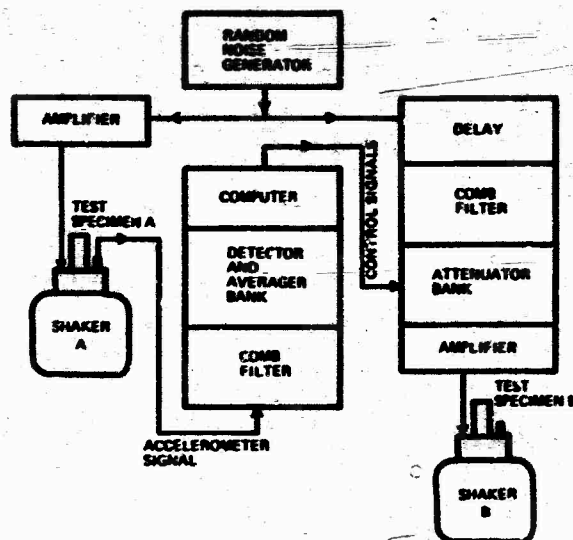


FIGURE 1 HYPOTHETICAL EQUALIZER SYSTEM WITHOUT FEEDBACK.

(U) For one special case, the precision of control is limited only by the performance of the computer. Let the narrow band estimates be on the basis of a true average over a sample of finite duration. This can be with a sample sliding along with time so that continuous correction of shaker B can be effected, or with a discrete sample in a series with the attenuator adjustment performed only at the end of each sample. Now let us introduce a time delay in system B equal to the sample duration. Equalization of system B no longer involves a prediction. The sample subjected to spectral analysis is the sample for which the attenuators are adjusted. The adjustment can in principle be made completely precise regardless of the sample duration.

(U) However, as the sample duration is shortened, the distribution for each narrow band becomes distorted. As an extreme case, imagine a narrow band channel of the spectral analyzer synchronizer to operate on each half sine wave. In the excitation of the test item on shaker B, for the same narrow band, all amplitudes become identical. The result is a sine wave of constant amplitude but varying phase. The distribution is not Gaussian but approximately that of an ordinary sine wave.

(U) With all channels of the analyzer operating this way, the distribution at a failure point within a test item becomes critically dependent on the bandwidth of the mechanical resonance with which the failure is associated. If the bandwidth is close to that of the analyzer, the distribution will be close to that for a single narrow band. If the bandwidth is

smaller, the amplitude will fluctuate somewhat with time. If the bandwidth is much greater, the mechanical resonator will respond to many of the phase-modulated sinusoids simultaneously, and the distribution will be more nearly Gaussian. This is not to say that such a system would never provide a useful test if it could be achieved in practice. But there is no reason to expect its effects to be simply related to those of a Gaussian vibration test.

(U) Now let us eliminate the time delay and thereby admit some uncertainty. As an indication of the precision of control, we require the conditional probability that the rms value of a narrow band sample be within dx of x_1 , where x_1 is the rms value for the previous sample.

(U) Suppose that in a large number of trials an event A is observed m times, and of these n are followed by an event B. Then the probability that the event B follows the event A is

$$P(B|A) = \frac{n}{m} = \frac{P(A,B)}{P(A)} \quad (1)$$

where $P(A,B)$ is the joint probability of events A and B occurring, and $P(A)$ is the probability that A occurs.

(U) By such reasoning, the probability density that an rms value is within dx of x_1 after a value x_1 has been measured is given by

$$p(x_2|x_1) = \frac{1}{2\pi\sigma_1\sigma_2(1-\rho^2)^{1/2}} \exp \left[\frac{1}{2(1-\rho^2)} \left(\frac{x_1^2}{\sigma_1^2} + \frac{x_2^2}{\sigma_2^2} - \frac{2\rho x_1 x_2}{\sigma_1\sigma_2} \right) \right]$$

(2)

$$\frac{1}{\sigma_1(2\pi)^{1/2}} \exp \left[-\frac{x_1^2}{\sigma_1^2} \right]$$

which is the ratio of a joint or two-dimensional Gaussian distribution to an ordinary one-dimensional Gaussian distribution. However, for the case at hand, we can assume equal standard deviations.

$$\sigma_2 = \sigma_1 \quad (3)$$

(U) Now, ρ is the autocorrelation function of the rms value, for a time delay equal to the sample duration. To obtain a feeling for the way in which $p(x_2|x_1)$ depends on sample duration, we will merely assume that ρ approaches zero for long durations, and that it would approach unity for short durations if we ignore any complications from having half cycles of non-zero duration.

(U) When ρ approaches zero, $p(x_2|x_1)$ approaches the distribution of x_1 , namely an ordinary one-dimensional distribution. If $x_2 \neq x_1$, it is readily shown by shifting the exponential to the denominator, expanding it as a Taylor's series, and multiplying each term by $(1-\rho^2)^{1/2}$, that $p(x_2|x_1)$ approaches zero as ρ approaches unity, or, in other words, as the sample duration approaches zero. On the other hand, if $x_2 = x_1$, we have

$$\begin{aligned} p(x_2|x_1) &= \frac{1}{\sigma_1(2\pi)^{1/2}(1-\rho^2)^{1/2}} \exp \left[-\frac{x_1^2(\rho^2 - 2\rho + 1)}{2(1-\rho^2)\sigma_1^2} \right] \\ &= \frac{1}{\sigma_1(2\pi)^{1/2}(1-\rho^2)^{1/2}} \exp \left[\frac{x_1^2}{2\sigma_1^2} \cdot \frac{1-\rho}{1+\rho} \right], \end{aligned} \quad (4)$$

which increases beyond limit as the sample duration approaches zero and ρ approaches unity. In other words, the shorter the sample, the more precise the control of rms value. This is just the opposite of what one obtains by assuming that the sample rms value must be used as an estimate of the rms value for infinite duration.

(U) However, if stability considerations did not limit the shortness of sample that can be used in a practical automatic equalizer, it still might be inadvisable to use very short durations because of the distortion that can result in the probability distribution of the instantaneous values.

FEEDBACK AND INSTABILITY

(U) We now proceed to the practical automatic equalizer of Figure 2. There is only one shaker and only one test item. Narrow band levels are set by an attenuator bank preceded by a comb filter and followed by a mixer. A second comb filter operating on the measured excitation of the test item makes possible the computation of narrow band rms values, which are used to adjust the corresponding attenuators. We now have a feedback system. As we shall see, it is possible to have an instability such that attenuator gain fluctuates widely or even diverges from its proper setting.

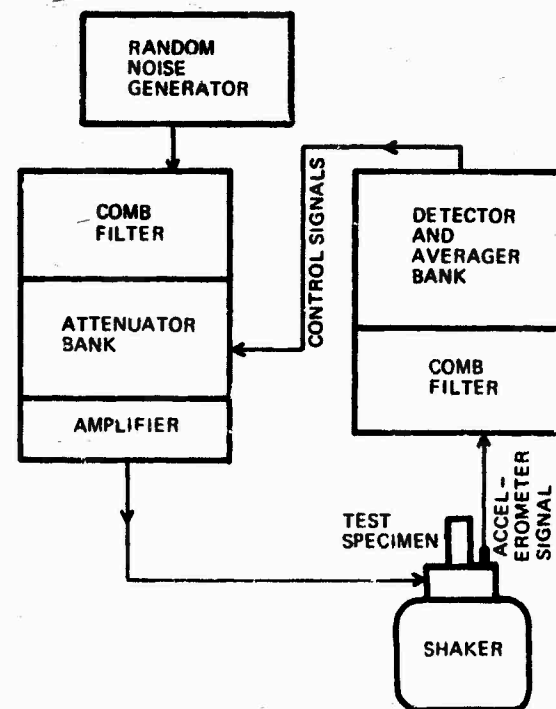


FIGURE 2

AUTOMATIC EQUALIZER SYSTEM WITH FEEDBACK

(U) In this paper, we will not attempt to calculate this phenomenon for a pure random signal. Rather, we will solve an easier substitute problem, from which the approximate behaviour with random or pseudo-random signals can be inferred. We will consider one narrow band system isolated from the others, as in Figure 3, and used to control the magnitude of a sinusoid. We will further assume that any mechanical resonance in the narrow band is centered, that the combined effect of filter and resonance is symmetrical about the center frequency, that the only additional delay or phase lag affecting the stability is in the averager, and the detector simply generates a signal proportional to the envelope.

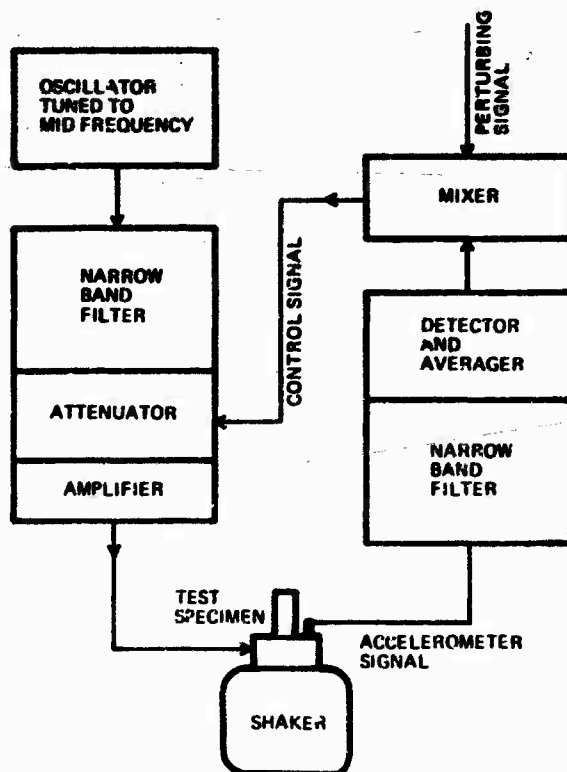


FIGURE 3

SINGLE NARROW BAND CHANNEL USED TO CONTROL THE LEVEL OF A SINUSOID

(U) As the sinusoid is a steady signal, and our ultimate objective is to understand the effect of the feedback loop on fluctuations, we must insert a perturbing signal as well. A small perturbing low frequency cyclical voltage is inserted at a point where the envelope serves as the signal. The mixer added to the circuit for this purpose is assumed not to load the averager or in any way effect the loop again. Our

strategy is to calculate loop gain as a function of frequency, express this as a Nyquist plot, and determine whether the response to perturbations over the frequency range of interest is stable or may tend to increase beyond limit at one or more frequencies.

(U) When the perturbing voltage reaches the attenuator adjuster, its effect is to modulate the sinusoid, thereby producing sideband signals whose phases and magnitudes are dependent on the selectivity curve.

(U) Let the sinusoid from the oscillator

$$v = V \cos 2\pi f t \quad (5)$$

be modulated by the low-frequency perturbing signal

$$v_m = V_m \cos 2\pi f_m t \quad (6)$$

to produce an amplitude modulated signal

$$\begin{aligned} v_{am} &= V[1 + m \cos 2\pi f_m t] \cos 2\pi f t \\ &= V \left[\cos 2\pi f t + \frac{m}{2} \cos 2\pi(f + f_m)t \right. \\ &\quad \left. + \frac{m}{2} \cos 2\pi(f - f_m)t \right] \end{aligned} \quad (7)$$

where m is a modulation coefficient normal by between zero and unity. The final form above, obtained by applying trigonometric identities, expresses the modulated sinusoid as the sum of three constant amplitude signals of different frequency—a carrier, a lower sideband signal, and an upper sideband signal.

(U) We now pass this through any mechanical resonance associated with the shaker and armature, and the narrow-band filter within the feedback loop and determine what has happened to the envelope. We assume each sideband signal becomes multiplied by a factor α , less than unity, relative to the amplitude of the carrier, that the lower sideband signal is shifted by a total lead angle θ , and that the upper sideband is shifted by a total lag angle also of magnitude θ . This yields a signal of form

$$\begin{aligned} v'_{am} &= V \left\{ \cos 2\pi f t + \frac{\alpha m}{2} \cos[2\pi(f + f_m)t - \theta] \right. \\ &\quad \left. + \frac{\alpha m}{2} \cos[2\pi(f - f_m)t + \theta] \right\} \\ &= V[1 + \alpha m \cos(2\pi f_m t - \theta)] \cos 2\pi f t \end{aligned} \quad (8)$$

(U) We see that the envelope is diminished by a factor α , the same as the sidebands, and delayed by a lag angle equal to the shift angle of the sidebands, but equivalent to a much longer time interval. In fact, if the upper half of the selectivity curve of the combined

filters plus any mechanical resonance were slid along a linear frequency scale to the origin, it would become the response curve of the envelope.

(U) In addition, the averaging network will diminish the envelope after detection, in accordance with an additional factor δ , less than unity, and delay it by an additional angle θ . Finally, we throw in an additional factor B to account for any additional amplifier gain at either the envelope frequency or the carrier frequency.

(U) Before attempting a Nyquist plot, we must express the foregoing in complex exponential or rotating vector form as opposed to dealing only with the projection on the axis of reals. Rather than by Equation (6), the perturbing voltage is expressed by

$$v_m = V_m e^{j2\pi f t} \quad (9)$$

(U) The loop gain is measured with the averager disconnected from the mixer, but it is assumed that the mixer, which is inserted in the circuit merely to facilitate the analysis, has no loading effect on the averager. The output voltage to this dummy load is

$$v_d = \alpha_m B V_m e^{-j(\theta+\phi)} e^{j2\pi f t} \quad (10)$$

and consequently, the loop gain is

$$A = \frac{v_d}{v_m} = \alpha_m B (V/V_m) e^{-j(\theta+\phi)} \quad (11)$$

(U) Let us complete the feedback loop. The signal v_d delivered now to the mixer is given by

$$v_d = A(v_m + v_d) \quad (12)$$

from which the gain with feedback becomes

$$G = \frac{v_d}{v_m} = \frac{A}{1 - A} = \frac{\alpha_m B (V/V_m) e^{-j(\theta+\phi)}}{1 - \alpha_m B (V/V_m) e^{-j(\theta+\phi)}} \quad (13)$$

where, for automatic control, the circuit is connected that for low frequencies A is negative. Then, at these frequencies, if A is large, G has unity magnitude, maintaining v_d equal in magnitude to v_m , so that the signal delivered to the shaker is free of the corresponding fluctuations in envelope.

(U) The Nyquist plot is a plot of the complex quantity A versus frequency. Three ex-

amples are given in Figure 4. The phase angle $\theta+\phi$ increases uniformly with envelope frequency and the product α_m eventually decreases with frequency. The typical behaviour is a spiral about the origin. The case for which the plot passes through the 1, 0 point (Figure 4b) is the theoretical landmark between the stable and the unstable. At the frequency corresponding to this point, G is infinite, and a sinusoidal variation in envelope can sustain itself without any dependence on the perturbing input. If the curve encircles the 1, 0 point as in Figure 4c it follows from the theory of residues in the complex plane that there is at least one pole (i.e. G is infinite) for a complex frequency corresponding to a sinusoid increasing exponentially with time. This will increase beyond limit or until the system is overloaded. The system is unstable. Finally, if the curve neither passes through the 1, 0 point nor encircles it (Figure 4a), any pole corresponds to a sinusoid decaying exponentially with time, and the system is stable.

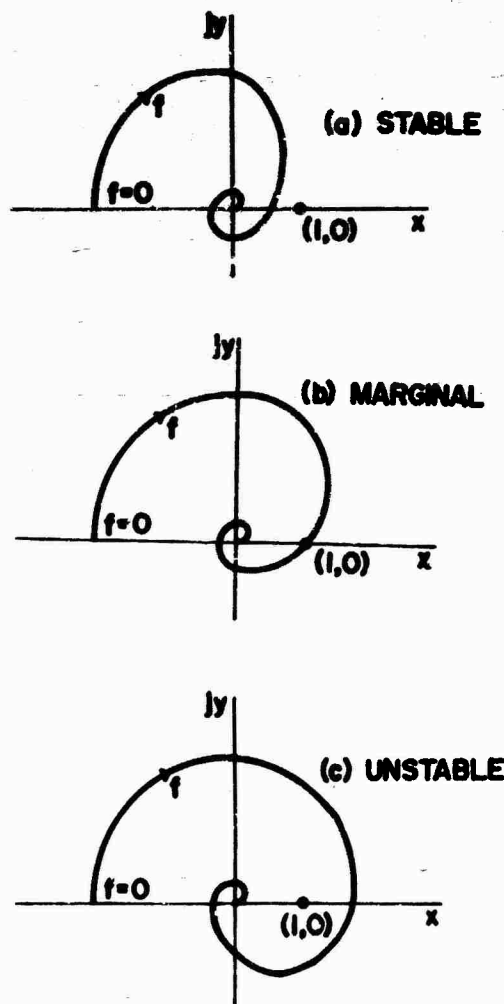


FIGURE 4 NYQUIST

(U) For most practical purposes, the system will be stable if the loop gain versus frequency decreases below unity before the phase shift reaches 180 degrees. Referring back to our analysis of modulation, filtering and detection, we can readily show that a narrow band filter consisting of a high-Q simple resonant circuit, acting on the modulated carrier, is equivalent to a single R-C low-pass filter beyond the detector and produces a 90 degree shift of the highest frequencies in the envelope. Such a filter plus a mechanical resonance of comparable bandwidth are equivalent to two cascaded R-C low-pass filters, with a total phase shift of 180 degrees. If, now, the averaging network is an actual R-C low-pass filter with a 3dB loss frequency in the same range as the others, the total is 270 degrees, and the phase shift as a function of frequency will reach 180 degrees before the loop gain decreases very much. With any practical loop gain, the system is unstable.

(U) In typical situations, the phase shift may be even more rapid. A narrow band filter may involve more than one tuned circuit and hence produce more phase shift in the pass band. (However, this may result in holes in the response in the crossover frequency regions when the various narrow bands are summed to reconstruct a broad band signal.) Any additional delay or phase lag in the practical feedback loop compounds the problem. To stabilize the feedback loop, it becomes necessary to lower the 3 db frequency of the averaging circuit until the loop gain decreases below unity before the filter, any mechanical resonance and any additional delay produce as much as 90 degrees shift. This in effect usually requires that $1/2\pi fC$ must be less than R in the R-C averaging circuit for f much less than half the bandwidth B of the narrow band filter.

$$1/2\pi fC < R \text{ for } f \ll B/2 \text{ or } \pi BCR \gg 1. \quad (14)$$

This is roughly equivalent to saying that the time-bandwidth product must be much less than unity, but the reasons at this point are stability and stability margin rather than statistical significance.

(U) There will be minor difference according to whether the averager is an R-C low pass filter or utilizes a true integrator. It is readily shown that the complex ratio of the output voltage of a single R-C low pass filter to the input voltage is

$$\frac{V_o}{V_i} = \frac{1/j2\pi fC}{R + 1/j2\pi fC} = \frac{1}{1 + j2\pi fCR}, \quad (15)$$

which approaches an inverse proportionality to frequency with a 90 degree phase lag. For the averager involving a true integrator, let the applied voltage be

$$V_i = e^{j2\pi ft} \quad (16)$$

The average over a duration T is related to the input by

$$\begin{aligned} \frac{V_o}{V_i} &= \frac{1}{T} \int_0^T e^{-j2\pi f(t+T)} e^{j2\pi ft} dt \\ &= \int_0^T \frac{1 - e^{j2\pi fT}}{2\pi f} dt \end{aligned} \quad (17)$$

(U) This tends to follow the same trend, but there is a cyclic variation in magnitude and phase according to whether f is such as to make T an integral number of periods. This is clearly the more complicated behaviour.

(U) There will also be minor differences according to whether there is a linear or square law detector, whether the source of signal in practice is random or pseudorandom, and whether a mechanical resonance is centered in the narrow band.

STABILITY WITH A RANDOM OR PSEUDO-RANDOM SOURCE

(U) The conclusions in the previous section about loop gain and stability would be unaltered if there were two or more perturbing frequencies or if the source supplied a modulated sinusoid with a complex wave envelope. Consequently, if a very slow single-frequency sweep were superposed on a random excitation, the stability criteria would apply accurately--at least when the signal frequency coincides with the center of a symmetrical narrow band.

(U) With a pure random signal, the envelope fluctuations result, not from interactions of sideband signals with the carrier, but from beating of one sideband signal with another. As the widest separation of such signals in frequency is twice the maximum separation from the carrier when present, the envelope fluctuations may be expected to extend higher in frequency. However, there is no reason to expect the stability criteria to be affected by more than a factor of two.

(U) Actually, a narrow band random voltage can be expressed as

$$V = V \cos(2\pi ft - \phi) \quad (18)$$

where both V and ϕ are random functions of time. While this can not be expressed in terms of a modulated carrier as in Equation (7), there is a similarity of form.

(U) A rigorous treatment of the pure random case in statistical terms would involve more sophisticated concepts than we have used in this

paper, and the existence of a nonstationary signal when the averaging time is short and level corrections are large. However, we can obtain a qualitative feeling for the stability problem by noting that the autocorrelation function of the output of a narrow band filter is an exponentially decaying oscillatory function of time delay. So also is the autocorrelation function of the envelope, but transposed to lower frequencies. Accordingly, if the averaging time is so short that the delay of the feedback signal corresponds to a large value of the autocorrelation function, the phasing may be such as to cause instability. There is no reason to expect markedly different behaviour with a pseudo random excitation.

DISTRIBUTION DISTORTION

(U) But were stability may not be enough. The effect of negative feedback in the frequency range in which it is effective is to eradicate any fluctuations in the envelope, whatever the origin. If A in Equation (13) is negative and large this implies that the narrow band peaks resulting from a random input will all be controlled to almost the same level. The distribution will tend to become similar to that of a sine wave, as in the section on equalization without feedback. If, however, the loop gain A should be positive in any frequency range, even though no instability results, this implies that the range of peak levels will be spread. The distortion will be of the opposite kind. Consequently, for the narrow band distribution to remain accurately Gaussian, the loop gain must be kept close to zero by the averaging circuit except at very low frequencies of the envelope.

CONCLUSION

(U) The familiar criterion expressing the uncertainty of a power spectral density estimate in terms of a time bandwidth product is not directly applicable to the typical automatic equalizer. It is ordinarily desirable to have the product large, but for reasons of stability, stability margin and narrow band Gaussian behaviour rather than statistical significance.

(U) Pseudo-random excitation may find useful applications in vibration testing, but there is no reason to believe that it will lead to a significant increase in the rapidity of automatic equalization. When test times become so short that equalization time becomes a serious matter, the test conditions may be questionable. Even if it were possible to equalize to perfection instantaneously at the beginning of test, damage to the test item is likely to be far from reproducible. For qualification purposes, it is generally desirable to have some margin built into the test conditions--in level, duration or both.

(U) Finally, not all pseudo-random signals proposed for application to vibration testing satisfy the criterion of a Gaussian narrow band distribution. If the criterion is to be vio-

lated, this should be done consciously for the sake of attainable and worthwhile advantage.

BIBLIOGRAPHY

- G. C. Anderson, B. W. Pinnie and G. T. Roberts, "Pseudo-Random and Random Test Signals," Hewlett-Packard Journal, September, 1967.
- C. P. Chapman, "A Digitally Controlled Vibration or Acoustics Testing System: Part I," Proc. 15th IES Annual Technical Meeting, April, 1969.
- W. D. T. Davies, "Generation and Properties of Maximum Length Sequences, Part II," Control, July, 1966.
- W. D. T. Davies, "Generation and Properties of Maximum Length Sequences, Part III," Control, August, 1966.
- C. L. Heizman, "A Digitally Controlled Vibration or Acoustics Testing System: Part III," Proc. IES Annual Technical Meeting, April, 1969.
- D. F. Hillyer, Jr., "An Automatic, Adaptive Servo Control for Stochastic Processes, Part I: Journal of the IES, February, 1966.
- D. F. Hillyer, Jr., "An Automatic, Adaptive Servo Control for Stochastic Processes, Part II," Journal of the IES, April, 1966.
- A. G. Ratz, "Statistical Effects in Automatic Random Equalizers," Trans. IEEE, Vol. IM-16, No. 4, 1967.
- A. G. Ratz, "The Speed of Response of an Automatic Random Equalizer," ISA Transactions, Vol. 5, October, 1966.
- A. G. Ratz, "Random Vibration Test Systems Using Digital Equalizers," Proc. 16th IES Annual Technical Meeting, April, 1970.
- J. Shipley, "A Digitally Controlled Vibration or Acoustics Testing System: Part II," Proc. IES Annual Technical Meeting, April, 1969.

A REGRESSION STUDY OF THE VIBRATION RESPONSE OF AN EXTERNAL STORE

Carl A. Golueke
Air Force Flight Dynamics Laboratory
Wright-Patterson Air Force Base, Ohio

Recent vibration prediction techniques for flight vehicles in their preliminary design stages oftentimes consider dynamic pressure as an important parameter related to excitation and surface density as a significant parameter related to vibration response. This paper presents the results of a statistical study in which a stepwise regression computer program was used to determine vibration amplitudes as a function of dynamic pressure and structural surface density. It was determined that vibration amplitudes increased with dynamic pressure, and for the case studied, the vibration response was found to be related to dynamic pressure raised to a power ranging between one and two. Dynamic pressure was effective only above 80 Hz. The effects produced by adding a surface density parameter were mild. The use of surface density weighting in the prediction equation improved the results in the frequency range from 50 to 630 Hz.

INTRODUCTION

Vibration prediction for flight vehicles in their early design stages is very difficult, especially for the higher frequency regime. One difficulty is the lack of design detail which is necessary for analytical approaches; therefore, one is forced into using empirical methods which are dependent upon past measurements. A review and assessment of the various vibration prediction methods can be found in Ref. [1].

It is the purpose of this paper to develop more confidence in the empirical approach in the area of higher frequencies by using flight test data in which dynamic pressure and surface density are known. Statistical confidence levels are also presented to permit a more conservative vibration prediction.

A well known prediction scheme is the Mahaffey-Smith method, Ref. [2]. This method follows the concept of first predicting the sound pressure level distribution over the vehicle in each octave band and then determining the corresponding octave band acceleration at a particular confidence level from plots. This method is convenient to use, but it does not include provisions for accounting for structural differences.

In order to account for some of the structural differences, Franken, Ref. [3],

suggested classifying missile structures into categories based on weight parameters and using this in his vibration prediction method. Piersol, Ref. [4], also suggested classifying aircraft structures into categories based on mass surface densities and using this in his prediction equation. Very little experience has been obtained on complex aeronautical vehicles to determine the validity of this approach, and therefore, the following study was conducted using flight test data from a relatively complex structure as basic input data.

APPROACH

Data from a previous flight test measurements program conducted by the Air Force Flight Dynamics Laboratory was used. The vibration data were obtained from external wing and fuselage mounted munitions stores. The selection of this particular data was based upon the fact that almost all of the excitation was due to boundary layer phenomena, and the stores contained accelerometers that were mounted on distinctly different types of structure within the stores. The data included flight conditions from Mach 0.65 to Mach 0.88 at 3,000 foot altitude, and it was analyzed in one-third octave bands. Eight pickups were mounted on identical light structure. Four pickups were mounted on medium structure. Three pickups were mounted on heavy structure. The pickups were mounted in the vertical, lateral, and

Preceding page blank

longitudinal direction with respect to the store. For the purpose of this paper, the light structure will be referred to as the bulkheads, the medium structure as trusses, and the heavy structure as hardbacks. The hardback is the main load carrying structure of the store. Fig. 1 is a photograph of the bulkhead. The thickness of the panel was 0.060 inches and the thickness of a channel behind the panel (not shown) was also approximately 0.060 inches. Fig. 2 is a photograph of the truss with a web thickness of approximately 0.35 inches. Fig. 3 is a photograph of the hardback and the thickness of the material at the accelerometer location was approximately 0.68 inches. Surface densities of 1.8, 5, and 10 lbs/sq ft were calculated for the bulkhead, truss, and hardback respectively.



Fig. 1 - Accelerometer Location on Bulkhead (Light Structure)



Fig. 2 - Accelerometer Location on Truss (Medium Structure)



Fig. 3 - Accelerometer Location on Hardback (Heavy Structure)

Fig. 4 shows a three dimensional plot of the average vibration amplitudes as functions of frequency and airspeed for all fifteen accelerometers. The envelope peak in the 25 to 31.5 Hz range is a normal mode of the store and its suspension system. Fig. 5 shows individual spectra for the average amplitudes of each of the three types of structures. It may be noted from these curves that the heavier, more massive hardback structure responds less than the other structures in the 40 to 2500 Hz range. This indicates that a factor such as surface density (SD) can be used for increasing the accuracy of a prediction technique. However, it is also to be noted that the use of this factor can result in errors in certain frequency ranges, e.g., the 530 to 1250 Hz range where the truss response exceeded the bulkhead response for the type of structure being considered.

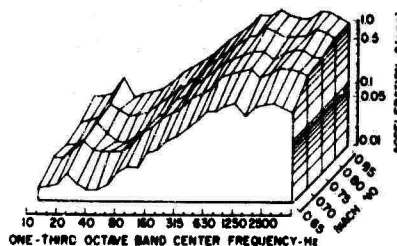


Fig. 4 - Mean Acceleration Amplitudes of Munitions Stores for All Accelerometers, Frequency Bands, and Airspeeds

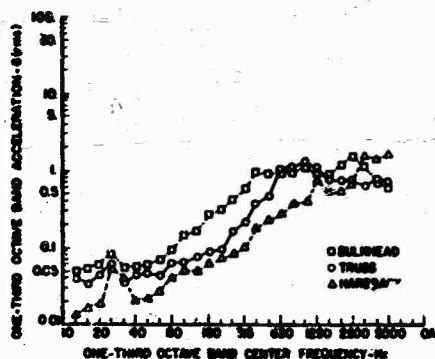


Fig. 5 - Average Vibration Amplitudes for Each of the Three Structures

In order to further examine the use of SD for vibration prediction purposes, a stepwise regression computer program was used in an analysis with three variables: dynamic pressure, surface density, and vibration amplitude. The regression technique is a useful tool which computes a sequence of multivariate linear regression equations in a stepwise manner. At each step, one variable is added to the regression equation. The variable added is the one which results in the greatest reduction in the error sum of the squares. Equivalently, it is the variable exhibiting the highest correlation after partialing on the variables which have already been added.

STEPWISE REGRESSION ANALYSIS

The basic equation was of the form

$$G_{rms} = K \frac{q^a}{(SD)^b}$$

where "K" is a regression coefficient, "b" and "a" are exponents to be determined, " G_{rms} " is the one-third octave band acceleration, "q" is the dynamic pressure in lbs/sq ft and "SD" is the structural surface density in lbs/sq ft. For this study, because of the complexity of the structure, the thickness of the structure to which the accelerometer was attached was used for calculating "SD". The variables in this equation were transformed into logarithmic form to obtain the following linear regression equation

$$\log G_{rms} = \log K + a \log q - b \log SD.$$

RESULTS

The above program was used to determine the multiple correlation coefficient "R" within the frequency range of 40 to 630 Hz. The results are shown in Fig. 6. The correlation trend curves were constructed from a third degree polynomial curve-fitting program. The curves indicate the effectiveness of using

"q" only or "SD" only or both. A much better correlation is obtained by using both in the region below 630 Hz. It is to be realized that these curves contain averaged results from all of the pickups at each 0.05 Mach increment. It is also to be noted that the correlation with "q" increases toward the higher frequencies, and the correlation with "SD" decreases toward the higher frequencies.

The regression program also calculates the "SD" exponent and its associated standard deviation. Fig. 7 is a plot of this exponent, and it indicates that it is quite small (less than 0.25).

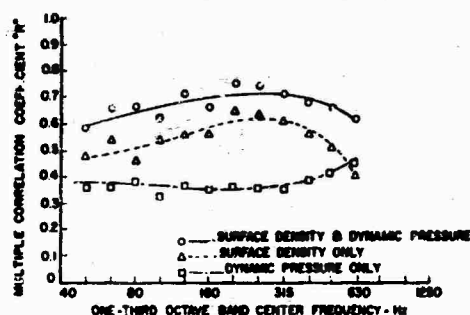


Fig. 6 - Trend Curves for the Effect of Using Dynamic Pressure, Surface Density or Both

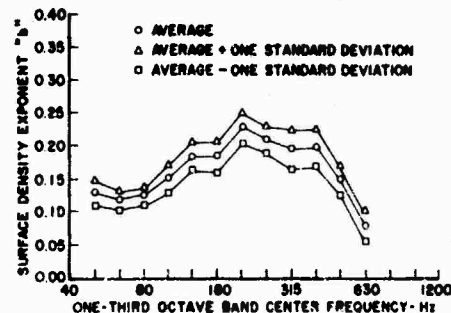


Fig. 7 - Surface Density Exponent "b" as a Function of Frequency

In order to investigate the correlation with dynamic pressure and to establish what frequency regions the correlations were high and low, an analysis was accomplished by using the output of each pickup for each of the six airspeeds in each frequency band thus resulting in 405 separate curves. High correlations were found in all bands above 80 Hz. Fig. 8 shows this characteristic for the average R of the fifteen pickups.

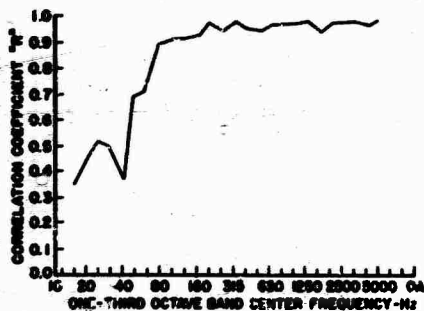


Fig. 8 - Correlation of Dynamic Pressure with Vibration Response

The regression coefficient (K) and the exponent of dynamic pressure were obtained from the program for each frequency band and for all fifteen pickups. The regression coefficient ranged from 0.016×10^{-5} to 13.01×10^{-5} . The exponent of "q" ranged from 1.32 to 2.04. There was no distinct trend in the "K" and "a" values in adjacent frequency bands over the full frequency range.

Table 1 shows the values of the regression coefficients and the 60% and 95% confidence limits. Also, the values for the exponent of dynamic pressure and the exponent for the surface density are shown in the table. Applications of the results of the regression analysis are shown in Fig. 9. This plot shows the comparison of the measured average vibration amplitude with the results of the regression analysis for a "q" of 1025 lbs/sq ft and 564 lbs/sq ft. In general, there is good agreement between the average values of measured data and the results of the regression analysis.

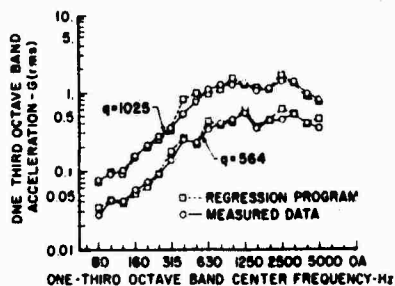


Fig. 9 - Comparison of Measured Average Vibration Amplitudes with Results of the Regression Analysis

A plot was prepared (Fig. 10) to show the scatter in the data and to compare the regression line, the 60 percent confidence line, and the 95 percent confidence line with all the measured data points at 0.75 Mach at 3000 feet

altitude. The dynamic pressure under this flight condition was 751 lbs/sq ft.

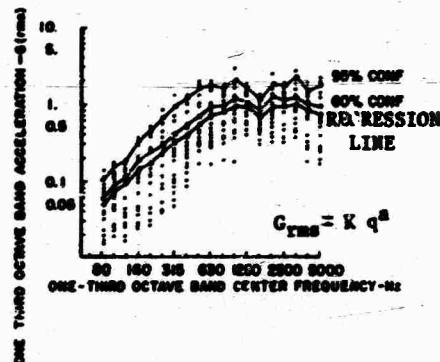


Fig. 10 - Regression Line and Confidence Limits when using the Regression Model for a Dynamic Pressure of 751 lbs/sq ft as Compared with the Measured Data

LIMITATIONS

The following limitations apply to the results of this study:

- Extrapolations below 80 Hz are not recommended.
- "q" ranges are between 500 and 1000 lbs/sq ft only
- The data used in this study was from a store configured without tail fins. In general, application of the results of this study should be limited to stores without tail fins. Further work, using data from several stores, is required for a more general vibration prediction method. The reason is that the in-flight fluctuating pressure environment, which is the principle source of excitation, is influenced strongly by the store suspension racks which are standard equipment and commonly used for many types of stores. For the store in this study, the fluctuating pressure coefficient P/q (root mean square fluctuating pressure divided by the dynamic pressure) was found to range from .011 to .02, except in areas near the racks and away braces [Ref. 5]. Measurements of flow turbulence aft of store suspension racks have indicated $P/q = .03$ in the transonic flight speed range. Stores with tail fins which are subjected to this high level of turbulence generally experience higher amplitudes of vibration than stores without tail fins.

CONCLUSIONS

This study presents a detailed empirical structuring of measured data to formulate a vibration prediction equation which contains a

TABLE I

NUMERICAL VALUES FOR $G_{rms} = K \frac{q^a}{SD^b}$					
FREQ.	$K \times 10^{-5}$			"a"	"b"
	K	K 60% CONF.	K 95% CONF.		
80	0.052	0.059	0.126	1.710	0.146
100	0.829	1.010	2.190	1.344	0.158
120	0.088	0.112	0.259	1.692	0.169
160	0.106	0.148	0.379	1.718	0.187
200	0.016	0.023	0.057	2.041	0.201
250	0.135	0.202	0.556	1.761	0.212
315	0.284	0.415	1.167	1.696	0.216
400	0.627	0.815	2.361	1.701	0.204
500	0.136	0.188	0.494	1.896	0.164
630	0.313	0.359	0.864	1.832	0.071
800	0.996	1.121	2.261	1.678	0
1000	1.373	1.603	3.695	1.645	0
1250	13.009	13.541	22.880	1.320	0
1600	0.396	0.403	0.676	1.805	0
2000	4.465	5.050	10.160	1.462	0
2500	2.735	3.269	6.483	1.555	0
3150	5.582	6.651	14.336	1.444	0
4000	3.694	4.302	7.538	1.470	0
5000	4.393	5.737	14.370	1.422	0

regression coefficient, a dynamic pressure exponent, and a surface density exponent. The results indicate that this approach is reasonable for the type of external store under consideration. It is shown that the dynamic pressure is closely correlated with amplitudes of vibration response throughout the frequency range of 80 to 5000 Hz. The effect of using a surface density parameter appears desirable only between 50 and 630 Hz. It is suggested that further similar efforts be conducted on

other structures to gain more statistical confidence.

ACKNOWLEDGEMENTS

Appreciation is expressed for the valuable assistance provided by R. Merkle and W. Stromberg of the Air Force Flight Dynamics Laboratory.

REFERENCES

1. H. Himmelblau, M. Fuller, T. Scharton, "Assessment of Space Vehicle Aeracoustic - Vibration Prediction Design and Testing," NASA CR-1596, Langley Research Center (1970)

2. P. T. Mahaffey and K. W. Smith, "A Method for Predicting Environmental Vibration Levels in Jet-Powered Aircraft," Noise Control 6, 168 (1960)

3. P. A. Franken, "Sound Induced Vibrations of Cylindrical Vehicles," J. Acoust. Soc. Am, 34 453-454 (1962)

4. A. G. Piersol, W. F. van der Leun, "Statistical Analysis of Flight Vibration and Acoustic Data," AFFDL-TR-68-92 (1970)

5. R. N. Bingman, "Aero-Acoustically Excited Vibrations of Internal Stores on Fighter Aircraft," Proceedings of the Aircraft/Stores Compatibility Symposium, Volume VI (1969)

DISCUSSION

Mr. Hughes (Naval Weapons Evaluation Facility): Could you define the surface density function?

Mr. Golueke: Some call it surface mass density. We found intuitively that things that are extremely heavy, especially in the high frequency region, do not tend to respond as much as some real light structural elements. In this particular study we took the thickness of the immediate structure to which the accelerometers were attached and used that as a function. When that mass density increased, it was in the denominator, it meant that the vibration level was decreasing. We looked at this in the regression study to see how much it goes down, if it is twice as thick does it go down to half as much? No it does not, only to a factor of about 0.25. We have been doing this for a long time even in our test specifications. All this says is that we do not have to vibrate a great big heavy object as much at high frequencies because the energy does not come through.

Mr. Curtis (Hughes Aircraft Company): I noticed that you did not use a Mach number in the regression analysis. Was this for some conscious reason or for convenience?

Mr. Golueke: No, fortunately or unfortunately, we always flew at 3,000 ft. so the dynamic pressure at a Mach number was directly correlated. You could not take a Mach number. We stayed at this same altitude so whether you use a q or a Mach number these coefficients will be different. But had we gone to several different altitudes we should have used a q. So I related it to the q. Actually we did go to some other altitudes.

Mr. Clevenson (Langley Research Center): Did Piersol do this regression analysis for you?

Mr. Golueke: No, we did that separately. I mentioned in the first part of the paper that we noticed that Piersol in his formulations used the surface density function, and we checked it out separately.

Mr. Clevenson: We enlisted the aid of Piersol in doing some similar regression analyses for predicting the environment of spacecraft of launch vehicles. He used other vehicle data to predict the Lunar Orbiter vibration environment. In a paper that I gave a couple years ago we showed that regression analysis usually ends up, as it did for the Lunar Orbiter, very very conservative giving values much higher that would be actually experienced in some cases. You did not really point out where this regression analysis would be useful other than after the fact.

Mr. Golueke: That is right. I read that paper. That regression analysis was only for that configuration. I would like to emphasize that this is good only for this store, and as I mentioned in the beginning, we are looking for trends and you might be several thousand per cent off trying it some place else.

Mr. Martin (Langley Research Center): From the table where you listed the different A's and B's and so on, are you using a different regression model for each frequency band in making these final predictions?

Mr. Golueke: No, the model is the same.

Mr. Martin: Did you use different exponents for each frequency band?

Mr. Golueke: We use the model separately for 1/3 octave bands. One might look at a particular 1/3 octave band and find a high constant and a low exponent. In the next band it might be just the opposite. This regression program gives the best fit for that particular

situation. Each frequency band is separate.

Mr. Martin: Have you considered, or is it beyond the realm of possibility, including a frequency function in your regression model?

Mr. Golueke: Yes, we have considered that and we have noted some kind of a trend in these exponents, and we took the polynomial curve through the exponents to see if we could collapse a case into a more rational trend. It worked out pretty well, but I am not in a position to put that forth right now.

**FACTOR ANALYSIS OF VIBRATION SPECTRAL DATA
FROM MULTI-LOCATION MEASUREMENTS**

Robert G. Merkle
Air Force Flight Dynamics Laboratory
Wright-Patterson Air Force Base, Ohio

Factor analysis techniques are employed to classify a number of structural vibration spectra into a smaller number of groups in such a fashion that pairs of spectra selected from the same group have similar spectral profiles while pairs selected from different groups have dissimilar spectral profiles. These groups are compared with other classifications obtained by using various observable structural characteristics. To determine the applicability of such grouping to the vibration prediction problem, statistical tests are employed to determine whether measured vibration spectral densities and computed regression statistics relating vibration to dynamic pressure were significantly more uniform in value for spectra selected from within groups than for spectra selected from different groups.

INTRODUCTION

Vibration surveys of aircraft or geometrically complex extended structures of any kind are typically conducted by recording for several seconds instantaneous acceleration time history data from numerous vibration sensors installed at various locations and directions throughout the structure. Using computers or special analysis equipment, these random time series data are transformed to mean square acceleration per Hertz in each frequency band within the full range of interest. When plotted against frequency, these spectral values appear as an uneven sequence of relative maxima and minima of irregular amplitudes. The number, position, and magnitude of these spectral maxima and minima depend very strongly on (1) the spectral distribution of the input excitation forces, (2) the detailed local structural geometry in the neighborhood of the measurement point, and (3) the mass density, stiffness, and energy absorption characteristics of the materials from which the structure is made. For a given structural system or configuration, one might hypothesize that all of these geometric characteristics and structural parameters will affect the observed vibration spectra in such a fashion that the measured spectral plots can be classified into a rather small number of groups characterized by quite similar within-group spectral profiles and by very dissimilar between-group profiles. The purpose of this paper is to show how such a classification system for sensor locations can be obtained

from spectral data by using factor analysis techniques that are commonly employed to define a large number of interrelated variables in terms of a much smaller number of more or less independent underlying factors. Interrelations among several variables are expressed by coefficients or correlation which are computed for the spectra of all pairs of sensors. These coefficients range from +1 to -1, the +1 indicating a perfect matching of spectral peaks and valleys with proportional amplitudes, and a -1 indicating a perfect mismatching of peaks with valleys, and a zero indicating no consistent peak and valley relationship. Graphical illustrations of correlation between two spectra are shown in Figure 1. Each of the plotted observation points represent spectral values at the same frequency band for two different measurement locations.

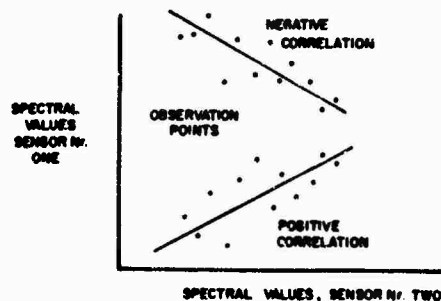


Fig. 1 - Scatter Plots

In practice, high negative correlation values do not occur. Coefficients of correlation among several spectra can be arranged into matrices in which both the row and column headings represent the same sequence of sensor location codes, and the value in each cell is the correlation between its row and column sensor locations. The matrix is thus symmetric.

The simplest possible illustration of a clear-cut factorization into two hypothesized groups would occur if a row-column sequence of sensor locations could be obtained in which the higher correlations occurred in two blocks along the principal diagonal and the lower correlations occurred in all other positions as shown in Table 1.

TABLE 1

CORRELATION MATRIX ILLUSTRATING TWO SIMPLE FACTORS

	A	B	C	D	E	F
A	1	0.72	0.63	0.09	0.04	0.01
B	0.72	1	0.51	0.15	0.16	0.09
C	0.63	0.51	1	0.14	0.15	0.09
D	0.09	0.15	0.14	1	0.57	0.63
E	0.04	0.16	0.15	0.57	1	0.72
F	0.01	0.09	0.09	0.63	0.72	1

Then pairs of sensor locations having row column intersections within any of these blocks would have highly correlated or similar spectral shapes while sensor pairs having row column intersections outside these blocks would have poorly correlated or dissimilar spectra. Sensor groupings obtained in this fashion are then compared with groupings obtained using various observable structural characteristics to ascertain their physical origin. Finally, the significance of such groupings in the vibration prediction area is examined.

SUMMARY OF VIBRATION DATA

The engineering results obtainable with this factor analysis technique are best described by illustrating its application to some specific data. Aircraft external store data used for this purpose consisted of twenty-seven third octave band spectral measurements taken at fifteen sensor locations at six different Mach numbers on munitions stores carried under the wings and fuselage of an RF4C aircraft. Some structural characteristics of the sensor locations are shown in Table 2. These structural characteristics which will be referred to later include the store location: wing or fuselage; the type of structure: bulkhead, truss, or keelspar; the directional orientation: vertical, lateral, or fore and aft; the axial position: forward, midsection, or aft; and the vertical position: upperside or lowerside.

TABLE 2

STRUCTURAL CHARACTERISTIC CODES FOR SENSOR LOCATIONS

STORE	TYPE OF	DIRECTION	AXIAL	VERTICAL
WING	TRUSS	VERTICAL	FORWARD	UPPERSIDE
1-Wing	2-Truss	3-Vertical	4-Forward	5-Upperside
6-Wing	7-Truss	8-Vertical	9-Forward	10-Upperside

STRUCTURAL CHARACTERISTICS OF SENSOR LOCATIONS

SENSOR NUMBER	1	2	3	4	5	6	7	8	9	10	11	12	13	14	15
TYPE STRUCTURE	0	0	0	0	0	0	0	1	1	1	1	1	1	1	1
TYPE DIRECTION	0	0	0	0	0	0	0	1	1	1	1	1	1	1	1
DIRECTION	0	1	1	1	1	1	1	0	0	0	0	0	0	0	0
AXIAL POS.	1	1	1	1	1	1	1	1	1	1	1	1	1	1	1
VERT. POS.	1	1	1	1	1	1	1	0	0	0	0	0	0	0	0

The third octave bands are the conventional ones centered at the following frequencies: 12.5, 16, 20, 25, 31.5, 40, 50, 63, 80, 100, 125, 160, 200, 250, 315, 400, 500, 630, 800, 1000, 1250, 1600, 2000, 2500, 3150, 4000, 5000 Hz. Complete spectral data from all fifteen sensors were taken at 3000 feet altitude at six airspeeds: Mach .65, .70, .75, .80, .85, .88, corresponding to dynamic pressures of 564, 654, 752, 856, 965, 1025 psf respectively.

COMPUTATION OF CORRELATION MATRIX

Spectral data at each Mach number can be arranged in a matrix of fifteen row variables each representing a vibration sensor and twenty-seven column observations each representing a spectral value at successive third octave frequency bands. The correlation matrix among the fifteen vibration sensor locations may be computed directly from this array through the following stepwise sequence of data processing operations. Step 1: Compute the mean value of each row and subtract this value from each element forming a modified row with zero mean. Step 2: Compute the mean square value of each modified row and divide its square root into each element forming a new row with a mean of zero and a mean square of one. These row elements are referred to as the standardized spectral values. Step 3: For each pair of rows compute all the cross-products of corresponding observations, then sum and average. The resulting value is the coefficient of correlation between the spectra of the two sensor locations associated with the selected rows. Step 4: The computed correlation coefficients for each pair of rows are then arranged in a fifteen by fifteen symmetric matrix. The off-diagonal elements are the correlation coefficients relating the row and column sensor locations and the diagonal elements are all ones, expressing the spectral correlation of each sensor location with itself. The correlation matrix for the spectra of the fifteen sensors at Mach .88 is shown in Table 3. Note that high and low values of the coefficients of correlation are more or less randomly distributed throughout the array. If the ordering of the matrix rows and columns were changed, the values of the matrix elements would appear in rearranged form.

For some new row column sequence, most of the higher valued matrix elements could be made to appear in blocks along the principal diagonal. The number of such blocks and the sensor locations assigned to each are obtainable by factor analysis techniques.

TABLE 3

CORRELATION MATRIX AMONG FIFTEEN VIBRATION SPECTRA

	1	2	3	4	5	6	7	8	9	10	11	12	13	14	15
1	1.0	.46	.34	.30	.26	.26	.26	.26	.26	.26	.26	.26	.26	.26	.26
2	.46	1.0	.34	.30	.26	.26	.26	.26	.26	.26	.26	.26	.26	.26	.26
3	.34	.34	1.0	.30	.26	.26	.26	.26	.26	.26	.26	.26	.26	.26	.26
4	.30	.30	.30	1.0	.26	.26	.26	.26	.26	.26	.26	.26	.26	.26	.26
5	.26	.26	.26	.26	1.0	.26	.26	.26	.26	.26	.26	.26	.26	.26	.26
6	.26	.26	.26	.26	.26	1.0	.26	.26	.26	.26	.26	.26	.26	.26	.26
7	.26	.26	.26	.26	.26	.26	1.0	.26	.26	.26	.26	.26	.26	.26	.26
8	.26	.26	.26	.26	.26	.26	.26	1.0	.26	.26	.26	.26	.26	.26	.26
9	.26	.26	.26	.26	.26	.26	.26	.26	1.0	.26	.26	.26	.26	.26	.26
10	.26	.26	.26	.26	.26	.26	.26	.26	.26	1.0	.26	.26	.26	.26	.26
11	.26	.26	.26	.26	.26	.26	.26	.26	.26	.26	1.0	.26	.26	.26	.26
12	.26	.26	.26	.26	.26	.26	.26	.26	.26	.26	.26	1.0	.26	.26	.26
13	.26	.26	.26	.26	.26	.26	.26	.26	.26	.26	.26	.26	1.0	.26	.26
14	.26	.26	.26	.26	.26	.26	.26	.26	.26	.26	.26	.26	.26	1.0	.26
15	.26	.26	.26	.26	.26	.26	.26	.26	.26	.26	.26	.26	.26	.26	1.0

FACTOR ANALYSIS SOLUTION

The high degree of intercorrelation among the fifteen sensor locations, shown in Table 3, indicates one or more common factors are influencing the spectral shape. The mathematical theory for determining both the number of such common factors and the relative influence of each factor on each of the sensor location variables is given by Harry H. Harman in Modern Factor Analysis, Ref. [1]. Basic concepts and their mathematical formulations are summarized in the appendix to this paper.

In terms of the factor analysis model, each standardized spectral value v_{ji} for sensor location j and frequency i can be expressed as a linear combination of a few standardized common factor spectral values F_{pi} and a unique factor spectral value U_{ji} :

$$v_{ji} = \sum_{p=1}^m a_{jp} F_{pi} + d_j U_{ji} \quad \begin{matrix} i = 1 \dots 27 \\ j = 1 \dots 15 \\ m=15 \end{matrix} \quad (1)$$

The computation of the original correlation matrix and the factor loading coefficients, a_{jp} and d_j , was carried out using program BMD 03M from Bio-medical Computer Programs, W. J. Dixon, editor, Ref. [2]. For the correlation matrix of Table 3, only three significant common factors were found. The loading coefficients, a_{jp} , having maximum variance (varimax), are shown in Table 4 as A, B, and C. The loading coefficients, d_j , associated with the corresponding unique factors are also shown, but an excellent approximation to the original correlation matrix could be obtained from the variables v_{ji} defined in terms of the common factor loadings alone. In mathematical terms, the coefficient of correlation r_{vjv_k} between spectrum v_j and v_k is given in terms of

the factor loading coefficients a_{jp} by

$$r_{vjv_k} = a_{j1} a_{k1} + a_{j2} a_{k2} + \dots + a_{jm} a_{km} \quad (1a)$$

When $k = j$ this expression defines the communality h_j of spectrum v_j

$$h_j = a_{j1}^2 + a_{j2}^2 + \dots + a_{jm}^2 = 1 - d_j^2 \quad (1b)$$

TABLE 4

FACTOR LOADINGS FOR FIFTEEN VIBRATION SPECTRA

SENSOR	COMMON FACTORS			UNIQUE FACTOR	SENSOR	COMMON FACTORS			UNIQUE FACTOR
	A	B	C			A	B	C	
1	.46	.34	.26	.26	9	.26	.26	.26	.26
2	.26	.26	.26	.26	10	.26	.26	.26	.26
3	.26	.26	.26	.26	11	.26	.26	.26	.26
4	.26	.26	.26	.26	12	.26	.26	.26	.26
5	.26	.26	.26	.26	13	.26	.26	.26	.26
6	.26	.26	.26	.26	14	.26	.26	.26	.26
7	.26	.26	.26	.26	15	.26	.26	.26	.26
8	.26	.26	.26	.26					

Since the sums of the squares of the loadings for each variable must equal one (geometrically they are direction cosines of angles between each of the factor axes and a line representing the variable), any factor with a loading greater than $\sqrt{.5} = .707$ must have a contribution to that variable exceeding that of all other factors combined. Applying the criteria to Table 4, one can see that factor A is characterized by sensors 2, 4, 6, 8, 9, and 10; factor B by sensors 1, 3, 7, and 13; and factor C by sensors 11, 14, and 15. Sensors 5 and 12 did not have predominant loadings on any one factor at Mach .88 for which these data are applicable. When the factor analysis of correlation matrices associated with the remaining five airspeeds were carried out, the same sets of sensors occurred together except for number 3 which dropped from large loadings on factor B to the last group (sensors 5 and 12) without dominant loadings on any factor. In Table 3, the correlation matrix was shown with the sensors in the sequence of arbitrarily assigned identification numbers. In Table 5 the same correlation matrix is shown with the sensors associated with factor A listed first, those with factor B listed next, then with factor C listed last, and the remaining sensors omitted. Note that in this rearrangement of the rows and columns of the correlation matrix, the highest correlations occur in the blocks along the diagonal with much lower correlations in the off-diagonal blocks. The mean correlation in the off-diagonal blocks is 0.49 and in the diagonal blocks is 0.81 excluding the unit self correlations along the principal diagonal. The high within-group spectral correlations occurring in the diagonal blocks of Table 5 certainly suggests the influence of some characteristics which are shared among the sensor locations within each associated group. What these characteristics are must be inferred by making various comparisons among the sensor locations within each of the groups and by contrasting locations from different groups. Structural features and excitation conditions

which are found to be homogeneous for within-group locations but heterogeneous among groups may provide a simple explanation for the factorization. In more complicated cases due to interaction effects, certain combinations of structural characteristics and excitation conditions, may be unique to one group with different combinations unique to other groups.

TABLE 5

CORRELATION MATRIX AMONG VIBRATION SPECTRA

	1	2	3	4	5	6	7	8	9	10	11	12	13	14	15
1	1.0	.48	.48	.48	.48	.48	.48	.48	.48	.48	.48	.48	.48	.48	.48
2	.48	1.0	.48	.48	.48	.48	.48	.48	.48	.48	.48	.48	.48	.48	.48
3	.48	.48	1.0	.48	.48	.48	.48	.48	.48	.48	.48	.48	.48	.48	.48
4	.48	.48	.48	1.0	.48	.48	.48	.48	.48	.48	.48	.48	.48	.48	.48
5	.48	.48	.48	.48	1.0	.48	.48	.48	.48	.48	.48	.48	.48	.48	.48
6	.48	.48	.48	.48	.48	1.0	.48	.48	.48	.48	.48	.48	.48	.48	.48
7	.48	.48	.48	.48	.48	.48	1.0	.48	.48	.48	.48	.48	.48	.48	.48
8	.48	.48	.48	.48	.48	.48	.48	1.0	.48	.48	.48	.48	.48	.48	.48
9	.48	.48	.48	.48	.48	.48	.48	.48	1.0	.48	.48	.48	.48	.48	.48
10	.48	.48	.48	.48	.48	.48	.48	.48	.48	1.0	.48	.48	.48	.48	.48
11	.48	.48	.48	.48	.48	.48	.48	.48	.48	.48	1.0	.48	.48	.48	.48
12	.48	.48	.48	.48	.48	.48	.48	.48	.48	.48	.48	1.0	.48	.48	.48
13	.48	.48	.48	.48	.48	.48	.48	.48	.48	.48	.48	.48	1.0	.48	.48
14	.48	.48	.48	.48	.48	.48	.48	.48	.48	.48	.48	.48	.48	1.0	.48
15	.48	.48	.48	.48	.48	.48	.48	.48	.48	.48	.48	.48	.48	.48	1.0

FACTOR INTERPRETATION

Table 6 shows the spectral groups and their structural characteristics taken from Table 2.

TABLE 6

STRUCTURAL CHARACTERISTICS OF GROUPED VIBRATION SPECTRA

	GROUP A					GROUP B					GROUP C				
SENSOR NUMBER	2	A	A	B	V	10	1	3	7	10	11	14	15		
TYPE STRUCTURE	0	0	0	0	1	0	0	0	0	1	0	0	0		
STORE LOCATION	0	0	0	0	1	0	0	0	0	1	0	0	0		
DIRECTION	1	1	1	1	V	V	V	V	V	V	1	1	1		
AXIAL POSITION	1	1	1	1	A	A	1	1	A	A	1	1	A		
VERTICAL POSITION	1	1	1	1	U	V	1	1	1	U	V	1	1		

None of these structural characteristics is unique to each group. Location is clearly not a basis of classification since both wing and fuselage positions occur in all three groups, likewise for axial position, since two of the three classifications occur in all three groups. Of the remaining structural characteristic codes, Group A contains only BLL and TVU combinations, Group B only BVL and KVV, and Group C only TLU and KLU. It is not intuitively evident why these structural combinations should result in the kind of spectral correlations actually observed. Before seeking a plausible rationale for explaining these observed spectral correlations in terms of structural characteristics and other possible parameters, inquiry should first be made as to whether the spectral correlations are related in any way to spectral levels or to various statistics relating vibration to airspeed variations. If this were the case, spectral correlations would have a strong bearing on the structural vibration prediction problem and further effort would be justified in seeking an engineering interpretation of the factor groupings.

AMPLITUDE LEVELS FOR CORRELATED VIBRATION SPECTRA

One might speculate from physical considerations that vibration amplitude levels would differ significantly between two groups of vibration spectra which exhibit high correlations (meaning similar spectral shapes) for within-group or intra-group data but low correlations (or dissimilar shapes) for between-group or inter-group data. One might also suppose that any pair of highly correlated spectra, both from within either one of these groups, would not differ appreciably in amplitude levels. Casting these conjectures into the null-hypothesis form for statistically testing the data at hand, results in the following six hypothesized contrasts in which the sensor location numbers in parentheses are to be replaced by spectral amplitudes for that sensor location number at the frequency band of interest.

There are no statistically significant differences between the mean vibration levels measured for groups ABC, i.e.:

$$(1) A-B = 1/6 (\#2 + \#4 + \#6 + \#8 + \#9 + \#10) - 1/3 (\#1 + \#7 + \#13) = 0$$

$$(2) A-C = 1/6 (\#2 + \#4 + \#6 + \#8 + \#9 + \#10) - 1/3 (\#11 + \#14 + \#15) = 0$$

$$(3) B-C = 1/3 (\#1 + \#7 + \#13) - 1/3 (\#11 + \#14 + \#15) = 0$$

nor do significant differences exist in the vibration levels between the two most highly correlated spectra within each group, i.e.:

$$(4) \text{Group A: } \#2 - \#4 = 0$$

$$(5) \text{Group B: } \#1 - \#7 = 0$$

$$(6) \text{Group C: } \#14 - \#15 = 0$$

These groups and spectral pairs were obtained from correlation and factor analysis for all six airspeeds not just the one illustrated above. To be useful in vibration prediction, the first three of these hypothesized zero contrasts should be rejected and the latter three not rejected since this would imply similar spectral amplitudes within groups of highly correlated spectra but significantly different amplitudes for poorly correlated spectra from different groups.

Since dynamic pressure constitutes the primary excitation for the measured data, the statistical tests of these six contrasts should account for variations in this quantity. The statistical theory for tests of this kind is given by Henry Scheffe in "Analysis of Variance," Chapters 3 and 6, Ref. [3]. The actual computations were carried out using the General Linear Hypothesis, Program BMD 06V, from Ref. [2] cited earlier. All six of the above

contrasts were tested at each of the 27 third octave frequency bands using the dynamic pressures associated with each of the air-speeds.

The basic vibration prediction model used in this program is:

$$v_{ji}(q) = a_{ji} + b_i(q - \bar{q}) \quad \begin{matrix} i = 1, \dots, 27 \\ j = 1, \dots, 15 \end{matrix} \quad (2)$$

where v_{ji} is the vibration spectral value for the j th sensor at the i th frequency band, q is the dynamic pressure, \bar{q} the mean dynamic pressure, the b_i are the regression coefficients expressing optimal linear relations between v and q at each frequency band and the a_{ji} are the regression constants, one for each sensor and frequency band denoted by the subscripts, j and i respectively. By using a logarithmic transformation of the input data, the resulting expression is

$$\log v_{ji}(q) = a_{ji} + b_i(\log q - \log \bar{q})$$

or equivalently

$$v_{ji}(q) = 10^{a_{ji}} (q/\bar{q})^{b_i} \quad \begin{matrix} i = 1, \dots, 27 \\ j = 1, \dots, 15 \end{matrix} \quad (3)$$

where the \bar{q} must now be interpreted as the geometric mean of the dynamic pressures. This seems to be a more reasonable prediction model for this kind of engineering data. Estimates of linear combinations of the a_{ji} as well as individual values are easily obtained. The six contrasts of the previous paragraph are clearly special linear combinations of particular interest. Applying appropriate statistical tests at the 0.995 confidence level for all six contrasts simultaneously but for each frequency separately, or about 0.87 for all contrasts for all frequencies, one finds the following results. Of the 27 frequency bands, vibration levels differ significantly at 19 for A-B, at 17 for A-C, and at 18 for B-C. However, vibration levels also differ significantly between the two most highly correlated spectra within one of the paired groups at 13 of the 19 frequencies for A and B, at 14 of the 17 for A and C, and at 12 of the 18 for B and C. Thus, the first conjecture that vibration levels differ significantly between two groups of vibration spectra which exhibit high correlations for within-group pairs and low correlations for between-group pairs does not hold consistently at all frequencies and where it does hold the second conjecture, that pairs of highly correlated spectra from within a group would not differ significantly in amplitude levels, usually fails.

REGRESSION STATISTICS FOR CORRELATED VIBRATION SPECTRA

In the course of preparing a companion paper for this symposium, Carl Golueke of the

Air Force Flight Dynamics Laboratory, has obtained 285 regression equations predicting vibration spectral values as functions of dynamic pressure for each of the same fifteen sensor locations at nineteen third octave frequency bands from 80 to 5000 cps, Ref. [4]. (The lower 8 third octave bands were found, as expected, to have markedly lower vibration/dynamic pressure correlations and correspondingly poorer prediction functions than the higher frequency range.) In the simple linear regression formula $v = a + bq$, the values of the variable v and q were replaced by their logarithms in computation to form the following equivalent prediction function which seemed more appropriate for this type of engineering data

$$v_{ji} = 10^{a_{ji}} q^{b_{ji}} \quad \begin{matrix} i = 1, \dots, 19 \\ j = 1, \dots, 15 \end{matrix} \quad (4)$$

where the v_{ji} are the vibration spectral values for the j th sensor and the i th frequency, q is the dynamic pressure, and the a_{ji} and b_{ji} are the regression components relating v to q at the j th sensor and the i th frequency. The actual computations were done using the stepwise regression program, BMD-02R given in Ref. [2]. Five outputs of the program are of interest:

- r : the coefficient of correlation between vibration amplitude and dynamic pressure
- a : the logarithm of the regression constant
- b : the exponent of the dynamic pressure
- s_b : the standard deviation of b
- s : the standard error of the estimate

Next, one might again conjecture that these values expressing the relationship between vibration and dynamic pressure might differ significantly between any two groups of vibration spectra which exhibit very high average correlations for within-group (intra-group) pairs of spectra but low average correlations for between-group (inter-group) pairs. Likewise, one might further suppose that the relationship between vibration and dynamic pressure does not differ significantly for the most highly correlated pair of vibration spectra selected from within any group. These hypotheses represent the same set of contrasts listed in the previous section except for replacement of the spectral amplitude values by one of the above regression statistics.

Again, the statistical tests were carried out using the same general linear hypothesis program, BMD-06V, and the same set of six contrasts used previously. This time the mathematical model is:

$$z_j(f) = c_j + d \log(f/\bar{f}) \quad j = 1, \dots, 15 \quad (5)$$

z_j = dependent variable, r , a , b , s_b , and s successively

c_j = regression coefficients for each one of 15 sensors

d = regression coefficient of the covariate $\log(f/\bar{f})$

f = frequency \bar{f} = geometric mean

The use of $\log f$ rather than f for the covariate serves both to reduce the extreme range of the frequencies (80 to 5000) and to make the third octave center frequencies equally spaced. Applying appropriate statistical tests at the 0.99 confidence level for all six contrasts simultaneously but for each variable separately, or about 0.95 for all contrasts for all variables, one finds that none of the variables r , a , b , s_b , and s , associated with the vibration-dynamic pressure relationship, differ significantly in value for any of the three group contrasts as conjectured. On the other hand, the two most highly correlated spectra in group B differ significantly in three of the variables r , s_b , and s contrary to the original hypothesis.

SUMMARY

In summary, the spectral profiles from twelve of fifteen locations on an aircraft external store can be classified into three groups characterized by quite similar within-group spectral profiles and by rather dissimilar between-group profiles. These groups of similarly shaped (highly correlated) spectral profiles do not consistently match up with variations in structural type, directional orientation, attachment location, or axial or vertical position of the measurement; nor are they associated with consistent differences in vibration amplitude levels across the frequency bands of interest; nor do they imply any corresponding association with the relationship between vibration and dynamic pressure.

From an engineering standpoint, the negative results obtained for vibration amplitude tests are by no means unexpected. Introducing a small amount of damping into a system, for example, will greatly reduce vibration amplitude values without noticeably affecting the general shape of the spectral profile. Furthermore, in view of the exceptionally high correlation between vibration amplitudes and dynamic pressure for this data [4], the results for the regression statistics tests should not differ from those for the vibration amplitude tests. As noted earlier, these tests were carried out only to take advantage of any positive results in formulating empirical vibration prediction functions.

None of the five structural character-

istics was found to be unique to any one of the three groups of similar spectral profiles. Two of them, store location and axial position, were found to be independent of the three correlated spectral groupings. Certain combinations of the remaining three structural characteristics were found to be unique to each group. However, because the eighteen possible combinations of three structural types, three directional orientations, and two vertical positions exceeded the fifteen locations instrumented, no really firm conclusions can be drawn in this area. Future analyses with larger numbers of sensor locations should yield the necessary clarifications.

The initial classification of spectral data into groups characterized by similar within-group profiles and dissimilar between-group profiles is the most notable result obtained in this data analysis program. The near identical groupings of sensor locations found at each of the six airspeeds greatly reinforces this conclusion. The existence of several sensor locations not clearly identified with any of the internally highly correlated groups is also to be expected. If vibration measurements at many locations are each thought of as a different linear combination of a relatively few underlying spectral profiles, then it is only reasonable to suppose that some of the measurement points will represent more or less equal contributions from each of these underlying profiles.

An extremely wide diversity of vibrational amplitudes and their associated spectral profile is characteristic of vibration surveys of high speed aircraft and other complex structures subject to high intensity excitation. The correlation and factor analysis techniques employed herein provide a means of quantifying the concept of spectral shapes and classifying them into distinct groups. In vibration surveys involving a hundred or more sensor locations, this can provide a very helpful means of organizing numerous vibration spectra into a much smaller number of meaningful categories for more detailed statistical and engineering analyses. Analyses which, when applied to more homogeneous groupings of spectral profiles, may well yield more meaningful results than would otherwise be the case. This should permit much deeper insight into the vibrational energy distribution in complex structures. Knowledge of this kind can, in turn, be quite useful both in designing reliable structures for operation in severe dynamic environments and in providing a more rational basis for locating vibration sensors in measuring the structural response to those environments.

APPENDIX

FACTOR ANALYSIS MODEL

The object of factor analysis is to define a large number of interrelated variables in terms of a much smaller number of more or less independent factors. The simplest mathematical model for describing a variable in terms of several others is the linear representation. For such a linear composite to be valid, however, all variable and factor measurements must be referenced to the same origin and scaled in the same units. To do this, one first subtracts from each observation x_i its mean value \bar{x} and then divides the resultant quantity by its standard deviation s_x , a measure of the dispersion or scatter in a set of observations. Thus transformed, the new standardized value expresses "distance" from the mean in standard deviation units. Expressed mathematically:

$$z_{ji} = (x_{ji} - \bar{x}_j) / s_{x_j} \quad \begin{matrix} i = 1 \dots N \\ j = 1 \dots n \end{matrix} \quad (1)$$

where

$$\bar{x}_j = \frac{1}{N} \sum_{i=1}^N x_{ji} \quad s_{x_j} = \frac{1}{N} \sum_{i=1}^N (x_{ji} - \bar{x}_j)^2$$

The classical factor analysis model may be written for the standardized value of the j th variable and the i th observation as follows:

$$z_{ji} = \sum_{p=1}^m a_{jp} F_{pi} + d_j U_{ji} \quad \begin{matrix} j = 1 \dots n \\ i = 1 \dots N \\ m < n \end{matrix} \quad (2)$$

In this expression F_{pi} is the standardized value of the common factor F_p for observation i , each of the m terms $a_{jp} F_{pi}$ represents the contribution of the corresponding factor to the linear composite, and the $d_j U_{ji}$ is the residual, specific, or unique contribution in the assumed representation of the observed measurement z_{ji} . In the geometric representation of this model, the unique factors are assumed to be mutually orthogonal and orthogonal to the common factors which are not necessarily assumed mutually orthogonal. Note that the representation is not unique since the total number of factors F_p, U_j exceeds the number of variables, z_j .

The complete set of n values for each of the N variables can be represented by the $n \times N$ matrix as follows:

$$Z = \begin{bmatrix} z_{11} & \dots & z_{1N} \\ \dots & \dots & \dots \\ z_{n1} & \dots & z_{nN} \end{bmatrix}$$

Similarly, the common and unique factors may be represented as

$$F = \begin{bmatrix} F_{11} & \dots & F_{1N} \\ \dots & \dots & \dots \\ F_{m1} & \dots & F_{mN} \end{bmatrix} \quad U = \begin{bmatrix} U_{11} & \dots & U_{1N} \\ \dots & \dots & \dots \\ U_{n1} & \dots & U_{nN} \end{bmatrix}$$

The coefficients of these factors in equation (1) may be represented by the n by m and n by n matrices as follows:

$$A = \begin{bmatrix} a_{11} & \dots & a_{1m} \\ \dots & \dots & \dots \\ a_{n1} & \dots & a_{nm} \end{bmatrix} \quad D = \begin{bmatrix} d_1 & \dots & 0 \\ \dots & \dots & \dots \\ 0 & \dots & d_n \end{bmatrix}$$

With these definitions, equation (1) may be written in matrix form

$$Z = AF + DU \quad (3)$$

The matrix of observed correlations among the variables can be defined in matrix notation by

$$R = ZZ' / N \quad Z' = Z \text{ transpose} \quad (4)$$

This is equivalent to the stepwise computational procedure given in a previous section entitled "Computation of Correlation Matrix".

If equation (3), the factor analysis model for the matrix Z , is substituted into this expression, we have

$$R = (AF + DU)(AF + DU)' / N$$

$$R = A(FF' / N) A' + A(FU' / N) D' + D(UF' / N) A' + D(UU' / N) D'$$

The first and last quantities in parentheses both having the same form as equation (4) are correlation matrices. The correlation matrix of the common factors is denoted by $\Phi = FF' / N$. The correlation matrix of the unique factors is an identity matrix since the unique factors are assumed to be uncorrelated, i.e., represented by mutually orthogonal axes. The remaining two terms in parentheses are both null matrices since the common and unique factors are assumed to be uncorrelated, i.e., mutually orthogonal. Thus, we have

$$R = A(FF' / N) A' + D(UU' / N) D' = A \Phi A' + DD' \quad (5)$$

If the common factors are also assumed to be uncorrelated or orthogonal

$$R = AA' + DD' \quad (6)$$

Clearly, the correlation matrix derived from the common factors only, is given by

$$R^* = AA' = \begin{bmatrix} a_{11} & \dots & a_{1m} \\ \dots & \dots & \dots \\ a_{n1} & \dots & a_{nm} \end{bmatrix} \begin{bmatrix} a_{11} & \dots & a_{n1} \\ \dots & \dots & \dots \\ a_{1m} & \dots & a_{nm} \end{bmatrix} \quad (7)$$

This matrix (equation 7) is the same as the former (equation 6) in the off-diagonal elements, but the diagonal elements, designated communalities, are numbers less than one. In terms of the matrix elements, they are given by

$$h_j^2 = \sum_{p=1}^n a_{jp}^2 \quad j = 1, \dots, n \quad (8)$$

These communalities are the squares of the correlations $r_{z_j z_1}$ between the total factor and the common factor representations of each of the variables as shown by the following:

$$\begin{aligned} \text{Given: } z_{j1} &= a_{j1}F_{11} + \dots + a_{jn}F_{n1} + d_j U_{j1} \\ z'_{j1} &= a_{j1}F_{11} + \dots + a_{jn}F_{n1} \end{aligned}$$

$$\begin{aligned} \text{then } r_{z_j z_1} &= \frac{\sum_{i=1}^n z_{ji} z'_{i1}}{\sqrt{\sum_{i=1}^n z_{ji}^2} \sqrt{\sum_{i=1}^n z_{i1}^2}} \\ r_{z_j z_j} &= h_j^2 / \sqrt{(1)(h_j^2)} = h_j \end{aligned}$$

The off-diagonal elements of equation (6) are, of course, the ordinary coefficients of correlation given in terms of the matrix elements for the variables j and k by

$$r_{z_j z_k} = \sum_{p=1}^n a_{jp} a_{kp} \quad (9)$$

NUMBER OF COMMON FACTORS

From matrix theory, it is known that the rank of AA' cannot exceed the rank of A which in turn cannot exceed its smaller dimension, in this case the number of columns n . Consequently, although the reproduced correlation matrix $R^* = AA'$ has order n equal to the number of variables, its rank cannot exceed n , the number of common factors. Since the number of common factors cannot be less than the rank of the reproduced correlation matrix, the minimum number of common factors must equal the minimum possible rank of the reproduced correlation matrix. Since the correlation matrix reproduced from the common factors differs from that reproduced from all the factors only in the diagonal elements, one of the major problems of factor analysis is to determine by how much the rank of a correlation matrix can be reduced from n by a suitable choice of communalities in the diagonal. The computation of such minimal rank communalities is so formidable even on modern computers that it is not normally attempted. Instead, they are approximated by the squared multiple correlations given by one minus the reciprocals of the corresponding elements in the diagonal of the inverse of the correlation matrix. The squared multiple correlations are known to be

lower bounds for true minimal rank communalities and approach the latter as the ratio of the number of factors to the number of variables approaches zero.

FACTOR SOLUTION

The solution for the a coefficients or loadings in the factor analysis model, equation (1), is an eigenvalue problem analogous to the one encountered in determining normal modes of vibration or principal axes of rotation in dynamics problems. The matrix equation in this case is

$$\begin{bmatrix} h_1^2 - \lambda_p & \dots & r_{1n} \\ \dots & \dots & \dots \\ r_{n1} & \dots & h_n^2 - \lambda_p \end{bmatrix} \begin{bmatrix} a_{1p} \\ \dots \\ a_{np} \end{bmatrix} = \begin{bmatrix} 0 \\ \dots \\ 0 \end{bmatrix} \quad \lambda_p^2 = \sum_{j=1}^n a_{jp}^2 \quad (10)$$

Here the r 's are correlation coefficients between the variables, the h 's are the communalities or rank minimizing values of the previous section, λ_p is one of the eigenvalues, and the column of a 's is the associated eigenvector, the elements of which serve as the coefficients or loadings of the p th factor for the n variables when the $\lambda_p = \sum_{j=1}^n a_{jp}^2$ condition is fulfilled. Some of the eigenvalues will be zero since selecting the diagonals to minimize rank is equivalent to maximizing the number of zero eigenvalues, thus minimizing the number of non-zero eigenvalues, or equivalently the number of common factors as desired. When the squared multiple correlation is used to approximate the true rank minimizing communalities in the diagonal, the exact positive semi-definite character of the matrix is destroyed and the zero eigenvalues are replaced with small positive and negative numbers which are simply ignored. In practice, only those factors associated with the few highest eigenvalues are needed in the factor analysis model (equation 2) since the correlation matrix reproduced from these alone often yield a very close approximation to the observed correlation matrix in the off-diagonal elements which are the elements of consequence.

FACTOR ROTATION

The form employed in deriving the factor coefficients or loadings a_{jp} has the property that the sum of the contributions of the successive factors makes the total communality a maximum under the conditions relating these coefficients to the off-diagonal correlations. As noted previously, no factor solution is unique and other factor loadings not having this property would yield identical correlation matrices.

Since factors are hypothetical constructs, their interpretation must be in terms of the observable variables. The simplest possible illustration of a clear cut factorization occurs when a sequence of variables can be found

in which the higher correlations occur in blocks along the principal diagonal of the correlation matrix and the lower correlations occur in all other positions. In terms of the factor analysis model (equation 2), this corresponds to a number of factors equal to the number of blocks, and each variable having a substantially higher squared loading coefficient on one factor than on any of those remaining, each variable then becoming an imperfect measure of one factor only. In slightly more complex illustrations, maximum squared loadings will occur on several factors with minimum loadings on all those remaining. Ideally then, for the simplest physically meaningful interpretation of the hypothetical factors in terms of observed variables, the squared loading coefficients should approach their upper and lower bounds, one and zero respectively. This implies the maximum possible variance in the squared loading coefficients. Clearly, there must be some orientation of the orthogonal factor axes for which the squared loading coefficients have greater variance than for any other. Mathematically, this requires rotations to maximize the following variance function, the new factor loadings now denoted by b's.

$$\frac{1}{n} \sum_{p=1}^n \sum_{j=1}^m \frac{b_{jp}^4}{h_j^2} - \frac{1}{n^2} \sum_{p=1}^n \sum_{j=1}^m \frac{b_{jp}^2}{h_j^2} \quad (11)$$

The b's are introduced so that in axes rotations each coefficient is weighted equally rather than in proportion to its communality which would otherwise be the case. The actual rotations required to maximize this function constitute a sequential iteration process. The resulting b_{jp} coefficients are called the varimax loadings.

REFERENCES

1. Harry H. Harman, "Modern Factor Analysis," University of Chicago Press, 1968
2. W. J. Dixon, Editor, "BMD: Biomedical Computer Programs," University of California Press, 1970
3. Henry Scheffe, "The Analysis of Variance," Chapters 3 and 6, John Wiley & Sons, 1959
4. Carl A. Golueke, "A Regression Study of the Vibration Response of an External Store," 42nd Shock and Vibration Bulletin, 1971

RESPONSES OF A MULTI-LAYER PLATE TO RANDOM EXCITATION

H. Saunders
General Electric Company
Aircraft Engine Group
Cincinnati, Ohio 45215

Formulas are presented that can be employed to determine the mean square acceleration, displacement and stresses of multi-layer plates due to an externally applied random excitation. The derived expressions are general and can be applied to multi-layer plates having different boundary conditions. The main theme in this paper is slanted towards all edges of the multi-layer plate being simply supported. Examples of a three layered plate and a sandwich plate having an external layer protecting the upper facing are given illustrating the method.

INTRODUCTION

The recent appearance of high powered jet engines and rockets has brought forth a new phase of mechanical vibration. These powerful propulsion units generate noise and vibrational energy which stem from the sources of excitation residing in the turbulent jet mixing zones or in the attached and separated turbulent boundary layers. The oscillatory energy contrived by these mechanisms is commonly referred to as random vibration or random processes. This is in contrast to the more popular deterministic process. For the latter, the recorded data indicates that an experiment conducted under the same conditions are always alike (discounting experimental inaccuracies). On the other hand where the researcher maintains the same identical conditions in his experiments and there is no resemblance in the records, this is random.

The basic fundamentals of this statistical approach are well documented in the literature and reference should be made to them for more intensive study. [1,2,3,6]

In modern engineering practice, the plate, beam and shell are the most prevalent elements comprising mechanical machines, mechanical devices and structures. The present problem emerged from the need in determining the rms stresses and accelerations in selected layers of a laminated plate when subjected to a random vibration environment. Stochastic processes are utilized and the important constituents of autocorrelation and spectral density functions for acceleration, displacement and stresses plus the associated cross-correlation and cross-spectral density functions are derived. The

resulting equations, although general in nature, are specifically applied to a simply supported laminated plate.

MATHEMATICAL ANALYSIS

Prior to beginning the response analysis investigation due to a random input, a number of assumptions are promulgated.

1. The random input is stationary and ergodic.
2. The inherent damping residing in the plates are small. The peaks are pronounced and the response at any near frequency will be dominated by its natural frequency. The associated bandwidth is narrow.
3. The power spectral density will be flat within the region of the natural frequency and is commonly denoted by the term "white noise".

The following analysis employs the generalized Fourier Analysis contrived by Weiner to the random vibration problem. Excellent sources of information are expounded in Refs. 4, 5 and 6.

A. A Mean Square Displacement

Consider a simply supported laminated plate (Fig. 1) whose layers are transversely isotropic and having different values of E_n , ν_n and h_n . Present, and soon to be introduced symbols, are explained in the nomenclature section with their

Preceding page blank

proper physical and geometrical meanings. Pister [7] shows that the fundamental equation of this type of laminated plate can be represented by

$$D_e \nabla^4 w(x, y, t) + (\rho h)_{eq} \ddot{w} = f(x, y, t) \quad (1)$$

where

$$D_e = \frac{E_1 D_1 - C_1^2}{A_1} \quad (2)$$

$$E_1 = \sum_n \frac{E_n}{1 - \nu_n^2} (x_n - x_{n-1}) \quad (3)$$

$$C_1 = \sum_n \frac{E_n}{1 - \nu_n^2} \frac{(x_n^2 - x_{n-1}^2)}{2} \quad (4)$$

$$D_1 = \sum_n \frac{E_n}{1 - \nu_n^2} \frac{(x_n^3 - x_{n-1}^3)}{3} \quad (5)$$

where all sums range from $n = 1, 2, \dots, s$.

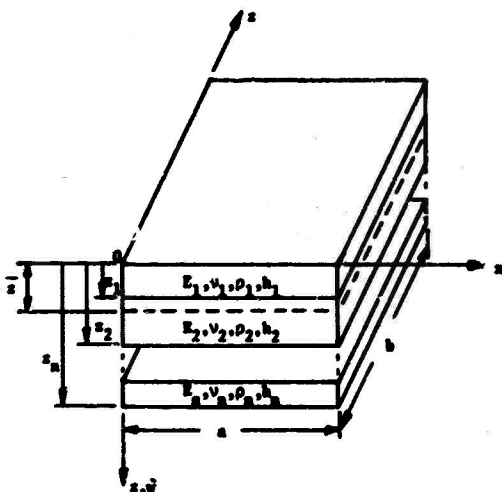


Fig. 1. Laminated Plate

Employing this innovation, the classical type solution [8] describing the vibration of a plate can now be employed. In the treatment to follow, special consideration is given to the application of modal functions. These orthogonal functions are extensively employed in the analysis of frequencies, dynamic responses and frequency analysis of beams and plates with various end conditions. [4, 9, 10]

Initially, assume a deflection curve for the plate which consists of a combined x and y displacement function, i.e.,

$$w(x, y, t) = \sum_{i=1}^{\infty} \sum_{j=1}^{\infty} \phi_i(x) \psi_j(y) q_{ij}(t) \quad (6)$$

where

$\phi_i(x)$, $\psi_j(y)$ are functions of x and y , respectively, and define the wave form, $q_{ij}(t)$ is the generalized coordinate.

Substituting Eq. (6) into Eq. (1), the following equation can then be obtained by the well-known orthogonality relationships.

$$\ddot{q}_{ij}(t) + \omega_{ij}^2 q_{ij}(t) = \frac{F(x, y, t)}{M_{(ij)}} \quad (7)$$

where

$$F(x, y, t) = \int_0^a \int_0^b f(x, y, t) \phi_i(x) \psi_j(y) dx dy \quad (8a)$$

and $M_{(ij)}$ is the generalized mass:

$$M_{(ij)} = \int_0^a \int_0^b (\rho h)_{eq} (\phi_i(x))^2 (\psi_j(y))^2 dx dy \quad (8b)$$

The primary advantage of this approach is to essentially uncouple the plate equation which has an infinite number of frequencies and thus operate upon simple equations containing the important frequencies. The equation of motion in the ij th mode can be written in a more amenable form by assuming that the modal coupling due to damping effects is small. If the introduction of equivalent viscous damping $c(x, y)$ to the laminated plate doesn't give rise to any coupling between the normal modes, Eq. (7) then becomes

$$\ddot{q}_{ij}(t) + \bar{C}_{ij} \dot{q}_{ij}(t) + \omega_{ij}^2 q_{ij}(t) = \frac{F(x, y, t)}{M_{(ij)}} \quad (9)$$

where

\bar{C}_{ij} denotes the generalized viscous damping in the ij th mode defined for the composite plate as

$$\int_0^a \int_0^b c(x, y) (\phi_i(x))^2 (\psi_j(y))^2 dx dy \quad (10)$$

This further assumes that $\bar{C}_{ij} = 2\zeta_{ij}\omega_{ij}(\rho h)_{eq}$ reduces the generalized damping, Eq. (10) to a form such that the orthogonality property can

be employed. Permit the capital letters to signify the Fourier Transform (F.T.); the "F.T." of Eq. (9) becomes [4].

$$Q_{ij}(\omega) = \frac{H_{ij}(\omega)}{M_{(ij)}\omega_{ij}^2} \int_0^a \int_0^b \phi_i(x) \psi_j(y) \cdot F(x,y,\omega) dx dy \quad (11)$$

where

$$H_{ij}(\omega) = \frac{1}{1 - \left(\frac{\omega}{\omega_{ij}}\right)^2 + i 2\zeta_{ij}\left(\frac{\omega}{\omega_{ij}}\right)} \quad (12)$$

The "F.T." of the response equation appears as

$$\begin{aligned} W(x,y,\omega) &= \sum_{i=1}^{\infty} \sum_{j=1}^{\infty} \phi_i(x) \psi_j(y) Q_{ij}(\omega) \\ &= \sum_{i=1}^{\infty} \sum_{j=1}^{\infty} \phi_i(x) \psi_j(y) \frac{H_{ij}(\omega)}{M_{(ij)}\omega_{ij}^2} \cdot \\ &\int_0^a \int_0^b \phi_i(x) \psi_j(y) \bar{F}(x,y,\omega) dx dy \quad (13) \end{aligned}$$

The correlation relating the responses at points (x,y) and (x',y') can be expressed [4].

$$\begin{aligned} \overline{w(x,y)w(x',y')} &= \lim_{T \rightarrow \infty} \frac{1}{2T} \int_{-T}^T w(x,y,t) \cdot \\ &w(x',y',t) dt \quad (14) \end{aligned}$$

where

$\overline{w(x,y)w(x',y')}$ is the time averaged spatial correlation. Employing a form of Parseval's theorem for integrals, [6] Eq. (13) becomes

$$\begin{aligned} \overline{w(x,y)w(x',y')} &= \frac{1}{2} \int_{-\infty}^{\infty} \lim_{T \rightarrow \infty} \frac{1}{2\pi T} \left[W(x,y,\omega) \cdot \right. \\ &\left. W^*(x',y',\omega) \right] d\omega \quad (15) \end{aligned}$$

In a similar fashion, the spatial correlation relating the applied forces at (x,y) and (x',y') can be defined as

$$\overline{f(x,y)f(x',y')} = \lim_{T \rightarrow \infty} \frac{1}{2\pi T} \cdot$$

$$\left[F(x,y,\omega) F^*(x',y',\omega) \right] d\omega$$

$$= \frac{1}{2} \int_{-\infty}^{\infty} G_F(x,y,x',y',\omega) d\omega \quad (16a)$$

where

$$G_F(x,y,x',y',\omega) = \lim_{T \rightarrow \infty} \frac{1}{2\pi T} \cdot$$

$$F(x,y,\omega) F^*(x',y',\omega) \quad (16b)$$

By substituting Eqs. (9), (16b) into Eq. (11) and simplifying

$$\overline{w(x,y,t)w^*(x',y',t)} = \frac{1}{2} \sum_{i=1}^{\infty} \sum_{j=1}^{\infty} \sum_{k=1}^{\infty} \sum_{l=1}^{\infty} \cdot$$

$$\left[\phi_i(x) \psi_j(y) \phi_k(x') \psi_l(y') \right]$$

$$\int_{-\infty}^{\infty} \frac{H_{ij}(\omega) H_{kl}^*(\omega)}{M_{(ij)} M_{(kl)} \omega_{ij}^2 \omega_{kl}^2} \int_0^a \int_0^b \int_0^a \int_0^b \cdot$$

$$G_F(x,y,x',y',\omega) \phi_i(x) \psi_j(y) \phi_k(x') \psi_l(y') \cdot$$

$$dx dy dx' dy' d\omega \quad (17)$$

Due to the complexity of the equations, simplifications are made. One can define

$$\begin{aligned} P_{ijkl}(\omega) &= \frac{1}{M_{(ij)} M_{(kl)} \omega_{ij}^2 \omega_{kl}^2} \int_0^a \int_0^b \int_0^a \int_0^b \cdot \\ &\left[G_F(x,y,x',y',\omega) \phi_i(x) \psi_j(y) \cdot \right. \\ &\left. \phi_k(x') \psi_l(y') dx dy dx' dy' \right] \quad (18) \end{aligned}$$

The integrand in Eq. (18) is an even function of ω , and the mean square response at any point (x,y) can be found by allowing $x = x'$, $y = y'$, thus

$$\overline{w^2(x,y)} = \sum_{i=1}^{\infty} \sum_{j=1}^{\infty} \sum_{k=1}^{\infty} \sum_{l=1}^{\infty} \phi_i(x) \psi_j(y) \phi_k(x) \psi_l(y) \cdot$$

$$\int_0^{\infty} [P_{ijkl}(\omega) H_{ij}(\omega) H_{kl}^*(\omega)] d\omega \quad (19)$$

For a weakly stationary and lightly damped system, the cross modal coupling contributions are small and can be disregarded, i.e., $i \neq k$, $j \neq l$ compared with the same products $i = k$, $j = l$. Based upon the above hypothesis, the mean square response can be designated in terms of physically recognizable spectra

$$\overline{w^2(x,y)} = \int_0^{\infty} G_R(x,y,\omega) d\omega \quad (20a)$$

The spectral density for the distributed system then becomes

$$G_R(x,y,\omega) = \sum_{i=1}^{\infty} \sum_{j=1}^{\infty} \sum_{k=1}^{\infty} \sum_{l=1}^{\infty} \phi_i(x) \psi_j(y) \cdot \phi_k(x) \psi_l(y) P_{ijkl}(\omega) H_{ij}^*(\omega) H_{kl}(\omega) \quad (20b)$$

Eq. (20a) is the general expression for a multi-laminated plate having general boundary conditions. Since the theme of this paper is slanted towards simply supported conditions on all sides, the following sections will dwell upon the simply supported multi-layer plate.

The deflection equation for a multi-layered simply supported plate can be represented by

$$w(x,y) = \sin \frac{i\pi x}{a} \sin \frac{j\pi y}{b} q_{ij}(t) \quad (21a)$$

where

$$\phi_i(x) = \sin \frac{i\pi x}{a}; \quad \psi_j(y) = \sin \frac{j\pi y}{b} \quad (21b)$$

Substituting into Eq. (8), the generalized mass yields

$$M_{(ij)} = \frac{(\rho h)_{eq.} ab}{4} \quad (22)$$

In a similar fashion, $G_R(x,y,x',y',\omega)$ yields

$$G_R(x,y,x',y',\omega) = \sum_{i=1,3,..}^{\infty} \sum_{j=1,3,..}^{\infty} \sum_{k=1,3,..}^{\infty} \sum_{l=1,3,..}^{\infty} \cdot$$

$$\left[\sin \frac{i\pi x}{a} \sin \frac{j\pi y}{b} \cdot \sin \frac{k\pi x'}{a} \sin \frac{l\pi y'}{b} \cdot \left\{ \frac{H_{ij}(\omega) H_{kl}^*(\omega)}{M_{(ij)} M_{(kl)} \omega^2 \omega_{ij}^2 \omega_{kl}^2} \right\} G_{ijkl}^{(F)}(\omega) \right] \quad (23)$$

The spectral density of the generalized force is

$$G_{ijkl}^{(F)}(\omega) = \int_0^a \int_0^b \int_0^a \int_0^b [(\rho h)_{eq.} (\ddot{\phi})_{eq.} (\ddot{\phi})'_{eq.}] \cdot$$

$$\sin \frac{i\pi x}{a} \sin \frac{j\pi y}{b} \cdot$$

$$\sin \frac{k\pi x'}{a} \sin \frac{l\pi y'}{b} G_{\alpha}(x,y,x',y',\omega) dx dy dx' dy'] \quad (24)$$

where the cross spectral density of the external acceleration loading is expressed by

$$G_{\alpha}(x,y,x',y',\omega) = \lim_{T \rightarrow \infty} \frac{1}{2\pi T} \ddot{W}(x,y,\omega) \ddot{W}^*(x',y',\omega) \quad (25)$$

Based upon our initial assumptions, the frequencies are widely separated. For white noise, the stimulation is uncorrelated with spatial position so that "F.T." are independent of positions (x,y) and (x',y') . Since the multi-layer plate has an equivalent mass/unit area, Eq. (24) can be represented by

$$G_{ijkl}^{(F)}(\omega) = [(\rho h)_{eq.}]^2 G_{\alpha}(\omega) \int_0^a \int_0^b \int_0^a \int_0^b \cdot$$

$$\left[\sin \frac{i\pi x}{a} \sin \frac{j\pi y}{b} \sin \frac{k\pi x'}{a} \sin \frac{l\pi y'}{b} dx dy dx' dy' \right] \quad (26)$$

The spectral density is illustrated in Fig. 2 and can be represented by

$$G_{\alpha}(x,y,x,y,\omega) \rightarrow G_0(\alpha)$$

After integration and simplification, Eq. (26) reduces to

$$G_{ijkl}^{(F)}(\omega) = [(\rho h)_{eq.}]^2 G_0(\alpha) \frac{16a^2b^2}{ijkl\pi} \quad (27)$$

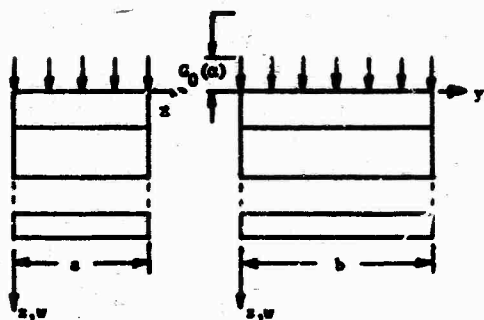


Fig. 2. Simply-supported multi-layer plate excited by a uniformly distributed white noise of density $G_0(\alpha)$.

Since the P_{ijkl} expression only has significance when $i = k, j = l$, this further simplifies to

$$P_{ijij}(\omega) = \frac{16a^2b^2[(\rho h)_{eq}]^2 G_0(\alpha)}{\pi^4 i^2 j^2 M_{ij}^2 \omega_{ij}^4} \quad (28)$$

Substituting Eq. (22) into Eq. (28) and after some algebraic manipulation, the P_{ijij} expression emerges as

$$P_{ijij}(\omega) = \frac{(16)^2 G_0(\alpha)}{\pi^4 i^2 j^2 \omega_{ij}^4} \quad (29)$$

The mean square response at the point x, y as shown by Eq. (19) plus due consideration to the aforementioned simplifications reduces to

$$\overline{w^2(x, y)} = \sum_{i=1,3..}^{\infty} \sum_{j=1,3..}^{\infty} \sum_{i=1,3..}^{\infty} \sum_{j=1,3..}^{\infty} \cdot \left[(\phi(x))^2 (\psi(y))^2 \int_0^{\infty} P_{ijij} |H_{ij}(\omega)|^2 d\omega \right] \quad (30)$$

The integrand of Eq. (30) can be evaluated by McCalley's method [12] or method of residues, i.e.,

$$\int_0^{\infty} P_{ijij} |H_{ij}(\omega)|^2 d\omega = \frac{(16)^2 G_0(\alpha)}{\pi^4 i^2 j^2} \left(\frac{\pi \omega_{ij}}{4 \zeta_{ij} \omega_{ij}^4} \right) = \frac{64 G_0(\alpha)}{\pi^3 \zeta_{ij} \omega_{ij}^3 i^2 j^2} \quad (31)$$

Substituting Eq. (31) into Eq. (30), the mean square response at point (x, y) becomes

$$\overline{w^2(x, y)} = \frac{64 G_0(\alpha)}{\pi^3 \zeta_{ij} \omega_{ij}^3 i^2 j^2} \sum_{i=1,3..}^{\infty} \sum_{j=1,3..}^{\infty} \cdot \left(\sin \frac{i\pi x}{b} \right)^2 \left(\sin \frac{j\pi y}{b} \right)^2 \quad (32)$$

B. Root Mean Square Acceleration

The mean square acceleration can be obtained in a simple manner by utilizing the basic Fourier Transform relationship between the mean square acceleration and mean square displacement, i.e.,

$$\overline{\ddot{w}^2(x, y)} = \omega^4 \overline{w^2(x, y)} \quad (33)$$

Thus after proper substitution and simplification, the mean square acceleration at point (x, y) can be expressed as

$$\overline{\ddot{w}^2(x, y)} = \frac{64 G_0(\alpha) \omega_{ij}^4}{\pi^3 \zeta_{ij} i^2 j^2} \sum_{i=1,3..}^{\infty} \sum_{j=1,3..}^{\infty} \cdot \left(\sin \frac{i\pi x}{a} \right)^2 \left(\sin \frac{j\pi y}{b} \right)^2 \quad (34)$$

C. Bending Moments, Stresses and Accelerations at Point (x, y)

To calculate the rms stresses, the rms bending moment must first be determined. The rms bending for the multi-layer plates at position (x, y) is given by

$$M_{rms}(x, y) = \sqrt{\overline{M^2(x, y)}} \quad (35)$$

The moments $M(x, y)$ are expressed

$$M_x(x, y) = -D_e \left(\frac{\partial^2 w}{\partial x^2} + \nu_e \frac{\partial^2 w}{\partial y^2} \right) \quad (36a)$$

$$M_y(x, y) = -D_e \left(\frac{\partial^2 w}{\partial y^2} + \nu_e \frac{\partial^2 w}{\partial x^2} \right) \quad (36b)$$

$$M_{xy}(x, y) = D_e (1 - \nu_e) \left(\frac{\partial^2 w}{\partial x \partial y} \right) \quad (36c)$$

Substituting Eq. (6) into Eq. (36a) and simplifying

$$\overline{M_x(x,y)} = -D_e \left[\frac{d^2 \phi_1(x)}{dx^2} \psi_j(y) + v_e \phi_1(x) \frac{d^2 \psi_j(y)}{dy^2} \right] \phi_{1j}(z) \quad (37)$$

Proceeding in a manner corresponding to the analysis described in the previous sections with the cross spectral densities being negligible, the mean square bending moment presents itself as

$$\overline{M^2(x,y)} = \int_0^\infty G_{M_x}(x,y,\omega) d\omega \quad (38)$$

where

$$G_{M_x}(x,y,\omega) = D_e^2 \sum_{i=1,3,\dots}^\infty \sum_{j=1,3,\dots}^\infty \left[\frac{d^2 \phi_i(x)}{dx^2} \psi_j(y) + v_e \phi_i(x) \frac{d^2 \psi_j(y)}{dy^2} \right]^2 P_{1j1j} H_{1j}(\omega) R_{1j}^*(\omega) \quad (39)$$

The expression in the integrand was previously evaluated and the mean square bending moment reduces to

$$\overline{M(x,y)} = \frac{64G(\alpha)}{\pi^2 \zeta_{1j} \omega_{1j}^2} D_e^2 \left[\left(\frac{1}{a} \right)^2 + v_e \left(\frac{1}{b} \right)^2 \right] \left(\sin \frac{1\pi x}{a} \right)^2 \left(\sin \frac{1\pi y}{b} \right)^2 \quad (40)$$

$$\therefore \overline{M(x,y)} = \frac{8\pi D_e}{1j\omega_{1j} a^2} \left[1^2 + v_e \left(\frac{1}{b} \right)^2 \right] \cdot$$

$$\left[\frac{G(\alpha)}{\pi \zeta_{1j} \omega_{1j}} \right]^{1/2} \sin \frac{1\pi x}{a} \sin \frac{1\pi y}{b} \quad (41)$$

The power spectral density is commonly represented by $G(f)$ which is in units of g^2/cps .

$$\therefore G_0(x) = \frac{G(f)(386)^2}{2\pi} ; f_{1j} = \frac{\omega_{1j}}{2\pi} \quad (42)$$

Substituting the quantities of Eq. (42) into Eq. (41), the results when simplified become

$$\overline{M_x(x,y)} = \frac{772 D_e}{1j f_{1j} \pi a^2} \left[\left(\frac{1}{j} \right)^2 + v_e \left(\frac{1}{b} \right)^2 \right] \cdot \left[\frac{G(f)}{\pi \zeta_{1j} \omega_{1j}} \right]^{1/2} \sin \frac{1\pi x}{a} \sin \frac{1\pi y}{b} \quad (43)$$

The expression for $M_y(x,y)$ and $M_{xy}(x,y)$ can be similarly derived. The rms stress at any location in the multi-layered plate is

$$\overline{\sigma_x(x,y)} = \frac{M_x(x,y) E z}{(1-\nu^2) D_e} \quad (44)$$

D. Root Mean Square Acceleration in Commonly Used Form of (g^2/cps)

In an analogous manner, the root mean square acceleration can be represented in the normally used (g^2/cps) form by substituting Eq. (42) into Eq. (33)

$$\overline{G(x,y)} = \frac{8f_{1j}}{1j\pi} \left[\frac{G(f)}{\pi \zeta_{1j} \omega_{1j}} \right]^{1/2} \cdot$$

$$\sum_{i=1,3,\dots}^\infty \sum_{j=1,3,\dots}^\infty \sin \frac{1\pi x}{a} \sin \frac{1\pi y}{b} \quad (45a)$$

where

$$\overline{G(x,y)} = \frac{\overline{\ddot{u}(x,y)}}{386} \quad (45b)$$

EXAMPLES

- A. Consider a simply supported ($a = 12''$, $b = 8''$) plate having three laminated sections (Fig. 3) with the following physical and geometrical properties. Determine the rms acceleration and the rms stress at the center ($x = a/2$, $y = b/2$) of the outermost portion of layer #1 when the plate is vibrated in the range of 50-1000 cps with a random vibration input level $[G(f)] = 2.0 g^2/\text{cps}$; $\zeta = 0.02$

The important physical parameters for the composite plate are:

$$D_e = 3.45 \times 10^3$$

$$\bar{z} = 0.241$$

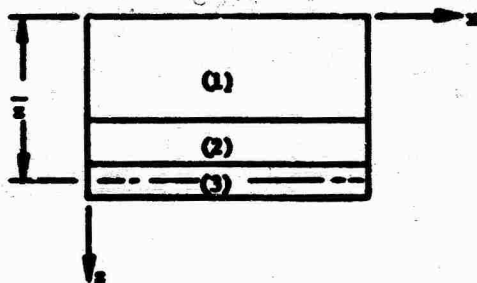


Fig. 3. Three layer plate.

Layer	$E \left(\frac{lb}{in^2} \right)$	ν	$\gamma \left(\frac{lb}{in^3} \right)$	$h(in)$
#1	5×10^5	0.3	0.008	0.2
#2	10×10^6	0.3	0.101	0.05
#3	30×10^6	0.3	0.283	0.03

The predominant natural frequencies are

$$f_{11} = 332 \text{ cps} ; \quad f_{13} = 2068 \text{ cps}$$

The rms moment $\overline{M_x(x,y)}$ at $x = a/2$, $y = b/2$ is

$$\overline{M_x \left(\frac{a}{2}, \frac{b}{2} \right)} = 9.203 \frac{in \text{ lb}}{in} \text{ (rms)}$$

The rms stress at point $x = a/2$, $y = b/2$ in Layer (1) is

$$\overline{\sigma_x \left(\frac{a}{2}, \frac{b}{2} \right)} = 353 \frac{lb}{in^2} \text{ (rms)}$$

and

$$\overline{G \left(\frac{a}{2}, \frac{b}{2} \right)} = 262 \text{ g (rms)}$$

Since f_{13} is out of range of vibration inputs to the composite plate, it is not considered any further.

- B. Consider for the preliminary design purposes a simply supported honeycomb plate ($a = 12"$, $b = 18"$) containing a thermal protection insulating outer layer (Fig. 4) having the following physical and geometrical characteristics. Determine the rms acceleration and rms stress of the center ($x = a/2$, $y = b/2$) of the outermost section of the bottom facing (#4) when the plate is vibrated in the range of 50-1500 cps with a random vibration input $[G(f)] = 2.0 \text{ g}^2/\text{cps}$.

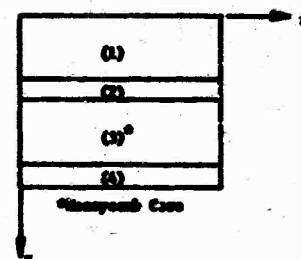


Fig. 4. Honeycomb and outer thermal protection layer.

Table 1a

Physical Characteristics

Layer	$E \left(\frac{lb}{in^2} \right)$	$\gamma \left(\frac{lb}{in^3} \right)$	$h(in)$	ζ^*
(1)	5×10^4	0.01	0.6	0.02
(2)	16×10^6	0.163	0.008	0.02
(3)	—	0.0075	0.5	0.02
(4)	16×10^6	0.163	0.008	0.02

*Assume viscous damping of 0.02 for entire composite plate.

The calculated frequencies derived using Table 1b are:

$$f_{11} = 1061 \text{ cps}$$

$$\therefore \overline{M_x \left(\frac{a}{2}, \frac{b}{2} \right)} = 22.4465 \frac{in \text{ lbs}}{in} \text{ (rms)}$$

The stress at bottom facing (#4)

$$\overline{\sigma_x \left(\frac{a}{2}, \frac{b}{2} \right)} = 2677 \frac{lb}{in^2} \text{ (rms)}$$

The acceleration response of the panel is

$$\overline{G \left(\frac{a}{2}, \frac{b}{2} \right)} = 468 \text{ g (rms)}$$

CONCLUSION

A procedure has been presented to determine the stochastic properties of displacement, acceleration and stress in a simply supported multi-layer plate when subjected to a random excitation. The auto-correlation and cross-correlation functions with corresponding spectral densities have been presented. Further extension to multi-layer plates with

Table 1b

Section Properties

	E	h	Area = Eh	z	Ehz	Y	Yh
(1)	5×10^4	0.6	3×10^4	0.3	0.9×10^4	0.01	6×10^{-3}
(2)	16×10^6	0.008	10.8×10^4	0.604	6.5232×10^4	0.163	1.304×10^{-3}
(3)	4	0.5	—	—	—	0.0075	3.75×10^{-3}
(4)	16×10^6	0.008	10.8×10^4	1.112	12.0096×10^4	0.163	1.304×10^{-3}
Σ			24.6×10^4		19.4426×10^4		12.358×10^{-3}

*Honeycomb core contributes very little to the overall bending of the composite plate but serves the extremely useful functions of transmitting shear between them.

$$\bar{z} = 0.79$$

$$B_1 = 31.42857 \times 10^4$$

$$C_1 = 25.1648 \times 10^4$$

$$D_1 = 23.018 \times 10^4$$

$$D_e = 2.8692 \times 10^4$$

other boundary conditions can be formulated by following the procedures detailed in the paper.

ACKNOWLEDGEMENT

The author would like to thank Dr. L. Beitch and B. L. Koff for use of facilities in calculating the results and to Carolyn Thall for typing the manuscript. Further thanks are tendered to Harry Himmelblau of North American-Rockwell, L. E. Chaump of GE-RESO for the many discussions pertinent to the paper.

NOMENCLATURE

B_1, C_1, D_1	Expressions employed in determining the natural frequency of the multi-layered plates; Eqs. (3-5)
$C(x)$	Viscous damping coefficient assumed to vary as a function of x, y .
D_e	Equivalent Plate Rigidity Eq. (2)
E_n	Modulus of elasticity in n layer
$f(x, y, t)$	Excitation or forcing function acting upon the plate

$f(x, y, t)f(x', y', t)$ Time averaged spatial correlation of external forces

$F(x, y, t)$	Generalized force in ij mode
$G(x, y)$	Acceleration (rms) of multi-layer plate at point (x, y)
G_0	Magnitude of uniform spectral density
$H(\omega)$	General notation denoting a frequency response function
P_{ijk2}	Spectral density of the external loading weighed by generalized masses and modal frequencies
i, j	Double subscript notation; i applies to x direction and y to j direction
$w(x, y, t)$	Lateral displacement of the plate from its static equilibrium position.
$w(x, y, t)w(x', y', t)$	Time averaged spatial correlation between the response at (x, y) and x', y'
T	Time duration of sampled record
t	Real time

ρ_n	Density of n^{th} layer
h_n	Thickness of n^{th} layer
z_n	Distance from origin to end of n^{th} layer (see Fig. 1)
$(\rho h)_{eq}$	Equivalent mass/unit area of multi-layer plate
ζ	Damping factor
ζ_{ij}	Damping factor for the ij^{th} mode defined as c_{ij}/c_{cr} where c_{ij} is the viscous damping coefficient for the ij^{th} mode of the multi-layer plate and $c_{cr} = 2(\rho h)_{eq} \omega_{ij}$ is the critical damping coefficient.
ω	Frequency of the forcing function in rad/sec
ω_{ij}	Natural frequency associated with ij^{th} mode of the system (rad/sec)

REFERENCES

- (1) S.H. Crandall, editor, Random Vibration, Vol. 1, Massachusetts Institute of Tech. (M.I.T.) Press, 1958.
- (2) S.H. Crandall, editor, Random Vibration, Vol. 2, M.I.T. Press, 1963.
- (3) Y.K. Lin, Probabilistic Theory of Structural Dynamics, McGraw-Hill Publishing Co., N.Y., 1967.
- (4) W.T. Thomson, Vibration Theory and Applications, Prentice Hall Pub. Co., Englewood Cliffs, N.J., 1965.
- (5) G.A. Korn and T.M. Korn, Mathematical Handbook for Scientists and Engineers, 2nd edition, Chapter 18, McGraw-Hill Publishing Co., N.Y., 1968.
- (6) J.D. Robson, An Introduction to Random Vibration, Elsevier Publishing Co., N.Y., 1964.
- (7) K.S. Pister, "Flexural Vibrations of Thin Laminated Plates", J. of Acoustical Soc. of Am., Vol. 31, No. 2, pp. 233-4, 1959.
- (8) S. Timoshenko, Vibrational Problems in Engineering, 3rd edition, D. Van Nostrand and Co., Princeton, N.J., 1955.
- (9) D. Young and R. P. Felgar, Jr., "Tables of Characteristic Functions Representing Normal Modes of Vibration", University of Texas Publication #4913, 1949.
- (10) G.E. Warburton, "Vibration of Rectangular Plates", Proc. of IME, Vol. 168, No. 12, pp. 371-384, 1954.
- (11) A. Papoulis, The Fourier Integral, McGraw-Hill Book Co., N.Y., 1962.
- (12) R.C. McCalley, Jr., "The Evaluation of Random Noise Integral", 25th Shock and Vibration Bulletin Pt. II, p. 243, Dec. 1957.

RESPONSE OF HELICOPTER ROTOR BLADES TO RANDOM LOADS NEAR HOVER

C. Lakshminathan and C. V. Joga Rao
Army Materials and Mechanics Research Center
Woburn, Massachusetts

The response of a flexible helicopter rotor blade to random loading is investigated, the random input being the vertical velocity component. The model takes into account blade flexibility in bending as well as torsion, and also general rotor-end fixity. The spectral density and the mean square value of the transverse displacement are computed for both hingeless and hinged rotor blades and the results are evaluated.

INTRODUCTION

Most of the investigations of helicopter rotor blades have been related to the flutter phenomenon, see for example Ref. 1, and as such form part of the classical stability (eigenvalue) problem. Here one is not interested in the entire response history but only in its deviation from a norm (infinitesimal or otherwise) at a critical value of the influencing parameter, say the angle of attack. While such investigations are useful for design purposes if the parameter is nonrandom, the entire response spectrum becomes important when it is a random function, as the failure of the structure may be dependent on the peak values of the response even though the critical value of the parameter is not reached.

Considering the often-turbulent environment in which a helicopter rotor blade operates, and also the various flight conditions under which random loads prevail on the blades, it is evident that the response of rotor blades to random inputs is of great design importance.

Research in this direction has barely begun: the only pertinent studies to the authors' knowledge^{2,3} are based on the very simplified model of a rotor blade as a rigid beam with a hinge at the rotor-end excluding all coupling effects; and hence are not too satisfactory from the standpoint of a structural designer.

Consequently, a fairly comprehensive program has been initiated at the Army Materials and Mechanics Research Center to study the response of rotor blades to random inputs including factors of blade flexibility, rotor-end fixity, coupling of bending and torsional effects and also to examine the possible nonlinearities.

This paper reports on the first phase of the program. Here a consistent first-order small-motions theory is utilized to obtain the governing equations of motion as a linear system. Also the forward speed of the vehicle is considered negligible in comparison with the tip speed of the blade and thus the linear system has constant, i.e., time-invariant coefficients. Finite forward speeds, introducing variable coefficients, will be dealt with in a sequel.

EQUATIONS OF MOTION

Generalized Force Balance Equations

The equations of motion of a rotating blade in an airflow have been derived in several places, see for example Refs. 1 and 4. However, most of these are explicitly written for a hinged or an articulated blade in terms of the rigid flapping angle.¹ Since we are interested in both hinged and hingeless blades, a general derivation is presented below.

Figure 1 shows a typical blade bent along its elastic axis in the X-Z plane rotating about the Z axis with a speed Ω . Figure 2 shows the blade section under a twist θ , as well as the respective locations of the aerodynamic and mass centers from the elastic axis.

It is convenient to nondimensionalize all lengths by choosing R , the blade length, as the unit. Thus all lengths, such as the chord, and displacement are ratios with respect to R . Then all the pertinent quantities for the dynamics of the problem have the units of mass and/or time only.

In order to obtain a consistent first-order system of equations, small angles and small motions are assumed allowing the principle of superposition to hold. Hence in deriving the

NOTATION

a	blade section lift-curve slope	z	dimensionless transverse displacement of blade
c	dimensionless blade section chord	α	inverse of relaxation time
E	blade modulus of elasticity	$\bar{\gamma}$	generalized Lock number
g_k	transverse displacement of k^{th} bending mode	η_k	k^{th} orthogonal mode shape
I	blade area moment	θ_k	blade section twist
I_0, I_0	section moments of inertia about the center of mass and elastic axis, respectively	ν_k	ratio of k^{th} bending frequency to the rotational speed
L	lifting force	ρ	air density
M_k, M_{y_k}	generalized masses	σ^2	variance
u_z, u_T	velocity component in the z and tangential directions, respectively	τ	generalized time (arbitrary time interval)
x	dimensionless coordinate along blade	Ω	blade rotational speed
y_A	dimensionless offset of aerodynamic center from the elastic axis	ω	frequency parameter for spectral density representation
y_I	dimensionless offset of center of mass from the elastic axis	ω_0	nonrotational torsional frequency of the blade

equations of motion, it is convenient to consider first the bending of the (untwisted) beam, Fig. 1, and add the torsional effects on the bending separately.

Thus the bending moment $M(x)$ at a current point x (Fig. 1) is given in terms of an arbitrary point s as:

$$M(x) = \int_x^L \left[\frac{dL}{ds}(s) - \ddot{z}(s) m(s) \right] (s-x) ds - \int_x^L s \Omega^2 m(s) [z(s) - z(x)] ds \quad (1)$$

where z is the nondimensional displacement and L , the thrust of the vehicle, acting along the z direction. Ω is the rotational speed and m the distributed mass of the blade.

Equation (1) takes into account only the centrifugal force produced by the rotation, as the Coriolis force for small motions is negligible in comparison with the centrifugal force.

Differentiating Eq. (1) twice with respect to x and introducing the linear beam flexural formula $M(s) = EIz''$, we have:

$$(EIz'')'' - z'' \int_x^L s \Omega^2 m(s) ds + z'(x) m(x) \Omega^2 + m(x) \ddot{z}(x) = \frac{dL}{dx} \quad (2)$$

In Eq. (2) the prime denote differentiation with respect to x and the dots, the time derivatives. We set

$$z = \sum_{k=1}^{\infty} \eta_k(x) g_k(t) \quad (3)$$

where $\eta_k(x)$ are the orthogonal mode shapes of free (natural) vibration of the rotating beam. Assuming a simple harmonic motion we let

$$g_k = \bar{g}_k e^{i \nu_k \Omega t} \quad (4)$$

where ν_k is the ratio of k^{th} bending natural frequency of the rotating beam to the speed of rotation Ω .

Substituting Eqs. (3) and (4) into Eq. (2) and recalling that no external forces are present during a free vibration, we find

$$(EIz'')'' - z'' \int_x^L s \Omega^2 m(s) ds + z'(x) m(x) \Omega^2 = \sum_{k=1}^{\infty} m \nu_k^2 \Omega^2 \eta_k g_k \quad (5)$$

Hence Eq. (2), the vertical (shear) force balance equation due to twistless bending of the elastic axis, becomes

$$\sum_{k=1}^{\infty} m \eta_k \left[\ddot{g}_k + \Omega^2 \nu_k^2 g_k \right] = \frac{dL}{dx} \quad (6)$$

In order to take into account the contribution of the twist to the vertical force balance, we assume that the torsional flexibility is all concentrated at the root. If θ is the twist angle, positive downward, Fig. 2, and y_I the location of the mass center from the elastic axis, then Eq. (6) becomes modified as:

$$\sum_{k=1}^{\infty} m \left[\eta_k \ddot{g}_k + \Omega^2 \nu_k^2 \eta_k g_k - y_I (\ddot{\theta} + \Omega^2 \theta) \right] = \frac{dL}{dx} \quad (7)$$

Multiplying Eq. (7) by η_k and integrating over the entire blade length, we find, after recalling the orthogonality of η_k that the following holds:

$$\ddot{z}_k \int_0^1 m \eta_k^2 dx + \nu_k^2 \Omega^2 z_k \int_0^1 m \eta_k^2 dx - (\ddot{\theta} + \Omega^2 \theta) \int_0^1 m y_1 \eta_k dx = \int_0^1 \eta_k \frac{dL}{dx} dx$$

$$k=1, 2, 3, \dots, \infty$$

Defining generalized masses

$$M_k = \int_0^1 m \eta_k^2 dx$$

and

$$My_k = \int_0^1 m y_1 \eta_k dx \quad (8)$$

we find:

$$M_k (\ddot{z}_k + \Omega^2 \nu_k^2 z_k) - My_k (\ddot{\theta} + \Omega^2 \theta) = \int_0^1 \eta_k dL \quad k=1, 2, \dots, \infty$$

If we restrict our attention to the first two significant bending modes of vibration of the rotating beam, as these usually carry most of the energy of vibration, thereby implying that z is now given by

$$z = \eta_1 z_1 + \eta_2 z_2 \quad (9)$$

we can write two equations of motion from Eq. (8) by setting $k=1$ and 2 respectively.

Next we consider the torsional motion of the blade. Figure 2 shows the blade section under the action of an aerodynamic moment dM_A about the elastic axis. If I_0 and I_0 are the section moments of inertia about the center of mass and the elastic axis respectively, and ω_0 is the nonrotating natural frequency of the blade in torsional motion we can write the following moment balance equation⁴ for the section

$$I_0 (\ddot{\theta} + \Omega^2 \theta) + I_0 \omega_0^2 \theta = \quad (10)$$

$$m \left[(\ddot{z} - y_1 \ddot{\theta}) + \Omega^2 (z - y_1 \theta) \right] y_1 = \frac{dM_A}{dx}$$

or

$$I_0 (\ddot{\theta} + \Omega^2 \theta) + I_0 \omega_0^2 \theta - m (\ddot{z} + \Omega^2 z) y_1 = \frac{dM_A}{dx}$$

We can again integrate Eq. (10) over the blade length and, utilizing Eq. (9), obtain

$$I_0 + I_0 (\Omega^2 + \omega_0^2) \theta - M_{y_1} (\ddot{z}_1 + \Omega^2 z_1) \quad (11)$$

$$M_{y_2} (\ddot{z}_2 + \Omega^2 z_2) = \int_0^1 dM_A$$

where

$$I = \int_0^1 I_0 dx \text{ and } M_{y_k} = \int_0^1 m y_1 \eta_k dx$$

Then from Eqs. (8) and (11) we can write the following implicit equations of motion for the combined bending and torsional vibration of the rotating beam:

$$M_1 (\ddot{z}_1 + \Omega^2 \nu_1^2 z_1) - M_{y_1} (\ddot{\theta} + \Omega^2 \theta) = \int_0^1 \eta_1 dL$$

$$M_2 (\ddot{z}_2 + \Omega^2 \nu_2^2 z_2) - M_{y_2} (\ddot{\theta} + \Omega^2 \theta) = \int_0^1 \eta_2 dL \quad (12)$$

$$M_{y_1} (\ddot{z}_1 + \Omega^2 z_1) + M_{y_2} (\ddot{z}_2 + \Omega^2 z_2) -$$

$$I [\ddot{\theta} + (\Omega^2 + \omega_0^2) \theta] = - \int_0^1 dM_A$$

Aerodynamic terms for the Random Problem

Since the forward speed of the vehicle is assumed to be negligible, the only velocity components that produce the lift and moment on a typical blade are: U_z , the velocity component in the Z direction and U_T the tangential velocity due to rotation of the blade. For the random problem it is convenient to assume that U_z is the only component that has random characteristics. This is in agreement with the usual aeronautical practice of considering only vertical turbulence. Furthermore, we assume that the random part of U_z is a stationary, ergodic random function of time, then we can write

$$U_z = U_{zd} + U_{zr} = \dot{z}(x, t) + \tilde{U} \quad (13)$$

Where U_{zd} , U_{zr} are, respectively, the nonrandom (deterministic) and the random parts of U_z .

The expressions for lift dL and the moment dM for our problem are taken from Refs. 5 and 6 which are based on the linearized aerodynamics of oscillating airfoils in incompressible flow. For any section located at x from root, they are given by

$$\begin{aligned} dL &= \left\{ -\frac{1}{8} \rho a c^2 \left[\ddot{z} + u_T \dot{\theta} - (y_A - c/4) \ddot{\theta} \right] \right. \\ &\quad \left. - \frac{1}{2} \rho a c u_T C'(k) \left[\dot{u}_z + u_T \dot{\theta} + (c/2 - y_A) \dot{\theta} \right] \right\} dx \\ dM &= \left\{ \frac{1}{8} \rho a c^2 \left[(y_A - c/4) \ddot{z} - u_T \dot{\theta} (c/2 - y_A) - \right. \right. \\ &\quad \left. \left. c^2/22 \ddot{\theta} - (y_A - c/4)^2 \ddot{\theta} \right] \right. \\ &\quad \left. + \frac{1}{2} \rho a c y_A u_T C'(k) \left[\dot{u}_z + u_T \dot{\theta} + \right. \right. \\ &\quad \left. \left. (c/2 - y_A) \dot{\theta} \right] \right\} dx \end{aligned} \quad (14)$$

where c is the chord length ratio, a the slope of the lift curve, y_A the distance of the aerodynamic center from the elastic axis. $C'(k)$ is comparable to the classical Theodorsen function and is related to the rotor wake effects. Since $c \ll 1$, Eqs. (14) may be considerably simplified by retaining only terms of the order c . $C'(k)$ is taken as 1, implying that the rotor wake effects are ignored.

Recalling that $u_T = \Omega x$ for any point on the blade, and using the notation of Eq. (13) we finally have

$$\begin{aligned} dL &= -0.5 \rho a c \Omega x (z + \Omega x \theta) - 0.5 \rho a c \Omega x \ddot{u} \quad (15) \\ dM &= 0.5 \rho a c y_A \Omega x (z + \Omega x \theta) + 0.5 \rho a c y_A \Omega x \ddot{u} \end{aligned}$$

Equations of Motion

Utilizing Eqs. (15) in the expressions of Eq. (12) we are in a position to write down the system of equations with constant coefficients with the right-hand side showing the random input functions as follows:

$$\begin{aligned} (\ddot{g}_1 + k_{11} \dot{g}_1 + \nu_1^2 \Omega^2 g_1) + k_{12} \dot{g}_2 &= \quad (16) \\ (\alpha_1 \ddot{\theta} + k_{13} \dot{\theta}) &= c_1 \ddot{u} \\ k_{21} \dot{g}_1 - (\ddot{g}_2 + k_{22} \dot{g}_2 + \nu_2^2 \Omega^2 g_2) &= \\ (\alpha_2 \ddot{\theta} + k_{23} \dot{\theta}) &= c_2 \ddot{u} \\ (\ddot{g}_1 + k_{31} \dot{g}_1 + \Omega^2 g_1) + \mu (\ddot{g}_2 + k_{32} \dot{g}_2 + \Omega^2 g_2) &= \\ \beta_1 (\ddot{\theta} + k_{33} \dot{\theta}) &= c_3 \ddot{u} \end{aligned}$$

where

$$\begin{aligned} k_{11} &= 0.5 \Omega \bar{\gamma} \int_0^1 x \eta_1^2 dx \\ k_{12} &= 0.5 \Omega \bar{\gamma} \int_0^1 x \eta_1 \eta_2 dx \\ k_{13} &= \alpha_1 \Omega^2 - 0.5 \bar{\gamma} \Omega \int_0^1 x^2 \eta_1 dx \\ k_{21} &= 0.5 (M_1/M_2) \Omega \bar{\gamma} \int_0^1 x \eta_1 \eta_2 dx \\ k_{22} &= 0.5 (M_1/M_2) \Omega \bar{\gamma} \int_0^1 x \eta_2^2 dx \\ k_{23} &= \alpha_2 \Omega^2 - 0.5 \frac{M_1}{M_2} \bar{\gamma} \Omega \int_0^1 x^2 \eta_2 dx \\ k_{31} &= 0.5 \frac{y_A}{\alpha_1} \Omega \bar{\gamma} \int_0^1 x \eta_1 dx \\ k_{32} &= 0.5 \frac{y_A}{\alpha_2} \frac{M_1}{M_2} \bar{\gamma} \Omega \int_0^1 x \eta_2 dx \\ k_{33} &= \Omega^2 + \omega_0^2 - \frac{M_1}{I} \Omega \frac{\bar{\gamma}}{8} y_A \\ c_1 &= -0.5 \Omega \bar{\gamma} \int_0^1 x \eta_1 dx \\ c_2 &= -0.5 \frac{M_1}{M_2} \Omega \bar{\gamma} \int_0^1 x \eta_2 dx \\ c_3 &= -0.25 \Omega \frac{y_A}{\alpha_1} \bar{\gamma} \\ \alpha_1 &= I_{y_1} = M_{y_1}/M_1 \\ \alpha_2 &= I_{y_2} = M_{y_2}/M_2 \\ \beta_1 &= I/M_{y_1} \\ \mu &= M_{y_2}/M_{y_1} \\ \text{and } \bar{\gamma} &= \frac{\rho a c}{M_1}, \text{ the generalized Lock number.} \end{aligned}$$

SPECTRAL SOLUTION OF THE EQUATIONS OF MOTION

Equations (16) are the equations of motion of a rotating beam with coupled bending and torsion, using two bending modes; the right-hand side being the input function. Being a linear system, if the input is a stationary ergodic random function of time then each of the outputs g_1, g_2, θ is a similar stationary, ergodic random function⁷. Moreover, the stability of the stationary ergodic random function g_1, g_2, θ implies that the general solution of the homogeneous set corresponding to Eq. (16) is the transient solution⁷ and hence we are only interested in the particular solution of Eq. (16). For the case of a linear system with constant coefficients such as Eq. (16), the particular solution is easily obtained in terms of the spectral representation of the input function.

Following Sveshaikov⁷ the spectral densities of g_1, g_2 and θ together with the pertinent cross-spectral densities can be obtained as linear functions of the input spectral density in terms of the cofactors of the following 3×3 matrix:

$$(A_{ij}) = \begin{pmatrix} -\omega^2 + ik_{11}\omega + \nu_1\Omega^2 & ik_{12}\omega & -\omega^2 + ik_{31}\omega + \Omega^2 \\ ik_{12}\omega & \alpha_1\omega^2 - k_{13} & -\omega^2 + ik_{22}\omega + \nu_2\Omega^2 \\ -\omega^2 + ik_{22}\omega + \nu_2\Omega^2 & \alpha_2\omega^2 - k_{23} & \mu(-\omega^2 + ik_{32}\omega + \Omega^2) + \beta_1(\omega^2 - k_{33}) \end{pmatrix} \quad (17)$$

If a_{ij} are the cofactors of the elements A_{ij} of the matrix, Eq. (17), and Δ , the determinant of (A_{ij}) , then the spectral densities of the output are given by:

$$|\Delta|^2 S_{g_1}(\omega) = [c_1^2 |a_{11}|^2 + c_2^2 |a_{21}|^2 + c_3^2 |a_{31}|^2 + 2\text{Re} \{ c_1 c_2 (\bar{a}_{11} a_{21}) + c_2 c_3 (\bar{a}_{21} a_{31}) + c_3 c_1 (\bar{a}_{31} a_{11}) \}] S_{\tilde{U}}(\omega) \quad (18)$$

$$|\Delta|^2 S_{g_2}(\omega) = [c_1^2 |a_{12}|^2 + c_2^2 |a_{22}|^2 + c_3^2 |a_{32}|^2 + 2\text{Re} \{ c_1 c_2 (\bar{a}_{12} a_{22}) + c_2 c_3 (\bar{a}_{22} a_{32}) + c_3 c_1 (\bar{a}_{32} a_{12}) \}] S_{\tilde{U}}(\omega)$$

$$|\Delta|^2 S_{g_1 g_2}(\omega) = [c_1^2 (\bar{a}_{11} a_{12}) + c_2^2 (\bar{a}_{21} a_{22}) + c_3^2 (\bar{a}_{31} a_{32}) + c_1 c_2 (\bar{a}_{11} a_{22} + \bar{a}_{21} a_{12}) + c_2 c_3 (\bar{a}_{21} a_{32} + \bar{a}_{31} a_{22}) + c_3 c_1 (\bar{a}_{31} a_{12} + \bar{a}_{11} a_{32})] S_{\tilde{U}}(\omega) \quad (19)$$

$$|\Delta|^2 S_{\theta}(\omega) = [c_1^2 |a_{13}|^2 + c_2^2 |a_{23}|^2 + c_3^2 |a_{33}|^2 + 2\text{Re} \{ c_1 c_2 (\bar{a}_{13} a_{23}) + c_2 c_3 (\bar{a}_{23} a_{33}) + c_3 c_1 (\bar{a}_{33} a_{13}) \}] S_{\tilde{U}}(\omega)$$

In Eqs. (18) and (19) bars denote complex conjugates and Re stands for real part of the quantity following.

From the assumed form of $z = \eta_1 g_1 + \eta_2 g_2$ and the transform duality relationship between the correlation function of a random variable and its spectral density^{7,8} in the case of a stationary random process, we can show that

$$\langle z^2 \rangle = \int_{-\infty}^{\infty} S_z(\omega) d\omega \quad (20)$$

(21)

$$S_z(\omega) = \eta_1^2 S_{g_1}(\omega) + \eta_2^2 S_{g_2}(\omega) + 2\eta_1 \eta_2 \text{Re} S_{g_1 g_2}(\omega)$$

where $\langle z^2 \rangle$ is the mean square value of z , the transverse displacement.

Assume for the input function the following auto-correlation function

$$R_U(\tau) = \sigma^2 e^{-\alpha|\tau|} \quad (22)$$

where σ^2 is the variance, $1/\alpha$ the relaxation time and τ the interval between any specified times.

We can obtain from Eq. (22), using the transform relationships of Ref. 7, the following expression for the spectral density of the input:

$$S_U(\omega) = \frac{\sigma^2 \alpha}{\pi(\alpha^2 + \omega^2)} \quad (23)$$

The correlation function defined in Eq. (22), being the standard form of a weakly stationary Markoff-Gauss process, occurs in many physical processes and hence is a reasonable choice for an input function. In fact in Ref. 2 a similar for S_U is derived on the basis of Karman's theory of isotropic turbulence.

With Eq. (23) defining the input spectral density, we can readily compute the mean square and the spectral density of the response z for given choice of the model shapes η_1 and η_2 .

Special solutions of interest are easily obtained by modifying Eq. (16) suitably. Thus for example the case of zero torsion (of interest for comparison) is obtained from the following 2x2 system:

$$(\ddot{g}_1 + k_{11}\dot{g}_1 + \nu_1^2 \Omega^2 g_1) + k_{12}\dot{g}_2 = C_1 \ddot{U} \quad (24)$$

$$k_{21}\dot{g}_1 + (\ddot{g}_2 + k_{22}\dot{g}_2 + \nu_2^2 \Omega^2 g_2) = C_2 \ddot{U}$$

ORTHOGONAL MODE SHAPES

(a) Hinged Blades

For the hinged or articulated blade, the normal modes of bending, η_j , and the ratios of bending frequencies to the rotational speed, ν_j ($j = 1, 2$), are taken as:

$$\begin{aligned} \eta_1 &= x & \eta_2 &= 3x - 4x^2 \\ \nu_1 &= 1 & \nu_2 &= 3 \end{aligned} \quad (25)$$

The orthogonal modes η_j of Eq. (25) are used extensively in the literature on rotor blades - see for example Ref. 4. The first represents a simple rigid flapping about the hinge and the second is a polynomial approximation to the actual mode shape of the rotating beam in bending.

(b) Hingeless Blades

For the hingeless blade, which has not received as wide attention as the hinged blades, though most rotor designs are closed to a hingeless configuration, no simple expressions comparable to Eqs. (25) are available. The first nontrivial mode for this case is treated usually as rigid flapping with an off-set hinge¹⁰. However, the model shapes used in this paper were computed from the numerical values presented in Ref. 11 where the natural vibration problem of rotating beams with various end conditions is treated in great detail. Since the modal shapes enter into the evaluation of integrals k_{ij} following Eq. (16), numerical integration was directly performed for k_{ij} with the values of η_j from Ref. 11. The ν_j values were also determined from Ref. 11 and were found to be

$$\nu_1 = 1.2 \quad \nu_2 = 2.7.$$

NUMERICAL CONSTANTS

General Constants

The following numerical values were for the general constants occurring in the problem:

$$\bar{\gamma} = 4 \quad \alpha = 2 \quad \sigma^2 = 1 \quad \Omega = 1$$

$\bar{\gamma}$, the generalized Lock number, is a measure of the loading on the blade and in the current usage has a range from 2 to 16. The remaining constants are all arbitrary as far as the response is concerned and hence have been chosen conveniently.

Blade Constants

Since most of the inertia terms occur as ratios, the simplest choice of the constants was obtained by treating the running mass of blade as a constant. The aerodynamic center and mass center eccentricity ratios y_A and y_1 respectively were taken as - 1/640 and 1/400. I , the integrated blade moment of inertia about the elastic axis, was obtained from

$$\frac{M_1}{I} = 3000 \int_0^1 \eta_1^2 dx.$$

Then the ratios α_1 , α_2 , μ and M_1/M_2 are obtained from the following simple relationships:

$$\alpha_\gamma = y_1 \frac{\int_0^1 \eta_\gamma dx}{\int_0^1 \eta_\gamma^2 dx} \quad \gamma = 1, 2$$

$$\mu = \frac{\int_0^1 \eta_2 dx}{\int_0^1 \eta_1 dx} \quad \frac{M_1}{M_2} = \frac{\int_0^1 \eta_1^2 dx}{\int_0^1 \eta_2^2 dx}$$

NUMERICAL RESULTS AND CONCLUDING REMARKS

Figures 3a and 3b show a plot of the spectral density, S_z , of the transverse response, evaluated at the blade tip ($x = 1$) for the hinged and hingeless cases, with and without torsional coupling; Fig. 4, similarly shows the spectral density S_θ , of the torsional response. Only the right half of each curve is shown as they are all even functions of ω . Figure 5 gives the mean square of the response z for the various cases.

Though these plots are only valid for the specific values chosen, yet some general observations are possible. Firstly, the response in the hinged case is, predictably, higher than that in the hingeless case. Secondly, the dip in Fig. 4 of the torsional response occurring at the corresponding peak of the bending response (Figs. 3a and 3b) shows that at those frequencies the energy is entirely taken up by the bending modes.

Next in order of importance is the absence of a second peak in the torsionless case of Figs. 3a and 3b and its presence in the coupled torsional case. Even with torsion, however, the second peak is prominent only because of the present plotting on a logarithmic scale. The second peak is at least two cycles in magnitude lower than the first, indicating that there is, perhaps, only one main energy-carrying mechanism, namely the fundamental bending mode.

Finally, we note from Fig. 5 that the tip deflection is a relatively high fraction of the blade length. This would indicate that the present linear model based on small displacement theory is only a first approximation: future analysis will have to consider large displacements.

We could carry the results one step further and compute the mean number of threshold crossings per unit time using the output spectral density⁷. Such calculations are useful, for example, in predicting the fatigue life of the rotor blade. However, this will be presented in a sequel where the forward speed of the vehicle is dealt with.

The principal aim of this paper has been to present a consistent first order set of equations for the problem of a rotating blade under random loading, with features including blade flexibility, root-end fixity and modal couplings. The results from this problem, thus,

could serve as limits on an actual rotor with an intermediate type of end fixity.

Though the random input choice has been, of necessity, arbitrary, yet since it is not entirely unrepresentative of the isotropic turbulence pattern chosen commonly^{2,3} it is possible to conclude from the results of Figs. 3a and 3b that the higher modes and modal couplings are perhaps not very significant at least for the linear system considered. It remains to be seen if this will be borne out in nonlinear systems due to large-displacement effects.

REFERENCES

1. C. W. Stammers, "The Flutter of a Helicopter Rotor Blade in Forward Flight," *The Aeronautical Quarterly*, Vol. 21, pp. 18-48, 1970
2. G. H. Gaonkar and K. H. Hohenemser, "Flapping Response of Lifting Rotor Blades to Atmospheric Turbulence," *Journal of Aircraft*, Vol. 6, pp. 496-502, 1969
3. G. H. Gaonkar and K. H. Hohenemser, "Stochastic Properties of Turbulence - Excited Rotor Blade Vibrations," AIAA paper No. 70-548, 1970
4. R. H. Miller and C. N. Ellis, "Blade Vibrations and Flutter," *Journal of American Helicopter Society*, Vol. 1, 1956. Also N. D. Ham, "Notes for UCLA Short Course on Helicopter Dynamics and Aerodynamics," (1970)
5. J. M. Greenberg, "Airfoil in Sinusoidal Motion in a Pulsating Stream," NACA TN 1526, 1947
6. R. L. Bisplinghoff, H. Ashley, and R. L. Halfman, *Aeroelasticity*, Addison-Wesley, 1955
7. A. A. Sveshnikov, *Applied Methods of the Theory of Random Functions*, Eng. Trans. Pergamon Press, London, 1950
8. J. D. Robson, *An Introduction to Random Vibration*, Elsevier Publishing Co., New York, 1964
9. D. R. Cox and H. D. Miller, *The Theory of Stochastic Processes*, John Wiley, New York, 1965
10. J. F. Ward, "A Summary of Hingeless-Rotor Structural Loads and Dynamics Research," *Journal of Sound and Vibration*, Vol. 4, pp. 358-377, 1966
11. R. T. Yntema, "Simplified Procedures and Charts for the Rapid Estimation of Bending Frequencies of Rotating Beams," NACA TN 3459, 1955

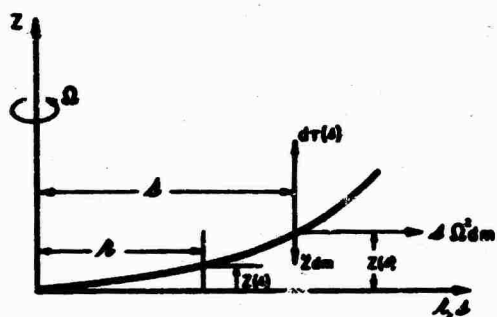


Figure 1. GEOMETRY OF A BENT BLADE

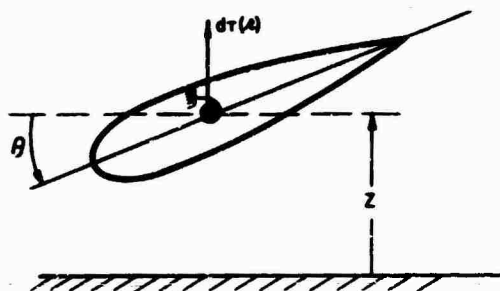


Figure 2. CROSS SECTION OF A BLADE

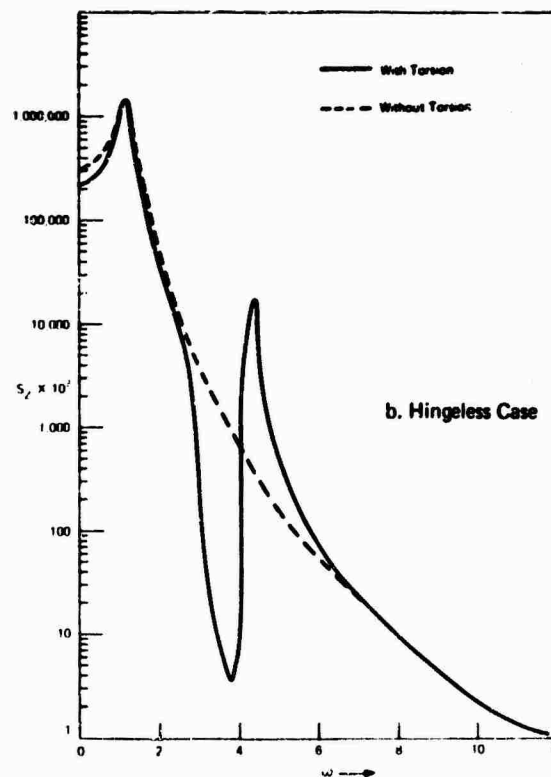
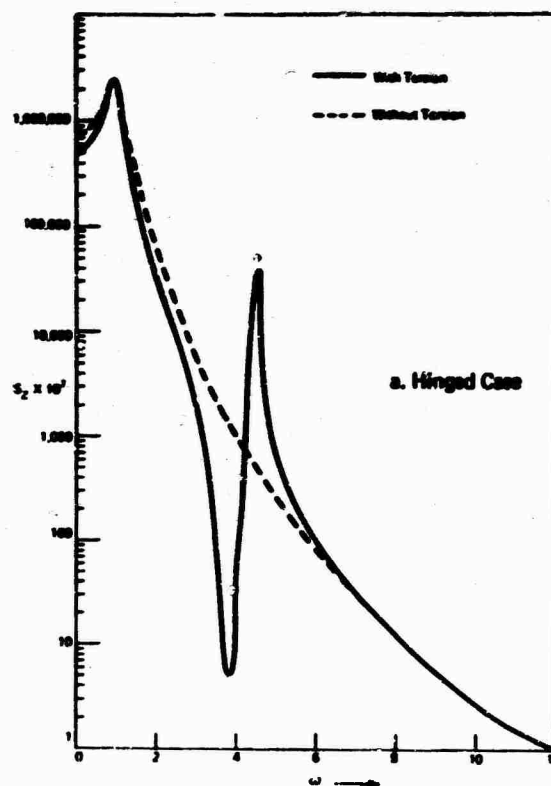


Figure 3. SPECTRAL DENSITY OF RESPONSE

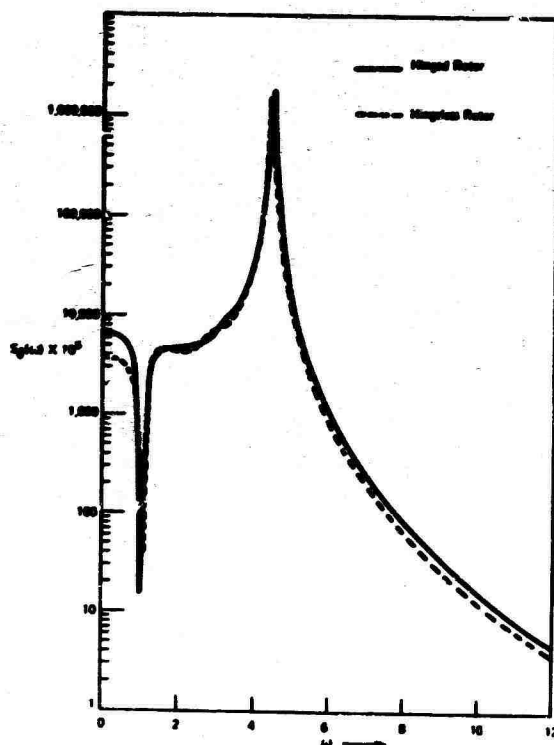


Figure 4. SPECTRAL DENSITY OF TORSIONAL RESPONSE

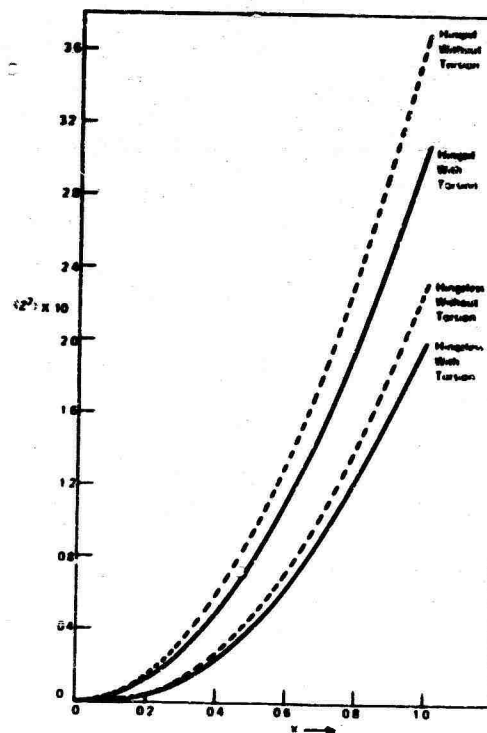


Figure 5. MEAN SQUARE RESPONSE

**INSTRUMENTATION TECHNIQUES AND THE APPLICATION
OF SPECTRAL ANALYSIS AND LABORATORY
SIMULATION TO GUN SHOCK PROBLEMS**

D. W. Culbertson
Naval Weapons Laboratory
Dahlgren, Virginia

and

V. F. DeVost
Naval Ordnance Laboratory
White Oak, Silver Spring, Maryland

Described are instrumentation techniques used in, and major results of, measuring the in-bore environment in 5" navy guns, performing spectral analysis of gun shock, and conducting laboratory simulation and correlation studies.

BACKGROUND AND INTRODUCTION

During 1969, a series of in-bore ammunition premature malfunctions was experienced during 5" naval gun firings. An extensive investigation identified the most probable cause of these malfunctions as reaction of defects in the projectiles' explosive filler to the gun ballistic environment. Accordingly, actions were taken to establish ammunition production improvements as well as inspection methods to detect and remove faulty ammunition from service use.

Subsequently, during 1970, additional in-bore prematures were experienced with inspected ammunition. At this time, examination of the accumulated in-bore premature history indicated a strong correlation between the observed events and the very early time gun ballistic environment produced by a particular propelling charge assembly, see Table 1. Renewed investigative efforts were directed toward definition of the early-time 5" gun environment and its effect on ammunition performance. The rather unique techniques involved in this investigation and the general findings are discussed herein.

The reported work was performed during the period November 1970 through May 1971. It was a major portion of a Naval Ordnance Systems Command sponsored program designed to determine causes of, and remedial measures for, in-service gun ammunition malfunctions. Actions of the overall program are currently being published [1], and will be

TABLE 1
Explosive-Propelling Charge Correlation
for 5"/38 Ammunition In-Bore Prematures

Selected Parameters of 1970 In-Bore Prematures			
Event No.	Type Explosive Load	Type Propelling Charge	Bore Travel to Reaction (in.)
1	A-3	Type A	1.8
2	A-3	Type A	11.0
3	A-3	Type A	10.0
4	A-3	Type A	6.0
Accumulated In-Bore Premature Rates for Six-Year Period			
A-3 Expl/Type A Prop Chg... $1/1.5 \times 10^4$			
A-3 Expl/Type B Prop Chg... $0/1.4 \times 10^6$			

available to qualified requesters from the Defense Documentation Center by about early December 1971.

PROCEDURES AND EQUIPMENT

Ballistic Performance Studies. Two principal experimental methods were used to measure the 5"/38 gun ballistic environment and its interaction with ammunition assembly components: a 5"/38 MARK 12 MOD 1 gun barrel was instrumented as shown in Fig. 1; and special test projectile assemblies were instrumented with either peak-reading

Preceding page blank

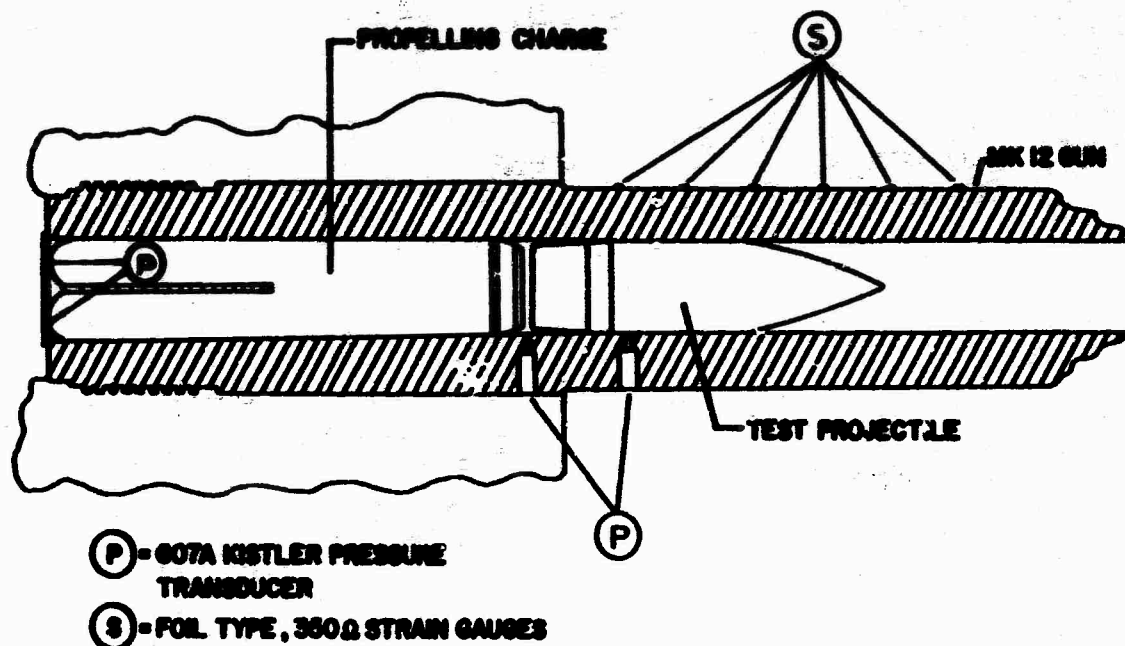


Fig. 1 - Instrumented 5"/38 gun test vehicle

mechanical transducers or continuous-recording pressure and acceleration transducers as shown in Fig. 2. The locations of these transducers were selected to provide information on the pressure-time history at the base and mouth of the propelling charge and the resulting pressure and shock loading on the projectile structure and components. Instrumentation characteristics were as follows:

a. The continuous-recording pressure transducers were exclusively the Kistler Model 607A, having a 75-ksi range and a 240-kHz resonant frequency. The continuous-recording accelerometers were either Endevco Models 2291 or 2292, having respective range and resonant frequency characteristics of ± 100 kg, 250 kHz and ± 20 kg, 125 kHz. Low noise coaxial cable was used throughout. Data recording was on a Honeywell Test Instruments Model 7620 wide-band magnetic tape system, double-extended mode, 432 kHz center frequency, D.C. to 80 kHz response at 120 inches per second recording speed. End-to-end system response was 80 kHz. For the instrumented projectile experiments, the transducers were "hard-wired" through the gun bore to the signal-conditioning and recording equipment; this technique provided from 0.5 to 1.5 milliseconds of recording time before adverse cable motion/destruction effects were experienced.

b. Mechanical gauges consisted of peak-reading, self-recording accelerometers and pressure transducers. The accelerometers were the Mindlin gauge copper-ball, used to measure set-back shock spectrally at four frequencies, and the NOL WOX-5A, used to measure transverse and spin accelerations [2]. The peak-reading pressure gauge consisted of a base-detonating fuze body modified to incorporate four peak-pressure-reading diaphragms; the diaphragms were located circumferentially on the fuze body just forward of the threaded portion. These gauges were calibrated in the NOL 21-inch Air Gun Facility, using a set-back simulator developed specifically for gun inertial loading studies of projectile fillers.

Shock Spectra Analysis. Shock data analysis consisted of determining the component frequencies of the projectile assemblies used in the investigations and performing analog computer analysis of the components' response to the early-time pressure and acceleration pulses measured in the ballistic performance studies.

a. For component frequency analyses, the projectile assemblies were simplified to a three-component structure: base, shell, and filler. The fundamental frequencies of individual components were computed using the longitudinal sound velocity in

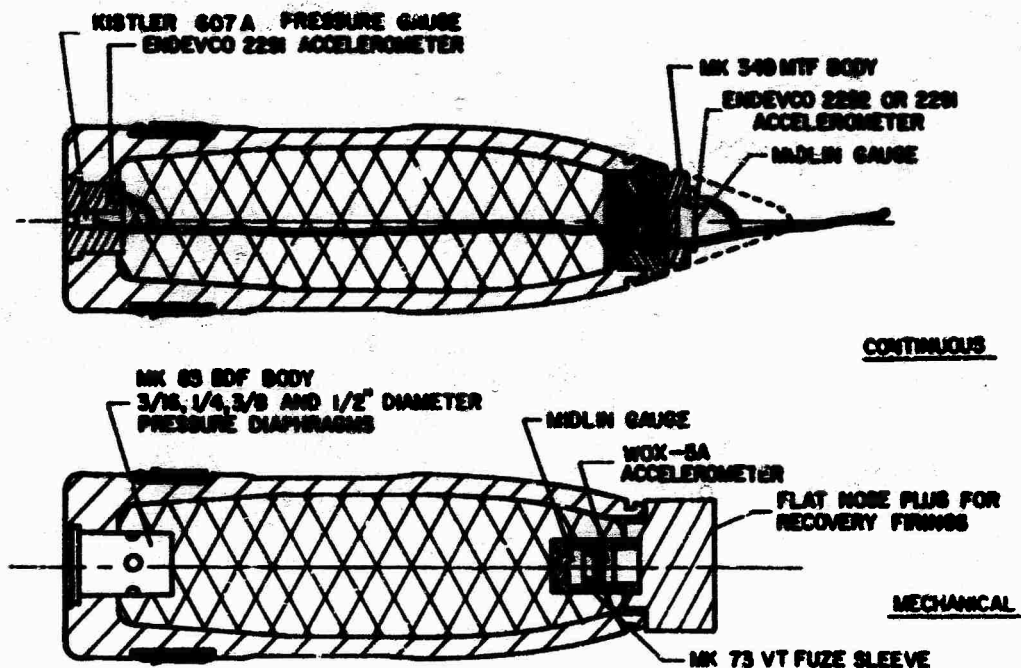


Fig. 2 - Projectile Instrumentation

materials theory [3], and were experimentally measured by monitoring the free-body ringing response. A schematic of the projectile and representative data obtained during the experiments are shown in Fig. 3. Tabulated results for empty and for inert and explosively loaded 5" projectiles are given in Table 2.

b. Single-degree-of-freedom (sdf) system responses to the experimentally determined gun-projectile pressure and acceleration pulses were computed using the NOL Analog Shock-Spectrum Analyzer. The analog analyzer was used in lieu of digital computer techniques because primary interest was only in the early-time, ≤ 1.0 millisecond, portion of the gun ballistic environment; additionally, many of the continuous shock recordings contained large signal errors at cable destruct times, which would have been difficult to correct on the digital system. Response accelerations were obtained for sdf system frequencies of from 430 Hz to 45 kHz; system damping was 2.0 percent of critical.

Simulation and Correlation Studies. Laboratory simulations and analytical modeling were performed during the investigations in order to obtain better understanding of observed experimental results and to minimize

costs of full-scale experiments. These efforts were primarily concerned with examination of the 5" propelling charge ignition-ammunition interaction phenomena; initial ballistic performance experiments suggested the presence of ignition compression waves possibly producing considerable grain and cartridge case closure plug motion in the Type A propelling charge. Flash X-ray experiments, using an unconstrained fiberglass cartridge case with standard primer, propellant, and closure plug components, were performed to obtain a more quantitative understanding of the phenomena. Concurrently, air gun experiments were performed; the apparatus is shown schematically in Fig. 4. The experiments were designed to establish an economical laboratory technique for simulating the observed early-time gun ballistic environment on the base of projectiles. The resulting technique was subsequently used to study the response of specific ammunition components, especially mechanical fuze components, to the simulated early-time gun environments.

MAJOR RESULTS AND DISCUSSION

Ballistic Performance Measurements. Data obtained from the high-response pressure-time instrumentation in the

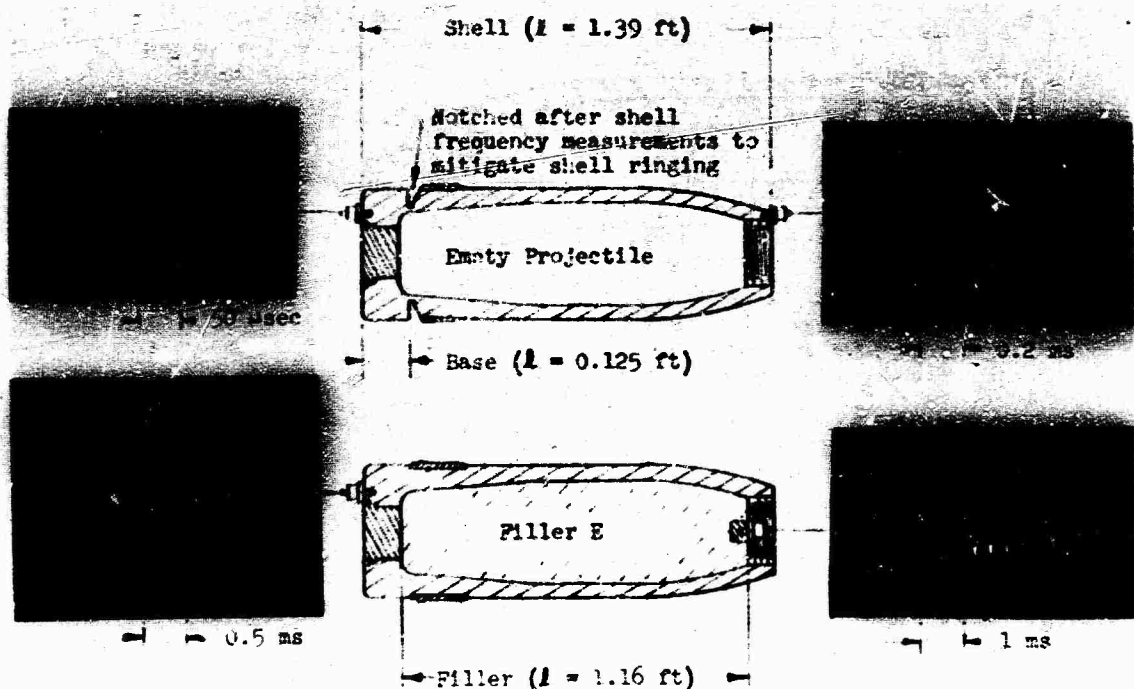


Fig. 3 - Component frequency measurements

Reproduced from
best available copy.

TABLE 2
Projectile Component Frequencies

Projectile Configuration	Component	Measured Frequency (kHz)	Computed Frequency (kHz)	Log Decrement Δ	Damping (% Critical)
Empty	Base	61.0	65.5	*	*
	Shell	5.8	5.9	1.05	<0.5
Inert Loaded (Filler "E")	Base	46.0	65.5	*	*
	Shell	5.8	5.9	1.14	2.0
	Filler	2.9	2.8	1.08	1.0
Live Loaded (COMP A-3)	Base	50.0	65.5	*	*
	Shell	5.5	5.9	1.2	2.6
	Filler	2.7	2.8	*	*

*Not Measurable

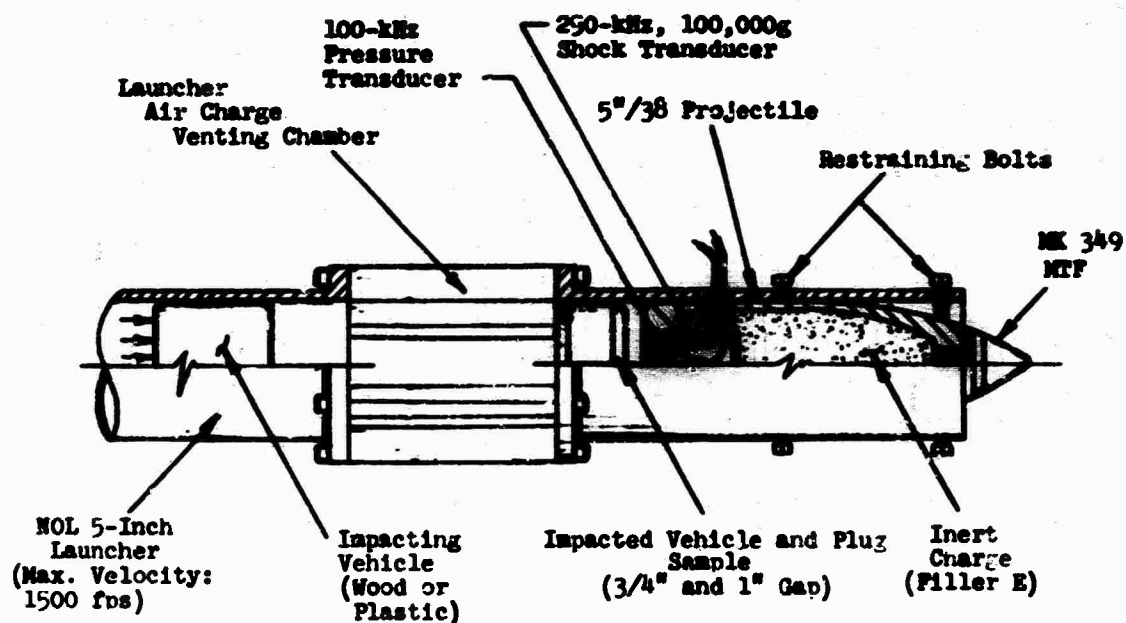


Fig. 4 - Air gun simulation facility

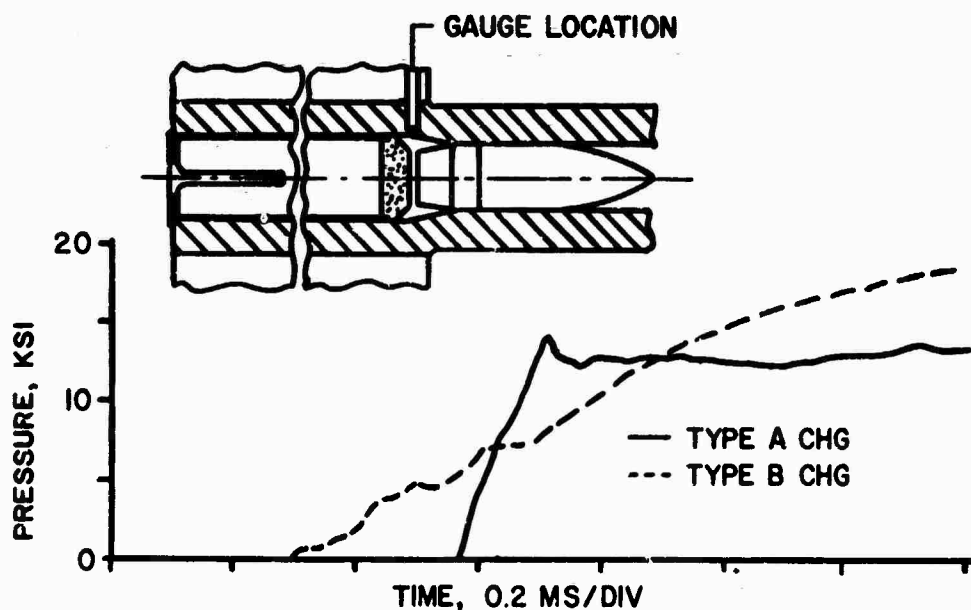


Fig. 5 - Comparison of initial case mouth pressure profiles for Type A and Type B propelling charge

gun chamber walls quickly identified a significant difference between Type A and Type B propelling charge ballistic performance; at the cartridge case mouth, the Type A charge consistently produced a characteristic step rise as compared to the more gradual rise characteristic of the Type B charge; see Fig. 5 for comparison. The overall pressure-time pulses for both types of charges are compared in Fig. 6; analyses of these profiles indicated that strong, combustion compression waves were present in both charges but that this phenomenon was more severe in the Type A charge. Further analyses, including consideration of pressure measurements made at various distances along the propellant bed, and the detailed design characteristics of the charge ignition systems, indicated that the observed wave action was related to initial propellant ignition and subsequent burning front development. Also, the analyses suggested that significant propellant mass was being accelerated behind the closure plug, adding to the mass impacting the projectile base.

Data obtained from the instrumented projectile experiments are given in Table 3 and recordings are shown in Fig. 7. While the mechanical gauge

effort was hampered by projectile recovery problems, useful data were obtained indicating that setback shocks, angular accelerations, and projectile filler base pressures were significantly higher in the rounds fired by the Type A propelling charge than in those fired by the Type B charge. The continuous-recording instrumentation provided useful data during the very-early-time charge ignition-projectile start period, about 0.5 to 1.5 milliseconds from initial projectile base pressure rise. These data, as shown in Fig. 7, established that the projectiles fired with Type A propelling charges were subjected to significantly more severe early-time shock than were those fired by the Type B charge. Of particular significance was the high-amplitude, short-duration pressure pulse observed by the pressure transducer in the projectile base; it was hypothesized that this pulse was caused by initial impact of the Type A propelling charge closure plug and accelerated propellant grain mass. This was verified and quantified during simulation studies as explained below and was found to be the most probable cause of explosive filler initiation in the service premature functionings.

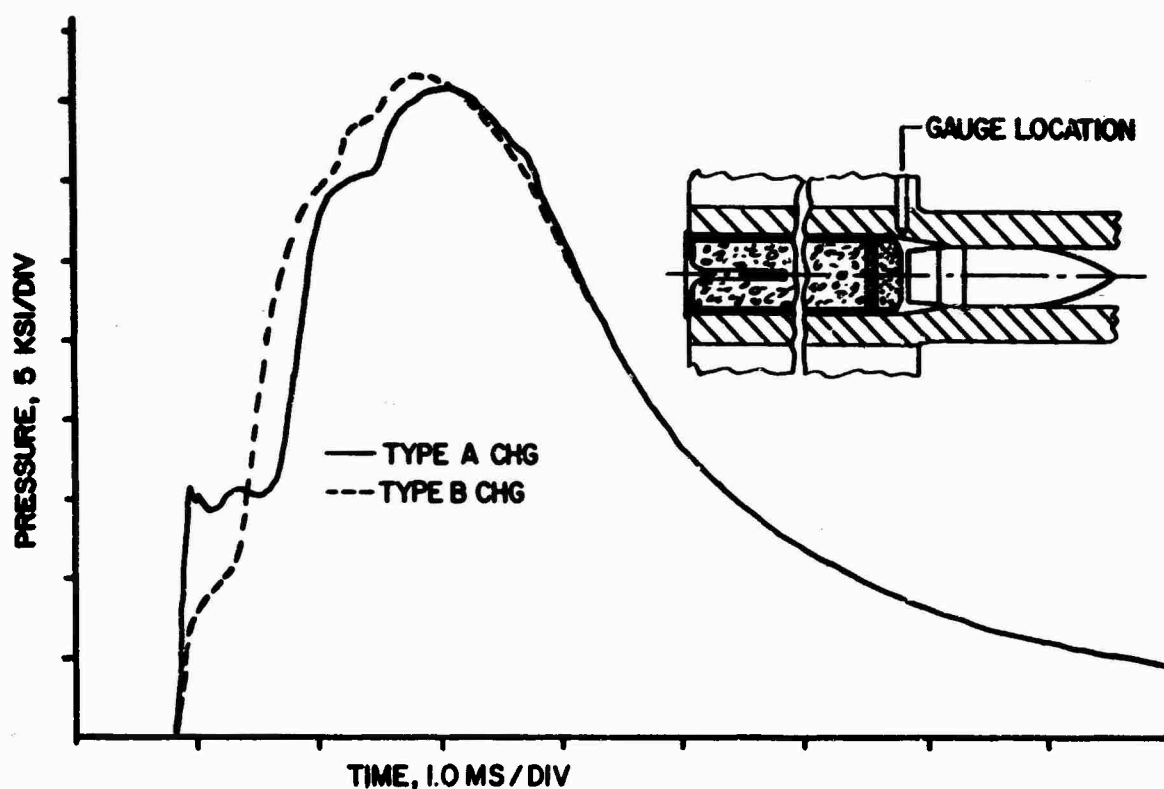


Fig. 6 - Comparison of pressure-time profiles for Type A and Type B propelling charge

TABLE 3
Mechanical Gauge Data

Type A Propelling Charge

Round No.	WOK-5A Spin Acceleration		Pressure Gauge		% Above Nominal Setback Pressure*
	Ball Deformation Avg (1/1000")	(Rad/Sec ²)	Diaphragm Deformation (1/1000")	Peak (psi)	
1	2.60	585,000	†	--	--
2	3.75	840,000	61.0	29,500	41.0
3	4.95	1,100,000	70.0	30,400	45.0

Type B Propelling Charge

1	‡	--	--	--	--
2	0.8	180,000	40.0	27,000	13
3	**	--	48.0	28,000	18

*20,900 psi for Type A and 23,800 psi for Type B charges

†Filler in the region around the gauge diaphragms was gouged when the base fuze was assembled and was not in contact with the diaphragms. Readings were very low.

‡Round broke up; none of the gauges were recovered.

**Apparently rotor inertia force was not high enough to overcome the setback frictional force — this happens frequently with Type B charge firings.

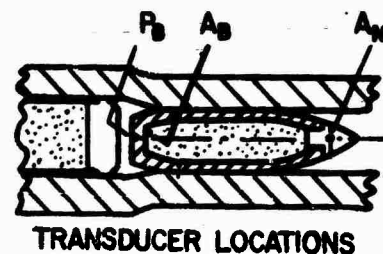
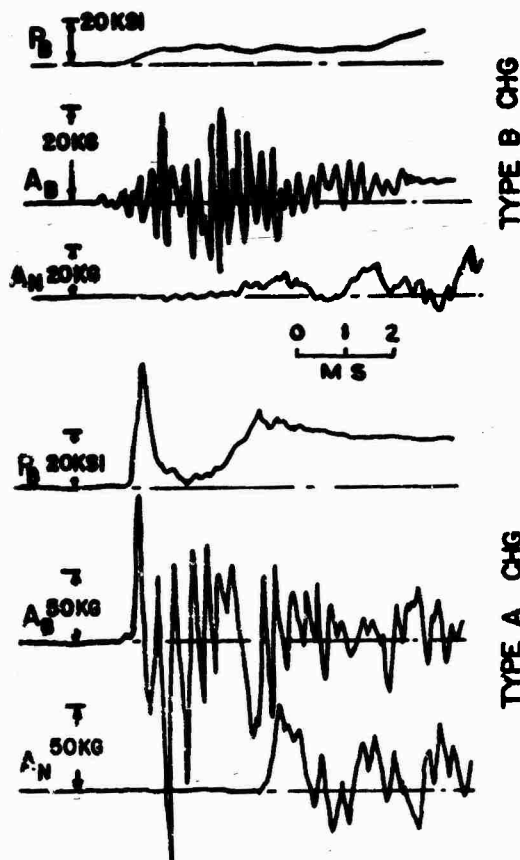


Fig. 7 - Typical continuous recordings

Reproduced from
best available copy.

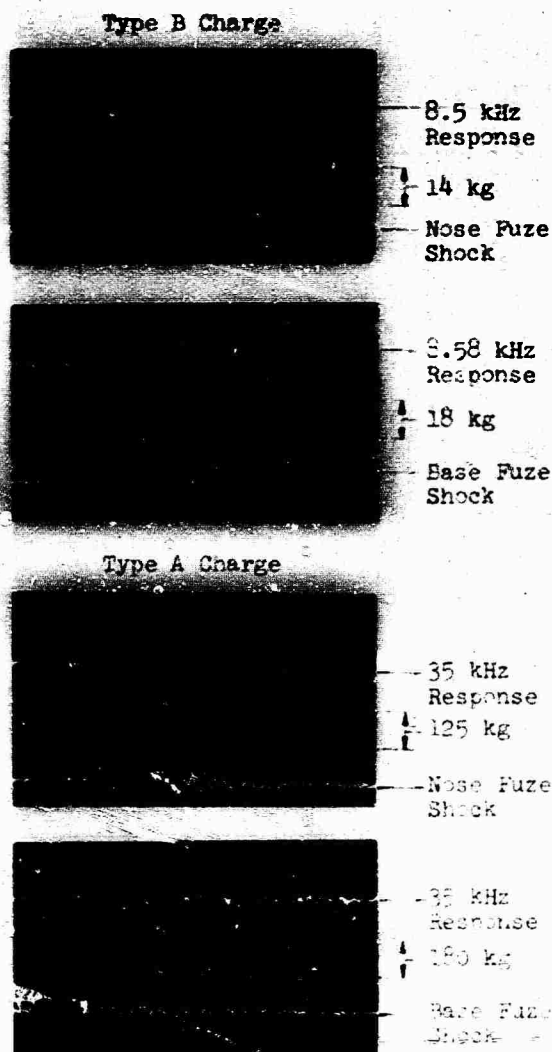


Fig. 8 - Comparison of propelling charge shocks and analog responses

Shock Analysis. Fig. 8 shows typical recordings and analog responses of Types A and B propelling charge-produced shocks measured at both projectile base and nose locations. Spectra of the shocks are shown by Fig. 9. These data show that the early-time shock peaks produced by the Type A propelling charge are more than four times higher than those produced by the Type B charge. As expected, responses approaching the natural frequency of the projectile base (46 kHz) are the highest; responses for the Type A propelling charge are from 1.7 to 21.6 times higher than comparable responses for the Type B propelling charge.

Simulation and Correlation Studies. Typical flash radiographs obtained during the special flash X-ray experiments are shown by Fig. 10. These exposures contrast the grain-closure plug performance exhibited by the Type A and Type B propelling charges. For the Type A charge, the cork closure plug, originally about three inches thick, has been compressed to approximately 0.5 inch thick, has assumed a convex striking surface, and is being accelerated toward the projectile base to a peak impact velocity of approximately 700 ft/sec. The closure plug fired with the Type B propelling charge disintegrates and impacts the projectile with considerably less velocity and force. This action is attributed to differences in propellant grain size and mass, and ignition development between the two charges; for the Type A charge, smaller propellant grains plus relatively small area of initial ignition action result effectively in a rather compact mass of propellant grains and compressed gas being driven toward the projectile seat. In the Type B charge, larger grain size permits more gas flow forward and through the unignited propellant bed. This results in less propellant motion and produces enough pressure against the closure plug to disintegrate it.

Typical results of air gun simulations of the closure plug/propellant mass and projectile base impact phenomena are shown by Fig. 11. To determine the conditions for equivalency with the measured 5"/38 gun parameters, the simulated propellant mass ranged from two ounces to five pounds, while plug impact velocities ranged from 280 to 1420 ft/sec. It is seen that with approximately a one-half inch convex plug leading edge shape, plus approximately 2.5 ounces of simulated propellant mass and a final plug impact velocity of 755 ft/sec, the projectile base pressure and acceleration profiles are essentially identical to those measured in the gun-fired instrumented projectile experiments.

These simulations provided clear evidence that the severe impacts and high impulsive pressures recorded at the bases of projectiles using the Type A propelling charge were produced by the grain-closure plug impact phenomenon. Further analysis indicated that the observed projectile base impact loading was subjecting the explosive filler at the projectile base-explosive interface to low level shock pressure pulses of about 0.4 to 1.5 kb with durations of approximately 30 to 50 microseconds. Through examination of

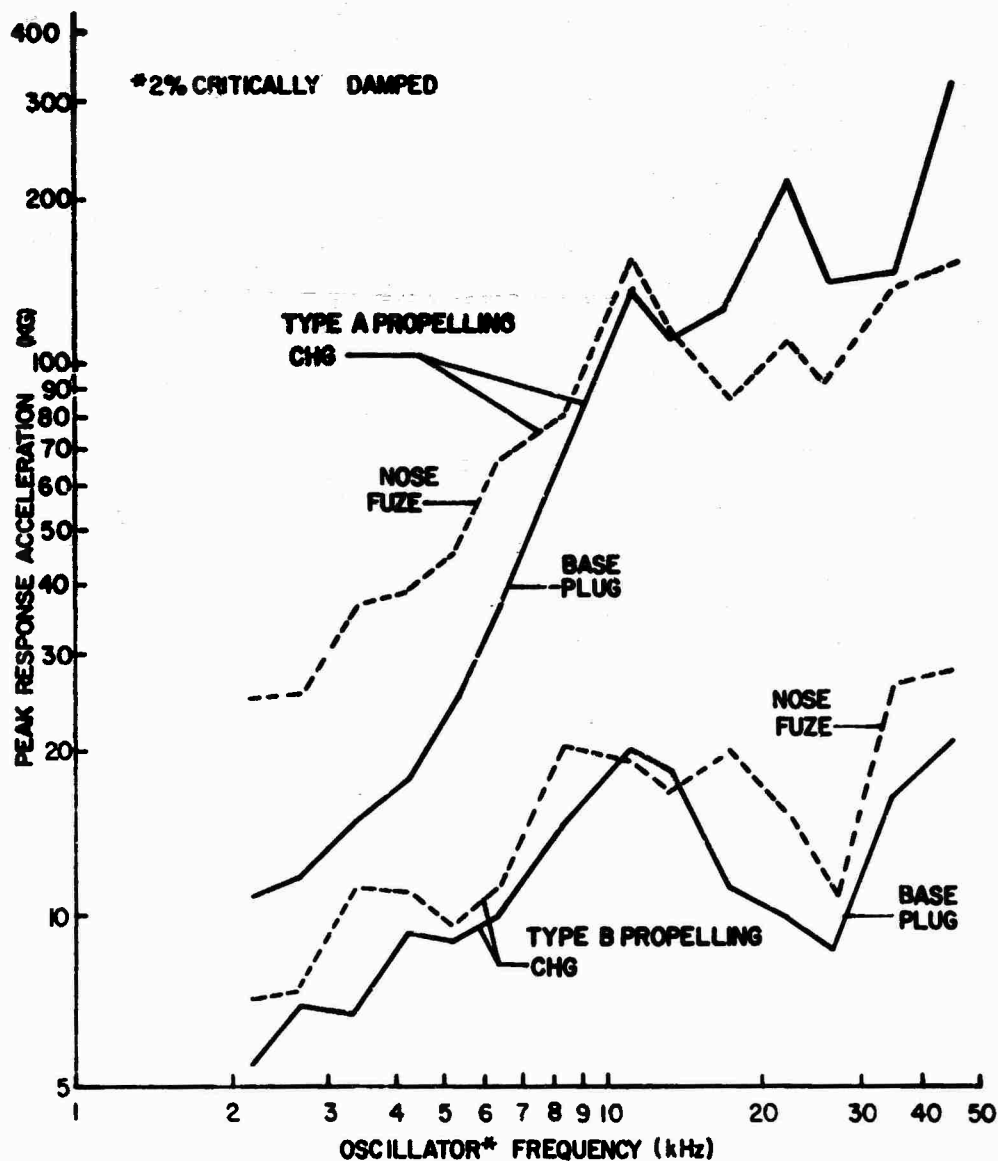


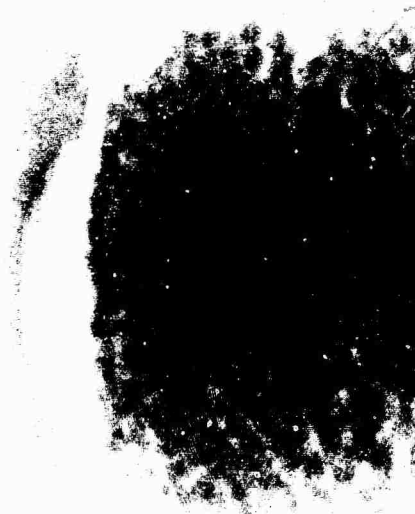
Fig. 9 - Early-time spectra of 5"/38 set-back shock

available shock initiation data for high explosives, it was possible to construct a family of initiation probability curves for Composition B explosive as a function of pressure level and pulse duration, see Fig. 12. Data from Ref. [4] were particularly useful here since these data allowed unique estimation of the 0.1% and 0.01% initiation probability curves to supplement the normally determined .50% probability curve. Entering these curves with the estimated average impact pulse characteristics, i.e., 1.0 kb and 40

microseconds, a predicted explosive initiation frequency of about one in 10^4 events is obtained. This compares closely with the observed service ammunition premature rate of about one in 15×10^3 events. It should be noted here that the Composition A-3 explosive involved in the service prematures is generally acknowledged to be somewhat more sensitive to shock initiation than Composition B explosive, for which the initiation probability data were available.



TYPE B PROPELLING CHARGE



TYPE A PROPELLING CHARGE

Fig. 10 - Flash radiographs of propelling charge closure plug performance

Reproduced from
best available copy.

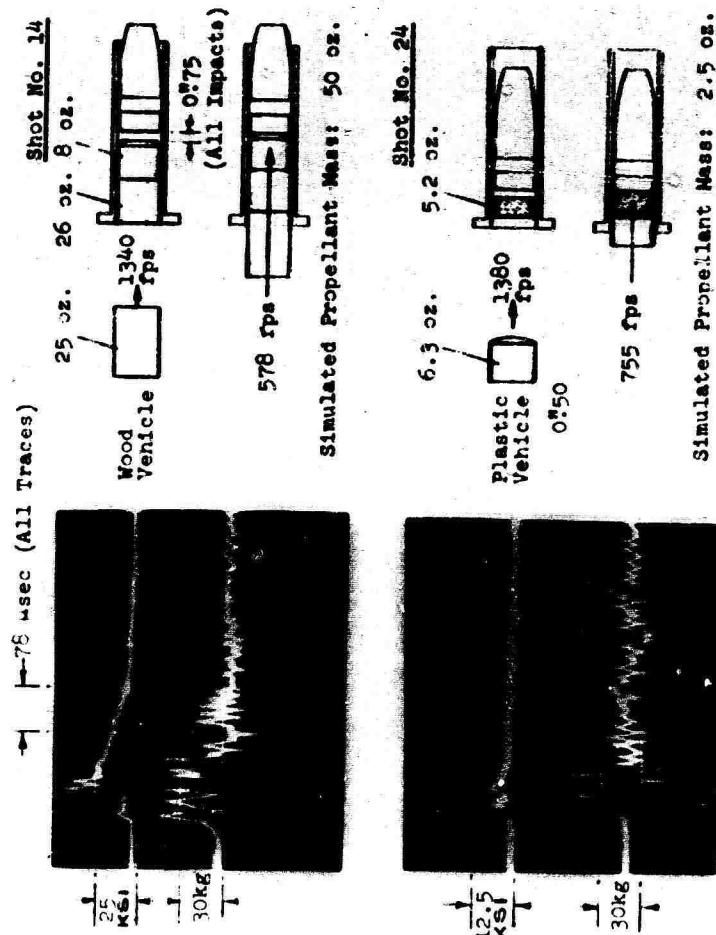


Fig. 11 - Air gun simulation data

Reproduced from
best available copy.

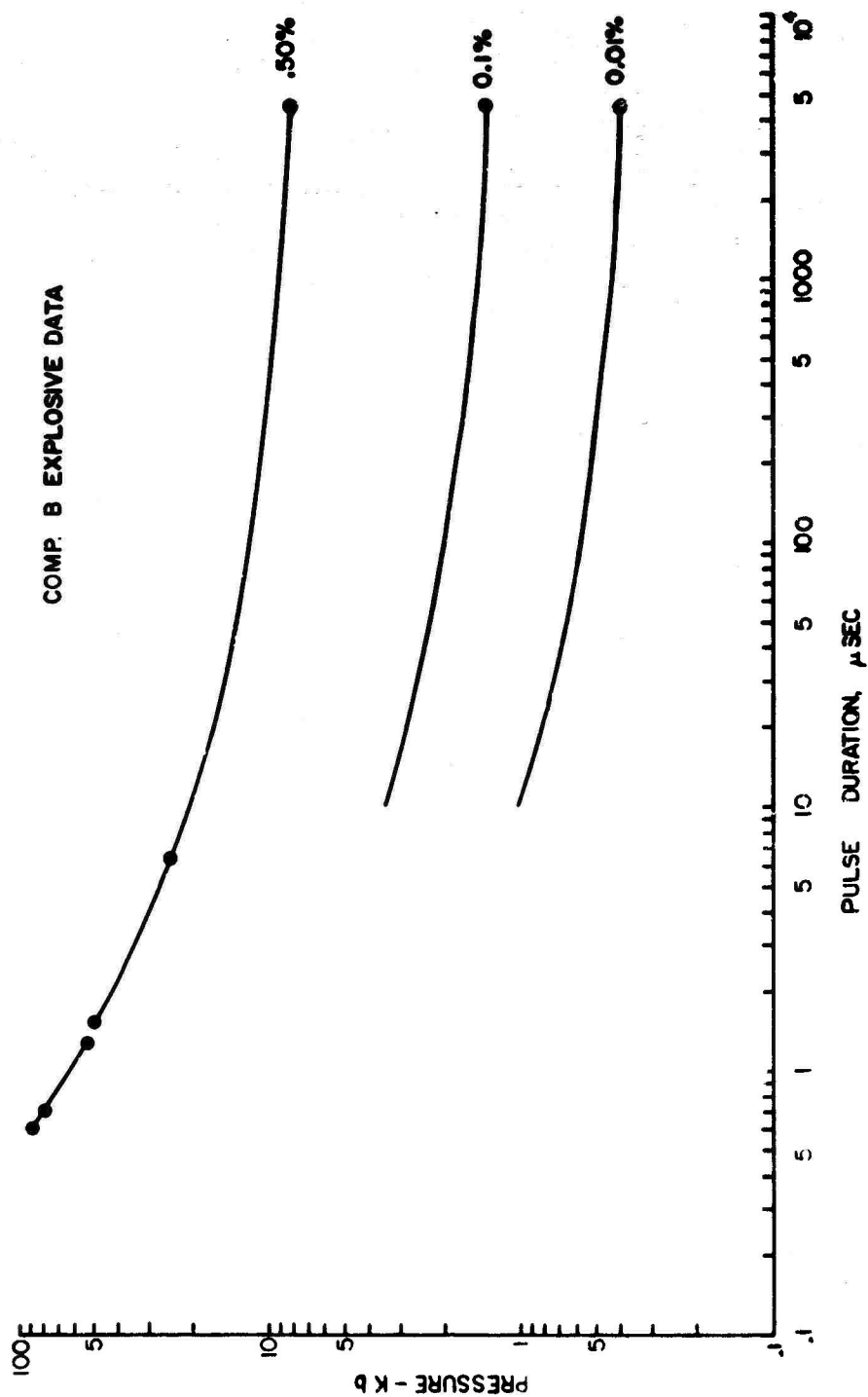


Fig. 12 - Shock initiation probability curves as function of pulse characteristics

CONCLUDING REMARKS

During this work, a great deal was learned that was not previously known about gun ballistic parameters. The techniques developed are proving of value in determining design adequacy and performance safety of other naval gun ammunition systems. Finally, it should be noted that the ballistic anomalies detected in the Type A propelling charge have been rather simply remedied; improvement of the charge ignition system has been effected, resulting in essentially identical ballistic performance for the two types of propelling charge assemblies.

REFERENCES

1. M.C. Shamblen et al, "Investigation of 5" Gun Ammunition Malfunctions," NWL Dahlgren Tech. Rept. TR-2624, Oct. 1971
2. V.F. DeVost, "WOX-5A Accelerometer (Artillery Projectile Copper-Ball Accelerometer)," NOL Tech. Rept. NOLTR 68-85, May 1968
3. L. Aronica, "Sound Velocity and Elastic Moduli Measurements on Several TNT Base Explosive Compositions," NAVORD Rept. 6087, Feb. 1961
4. R.T. Schimmel et al, "Effect of Base Separation and Loading Density on the Setback Sensitivity of Composition A-3," Picatinny Arsenal Tech. Rept. 4147, Nov. 1970

THE EFFECT OF "Q" VARIATIONS IN SHOCK SPECTRUM ANALYSIS

M. B. McGrath
Martin Marietta Corporation
Denver, Colorado

and

W. F. Bangs
National Aeronautics and Space Administration
Goddard Space Flight Center, Maryland

The response shock spectrum is a function of the assumed damping or amplification factor, Q . The wide range of Q values used in the aerospace industry complicates the comparison of shock spectra. One method for estimating the sensitivity of a shock spectrum to a variation in damping is to perform a statistical analysis of shock data. This paper presents the results of such an analysis in the form of conversion factors that can be used to adjust a spectrum from one value of Q to another. The conversion factors are supplemented with an estimate of the variance and the probability distribution of the data. The data are further used to estimate the average number of equivalent cycles of sinusoidal motion present in the complex wave.

INTRODUCTION

The amplification factor, or Q , used in shock spectrum analysis varies throughout the aerospace industry. Values ranging from five to 50 are typical, but there is no one standard value. Often a shock spectrum is available, but with a Q different than the analyst desires; converting the spectrum to the desired Q value requires recomputing the spectrum using the original acceleration time history. In cases where the original data are not available or it is too costly to recompute the spectrum, another method is obviously needed. This paper presents two empirically derived curves that can be used to adjust shock spectra from one Q value to another. The curves are based on data from pyrotechnic shock tests conducted under Contract NAS5-15208 for Goddard Space Flight Center and discussed at the 41st Shock and Vibration Symposium [1]. A total of 16 measurements of acceleration time histories were used in the analysis. Shock spectra were computed for the 16 measurements at third octave frequencies for $Q = 5, 10, 20, 30, 40$, and 50. The resulting data were normalized to the $Q = 10$ spectrum and a statistical analysis was performed on the data. The results are two curves, one for peak values of spectra and one for non-peak values of spectra, giving a conversion ratio or adjustment factor for Q values from five to 50.

The conversion factors represent the average of ratios between two spectra for the same acceleration-time history for two different values of Q . The data points of a spectrum to be adjusted

from a given Q to a new value of Q are multiplied by the simple conversion ratio from the curves that relates these two amplification factors. The non-peak and peak values of the spectrum are multiplied by two different factors. This method allows an approximate new spectrum to be calculated with little effort and time.

The adjustment factors and the transient response of an oscillator to a sinusoidal base input are related in the paper to allow one to estimate the average number of equivalent cycles of sine motion present in an acceleration-time history for various values of Q .

The paper also presents the average ratios for conversion and the standard deviation of the conversion ratios, and discusses the statistical distribution of ratios. These statistics allow the user to incorporate varying degrees of conservatism into his analysis.

SHOCK SPECTRUM FUNDAMENTALS

A shock spectrum is defined in terms of the maximum response of a series of single-degree-of-freedom spring-mass-damper systems. The maximum response of each oscillator to an input base acceleration is plotted either as a function of the oscillator frequency for one damping ratio, ζ , or as a function of the amplification factor, Q . The most common spectrum in use is the maximum spectrum, in which the response is the absolute acceleration of the oscillator mass. For this model the governing differential equation

Preceding page blank

is

$$\ddot{z} + 2\zeta\omega_n \dot{z} + \omega_n^2 z = -\ddot{y}(t), \quad (1)$$

where

$z = x - y$ = relative displacement of the mass;

x = absolute displacement of the mass;

y = absolute displacement of the base;

$\omega_n^2 = k/m$ = natural frequency of the oscillator;

$\zeta = C/C_c$ = damping ratio;

$Q = 1/2\zeta$ = amplification factor;

$\ddot{y}(t)$ = specified absolute acceleration of the base.

The response of the system to a relative deflection for zero initial conditions and for $\zeta^2 \ll 1$ is

$$z(t; \omega_n, \zeta) = -\frac{1}{\omega_n} \int_0^t \ddot{y}(\tau) e^{-\zeta\omega_n(t-\tau)} \sin \omega_n(t-\tau) d\tau \quad (2)$$

The approximate response due to absolute acceleration is related to the relative deflection by

$$\ddot{x}(t) \approx -\omega_n^2 z(t).$$

For a specified frequency, the response will depend on the excitation, $\ddot{y}(t)$, and the damping ratio, ζ . For a simple pulse that can be expressed analytically, the response can be determined by integrating Eq. 2, and the relation between two spectra for different values of Q can then be calculated. The shock spectra derived from measured acceleration time histories will have a complex response; the effect of damping can only be determined by actually integrating Eq. 2 for each value of Q desired. No simple method exists for predicting the effect of damping on a spectrum. One approach is to use a statistical analysis of sufficient data to determine the sensitivity of a spectrum to damping on an average basis.

DATA ANALYSIS

Sixteen shock spectra, taken from a series of pyrotechnic shock tests performed on the truss frame of a launch vehicle, were used as the basis for a statistical analysis. The spectra were taken from locations that varied from a few inches to over 180 inches from the source. For each of the 16 complex acceleration-time histories, spectra were produced for values of Q of 5, 10, 20, 30, 40, and 50. The spectra were normalized to the $Q = 10$ spectrum by dividing each spectrum value, at the 1/3 octave band frequencies, by the corresponding value on the $Q = 10$ spectrum. This resulted in a 16 x 18 matrix of data ratios for each value of Q from five to 50.

Because the plots of the original spectra and the normalized data indicated that the values were randomly spread over the entire frequency range, the data were averaged for each value of Q . The results are plotted in Fig. 1. The

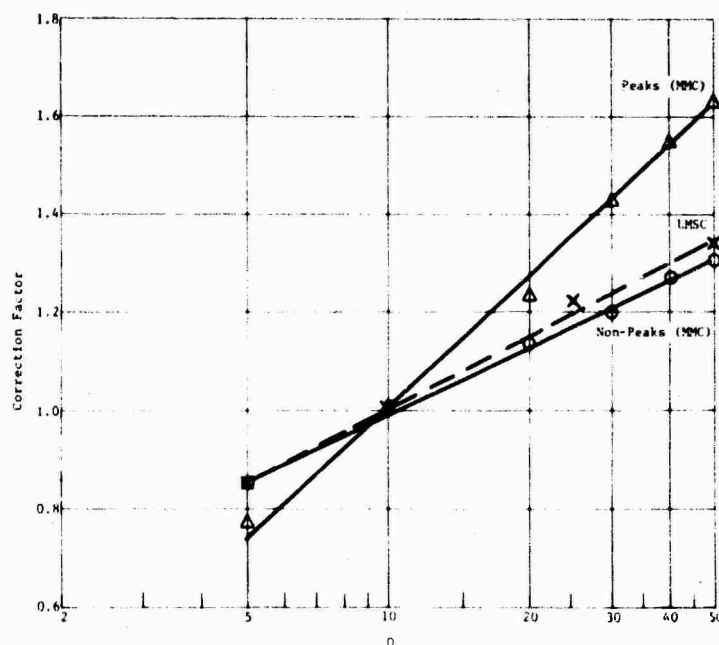


Fig. 1 Correction Factor vs Q From Data

averaging process was carried out for the non-peak and peak values of the spectra, with the peak values having a much smaller sample. The two curves in Fig. 1 show the sensitivity of the data to Q and clearly demonstrate that the peaks are more sensitive than the non-peaks. The ordinate is the correction factor, which is the ratio of the spectra value for various Q's normalized to Q = 10.

Under the contract is Ref. (1), Lockheed carried out the same type of statistical estimate of sensitivity to varying Q values. Shock spectra were produced for 10 measurements from primary structure for Q's of 5, 10, 25, and 50. The data were then normalized for center band frequencies to a Q of 25. The spread of data appeared to be random in nature, and a mean value for the data for each value of Q was determined. These results, renormalized to a Q of 10, are plotted in Fig. 1.

The Lockheed analysis included both the peak and non-peak data without discrimination. The Lockheed curve falls between the peak and non-peak curves, indicating good agreement between the two sets of independent data.

The correction factor curves can be used to adjust a spectrum involving Q's other than Q = 10 by considering the process as a two-step operation. For example, in converting non-peak data from a Q of 20 to a Q of 50, we first convert from 20 to 10 using 1./1.13 from Fig. 1. To get from 10 to 50, we use the factor 1.30. The total mean correction factor is then 1.30/1.13.

To add conservatism to the adjustment factors, the variances of the data were calculated since the ratios are scattered somewhat. The 1-sigma values for the non-peaks and peaks are given in Table 1.

TABLE 1 Calculated Standard Deviations, σ , for Correction Factors

Q	Non-Peak Data	Peak Data
5	0.085	0.10
10	0	0
20	0.10	0.15
30	0.15	0.24
40	0.19	0.30
50	0.21	0.34

Notice that the σ values are different for each curve. The correction factor for the normalized Q value is one by definition and the variance for the normalized Q = 10 point has a zero variance.

The values in Table 1 represent one-sigma numbers: the amount of conservatism to be added can be determined by the user. The statistical distribution of correction factors was examined by plotting a histogram of the points representing the ratio of Q = 20 to Q = 10 for non-peaks. This distribution is shown in Figure 2.

It is fairly certain that the data are not normally distributed because of the severe skewness of the curve. Note that there are points below 1.00, which is unlikely; therefore, these points represent accumulated errors in spectral computations, plot reading, etc. We would expect the correction factor to be bounded by 1.00 on the low end and 2.00 on the high end because the maximum response of a Q = 20 oscillator is twice that of a Q = 10 oscillator. Bounded distributions, shaped like that of Fig. 2, are typical characteristics of the beta or Pearson Type I density functions.

Figure 3 is the cumulative distribution plotted from the same data used for Fig. 2. In converting spectra from Q = 10 to some other Q value, one can quantify his conservatism by using the appropriate σ value to determine the probability of being too low. For example, the mean values of Fig. 1 will be conservative about 65% of the time; the mean plus σ will be high about 93% of the time, etc. In two-step operations, the probability is not cumulative and the values in Fig. 3 apply.

EQUIVALENT NUMBER OF CYCLES

Knowing the correction factors for a set of typical data, it is possible to determine the equivalent number of sinusoidal cycles present in the data. This may be of interest in fatigue problems or in comparing transient and sinusoidal tests.

It is first necessary to calculate the correction factors for the idealized sine input of N cycles duration. From Ref. 2, the expression for the response of a single-degree-of-freedom oscillator to sinusoidal base excitation at its natural frequency is

$$\ddot{y} = Q\ddot{x} \left(1 - e^{-\pi N/Q} \right) \cos \omega_n t, \quad (4)$$

where the notation is the same as in Eq. 1. The correction factors for sinusoidal motion are then derived by dividing by the peak response for Q = 10, giving

$$\frac{(\ddot{y})_Q}{(\ddot{y})_{Q=10}} = \frac{Q \left(1 - e^{-\pi N/Q} \right)}{10 \left(1 - e^{-\pi N/10} \right)}. \quad (5)$$

Plotted in the same format as the data in Fig. 1, Eq. 5 results in the curves shown in Fig. 4. For values of Q less than 10, the curves are not reliable since Eq. 4 is only valid for small damping.

Note that in these semi-log plots, the actual data (Fig. 1) result in a line, but that the sinusoidal input produces curves. This indicates that actual shocks do not contain a unique number of equivalent sinusoidal cycles. The broken line in Fig. 4 is the data line from Fig. 1 for spectral peaks. The number of cycles

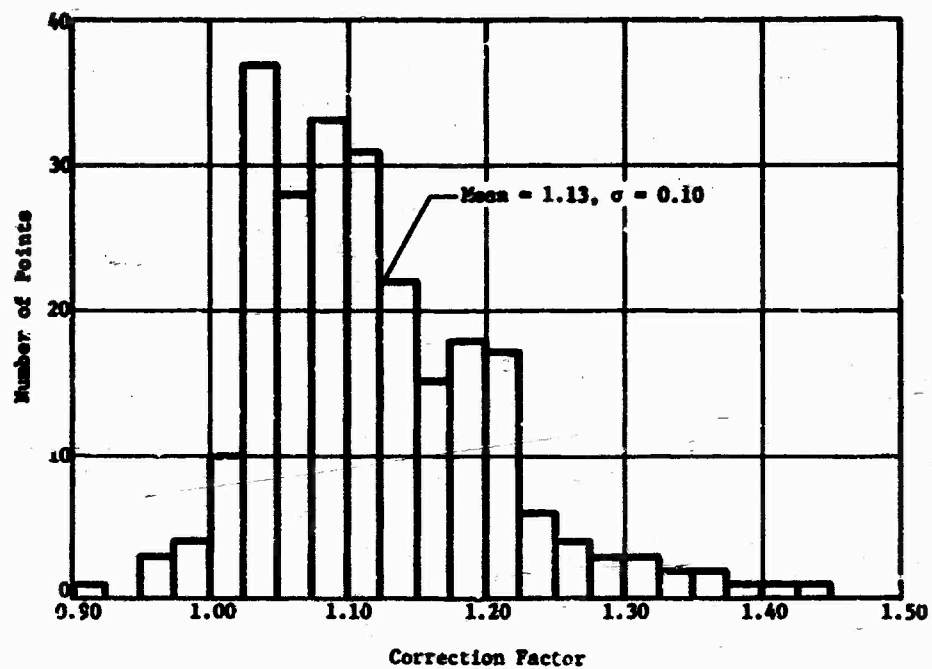


Fig. 2 Histogram of $Q = 20$ Data Normalized to $Q = 10$ (Non-Peaks); 242 Data Points

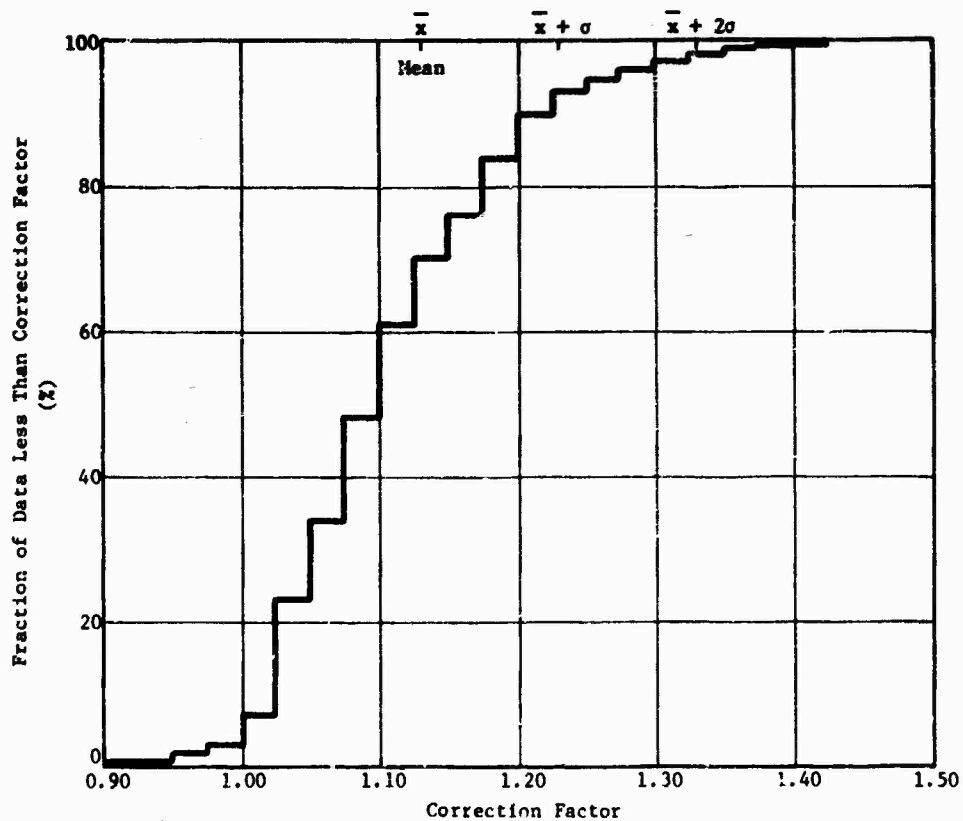


Fig. 3 Cumulative Distribution of $Q = 20$ Data Normalized to $Q = 10$ (Non-Peaks); 242 Data Points

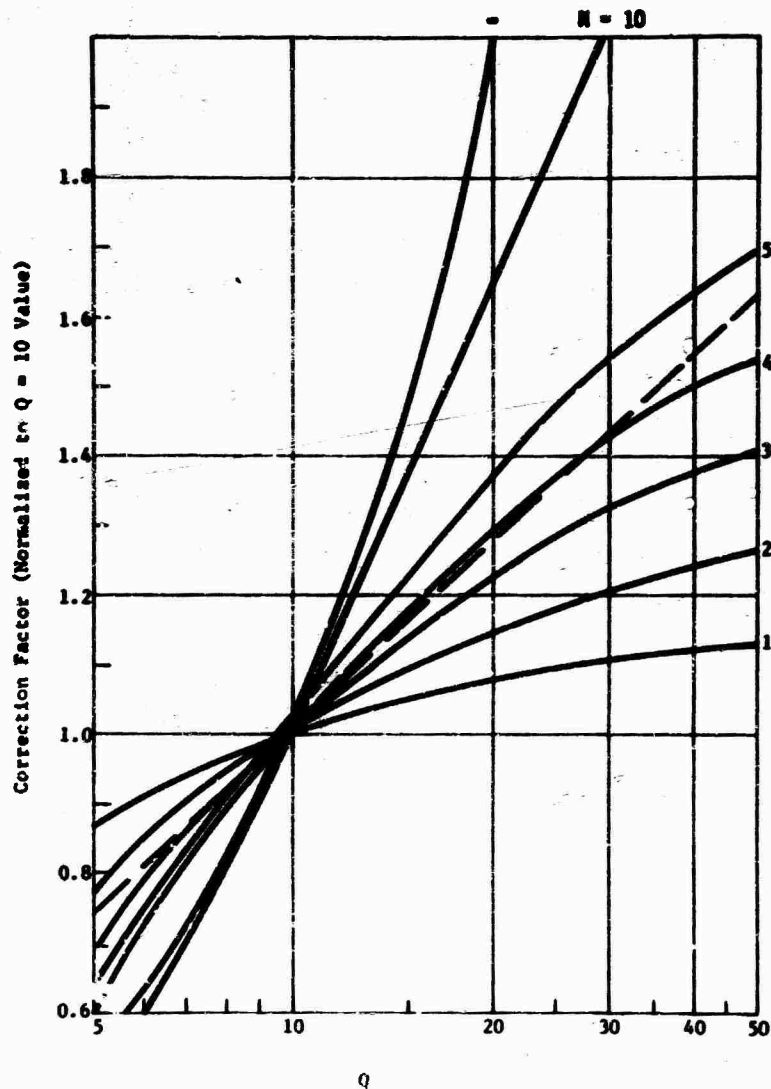


Fig. 4 Correction Factor vs Q for Sine Input of N Cycles

giving the same correction factor as data is a function of the assumed damping. For Q's of 10 to 20, 3.5 to 4 cycles of sine input have the same correction characteristics as data. For higher-Q systems, 40 to 50 for example, four to five cycles is more realistic in terms of correction factors.

The most important conclusion drawn from this figure is that one cannot choose a sine burst type of input to represent field data for a wide range of Q's. Such an equivalence does not exist. Practically speaking, however, if one were to use an input of four sinusoidal cycles and match spectra for a Q of 10, the error in response would be only +3.3% and -6.7% for Q's of 10 to 50. Such an equivalence is, of course, limited to the narrow frequency band about the peak in the data spectrum.

CONCLUSIONS

The data in Fig. 1 allow a spectrum to be adjusted for any given value of Q between five and 50 to any other value of Q in that range. This adjustment procedure is based on a sizable amount of data and good agreement between two independent sets of data. The method of estimating the new spectrum is most effective when the original data are not available or when the costs involved are prohibitive.

A degree of conservatism can be added to the adjustment by using the computed standard deviations of Table 1 and the cumulative probability plot of Fig. 3. The maximum number of equivalent sinusoidal cycles to be expected in a shock signal is a function of the Q of the system being excited. However, the number of cycles present in an average signal may be estimated by comparing the adjustment factors of Fig. 1 to those of Fig. 4.

REFERENCES

1. W. F. Rader and W. F. Rango, "A Summary of Pyrotechnic Shock in the Aerospace Industry," Shock and Vibration Bulletin, Part 5, December 1970.

2. J. D. Cron and R. L. Grant, "Transient Pulse Development," Shock and Vibration Bulletin, Part 5, December 1970.

DISCUSSION

Mr. Trummel (Jet Propulsion Laboratory): You have presented a nice relatively simple and useful concept. But you worked entirely in $1/3$ octaves. It seems that the effect of Q is related to the resolution required in the shock spectrum. Have you looked at the effect of resolution in the measurements?

Mr. McGrath: We performed the shock spectrum using a digital computer so that, unlike the analog method, we were not bothered by the bandwidth of an analyzer. We had the exact response, but one might question whether there is enough definition in the spectrum since we have only plotted $1/3$ octave frequency points. The reason for using $1/3$ octave points is that it begins to get pretty expensive when you go beyond that point. It is expensive as it is when you are analyzing quite a few pieces of data. But it is not the same thing as an analog, and I do not think one needs to worry about the sensitivity of the bandwidth.

Mr. Trummel: Did you use the $1/3$ octave resolution or not?

Mr. McGrath: I do not think that term applies when using a digital solution unless I misunderstand your question. I think your question is related to an analog computer. Perhaps in between the $1/3$ octave points there may be a peak that will be much higher than is shown. During a study that we did for the Goddard Space Flight Center we analyzed a bunch of $1/6$ octave data and we found that there were very few cases, other than one case in which the data were questionable, where this had a real effect. Of course you will miss the peak, and you will miss the peak by a certain error, but it appeared to us during that study that a $1/3$ octave analysis was sufficient to get close to the peaks and that you would not miss them.

Mr. Wada (Jet Propulsion Laboratory): At JPL we also fire various types of pyro charges to get measured data, and our structures might be quite different from yours. If we used the type of data that you have presented is there any word of caution as to how we might apply your data to structures that might be of different

character to those that you have used to analyze your shock spectrum data?

Mr. McGrath: As I tried to point out in the beginning these data were taken from a large truss and the locations varied from close to the source to far away. Lockheed's data was plotted from their barrel tester, which is a skin-ring-frame type of structure, and in this particular case, gave a reasonable agreement. You can not really extrapolate since you just do not know all the variables, I would have some confidence but I would not say you could go with 100 percent confidence. You would need more data. However, this is a start in the absence of any other method.

Mr. Wada: You have used truss type data and skin-stringer type data. Do you feel that these represent the extreme bounds to conditions that might exist in real structures? Our structure might be different because it contains many interfaces and I wonder if I can use the data with confidence or should I be very cautious?

Mr. McGrath: I would be a fool to say anything other than you would have to be cautious.

Mr. DeVost (Naval Ordnance Laboratory): This is not necessarily addressed to your paper. I would like to expand a little bit on what I said to Mr. Martin when he asked how much or what Q factor or how much damping we used in our analysis. In Mr. Culbertson's presentation he showed a slide in which we had analyzed the components of the projectile with which we were dealing, and we found that the higher frequency components of the projectile were somewhere near 1 to 1-1/2 percent damping, and the filler which is a soft material had around 3 percent damping. We selected 2 percent damping for all our analysis because we were comparing two bullets fired by different propellants.

Mr. Martin (Langley Research Center): This is what each manufacturer does. If he feels that the highest Q he has on board is 10, he will usually analyze for 10. With each one using different values of Q it makes it difficult when you have picked the value that you are going to use and it is different from what they have.

Voice: Based on your experience what sort of Q factor should one use to correlate some of your data compared with some of the experimental data reported in your analysis?

Mr. McGrath: There does not seem to be any reason that I know of to use one Q factor or the other in pyrotechnic data. I would suggest that perhaps one should develop more the concept of a Fourier transform since it has more information than shock spectrum and it does not depend on damping. There is damping in a structure but I do not know what it really means to use this, or to estimate it in a shock spectrum.

Voice: You have no guidelines as to what damping could be used, based upon your experience?

Mr. McGrath: No, we in our particular case we use a Q of 10 just from past experience. I think this is true across the industry and there is really no reason for it, which is unfortunate. This is a particular area where some more work should be done and I think some people are working on that.

RAPID FREQUENCY AND CORRELATION

ANALYSIS USING AN ANALOG COMPUTER

Jack G. Parks
Research, Development and Engineering Directorate
U. S. Army Tank-Automotive Command
Warren, Michigan

Analog computer circuits are described which provide a complete Fourier Analysis of repetitive data signals. The approach is a two step operation which begins with the computation of the Fourier Sine Integral of the signal to be analyzed. This integral serves as a low band pass filter for the frequency-difference component of the data signal and the test sine wave signal. The frequency of the test sine wave is increased until a threshold detector indicates that a frequency resonance is present. At this point, a computer subcircuit examines one cycle of the Fourier Sine Integral and provides outputs which establish the amplitude, phase angle, and frequency of the signal component under study. The main circuit is then allowed to continue until the next frequency component is encountered. Results are presented for special wave forms. Frequency resolution and operational limitations are discussed.

INTRODUCTION

Commercial instrumentation currently available for the frequency analysis of complex signal wave forms provide a wide variety of computation outputs. As a direct consequence of the associated sophistication this equipment is often expensive and frequently exceeds the budget limitations of small research groups. However, most laboratories have small analog computers or can justify their acquisition based on their utility as a general computation tool.

Simplified instrumentation is described in which analog computer techniques are used to permit rapid frequency and correlation analysis of repetitive signal wave forms. Signals may be obtained from multi-channel magnetic tape loops which contain a logic signal to synchronize the operation of the computer or from

excitation systems causing the signal generation. Output results provide frequency of the Fourier components, phase angles relative to the onset of computer logic, and absolute amplitude values through the use of counters and digital voltmeters.

The method is a two step operation which starts with the computation of the Fourier Sine Integral of the signal to be analyzed. The integral acts as a low band pass filter which transmits the frequency-difference component of the data/test signal combination only in the near-frequency region of the data signal frequency. The frequency of the test sine wave is increased until a threshold detector indicates that a frequency component is present.

At this juncture, a subcircuit examines one cycle of the Fourier Sine Integral computation considered as a function of integration time and

Preceding page blank

provides outputs which establish the amplitude, phase angle, and frequency of the signal frequency component under study. The main circuit is then allowed to continue, either manually or automatically by means of a logic clock, until the next frequency component is encountered.

THEORY

The Fourier Sine Integral of a function of time, $f(t)$, is given by

$$F = A \int_0^T f(t) \sin(\omega t + \phi) dt \quad (1)$$

where $f(t)$ according to the Fourier theorem is

$$f(t) = \sum_{n=0}^{\infty} A_n \sin(\omega_n t + \phi_n) \quad (2)$$

The evaluation of Eq. (1) for one value of n yields

$$F_n \approx A_n A [S_{\Delta\omega T + \Delta\phi} - S_{\Delta\phi}] / 2\Delta\omega \quad (3)$$

where $S_{\Delta\omega T + \Delta\phi} = \sin[(\omega_n - \omega)T + (\phi_n - \phi)]$

Terms in Eq. (3) involving $\omega_n - \omega$ are considered negligible. The form of Eq. (3) is useful in locating values of ω_n by varying ω and performing the integral on an analog computer. However, Eq. (3) does not lend itself to simple application in the determination of phase angle or amplitude. If Eq. (3) is considered, however, as a function of T only (all other variables being held constant) then phase angles and amplitudes are readily available parameters through an examination of the behavior of $F_n(T)$.

Parameter examination may be accomplished by using the following analytic factors: At time $T=0$, $F_n(T=0) = 0$. The period, T_b , required for $F_n(T)$ to repeat itself is directly related to f , the frequency of the test sine function, and f_n , the frequency component of the data signal.

$$f_n = f \pm T_b^{-1} \quad (4)$$

where the plus (minus) sign is used when f is less (greater) than f_n .

The phase angle, ϕ_n , may be obtained by examining the zero root of $F_n(T)$ between $T=0$ and $T=T_b$, defined here as T_a

$$\frac{\phi_n}{\pi} = b \frac{T_a}{T_b} + \frac{m}{2} + \frac{\phi}{\pi} \quad (5)$$

where $b = -1 (+1)$ for $\Delta f > 0 (< 0)$ (6)

Values of m for general values of $\phi_n - \phi$ as well as values of $\Delta\phi$ in specific cases are determined from the conditions listed in Table I.

The integral of $F_n(T)$ from $T=0$ to $T=T_b$ provides a method for determining the amplitude, A_n , of the n th frequency component.

$$A_n = - \frac{4\pi \int_0^{T_b} F_n(T) dT}{A T_b^2 S_{\Delta\phi}} \quad (7)$$

TABLE I
Values of m and $\Delta\phi$

$\int_0^{T_b} F_n(T) dT$	$\left. \frac{dF_n(T)}{dT} \right _{T_a}$	$\Delta f > 0$	$\Delta f < 0$
> 0	< 0	+5	-1
> 0	> 0	+3	+1
< 0	> 0	+3	+1
< 0	< 0	+1	+3
		$\Delta\phi$	
> 0	$= 0$	$3\pi/2$	$\pi/2$
< 0	$= 0$	$\pi/2$	$3\pi/2$
$= 0$	> 0	π	
$= 0$	< 0	0	

COMPUTATION CIRCUITS

The circuits to be described were tested on an Electronic Associates Inc. Model 380 Analog Computer and consequently display many characteristics particular to this machine. The control and operational characteristics of the analog and logic components will be explained during the discussion which follows.

A schematic drawing of the circuit used to locate frequency resonances is shown in Figure 1. The output of a signal oscillator, frequency controlled by the application of an external voltage from a ramp function generator, serves as one input to a four quadrant multiplier. The second multiplier input is the data signal to be analyzed, $f(t)$. The oscillator and the ramp function generator are controlled in a complementary fashion by the magnetic tape logic signal. When the magnetic tape logic is high ($L=1$) the oscillator is triggered to provide a sine wave signal whose frequency is determined by the output of the ramp function generator which is constant for $L=1$. With the onset of $L=0$ the oscillator stops and the ramp function generator increases its output voltage to provide a new value of ω for the next computation cycle.

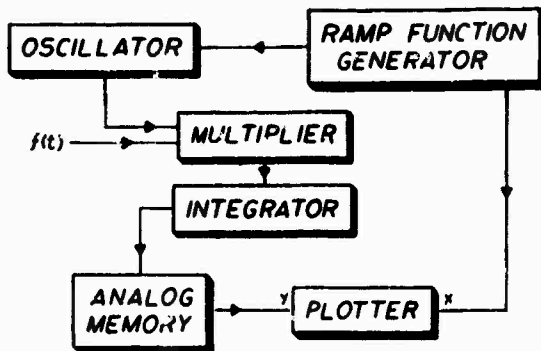


Figure 1
Frequency Spectrum Analysis Circuit

An analog memory circuit is included to provide a dc voltage equal to the successive outputs from the integrator at times $L=T$. The output of the integrator is reset to zero

when $L=0$. The output of the memory circuit serves as the y-axis input signal for a xy recorder while the x-axis input is the output of the ramp function generator. The resulting recording is a histogram representation of the continuous function $\bar{F}_N(\Delta\omega)$.

Each component in the spectrum analysis circuit is given in greater detail in Figure 2. The oscillator may be constructed as a simulation of the simple harmonic oscillator differential equation[1]. This arrangement is satisfactory for frequencies below 100 Hz. Above this limit, however, the output of the circuit either decays with time due to capacitor leakage or becomes unstable. As an alternative the oscillator may be of commercial origin which can be frequency controlled by means of a voltage input. A unit which was successfully employed was the Wavetek Model 114. The ramp function generator is an integrator with constant voltage input. The unit titled analog memory consists of two track and store units commonly found on analog computers. A track and store unit follows the analog input as long as its logic input is high. When the logic input is low, the unit holds its last analog input voltage prior to the onset of zero logic.

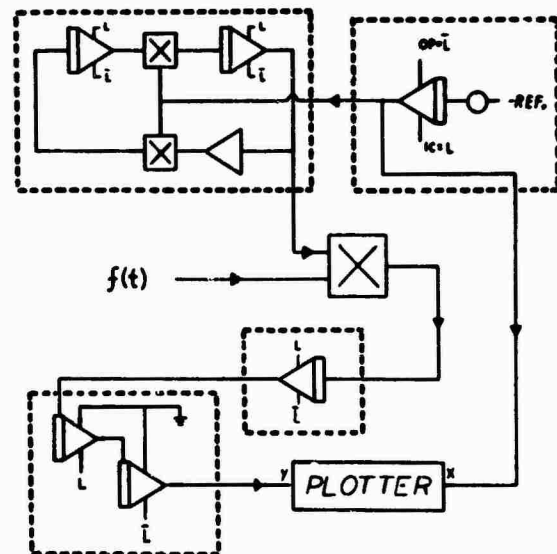


Figure 2
Details of Frequency
Spectrum Analysis Circuit

Once the frequency spectrum circuit has an output which exceeds a predetermined threshold (i.e., when a frequency resonance is reached), then a second circuit is introduced to examine $\mathcal{F}_n(T)$ parameters. Figure 3 depicts this subcircuit in block diagram form.

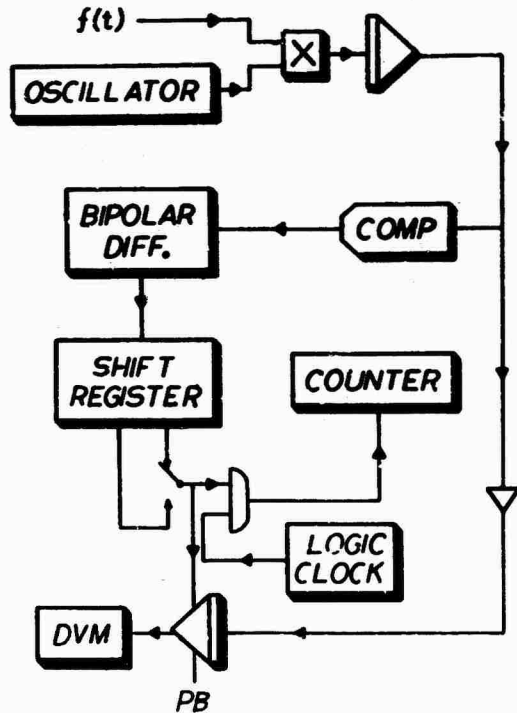


Figure 3
The $\mathcal{F}_n(T)$ Circuit

The data signal and a test signal from an oscillator gated by the logic signal, L , from the magnetic tape channel, are multiplied and integrated to form $\mathcal{F}_n(T)$. The integrator integrates when $L=1$ and returns to zero when $L=0$. $\mathcal{F}_n(T)$ is then used as the input to an electronic comparator. (COMP)

A comparator is a device with a logic one (zero) output when the algebraic sum of its analog inputs is greater (less) than zero. The comparator is frequently a package unit on most analog computers but may be constructed from accessory items by using the circuit [2] shown in Figure 4. The high-gain amplifier has no feedback except the diode limiting networks. Hence its output is always at one or the other of its two limiting states. When the sum of the analog inputs is

positive, the output becomes negative but the upper diode limits it to about -0.5 volts, which is close enough to 0 volts to count as a logic ZERO. When the net analog input is negative, the amplifier output becomes positive, and the diode-resistor network limits it to +5 volts (logic ONE on Model 380 computer).

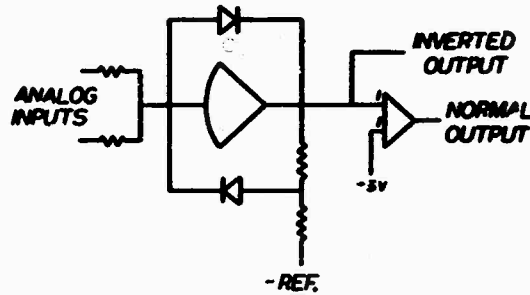


Figure 4
Circuit For an Electronic Comparator

The bipolar differentiator is a misnomer in the sense that it is not a rate of change indicator of an analog signal but rather a device which gives a logic pulse whenever its logic input signal has changed state. Figure 5 depicts a bipolar differentiator made from flip-flops and AND gates. The length of the output pulse is generally from one clock pulse to the next clock pulse.

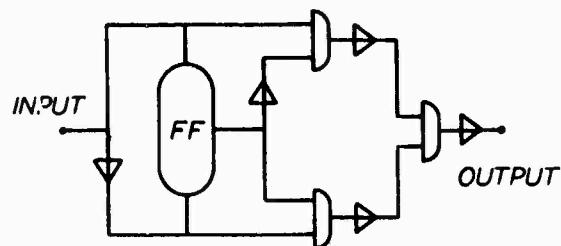


Figure 5
A Bipolar Differentiator

The output of the bipolar differentiator is then supplied to a shift register. As $\mathcal{F}_n(T)$ changes polarity, a logic bit is shifted through the

register. Selected states of the shift register provide a logic signal to gate the counting of logic clock pulses. This same logic signal controls the integration of $\mathcal{F}_n(T)$ during shift register states. Final values of $\mathcal{F}_n(T)$ are displayed on a digital voltmeter (DVM). A push-button gate (PB) initializes the integrator.

The implementation of the $\mathcal{F}_n(T)$ circuit involved some unique precautions. Primary among these was the realization that $\mathcal{F}_n(T)$ actually contains two parts, one oscillatory term with frequency $(\omega_n - \omega)/2\pi$ and a second term where $(\omega_n + \omega)/2\pi$ is the frequency. For low values of f_n , $\mathcal{F}_n(T)$ shows considerable evidence of $\omega_n + \omega$ which appears as a high frequency oscillation superimposed on a low frequency variation. When the $\omega_n + \omega$ term is sufficiently large, the comparator tends to change state several times for one polarity change of the $\omega_n - \omega$ part of $\mathcal{F}_n(T)$. This condition can be avoided by using the circuit shown in Figure 6. The series feedback circuit of R_1 and C_1 serve to differentiate the output of the comparator and cause the response shown in Figure 6 for the sum of the comparator inputs. [3]

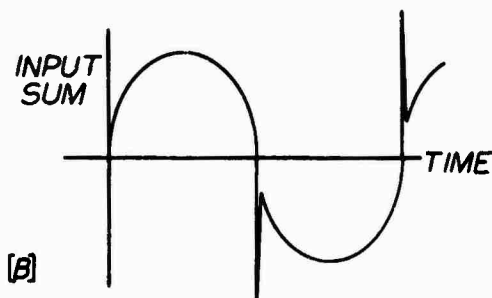
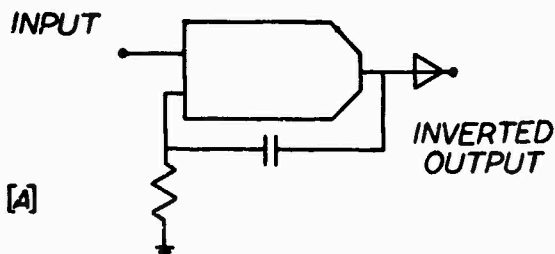


Figure 6
A Low Band-Pass Comparator [A]
Circuit [B] Input Characteristics

Another problem is the choice of a clock rate selected for the program. Shift register and gate actions are

synchronous with the computer clock rate. That is to say a bit is not shifted nor a gate opened or closed at the instant of command but such actions are accomplished at the next clock pulse. If the clock rate is 10 pulses per second and T_b is 1 second, the error in measuring T_b due to synchronization could be as high as 20%. However, with 10^5 clock pulses per second, the error limit is 0.002%.

TEST RESULTS

Figure 7 shows the results of using the $\mathcal{F}_n(\Delta\omega)$ approach on a square wave with frequency of 2 Hertz and a computation time of 2 seconds. The ripples observed in the recording are a natural consequence of the mathematical form of $\mathcal{F}_n(\Delta\omega)$ and in this case have a "period" (in the frequency domain) of 0.05 Hertz (i.e., T^{-1}).

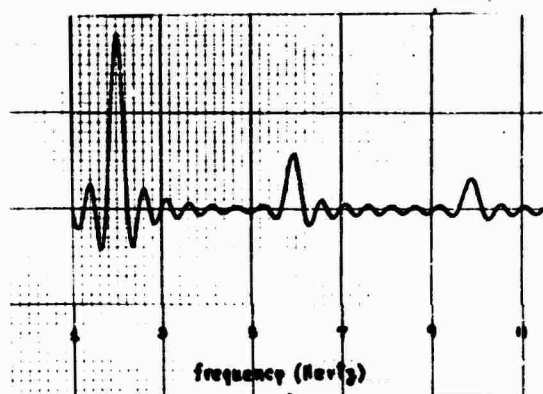


Figure 7
Square Wave Analysis

It is possible to determine the Fourier analysis parameters from the $\mathcal{F}_n(\Delta\omega)$ method but the total computation time is exorbitant. In the case of Figure 7, the time required to traverse from 1 Hertz to 11 Hertz is 22 minutes. By interchanging the logic controls of the integrator used as a ramp function generator in Figure 2, a knowledge of Fourier analysis parameters is sacrificed in order to gain analysis speed and to obtain a result usable for $\mathcal{F}_n(T)$ application. Under these conditions generation of Figure 7 would require less than 2 minutes.

Extensive measurements of the three parameters of interest (i.e., ω_n , ϕ_n , and A_n) over a frequency range from 10 to 500 Hertz indicated that the ratios of the standard deviation of the measurements to the mean value of the measurement were as follows:

Parameter, X	$\sigma_x/\langle x \rangle$	Range of X
Δf	2.4×10^{-3}	0.5 to 2.0 Hz
$\Delta \phi$	2.5×10^{-3}	0° to 360°
A_n	2.8×10^{-2}	0.1 to 10 volts

Therefore, a measurement involving $\Delta f = 1 \text{ Hz}$, $\Delta \phi = 200^\circ$, and $A_n = 10$ volts has expected errors of the order of 2.5 millihertz (Δf) 0.5° ($\Delta \phi$) and 0.28 volts (A_n).

Systematic variations of T_b and A_n considered as functions of $\Delta \phi$ were observed. This phenomenon is attributed to the constant small bias voltage to be found on oscillators built from analog computer components. The output of the integrator is in reality $\tilde{F}_n(T) + \epsilon T$. Fortunately, ϵ is a small voltage and produces no substantial consistent errors.

An analysis of a 30 Hertz square wave was performed using the $\tilde{F}_n(T)$ method. The results are shown in Table II. The square wave amplitude was 3.00 volts (peak value). The various order frequency components all have 0° phase angles and amplitudes given by the expression

$$A_n = \frac{2h}{n\pi} [1 - \cos(n\pi)] \quad (8)$$

where h is the amplitude.

The theoretical values of $\Delta \omega$ in Table II were determined by measuring the frequency difference between the test oscillator and the data oscillator. The phase angle of the test oscillator was purposely retarded by 40° to allow accurate measurement of A_n since small values of $\sin(\Delta \phi)$ contribute large errors in the use of Equation 7.

TABLE II
Square Wave Analysis

$n = 1 \quad f = 29.043 \text{ Hz}$		
	THEORETICAL	EXPERIMENTAL
$\Delta \omega$	0.9571 Hz	0.9584 Hz
$\Delta \phi$	$+ 40.0^\circ$	$+ 40.7^\circ$
A_n	3.82 volts	3.86 volts
$n = 3 \quad f = 89.229 \text{ Hz}$		
$\Delta \omega$	0.7709 Hz	.7720 Hz
$\Delta \phi$	$+ 40.0^\circ$	$+ 41.3^\circ$
A_n	1.27 volts	1.28 volts
$n = 5 \quad f = 148.97 \text{ Hz}$		
$\Delta \omega$	1.0284 Hz	1.0335 Hz
$\Delta \phi$	$+ 40.0^\circ$	$+ 40.9^\circ$
A_n	0.764 volts	0.758 volts

The use of the analog computer program discussed here is frequency limited. Oscillators built from computer operational amplifiers show considerable decay with time at frequencies in excess of 500 Hertz. This phenomenon is due primarily to the leakage of capacitors used in the feedback loops of the oscillator. This limitation can be avoided by using a commercial oscillator which can be gated by the computer. The upper limit in this case is approximately 900 Hertz.

Not all values of phase angle permit satisfactory operation of the $\tilde{F}_n(T)$ method. Noise problems coupled with comparator dead zone reaction (i.e., voltage range near zero where the comparator action is uncertain) prohibit measurements at $90^\circ \pm 15^\circ$ and $270^\circ \pm 15^\circ$. This situation is readily apparent to the computer operator and may be solved by either advancing or retarding the phase angle of the test oscillator by 45° and considering this change in subsequent calculations.

CONCLUSIONS

The frequency resolution obtainable from the $\tilde{F}_n(T)$ method can be estimated

by first examining $F_n(\Delta\omega)$. The distance between minor peaks in a recording such as exemplified in Figure 7, is a frequency, f_r , which is equal to the reciprocal of T , the computation time. Two frequency components separated by a frequency δf show some interference through the distortion of the envelope of the minor peaks. This envelope is essential to the determination of Fourier parameters for each frequency component. If each component is of equal magnitude and P is the percentage of interference, then frequency resolution for $F_n(\Delta\omega)$ is given by the relation

$$P = f_r / 2\pi \delta f \quad (9)$$

A permissible value of P of 0.01 for two frequency components separated by 1 Hertz therefore requires that $T=16$ seconds. For the $F_n(T)$ method the equivalent expression for equation (9) is

$$P = \Delta f / (\delta f \pm \Delta f) \quad (10)$$

where Δf is T_b^{-1} , δf is the frequency difference between the two components, and the minus (plus) sign is used when the test signal frequency is (is not) between the frequency components. Therefore, if δf is 5 Hz and $P = 0.05$, then $\Delta f = 0.25$ Hertz (or $T_b = 4$ seconds) under both frequency conditions.

Several circuit improvements were conceived during the latter stages of this program but were not implemented due to a lack of time and/or equipment. One modification is to obtain the logarithm of $F_n(T)$ in analog form and change its polarity when the polarity of $F_n(T)$ changes. This would have the effect of making the zero crossing times more exact and should reduce the phase angle dead zone. A second circuit variation is to replace the bipolar differentiator with a leading edge differentiator and a circuit to provide the absolute value of $F_n(T)$ rather than $F_n(T)$. This change should theoretically increase the reliability of the counting periods.

There exists another alternative to the method of measuring zero crossing times in order to establish $F_n(T)$

parameters. This alternate method centers around the generation of two functions:

$$F_s(T) \equiv A_n A \int_0^T S_{\omega_n t + \phi_n} S_{\omega t + \phi} dt$$

$$= F_n(T)$$

$$F_c(T) = A_n A \int_0^T S_{\omega_n t + \phi_n} C_{\omega t + \phi} dt$$

$$= -A_n A (C_{\Delta\omega T + \Delta\phi} - C_{\Delta\phi}) / 2\Delta\omega$$

$$\text{Now } F_s(T) = 0 \text{ when } T = T_b$$

$$\text{and } T = (\pi - 2\Delta\phi) / \Delta\omega \equiv T_a^s$$

$$F_c(T) = 0 \text{ when } T = T_b$$

$$\text{and } T = (2\pi - 2\Delta\phi) / \Delta\omega \equiv T_a^c$$

when F_s or F_c is evaluated at its complementary value of T_a we find

$$F_s(T_a^c) = -\frac{A_n A}{\Delta\omega} S_{\Delta\phi} \quad F_c(T_a^s) = \frac{A_n A}{\Delta\omega} C_{\Delta\phi}$$

Therefore, measurements of T_b , $F_s(T_a^c)$ and $F_c(T_a^s)$ provide measure of $\Delta\omega$, $\Delta\phi$, and A_n . Circuits required to implement this method were more numerous because F_s and F_c must be generated simultaneously and two shift registers are now required. One counting measurement and an integration have, however, been eliminated. The added complexity of this approach is not compensated by any appreciable increase in accuracy.

REFERENCES

1. C. L. Johnson, Analog Computer Techniques, pg. 114, McGraw-Hill Book Company, New York 1963.
2. C. L. Johnson, Analog Computer Techniques, pg. 184, McGraw-Hill Book Company, New York 1963.
3. L. Cartwright, Private Communication, July 1971.

DISCUSSION

Mr. Rymer (Naval Air Test Center): You mentioned that you had about 2 millihertz frequency accuracy. At what frequency was that and at what sweep rate? That varies depending on these two factors.

Mr. Parks: The range of frequencies that I examined went up to a maximum of about 450 Hz, and I had to make some modifications on the integrators that went to make up the oscillator in order to obtain this kind of frequency and have them hold their values. They tended to drift and there were some leakages on the capacitor, so there had to be some modifications to get to that frequency. Actually, you do not have to use an oscillator built into the analog computer, very inexpensive oscillators are commercially available that can be controlled, they can be gated, they can be increased in frequency by putting the voltage into them, and they are very stable. One does not have to be tied to a limit of, say, 400 Hz such as on an analog computer oscillator. The sweep rate does not come into this picture because these values which you saw and the ones I quoted were dependent on the fact that you get up to the resonance, stop, and then you take measurements. You are measuring the difference between a signal, or an oscillator frequency which is fixed, and the term you are trying to measure; all you have to do is to measure the frequency of the analog oscillator and the parameters that evolve from the computer program tell you how far you are away from that other resonance, and it turns out to be quite accurate.

**INVESTIGATION OF LAUNCH TOWER MOTION
DURING AEROBEE 350 LAUNCH**

Ron L. Kinsley and William R. Case
NASA, Goddard Space Flight Center
Greenbelt, Maryland

One of the initial launches of an Aerobee 350, a NASA Sounding Rocket, experienced a significant dispersion from its predicted impact point. Rate gyro data provided evidence that the vehicle's attitude was disturbed as it exited from the launch tower. A task team was formed to investigate the possibility that launch tower motion was the source of this anomaly.

Efforts of the task team consisted of an extensive field measurements program and a rigid body dynamic analysis of the vehicle/tower combination. Aerobee launch towers at both Wallops Island, Virginia, and White Sands, New Mexico, were instrumented with accelerometers for several launches.

It was discovered that the tower's second mode was consistently excited at launch. The potential for tip-off as a result of the measured tower motion was determined analytically.

The excitation mechanism was isolated and found to be a low frequency pressure oscillation in the building hut created by the rocket blast. The recommended solution of the problem was to remove hut panels to prevent the initial pressure buildup.

INTRODUCTION

(a) Launch Vehicle

The Aerobee 350 is a four-finned, two-stage Sounding Rocket employed by NASA for a wide range of scientific investigations. Its first stage uses a NIKE M5E1 solid propellant motor that is ignited at launch and burns for approximately 3.5 seconds. The second stage is propelled by a cluster of four Aerobee thrust chambers that use inhibited red fuming nitric acid and a mixture of aniline and furfuryl alcohol as liquid propellants. After about 52 seconds of burning, the rocket follows a ballistic trajectory until impact. Basic physical dimensions of the Aerobee 350 are presented in Figure 1.

(b) Launch Tower

The rocket is designed for firing from the four-rail launch towers at NASA Wallops Station, Wallops Island, Virginia, and at White Sands Missile Range (WSMR), White Sands, New Mexico. The launch tower is 160 feet in height and consists of 21 levels at 8-foot spans which provide access to the launch rails. The levels are designated L1 through L21 as shown in Figure 2. The four launch rails run the entire length of the tower. There are three sets of riding shoes (each set consisting of four shoes) on the Aerobee 350. Their locations, as shown in Figure 1, are at the base of the NIKE, at the base of the second stage and at the top of the second stage. One of the shoes at the

base of the NIKE has a key arrangement and remains in contact with the launch rail until the vehicle exits from the tower. The remaining shoes merely butt against the rails and maintain proper alignment of the vehicle in the tower.

The lower half of the tower is enclosed in a building structure which maintains necessary environmental conditions for the scientific payloads. The entire weight of the tower is supported completely by the building. The only structural connection between the building and the tower is at L11. This structural connection takes the form of a gimbal system whereby the tower is gimballed relative to the building in two axes at L11. This gimbal arrangement is the mechanism by which the proper tower elevation and azimuth angles are obtained. Exact tower settings for a given launch are dictated by existing wind conditions. The base of the tower is positioned by means of a pin which is attached to a movable turntable located in the floor of the building. This pinning arrangement serves only as a positioning mechanism (for different tower settings) and does not carry any load. All of the loads are carried through the gimbals at L11.

(c) Background

One of the initial launches in the Aerobee 350 program, NASA 17.05, experienced an excessive dispersion from the predicted impact point. Rate gyro data from the flight indicated that as the vehicle exited from the launch tower it experienced a pitching motion, about its center of gravity, of approximately $3.5^{\circ}/\text{sec}$. Subsequent analysis showed that such a "tip-off rate" could generate substantial dispersions. Any exact number is dependent on several parameters such as payload weight and tower settings, but a typical value for an Aerobee 350 was shown to be 5 miles of impact dispersion for every $1.0^{\circ}/\text{sec}$. of tip-off. As a result of the NASA 17.05 impact dispersion, future launches from WSMR were placed in jeopardy due to stringent range limitations.

The mechanics of how the tip-off was produced were unknown, but it was felt that the problem was related to motion of the launch tower. A task team made up of members of the Structural Dynamics Branch of the Test and Evaluation Division at the Goddard Space Flight Center was formed. The assignments of the task team were as follows: (1) Completely define launch tower motion; (2) Determine the vehicle tip-off potential as a result of such tower motion; (3) Isolate the excitation

forces which produce tower motion; and (4) Recommend methods for reducing tower motion.

FIELD MEASUREMENT PROGRAM

The initial efforts of the task team consisted of an extensive field measurements program. The following is a general description of the instrumentation setup used in this measurements program.

(a) Instrumentation Setup

The basic purpose of instrumenting the tower was to determine if there existed tower vibratory motion capable of imparting a significant perturbation to flight dynamics. Any such motion would have to consist of substantial velocity and displacement and consequently be of low frequency content. For this reason, lister 303-B servo-accelerometers were employed for tower instrumentation. The characteristics of this accelerometer are such that its response is linear in the frequency range from 0-150 Hz.

Since the accelerometers had to function in the extremely severe acoustical and thermal environment created by the rocket blast, a method of shielding the accelerometers had to be used. The accelerometers were enclosed in an aluminum box which was in turn covered with lead sheeting. The entire assembly was then wrapped with asbestos tape. Another problem inherent in this particular measurement program was to decipher low frequency (low acceleration) data from a dynamic environment in which there was an abundance of high frequency (high acceleration) data. It was discovered that without some sort of isolation system the accelerometer output was saturated by extremely high acceleration, high frequency inputs. This problem was eliminated by mounting the accelerometers on rubber pads whose frequency response was such that they rolled off sharply above 50 Hz.

Slight variations in the exact instrumentation were employed for the different launches but in general accelerometers were mounted on about 6 of the 21 levels. At each level instrumented there were two accelerometers mounted in perpendicular axes, one in Building axis A and the other in Building axis B (see Figure 2). Levels 1, 11 and 21 were always instrumented.

In addition to the accelerometers a trip wire system was also used in the

instrumentation program. Thin wires were positioned across the fin wells at various tower levels. As each wire was severed by the sustainer fin a voltage step was generated. This provided a means of correlating vehicle position in the tower with the acceleration time histories of various points on the 160-foot tower.

All data obtained were recorded on magnetic tape for analysis purposes.

(b) Launches Instrumented

Due to the relatively low frequency of Aerobee 350 launches it was concluded that the launch tower should be instrumented for launches of Aerobee 170's to supplement the data from launches of Aerobee 350's. The justification for this approach is that both vehicles are launched from the same tower and that the vehicles are similar in that they both employ the NIKE M5E1 first-stage. The basic difference between the two is that the Aerobee 350 uses a cluster of four Aerobee thrust chambers in its second-stage whereas the Aerobee 170 uses only one. Also, Aerobee 350 payloads are generally larger and heavier than Aerobee 170 payloads.

The two towers were instrumented for a total of seven launches. Two of the launches were Aerobee 170's, four were Aerobee 350's and the seventh was a Black Brant VC. The results obtained from instrumenting the Black Brant VC launch will be discussed in a later section.

(c) Results

In addition to the launch data obtained considerable data from a series of manual excitations were obtained. This manual excitation was accomplished by two men pushing back and forth against the launch rails at L21. Obviously the acceleration levels generated by this action were very small but were sufficient to provide a clear definition of the tower's first two normal mode shapes and frequencies. Normalizing the filtered acceleration time histories at various points on the tower for a given instant of time provided the mode shapes. The first two mode shapes whose frequencies are approximately 1.2 Hz and 4.5 Hz respectively, are presented in Figure 3. The mode shapes and frequencies were essentially the same in Building axes A and B.

As will become evident shortly the second mode is of primary concern in the tip-off problem. This mode shape

reveals some important qualities about the dynamic response of the tower, namely, that there is motion present at the global point and at the base of the tower. The tower behaves very much like a free-free beam with a flexible restraint at the gimbal. This is consistent with the actual physical structure of the tower. Due to the small displacements ($\leq 0.5"$) in question the base of the tower is essentially free due to the slop in the pinning mechanism; for very large displacements the pin would provide lateral restraint. At L11 the building provides a certain degree of lateral restraint. The building does indeed move but tends to suppress motion of the tower as evidenced by the tower's second mode shape.

Tower data from all the launches exhibited several basic common characteristics. The predominate low frequency oscillation of the tower was always the second vibratory mode of the tower. This second mode oscillation was always substantially greater in Building axis A than in Building axis B. Table 1 presents a tabulation of the peak second mode accelerations measured at L21 in axes A and B for each of the seven instrumented launches. With the exception of the Black Brant VC launch the peak levels are of comparable value. Peak levels for the Aerobee 350 launches range from 0.34g's to 0.50g's while the Aerobee 170 launches produced peak tower accelerations of 0.34g's and 0.38g's. An example of the displacements associated with these motions is as follows: an acceleration of 0.40g's at 4.5 Hz corresponds to a double amplitude displacement of 0.40 inch.

Presented in Figure 4 are the filtered second mode acceleration time histories at L21 from the launch of NASA 17.08. This is very typical of the time histories obtained from each of the launches. As can be seen the acceleration in axis A builds up to its maximum value very quickly after ignition, the level then decreases only slightly over the next several cycles but then damps out rapidly after the vehicle has exited from the tower.

Extensive comparisons of the narrow band filtered acceleration time histories from the different launches were made. A close scrutinization revealed that the filtered acceleration time histories at L21 from the two Aerobee 170 launches were remarkably similar. The magnitudes and phasing as functions of time were almost identical for the two launches. Similarly after comparing the second mode acceleration time histories from the four

Aerobee 350 launches it was determined that the initial portion of the time histories were amazingly similar. However, once the vehicle was in the upper portion of the tower the similarities ended. The phasing and magnitudes of the traces were no longer consistent from one launch to another.

The tower's first mode was never excited to a measurable level during any of the instrumented launches. Since the first mode was easily excited during the manual shakes the fact that the first mode was not excited during launch provided a key to the nature of the excitation force. The theory that the excitation force was in some way related to pressure buildup in the tower hut evolved. To investigate this, pressure transducers were mounted at various locations in the tower hut for several launches. The data revealed that there was a 6 Hz pressure oscillation, with a peak magnitude of 0.6 PSIG, generated in the building at ignition.

ANALYSIS

In conjunction with the field measurements program, analyses were performed to estimate the magnitude and possible causes of the tip-off phenomena. Since the Aerobee vehicles have no attitude rate control, large dispersions in the final range of the vehicle can result from tower induced motions at the time the vehicle exits the tower. Based on trajectory analyses performed by the Goddard Sounding Rocket Division, it was determined that the Aerobee 350, for example, could experience range dispersions of 20nm if the vehicle attitude rate at tower exit were as much as 4 degrees per second. During the time between second and third riding shoe exit from the tower, the vehicle is free to pitch relative to the tower and if the tower is vibrating during this time it imparts a rigid body pitching motion to the vehicle. For the Aerobee 350 the time between second and third shoe exit is approximately 0.05 second. Since this corresponds to approximately one-quarter of a cycle of the observed tower motion in its 4.5 Hz mode, it was felt that tower motion could have an appreciable effect on the vehicle attitude rate at third shoe exit and an analysis was made to determine this effect.

Figure 5 shows, schematically, the tower and vehicle during the period between second and third shoe exit. From measured tower mode shapes the 4.5 Hz mode is very nearly straight over the portion of the tower from the tip inboard to the third shoe location

(distance "b" on Figure 5) when the second shoe is exiting. Also over the 0.05 second time between second and third shoe exit, the vehicle forward velocity is nearly constant and the tower motion sinusoidal. Utilizing these facts and assuming the third shoe to remain in contact with the tower rails, the vehicle rigid body equation of motion in one plane is

$$\ddot{\theta}_v - \omega_v^2 \theta_v = \omega_v^2 \left[\theta_{to} \left(1 - \frac{X_2 - V_0 t}{b} \right) \sin(\omega t + \alpha) \right] \quad (1)$$

where ω_{to} and α are the tower acceleration magnitude (g's) and phase (relative to its undisturbed position) at second shoe exit, X_2 is the distance between second and third shoes on the vehicle, V_0 is the vehicle forward velocity, t is the time from second shoe exit, ω is the tower vibration frequency and

(2)

$$\omega_v^2 = \frac{g X_0}{\zeta_o^2 + X_0^2}$$

where ζ_o is the radius of gyration of the vehicle about its center of gravity (c.g.), X_0 is the distance from the c.g. to the third shoe and g is the acceleration due to gravity.

All of the coefficients in equation (1) are functions of the particular vehicle (Aerobee 350 or 170) with the exception of the tower acceleration magnitude and phase at second shoe exit. Thus we can solve (1) as a function of these two parameters, which may vary from one launch to another, for a particular vehicle. Of particular importance are the vehicle pitch rate ($\dot{\theta}_v$) and attitude (θ_v) at the time of third shoe exit. These are the so called tip-off conditions which, for the Aerobee 350, can have a large effect on the resulting range of the vehicle.

Figure 6 shows the pitch rate and attitude at time of third shoe exit as a function of the tower phase (α) at second shoe exit for the Aerobee 350 using measured acceleration magnitudes. The convention on tower phase at second shoe exit is that $\alpha=0$ corresponds to the tower passing through its undisturbed position pitching down range. As indicated, the highest pitch rates occur in the vicinity of $\alpha=15$ deg. and the pitch rates can be either positive (pitching vehicle nose down) or negative (pitching vehicle nose up). Thus, one would expect that if the vehicle is riding the rails quietly (that is, no hanging of the vehicle on the rails)

that range dispersions would be only as predictable as the tower motion. If the tower motion at second shoe exit were one-half cycle different in phase between two flights the resulting range dispersions would in one case cause the vehicle to go long and in the other case cause it to go short. However, the maximum pitch rates that can be attained are large enough to cause appreciable range dispersions for the Aerobee 350. A similar analysis on the Aerobee 170 resulted in tip-off pitch rates on the order of 1.5 to 2.0 degrees per second.

Having established the fact that, for the Aerobee 350 at least, the tip-off rates could be a serious problem, several analyses were performed to determine the probable source or sources of the tower motion so that recommendations could be made to reduce the acceleration levels. In these analyses, the tower was idealized as a uniform beam whose properties were obtained by matching the measured 4.5 Hz bending mode. In order to include the effect of building stiffness, the beam was connected to ground through a spring at the 80-foot level and this spring rate was obtained empirically from the measured mode shape in the 4.5 Hz mode. Using this empirically obtained mathematical model of the tower, the first two modes agreed excellently with the measured 1.2 and 4.5 Hz modes as shown on Figure 7. Note that good mode shape agreement occurs for the 4.5 Hz mode assuming the bottom of the tower is unrestrained while for the 1.18 Hz mode it is best if the bottom is assumed pinned. This is very likely due to the fact that the connection at the bottom slips at the higher frequencies where the inertia loads are higher but is more effective at the lower frequencies.

Using this mathematical model of the tower, several possible sources of excitation were investigated for their influence on tower motion. The most promising candidates were an assumed low-frequency oscillating pressure loading in the building being transmitted through the tower gimbal into the tower, and a possible impacting of the vehicle on the tower rails near the time of vehicle exit from the tower. Although no quantitative estimate of the effect of a low-frequency pressure oscillation could be obtained without a mathematical model of the building, it was demonstrated that the theoretical buildup of tower tip acceleration from the time of liftoff was quite similar to the measured accelerations.

Using measured tower accelerations and measured pitch and yaw attitudes

from an Aerobee 170 launch, an analysis was made to determine the effect of an impact of the vehicle and tower near tower exit. The measured data seemed to point strongly to this possibility evidenced by the sudden change in tower acceleration levels when the vehicle was exiting the tower and also on a sudden change in slope of the yaw attitude gyro. Assuming an impact between the front riding shoes and the top of the tower occurred, it was demonstrated that the resulting change in acceleration amplitude indicated an impulsive loading on the vehicle which would theoretically give a 4.2 degree per second change in yaw attitude rate. The yaw attitude gyro indicated a sudden change in slope of 4.7 degrees per second. Since the measured tower accelerations on several Aerobee flights have the characteristic of changing amplitude as the vehicle exits, it was thus concluded that an impact of this type was a strong possibility.

Based on the analyses it was concluded that building pressure and vehicle-tower impact were causing the high tower accelerations. Venting of the building roof was recommended to reduce the pressure loading and a better restraint system for the tower bottom was recommended since the analyses indicated that for all of the possible excitation sources, the tower tip acceleration would be reduced if the bottom were pinned more securely.

FINAL STATUS

After evaluating the results from both the measurements program and the analytic effort the following conclusion has been drawn. The excitation force generating tower motion is a low-frequency (≈ 6 Hz) pressure oscillation in the tower hut created by the exhaust blast of the NIKE M5E1 second-stage. The supporting evidence for this conclusion is as follows.

- (1) The second mode (4.5 Hz) of the tower is excited instead of the first mode (1.2 Hz). A 6 Hz pressure oscillation would indeed excite the second mode more than the first.

- (2) Tower motion is substantially greater in Building axis A than in Building axis B. Looking at the symmetry of the building indicates that a pressure buildup would result in a non-zero resultant lateral force on the tower in axis A. In axis B the resultant force on the tower would ideally be zero. An oscillating pressure wave in the building would result in an oscillating force applied to the tower in

axis A. Analyses showed that such an excitation could produce the tower motions which have been measured.

(3) Tower motion measured during the launch of the Black Brant VC was less by an order of magnitude than that from Aerobee launches. A conservative comparison indicates that the NIKE MSE1 mass flow rate is greater by a factor of three than that of the Black Brant VC. In other words the launch of a Black Brant VC did not generate hut pressures severe enough to result in significant tower motion.

It can be expected that cross range dispersions due to tip-off will be minimal since tower motion in Building axis B is of an acceptable level. This is an important consideration since at WSMR the range is quite long but is very narrow. Therefore significant down range or up range dispersions can be tolerated but cross range dispersions cannot.

As was stated previously, comparisons of the second mode acceleration time histories from the Aerobee 350 launches revealed the initial portion of the time histories to be similar. However, once the vehicle gets in the upper half of the tower the similarities end. It is felt that the reason for this is as follows. The pressure blast generated at liftoff is of a repeatable

nature. This pressure blast which is the initial excitation force then results in a repeatable tower response. Once the vehicle starts moving and reaches the upper half of the tower, vehicle impacts against the rails affect the response of the tower. These vehicle-to-rail impacts are obviously random in nature and therefore have a random effect on tower motion. Therefore, the final result is an initial tower response which is repeatable until the time at which vehicle impacts alter the tower motion.

Reduction of dispersion due to tower motion can be accomplished by increased ventilation of the tower hut to prevent pressure buildup. Removal of all hut panels prior to launch would reduce dispersion due to tower motion to essentially zero.

Concluding, it can be said that all objectives of the task team have been accomplished. A clear definition of the entire tip-off problem has been provided. Tower motion at launch has been defined; the potential for tip-off as a result of the measured tower motions has been established; the excitation force has been identified; and, a method for eliminating tip-off has been recommended. The decision to remove hut panels for a given launch or to install a permanent system which can provide increased ventilation area is up to Sounding Rocket personnel.

TABLE 1
MAXIMUM ACCELERATIONS MEASURED AT TOWER LEVEL 21
DURING LAUNCH

Launch Date	Launch Site	Payload	Max. Levels	
			Building Axis A	Building Axis B
8/13/70	Wallops Is.	NASA 17.06 (Aerobee 350)	0.5g's	0.12g's
10/31/70	White Sands	NASA 13.41 (Aerobee 170)	0.38g's	0.20g's
12/19/70	White Sands	NASA 13.11 (Aerobee 170)	0.34g's	0.22g's
2/21/71	Wallops Is.	NASA 17.09 (Aerobee 350)	0.34g's	0.17g's
6/23/71	White Sands	NASA 17.08 (Aerobee 350)	0.42g's	0.22g's
6/10/71	Wallops Is.	NASA 17.11 (Aerobee 350)	0.40g's	0.28g's
7/21/71	Wallops Is.	NASA 21.04 (Black Brant VC)	0.06g's	≈ 0.00g's

OVERALL VEHICLE DATA		
Booster Thrust.....	kg	22,000
	lb	48,700
Maximum Diameter.....	cm	56
	in	22
Weight Less Payload..	kg	3,000
	lb	6,600
Number of Stages.....	2	
Prime Contractor.....	Aerojet General	

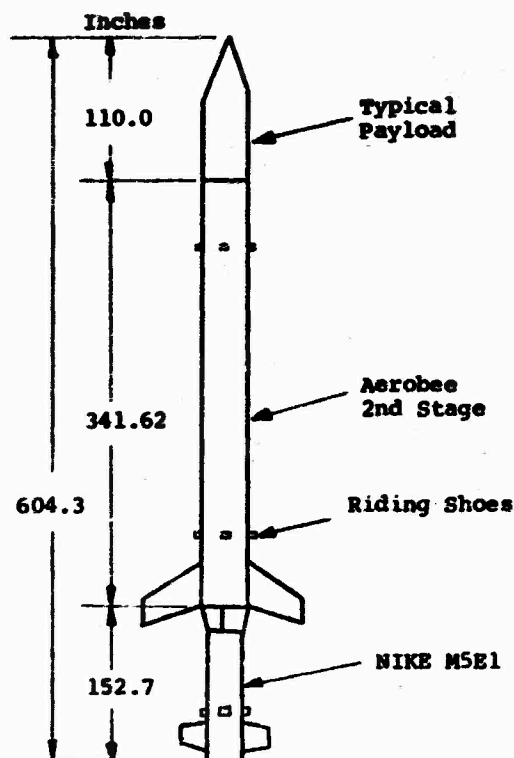


FIGURE 1
AEROBEE 350 SOUNDING ROCKET

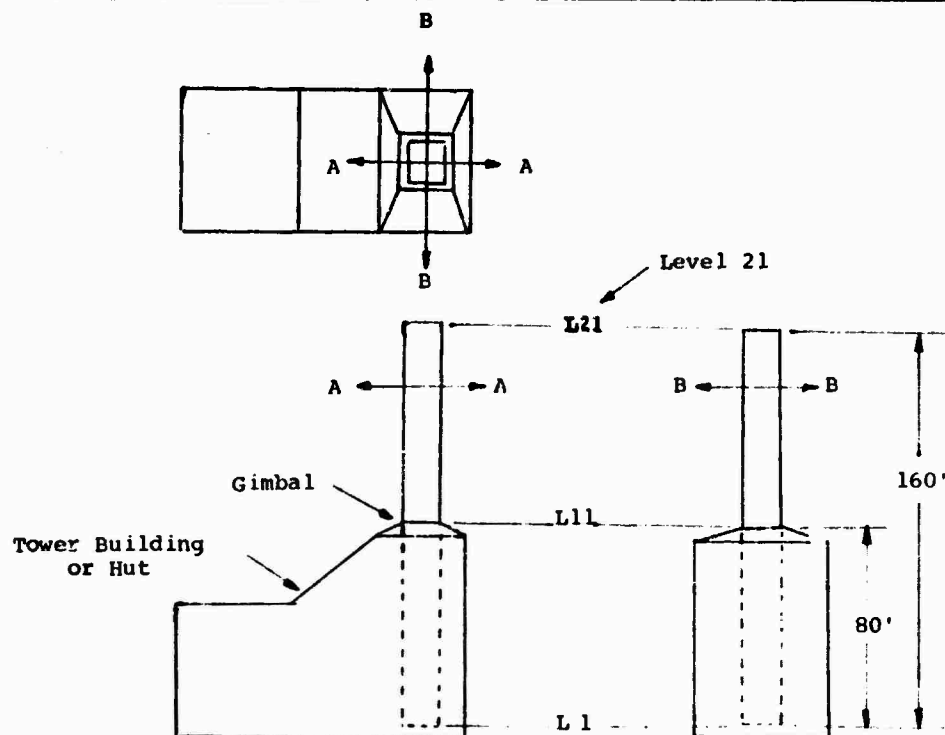


FIGURE 2
AEROBEE LAUNCH TOWER AND BUILDING STRUCTURE
(BUILDING AXES A AND B ARE AS DESIGNATED ABOVE)

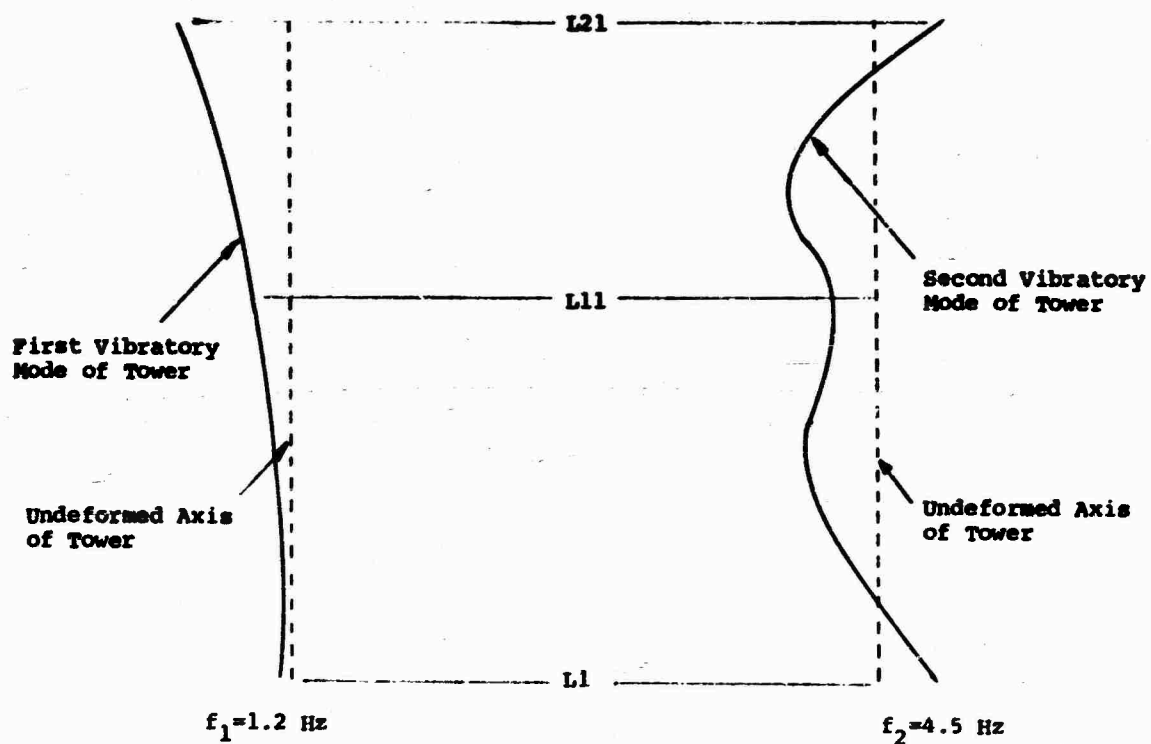


FIGURE 3
FIRST AND SECOND TOWER MODE SHAPES

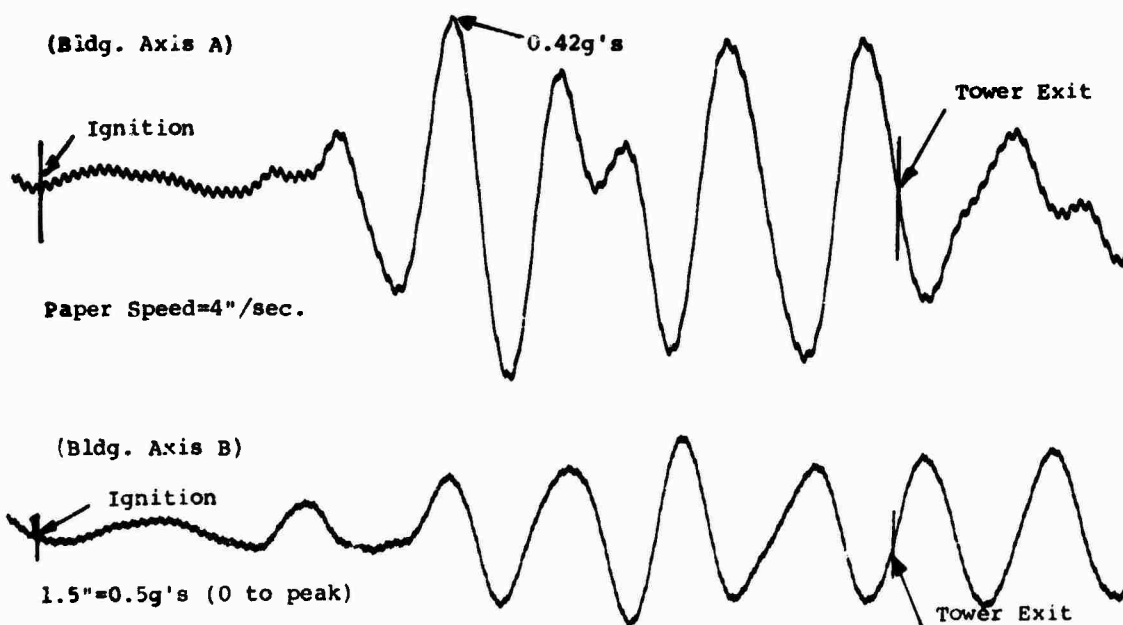


FIGURE 4
FILTERED SECOND MODE ACCELERATION TIME HISTORIES
MEASURED AT L21 DURING THE LAUNCH OF NASA 17.08

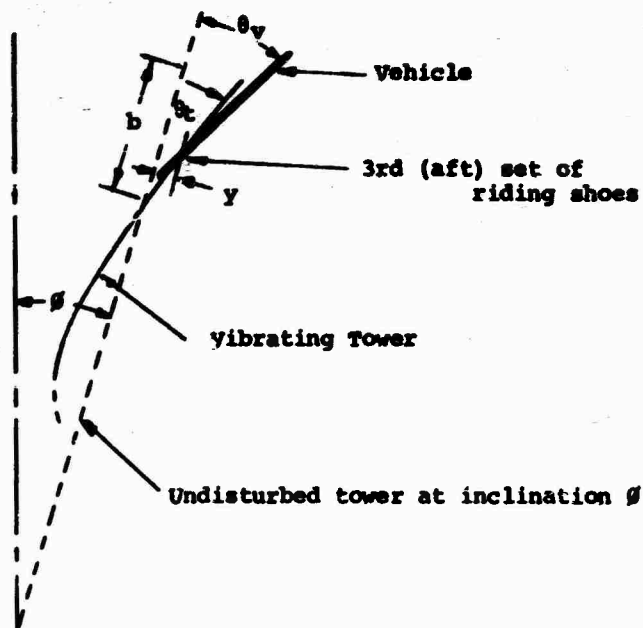


FIGURE 5
SCHEMATIC REPRESENTATION OF TOWER AND
VEHICLE DURING THE INTERVAL BETWEEN 2nd AND 3rd SHOE EXIT

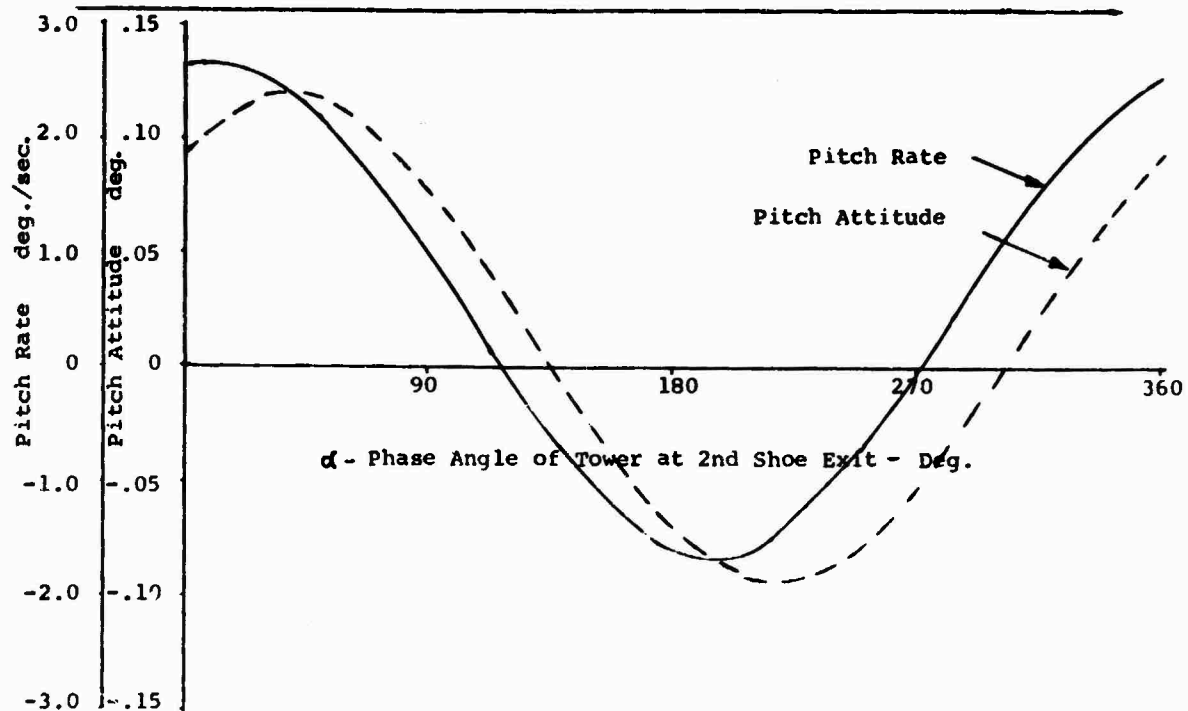
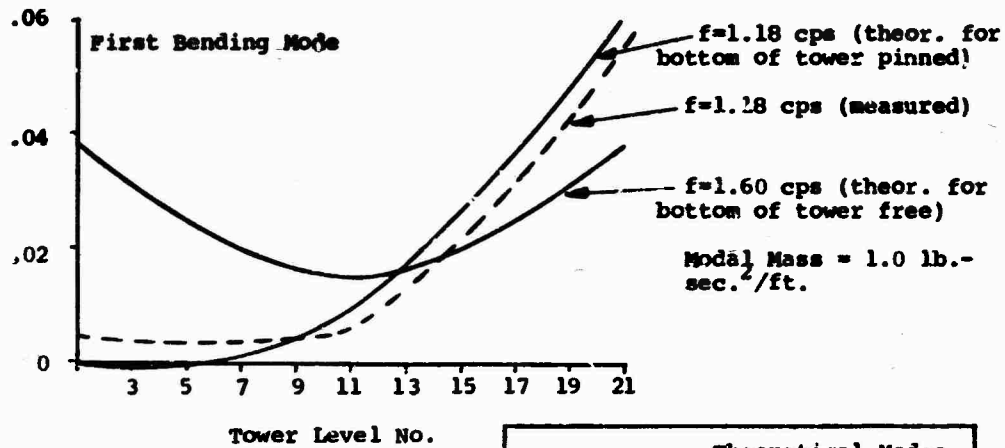


FIGURE 6
AEROBEE 350 - FLIGHT 17.08
RIGID BODY PITCH RATE AND ATTITUDE
AT 3rd SHOE EXIT FROM TOWER

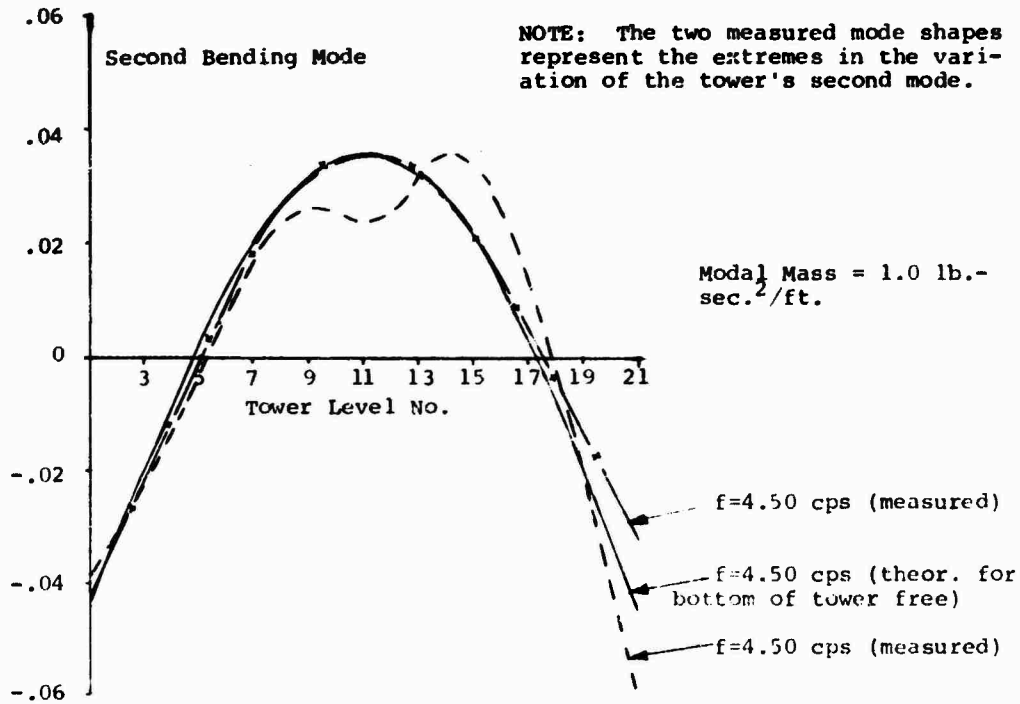
FIGURE 7
COMPARISON OF THEORETICAL AND MEASURED
MODE SHAPES OF WHITE SANDS LAUNCH TOWER

Mode Shape Value
 (Norm to Unit Modal Mass)



NOTE: The two measured mode shapes represent the extremes in the variation of the tower's second mode.

Mode Shape Value
 (Norm to Unit Modal Mass)



ON THE USE OF FOURIER TRANSFORMS
OF MECHANICAL SHOCK DATA

Dr. H. A. Gaberson and Mr. D. Pal
Naval Civil Engineering Laboratory
Port Hueneme, California

Some uses and analyses of Fourier transforms of mechanical shock motions are presented. A simplified proof that the magnitude of the acceleration transform is the residual velocity shock spectrum is given in a form that readily introduces the "running" Fourier transform. A method is presented for analyzing high narrow peaks on actual Fourier transforms to determine the actual excursion associated with the peak frequency. The effects of truncating the record of a slowly decaying transient is also considered. The paper closes with a discussion of the merits of the various transforms.

INTRODUCTION

For quite some time now, several authors including ourselves have advocated the use of Fourier transforms as an improved descriptor of mechanical shock motions, and yet very little has been written on the actual use of the transform. Naval Civil Engineering Laboratory (NCEL) under the sponsorship of the Naval Facilities Engineering Command has been studying the use of Fourier transforms as possible improved descriptors of equipment shock hardness; in this study the transform has shown promise of becoming a considerable designer aid. The main reason for our continued study of the Fourier transform is that it contains a mathematically complete description of the time history of the shock organized with respect to frequency and that it is inexpensive to compute, especially in comparison to the shock spectrum, a close relative and widely used. In this paper we present a short collection of analyses which we have found useful in utilizing Fourier transforms in connection with mechanical shock.

Magnitude of Fourier Transforms

Rubin [1] has suggested a most helpful way of looking at the information contained in a Fourier transform of a shock motion; it can be explained as follows. If $y(t)$ is an acceleration time history that begins at $t = 0$ its Fourier transform may be written as

$$Y(\omega) = \int_0^{\infty} \ddot{y}(t) e^{-i\omega t} dt. \quad (1)$$

Here ω is frequency in radian measure, equal to $2\pi f$, where f is frequency in cycles per unit time. By using Euler's formula

$$e^{-i\omega t} = \cos \omega t - i \sin \omega t, \quad (2)$$

Equation (1) may be broken into two integrals to form the real and imaginary parts of the Complex Fourier Transform:

$$Y(\omega) = R(\omega) + i I(\omega), \quad (3)$$

where

$$R(\omega) = \int_0^{\infty} \ddot{y}(t) \cos \omega t dt, \quad (4a)$$

$$I(\omega) = -\int_0^{\infty} \ddot{y}(t) \sin \omega t dt. \quad (4b)$$

The transform, $Y(\omega)$, may also be written in terms of its amplitude, $A(\omega)$, and phase, $\gamma(\omega)$, as follows.

$$Y(\omega) = A(\omega) e^{i\gamma(\omega)} \quad (5a)$$

where

$$A(\omega) = \left[R(\omega)^2 + I(\omega)^2 \right]^{1/2}, \quad (5b)$$

$$\alpha(\omega) = \tan^{-1} (I(\omega)/R(\omega)), \quad (5c)$$

$$= \sin^{-1} (I(\omega)/A(\omega)), \quad (5d)$$

$$= \cos^{-1} (R(\omega)/A(\omega)). \quad (5e)$$

Thus

$$R(\omega) = A(\omega) \cos \alpha(\omega), \quad (5f)$$

$$I(\omega) = A(\omega) \sin \alpha(\omega). \quad (5g)$$

Now consider the response of an undamped single degree of freedom system as indicated in Figure 1.

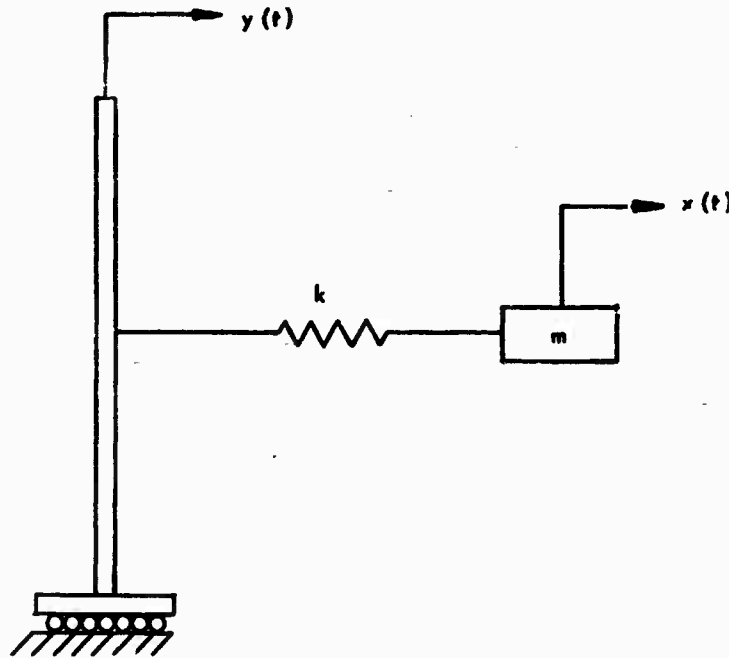


Fig. 1 - Base excited simple system.

A free body diagram of the mass yields the familiar

$$m \ddot{x} + k(x - y) = 0 \quad (6)$$

Changing the variable to the relative motion, $z = x - y$, yields another familiar form

$$\ddot{z} + \omega^2 z = -\ddot{y}(t), \quad (6a)$$

where

$\omega = \sqrt{k/m}$, is the natural frequency.

Virtually all texts [2,3] that in any manner treat transient excitations ask you to consider the excitation as a sequence of impulses that leads to the Duhamel's integral

$$z(t) = -\frac{1}{\omega} \int_0^t \ddot{y}(\tau) \sin \omega(t - \tau) d\tau. \quad (7)$$

The above solution implies that both z and \dot{z} are zero at $t = 0$. If the derivation presented in texts is unsatisfying, the correctness of the solution can be somewhat comfortingly verified by direct substitution back into the differential equation, Equation (6a); care must be exercised in differentiating a definite integral with respect to its limits

as is explained in Pipes [4, p. 320].

Rubin [1] used Equation (7) to provide a relationship with the Fourier transform. From the formula for the sum of the difference of two angles, Equation (7) may be written as

$$z(t) = -\frac{1}{\omega} \int_0^t \ddot{y}(\tau) (\sin \omega t \cos \omega \tau - \cos \omega t \sin \omega \tau) d\tau, \quad (8a)$$

and since t is a constant during the integration

$$z(t) = -\frac{1}{\omega} \left[\sin \omega t \int_0^t \ddot{y}(\tau) \cos \omega \tau d\tau - \cos \omega t \int_0^t \ddot{y}(\tau) \sin \omega \tau d\tau \right] \quad (8b)$$

Now, inserting Equations (4a and b) in Equation (8b) we have

$$z(t) = -\frac{1}{\omega} \left[\sin \omega t R(\omega, t) + \cos \omega t I(\omega, t) \right], \quad (8c)$$

where $R(\omega, t)$ and $I(\omega, t)$ are the real and imaginary parts of the "running" Fourier transform [5], i.e., the transform of the function $\ddot{y}(t)$ terminated at the time, t .

Finally from Equations (5f and g) we obtain

$$z(t) = -\frac{A(\omega, t)}{\omega} \left[\sin \omega t \cos \alpha(\omega, t) + \cos \omega t \sin \alpha(\omega, t) \right] \quad (8d)$$

or

$$z(t) = -\frac{A(\omega, t)}{\omega} \sin [\omega t + \alpha(\omega, t)] \quad (9)$$

Equation (9) is one of Rubin's results [1]. It states that the response of an undamped single degree of freedom system at anytime, t , is given by the Fourier transform of the excitation between 0 and t , evaluated at ω , the system natural frequency.

Suppose the shock excitation has a duration, T ; Equation (9) with time removed from its argument applies to all times greater than T , since the running transform only accumulates values between 0 and T . When Equation (9) is used for times shorter than T , the duration of the shock excitation, $A(\omega, t) e^{i\alpha(\omega, t)}$, is the running transform of only that portion of the pulse between 0 and t . For all time equal to or greater than T , the running transform is given by the Fourier transform of the complete excitation, $A(\omega) e^{i\alpha(\omega)}$. Thus for time greater than or equal to T the response is simply given by

$$z(t) = -\frac{A(\omega)}{\omega} \sin [\omega t + \alpha(\omega)], \quad (9a)$$

which is a result previously reported [6].

If $A(\omega)$ and $\alpha(\omega)$ represent the amplitude and phase of the Fourier transform of the non-zero portion of the pulse, then Equation (9a) gives the residual response of any undamped oscillator to the pulse. Thus $A(\omega)/\omega$ is the displacement residual shock spectrum of the excitation where $A(\omega)$ is the magnitude of the Fourier transform of the excitation acceleration. Since the undamped residual response is purely sinusoidal as shown, and continues for all time, Equation (9) can be differentiated to give the velocity and acceleration as

$$\dot{z}(t) = -A(\omega) \cos (\omega t + \alpha) \quad (9b)$$

$$z(t) = \omega A(\omega) \sin (\omega t + \alpha). \quad (9c)$$

Thus $A(\omega)$, the magnitude of the Fourier transform of the excitation acceleration is the residual undamped shock spectrum of the pulse expressed in terms of velocity, and $\omega A(\omega)$ is the residual shock spectrum expressed in terms of displacement.

Fourier transforms of integrals and derivatives of functions can be written in terms of the transform of the function, when these transforms actually exist [5]. For example,

if the Fourier transform of an acceleration is $A(\omega) e^{i\alpha(\omega)}$, one can integrate the defining equation by parts to obtain the transform of the velocity. Thus if

$$A(\omega) e^{i\alpha(\omega)} = \int_{-\infty}^{\infty} \dot{y}(t) e^{-i\omega t} dt, \quad (10a)$$

we integrate by parts letting $u = e^{-i\omega t}$ and $dv = \dot{y}(t) dt$, which yields

$$A(\omega) e^{i\alpha(\omega)} = i\omega \int_{-\infty}^{\infty} y(t) e^{-i\omega t} dt. \quad (10b)$$

Defining the Fourier transform of the velocity to be

$$V(\omega) e^{i\varphi(\omega)} = \int_{-\infty}^{\infty} \dot{y}(t) e^{-i\omega t} dt, \quad (10c)$$

we obtain

$$A(\omega) e^{i\alpha(\omega)} = i\omega V(\omega) e^{i\varphi(\omega)}. \quad (10d)$$

Thus

$$A(\omega) = \omega V(\omega), \quad (10e)$$

$$\alpha(\omega) = \varphi(\omega) + \frac{\pi}{2}. \quad (10f)$$

Continuing the above reasoning, one can construct the following table which gives the relationships between the transforms of acceleration, velocity or displacement can be expressed in terms of any of the other transforms.

The previous comment mentioning possible nonexistence of some of the transforms can be understood as follows. The condition generally given as requisite for the existence of a Fourier transform is [5]

$$\int_{-\infty}^{\infty} |f(t)| dt < \infty. \quad (11)$$

In practical cases the portion of the transient analyzed may be insufficient to bring the velocity or displacement back to zero; in such a case the transform of the velocity or displacement would not strictly exist and condition (11) would not be satisfied. If a net velocity change or displacement occurs, those transforms will yield unreasonable values at zero frequency. These difficulties are really more mathematical than practical. In cases where extremely low frequency values of computed spectra seem to indicate problems, the solution will be indicated by considering a longer portion of the time history.

In terms of the transform of:	The Fourier transform of:		
	$\dot{y}(t)$	$\dot{f}(t)$	$y(t)$
$\dot{y}(t)$	$A(\omega) e^{i\alpha(\omega)}$	$\frac{1}{\omega} A(\omega) e^{i\left[\alpha(\omega) - \frac{\pi}{2}\right]}$	$\frac{1}{\omega^2} A(\omega) e^{i\left[\alpha(\omega) - \pi\right]}$
$\dot{f}(t)$	$\omega V(\omega) e^{i\left[\phi(\omega) + \frac{\pi}{2}\right]}$	$V(\omega) e^{i\phi(\omega)}$	$\frac{1}{\omega} V(\omega) e^{i\left[\phi(\omega) - \frac{\pi}{2}\right]}$
$y(t)$	$\omega^2 D(\omega) e^{i\left[\delta(\omega) + \pi\right]}$	$\omega D(\omega) e^{i\left[\delta(\omega) + \frac{\pi}{2}\right]}$	$D(\omega) e^{i\delta(\omega)}$

DECAYING SINUSOIDS

This section treats transforms and response to decaying sinusoids and is almost detached from the previous discussion, but the study has added to our understanding of Fourier and response spectra or shock spectra. Virtually all experience leads one to conclude that responses to shock loadings are composed of at least many decaying vibrations. Although the vibrations probably decay in complicated ways by many different mechanisms, we chose to begin a study of decaying vibrations by studying the simplest one we know, the linearly damped or viscously damped sinusoid. The function considered is the familiar damped response of a simple oscillator to an initial acceleration, thus

$$\ddot{y}(t) = \ddot{y}_0 e^{-\zeta \omega_0 t} \sin \Omega t, \quad (12)$$

where

$$\omega_0^2 = k/m$$

$$\zeta = \frac{c}{2m} = \text{damping ratio}, \quad (12a)$$

$$\Omega = \omega_0 \sqrt{1 - \zeta^2} = \text{damped natural frequency.} \quad (12b)$$

We have also considered the damped cosine wave, but the results are not substantially different, and so the damped sine will be used for presentation. The Fourier transform of a lightly damped decaying sinusoid contains a severely responding peak and hence can be used as a model to determine maximum modal excursions associated with severely responding peaks in actual records. Thus we presume that many of the sharp peaks in experimentally determined Fourier transforms of complex motions are completely due to the presence of a damped sinusoid in the total motion.

The total response at any measurement station of shock excited equipment is probably composed of the sum of many elementary responses thus we think of the total response as

$$f_{\text{total}} = f_1(t) + f_2(t) + f_3(t) + \dots + f_n(t). \quad (13)$$

By the definition of the Fourier transform, the total transform of a sum of functions is the sum of the transform of the elementary functions thus

$$FT(f_{\text{total}}) = FT(f_1) + FT(f_2) + FT(f_3) + \dots + FT(f_n). \quad (13a)$$

If one of these elementary functions is a lightly damped sinusoid, the magnitude of the transform will become large near its responding frequency and dominate the total transform in that region. If the transforms of the other functional elements of the total response are not rapidly varying near this frequency the geometry of the peak of decaying sinusoid transform will be apparent and available for analysis.

Consider the Fourier transform of the acceleration given in Equation (12) for time greater than zero. From the definition of Equation (1), it is given by

$$Y(\omega) = \int_0^{\infty} \ddot{y}_0 e^{-\zeta \omega_0 t} \sin \Omega t e^{-i\omega t} dt. \quad (14)$$

Equation (14) can be evaluated by standard formulae given in all math tables (for example, Case 312, [7]). After simplification one obtains

$$\frac{\omega_0^2 Y(\omega)}{\ddot{y}_0} = \frac{\sqrt{1 - \zeta^2}}{1 - R^2 + 2i\zeta R} \quad (15)$$

where

$$R = \frac{\omega}{\omega_0}. \quad (15a)$$

The Fourier spectrum or the magnitude of the Fourier transform is obtained by taking the absolute value of Equation (15) which yields

$$\frac{\omega_0 A(\omega)}{y_0} = \left[\frac{1 - f^2}{(1 - R^2)^2 + 4f^2 R^2} \right]^{\frac{1}{2}} \quad (15b)$$

where $A(\omega)$ is the magnitude of the Fourier transform or the Fourier spectrum. Taking the derivative of Equation (15b) with respect to R , the frequency ratio, one finds that the transform has zero slope for zero frequency and a peak value given by

$$\frac{\omega_0 A(\omega)}{y_0} \max = \frac{1}{2f}, \text{ at } R = \sqrt{1 - 2f^2}. \quad (16)$$

At zero frequency the intercept is

$$\frac{\omega_0 A(\omega)}{y_0} = \sqrt{1 - f^2}, \text{ when } R = 0. \quad (16b)$$

For very large values of R

$$\frac{\omega_0 A(\omega)}{y_0} = \frac{\sqrt{1 - f^2}}{R^2} \text{ when } R \gg 1. \quad (16c)$$

Figure 2 is a plot of the magnitude of the transform for two values of f . Note that even on the logarithmic plot the peak is extremely pronounced, thus we might well expect that it will be apparent and distinct from the remainder of the transform. One also finds that the transform of a decaying cosine wave has differing asymptotic and zero frequency values but in the neighborhood of the peak f : a lightly damped decay, has a substantially similar geometry.

Now that we realize that the transform will contain these peaks at the responding frequency of the decaying sinusoid, let us consider the converse problem of determining the constants in equation (12) from the geometry of the peak of the transform. Consider the width of the transform peak when the magnitude is some fraction, ϕ , of the maximum value. The ratio ϕ^2 equal to the square of the magnitude, Equation (15b) divided by the square of the maximum magnitude, Equation (16) is given by

$$\phi^2 = \frac{4f^2 \sqrt{1 - f^2}}{(1 - R^2)^2 + 4f^2 R^2}. \quad (17a)$$

After rearranging, the following equation results.

$$R^4 - 2(1 - 2f^2)R^2 + \frac{4f^2(1 - f^2)}{\phi^2} = 0. \quad (17b)$$

The above equation is quadratic in R^2 and has two distinct roots yielding R_1 and R_2 . These can be directly computed and subtracted to give the peak width at ϕ , or by rearranging

one can find the width ΔR given by

$$\Delta R^2 = 2(1 - 2f^2) - \frac{2}{\phi} (\phi^2 - 4f^2 + 4f^4)^{\frac{1}{2}}. \quad (17c)$$

Figure 3 is a graph of the values of the peak width, ΔR for values of ϕ , with varying amounts of damping, f .

Now, given the above theory, let us consider the application. Figure 4 shows a hypothetical Fourier amplitude spectrum of an acceleration time history of a mechanical shock. It has a narrow distinct peak of magnitude A_{\max} situated at a frequency f_p . This peak is presumed due to a decaying sinusoid contained in the original time history. We are concerned about the magnitude of the velocity indicated by the peak value and would like to estimate the maximum modal velocity that actually existed at this frequency at our measurement station. Maximum modal velocity has been shown to indicate response severity [8]. It must be realized that the transform of this decaying sinusoid is superimposed on other transform values from other functional elements of the shock pulse but assume that the magnitude of the transform of the remainder of the shock pulse is some constant value, A_s , in the region of the narrow transform peak.

The final relations are developed as follows. Consider an amplitude A_1 in the narrow peak region of Figure 4. A horizontal line at amplitude A_1 intersects the narrow peak where it has a width Δf_1 . Let f be the measured peak frequency and A_{\max} the measured peak magnitude. ΔR is then given by

$$\Delta R = \frac{\Delta f_1}{f_p}. \quad (18a)$$

The magnitude of the decaying sinusoid transform at the peak will be A_{\max} less A_s , thus from Equation (16)

$$A_{\max} - A_s = \frac{y_0}{2f\omega_0}. \quad (18b)$$

The value of ϕ_1 corresponding to Δf_1 is given by

$$\phi_1 = \frac{A_1 - A_s}{A_{\max} - A_s}. \quad (18c)$$

Finally solve Equation (18b) for A_s and substitute the value into (18c) which yields

$$1 - \phi_1 = \frac{2f\omega_0}{y_0} (A_{\max} - A_1) \quad (18d)$$

Two sets of values of Δf and A are required and must be measured from the narrow peak

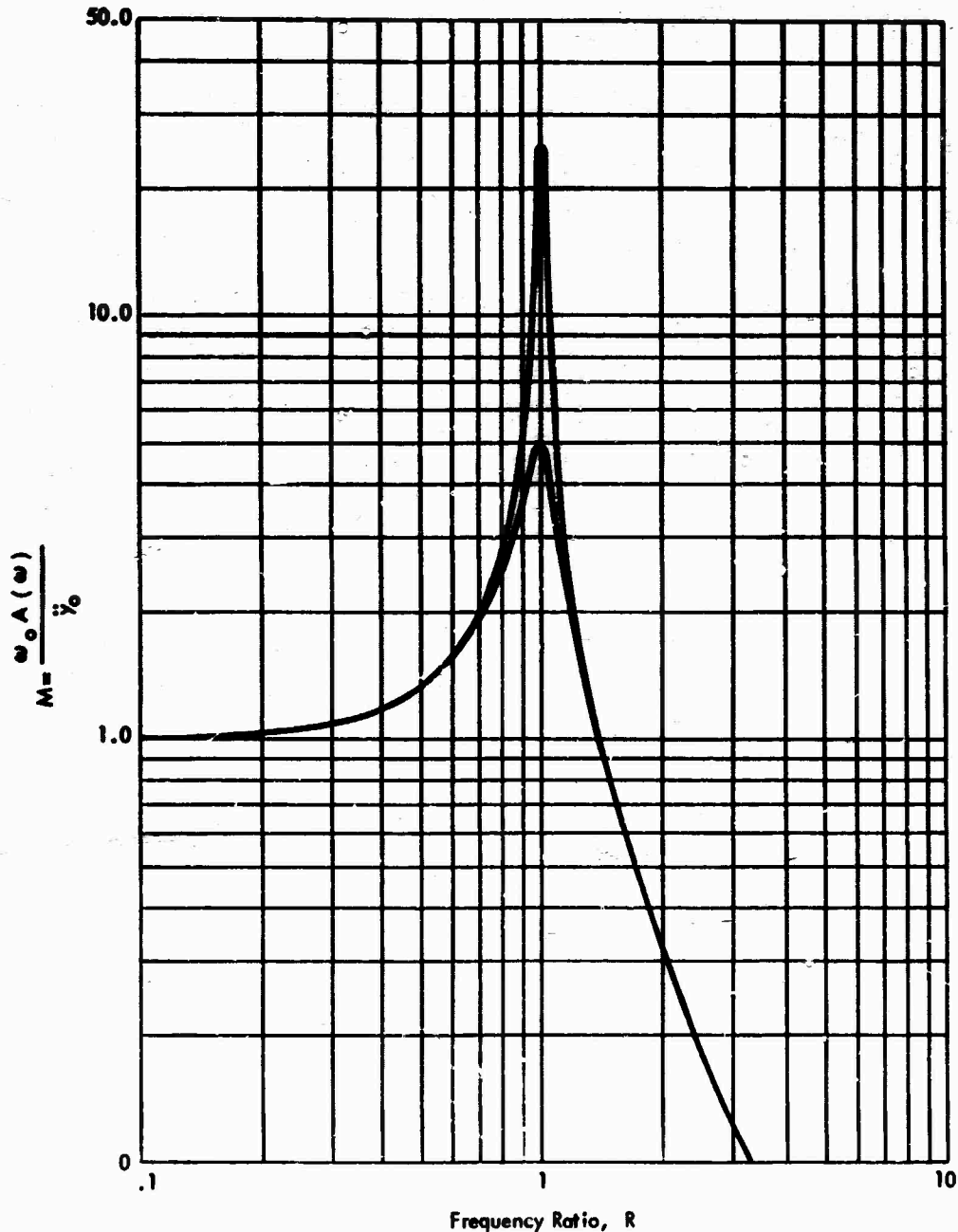


Fig. 2 - Fourier transform magnitude of a decaying
Sinusoid for $\zeta = 0.02$, $\zeta = 0.1$

as shown in Figure 4; thus two Equations (18d) will be obtained, one for A_1 and one for A_2 . Dividing the equation for A_1 by that for A_2 yields

$$\frac{1 - \phi_1}{1 - \phi_2} = \frac{A_{\max} - A_1}{A_{\max} - A_2} \quad (18e)$$

In Equation (18e) A_{\max} , A_1 and A_2 are measured values from the transform graph; therefore, Equation (18e) is a relationship between ϕ_1 and ϕ_2 . Equation (17c) gives a relationship between ζ , ϕ and ΔR which is expressed as a graph in Figure 3. Since ΔR_1 and ΔR_2 are known, select a trial ζ on Figure 3 and determine a trial value of ϕ_1 and ϕ_2 . Test these values in Equation (18e). Continue selecting new values

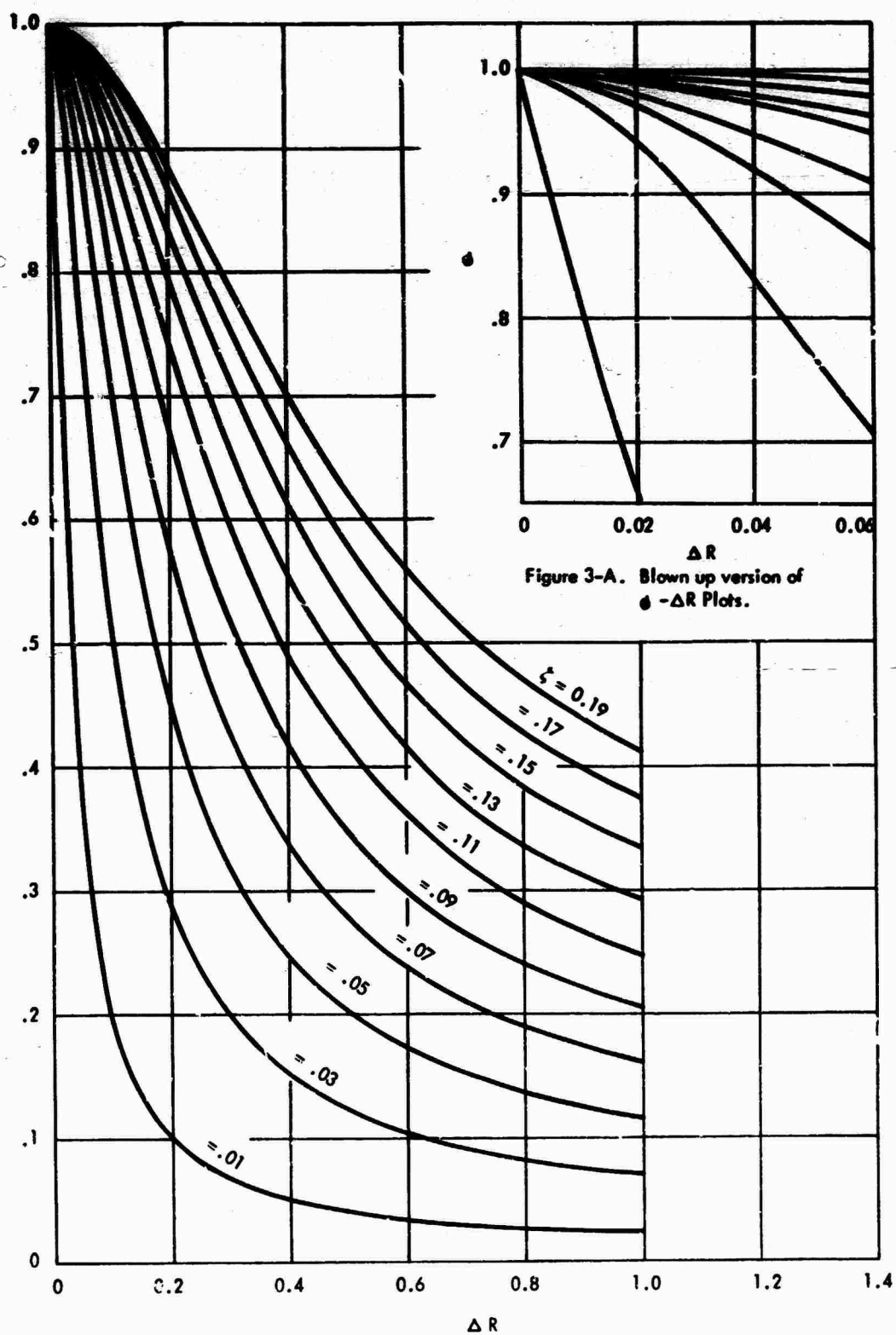


Figure 3-A. Blown up version of $\phi - \Delta R$ Plots.

Fig. 3 - Curves for finding ϕ and ζ for a given ΔR .

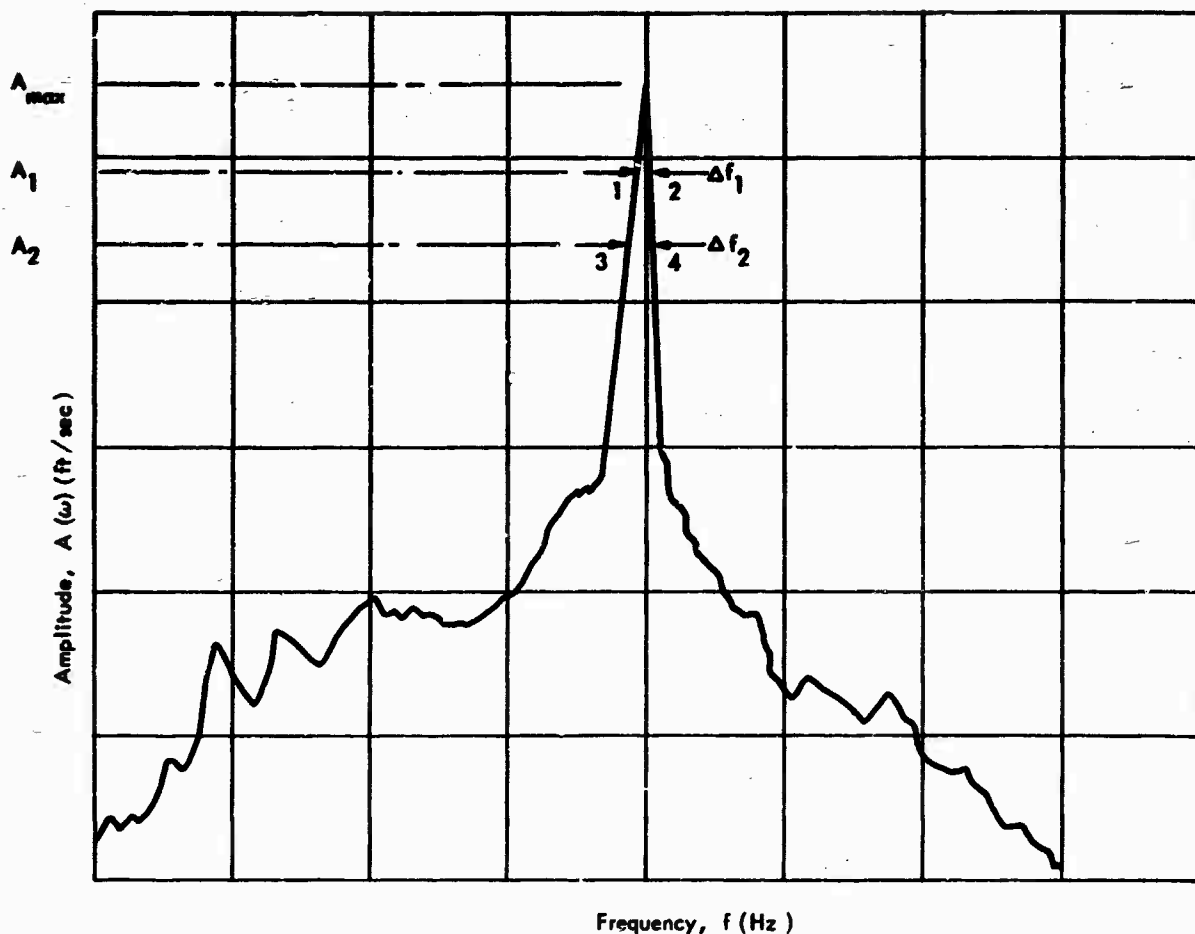


Fig. 4 - Fourier amplitude spectrum of the acceleration-time history of a complete shock.
(The peak on this plot has been enlarged widthwise for illustration)

of ζ and testing the resulting values of ϕ_1 and ϕ_2 until a value of ζ is found that yields ϕ 's at ΔR_1 and ΔR_2 on Figure 3 that satisfy Equation (18e). Thus the value of ζ is determined.

Since this procedure should only be used on high narrow peaks that are due to low damping, ω_0 is very close to $2\pi f_p$ (see Equation (16)). With ω_0 and the value of ζ obtained above, \dot{y}_0 can be computed from Equation (18d).

It was previously stated that the maximum modal velocity was a quantity of interest to be determined from the foregoing. Since it is expected that each individual mode will respond with a decaying sinusoidal motion, the maximum velocity associated with this decaying motion is an observed modal velocity. The maximum velocity is therefore obtained by

integrating Equation (12). However when Equation (12) is integrated to velocity an arbitrary constant necessarily appears which can clearly alter the maximum modal velocity obtained. The constant is evaluated by the observation that the velocity must go to zero when time goes to infinity. Equation (12) so integrated and evaluated yields

$$\dot{y} = \frac{\dot{y}_0}{\omega_0} \left[-e^{-\zeta\omega_0 t} (\zeta \sin \Omega t + \sqrt{1 - \zeta^2} \cos \Omega t) \right] \quad (19)$$

This equation has its maximum at time equal to zero and the maximum modal velocity is

$$\dot{y}_{\max} = \frac{\dot{y}_0}{\omega_0} \sqrt{1 - \zeta^2} \quad (19b)$$

If the decaying sinusoid were assumed a decaying cosine, the maximum velocity is substantially

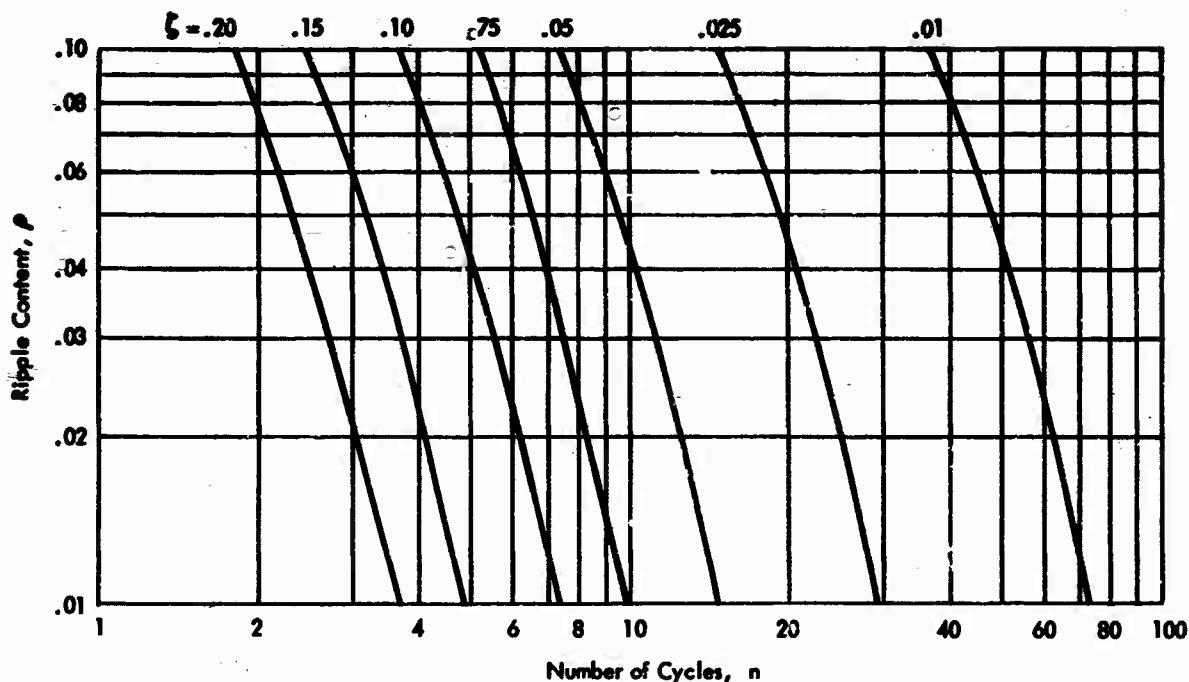


Fig. 5 - Ripple content versus truncation
for a decaying sinusoid

the same for very low damping, but is reduced by a factor, μ , which is given by

$$\mu = \exp \left(\frac{-\pi \zeta}{2 \sqrt{1 - \zeta^2}} \right). \quad (19c)$$

TRUNCATION EFFECTS

A practical problem in shock data analysis that routinely occurs is the determination of the length of time history that should be analyzed. Oftentimes in lightly damped structure the response decays very slowly. A theoretical example of the effects of truncating the acceleration time history of a decaying sinusoid is presented here to offer some insight into the problem.

Consider the running Fourier transform corresponding to Equation (14), but only for integral numbers of cycles. Thus rather than integrate Equation (14) from 0 to ∞ , integrate from 0 to $2\pi n/\Omega$. The magnitude of this pseudo running Fourier transform is given by

$$\frac{A(\omega, n)}{y_0} = \left[\frac{1 - \zeta^2}{(1 - R^2)^2 + 4 \zeta^2 R^2} \right]^{\frac{1}{2}} \times (1 + e^{-2\gamma \zeta} - 2e^{-\gamma \zeta} \cos \gamma R)^{\frac{1}{2}}, \quad (20)$$

where

$$\gamma = \frac{2\pi n}{\sqrt{1 - \zeta^2}}. \quad (20a)$$

Comparing Equation (20) with Equation (15b), it is observed that the result is similar except for the addition of a truncation correction factor, TCF. Consider just the truncation factor alone.

$$TCF = (1 + e^{-2\gamma \zeta} - 2e^{-\gamma \zeta} \cos \gamma R)^{\frac{1}{2}}. \quad (20b)$$

It will be noted that as γ or n , the number of cycles, gets very large, the TCF approaches unity. For a sufficiently small n or γ the average value of the magnitude is reduced, but even further the TCF imposes a ripple on the magnitude of about n cycles per unit change of R . At least the ripple is intolerable and would be confusing so that a sufficient number of cycles should be taken to assure that the TCF is negligible. Rewriting the TCF in simpler notation,

$$TCF = (B - C \cos \gamma R)^{\frac{1}{2}}, \quad (20c)$$

where

$$B = 1 + e^{-2\gamma \zeta}, \text{ and } C = 2e^{-\gamma \zeta}.$$

The average amplitude of the ripple can be expressed as

$$\rho = \frac{1}{2} \left[\sqrt{B + C} - \sqrt{B - C} \right]. \quad (20d)$$

Values of the average ripple content, ρ , plotted against n , the number of cycles included in the running transform are plotted in Figure 5, for various values of ζ . For example, if $\zeta = 0.05$, 15 cycles are required to assure a ripple content of 1%.

The same truncation correction factor occurs if a decaying cosine is truncated after n cycles.

The practical significance of this result must be examined further. It may mean that one must be cautious when truncating a record; conversely since the damage often occurs during the first part of the pulse, it may indicate that the Fourier transform is sensitive to unimportant information about the shock.

CONCLUSION

In conclusion we have presented a method for determining the maximum modal excursion at a point from narrow peaks in a Fourier transform. These responses can be considered maximum modal velocities to the extent that they do constitute a lower bound. In that sense they do indicate for example the severity of a beam response as has been shown in [10].

Jenshke [9] has presented a proof which shows the envelope of the magnitudes of the running Fourier transform to be an upper bound to the overall shock spectrum for velocity. If this envelope can be inexpensively computed it may provide wide availability of a new shock severity evaluation. Reference [9] also presents some computed results of a running transform, undamped shock spectrum and Fourier transform. It is interesting to note that at the high peaks in his spectra, the Fourier transform does yield the same result as the other spectra. The Fourier transform appears to heavily weigh repeated cycles at the same frequency as was clearly shown in the decaying sinusoid analysis. It may well be that for structures that are sensitive to repeated excursions the Fourier transform may provide a more reliable indicator of damage. Yet the fact that the magnitude is only a residual spectrum and misses the maximum excursions during the pulse does detract from its apparent usefulness in a structure which fails due to the single highest peak.

Linear system theory demonstrates that by knowing the complex frequency response between any desired measurement station and an input point, inverse Fourier transformation of the product of the transform of the excitation and the system function will yield the exact time response to the transient at the measurement station. This is an attractive idea and could be subjected to any recorded excitation on the computer. However many different system

functions would have to be measured to find motions at adjacent stations to compute stresses, and we wonder about the cost of determining all of these system functions. We have not heard of anyone currently accomplishing shock analysis by these means.

Normal mode theory through the shock spectrum yields the maximum response of each mode, but does not give a convincing method for combining the responses of the separate modes in a not overly conservative manner.

Much work remains to be done to firmly establish the place of the Fourier transform in the analysis of mechanical shock data. It is hoped that these ideas will stimulate others to pursue the question.

ACKNOWLEDGMENT

This work was supported by the Naval Facilities Engineering Command under the cognizance of Capt. P.A. Phelps, Assistant Commander for Research and Development, and M. S. Rockefeller, Chief Research Engineer. Mr. H. Lamb monitors the contract.

REFERENCES

1. Rubin, S.; private communications beginning October 1970.
2. Timoshenko, S.; "Vibration Problems in Engineering"; 3rd. Ed.; D.Van Nostrand Company, Inc.; New York; 1955.
3. Thomson, W.T.; "Vibration Theory and Applications"; Printice-Hall, Inc.; Englewood Cliffs, New Jersey; 1965.
4. Pipes, L.A.; "Applied Mathematics for Engineers and Physicists"; 2nd. Ed.; McGraw-Hill Book Company, Inc.; New York; 1958.
5. Papoulis, A.; "The Fourier Integral and its Applications"; McGraw-Hill Book Company, Inc.; New York; 1962.
6. Rubin, S. "Concepts in Shock Data Analysis"; Chapter 23 in "Shock and Vibration Handbook" by Harris, C.M. and Crede, C.E.; McGraw-Hill Book Company, New York; 1961, p. 23-23.
7. Burington, R.S.; "Handbook of Mathematical Tables and Formulas"; Handbook Publishers, Inc.; Sandusky, Ohio; 1955.
8. Gaberson, H.A. and Chalmers, R.H.; "Modal Velocity as a Criterion of Shock Severity"; The Shock and Vibration Bulletin; No. 40, Part 2, p 31-49.
9. Jenshke, V.A.; "Relations Between Response and Fourier Spectra of Shock Functions"; Int. J. Solids Structures. Vol. 6, 1970; pp 1259-1265.

WAVE ANALYSIS OF SHOCK EFFECTS IN COMPOSITE ARMOR

Gordon L. Filbey, Jr.
USAAADC Ballistic Research Laboratories
Aberdeen Proving Ground, Maryland

Enhanced performance by composite armor in layered configurations against kinetic energy projectiles, hypervelocity particles and metal jets has been an accepted fact based on numerous observations. A rationale for this improved performance is given in this paper in terms of an analytic model based on one-dimensional nonlinear wave propagation and reflection at material interfaces. Included as special cases are 1-D hydrodynamic shock waves and elastic waves. The model is specifically worked out for the dispersive wave case of a plastically deforming metal in uniaxial stress on one side of a boundary against a linearly elastic metal on the other side, but the principles apply generally. Details of the calculations of the developed stress fields in the two material case are carried through and compared favorably with experiment. It is definitively shown that regions occupied by "harder" materials are those subjected to the larger stresses and thus these "harder" materials may be thought of as stress raisers.

INTRODUCTION

The notion of using stress wave analysis to predict failure modes in composite armor, such as penetration, fracture and spallation, is not a new one. A frequently mentioned reference in this context is the 1965 work of Kinslow [1]. Kinslow [1] considered in detail a 30 layer laminate constructed of two alternating elastic materials. Although limited to one dimensional elastic dilatational waves at normal incidence, the analysis demonstrated that shock mitigation may be produced by laminating two materials. The analysis, coupled with several different experiments, demonstrates conclusively that defeat enhancement may be achieved with the concept of lamination. That is, there is definitely an advantage over the construction of a target from the single harder material of the two used in the laminate construction. In a different sort of problem, Horie [2] has demonstrated that, from the standpoint of momentum transfer into an armor plate, an optimum thin bumper of soft material may be added to the front face to reduce the total momentum initially transferred into the armor plate. In these cases as in uncited numerous others, the analysis always seems to be limited to the use of linear elastic constitutive relations for the one dimensional shocks treated, -- usually on the grounds that this is the only case that can be treated with any simple sort of analysis. At the opposite end of the spectrum of course computer programs exist

which may be used to calculate the detail in any specific instance. But very often, in order to achieve penetration data for ten or twenty or fifty microseconds, the expense and running time on the machine is prohibitive. Hence a need exists for an analytical or quasi-analytical tool for those problems in which plastic deformation is caused in the target by the impactor. It is the intent of this paper to outline an approach which may be developed towards this goal.

PLASTIC WAVES

An underlying assumption made here is that armor penetration by impactors - be they kinetic energy projectiles, hypervelocity particles or metal jets - is accompanied by plastic deformation, and in this process waves of plastic deformation are forerunners of the impactor tip. Since typical armors are bounded media, the wave reflection and interaction processes build up conditions which ultimately determine material failure. Hence it is instructive to examine some simple generalities of the wave propagation process, and as we shall later see, interaction conditions which may exist at material interfaces within the target.

Assume, for the "softer" target materials, an equivalent one-dimensional uniaxial stress model that, within the time scale of wave propagation processes, is rate-independent.

Hence take a 1-D stress-strain relationship of the form

$$\sigma = A\epsilon^a \quad (1)$$

Some theoretical justification exists for choosing this form, as discussed elsewhere by Filbey [3]. Plastic waves are propagated within this 1-D framework governed by a quasi-linear wave equation

$$\frac{\partial \sigma}{\partial \epsilon} \frac{\partial^2 \epsilon}{\partial x^2} = \rho \frac{\partial^2 \epsilon}{\partial t^2} \quad (2)$$

which identifies a wave velocity c_p for each level of strain ϵ by

$$c_p = \left[\frac{\partial \sigma}{\partial \epsilon} \right]^{1/2} \quad (3)$$

Note that this may also be expressed as

$$d\epsilon = \frac{d\sigma}{\rho c_p^2} \quad (4)$$

once a stress-strain relation $\sigma(\epsilon)$ is given. For semi-infinite media, the particle velocity relative to the material at rest (at infinity) is found from

$$v = \int c_p d\epsilon = \int c_p \frac{d\sigma}{\rho c_p^2} = \int \frac{d\sigma}{\rho c_p} \quad (5)$$

upon using (4). For details of the above, see Bell [4]. Differentiating, one may relate an (+) increment in particle velocity to a (+) increment in stress as

$$\Delta v = \frac{\Delta \sigma}{\rho c_p} \quad (6)$$

Substituting (1), (6) becomes

$$\Delta v = \frac{\Delta \sigma}{\sqrt{\rho_0 A^{1/a}} \sigma^{1/2(a-1/2)}} \quad (7)$$

The case of most intensive study and interest, and with physical supportive evidence, is when the coefficient $a = 1/2$ and $A = \beta$, again as discussed in Bell [4]. Under those assumptions, write (7) as

$$\Delta v = \sqrt{\frac{2}{\rho_0 \beta^2}} \sigma^{1/2} \Delta \sigma \quad (8)$$

Incidentally, the elastic case is covered by setting $a = 1$ and $A = E$ in (1), or some modified version of elastic constants for uniaxial strain. To keep things simple algebraically, we shall symbolically follow the former. For elastic waves then, (7) becomes the familiar connection between particle velocity and stress

$$\Delta v = \frac{1}{\rho c_0} \Delta \sigma \quad (9)$$

where c_0 is a constant elastic wave speed. Hence an important distinction is noted between (8) and (9) -- particle velocity changes for stress increments in the elastic domain are proportional only to the stress increment, whereas in the plastically deforming material depend additionally on the "ambient" stress level, through the $\sigma^{1/2}$ factor.

WAVE INTERACTION

Consider now the two material case which might exist at an interface in layered composite armor, as indicated diagrammatically in Figure 1. Take the case of an increment

ELASTIC-PLASTIC

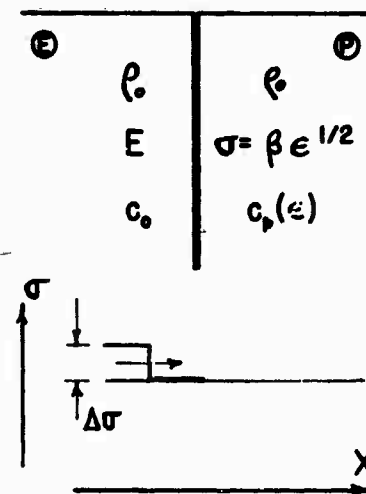


Figure 1

of compressive stress propagating to the right from the "hard" elastic material into the "softer" plastically deformable material, in the presence of an ambient compressive stress σ on both sides of the interface. The simplest situation which satisfies jump conditions on mass and momentum across the interface are to allow for a compressive incident stress increment with associated positive particle velocity increment, a tensile reflected stress increment with associated positive particle velocity increment, and a compressive transmitted stress increment with associated positive particle velocity

Use subscripts i , r , and t to denote incident, reflected and transmitted components, and use circled letter superscripts \textcircled{P} and \textcircled{E} to denote the plastic and elastic components in Figure 1. Then the jump conditions across the material interface requiring continuity of normal stress and velocity yield

$$\begin{aligned}\Delta v_i + \Delta v_r &= \Delta v_t \\ \Delta v_i - \Delta v_r &= \Delta v_t\end{aligned}\quad (10)$$

Define reflection and transmission coefficients r and τ by

$$r = \frac{\Delta v_r}{\Delta v_i}, \quad \tau = \frac{\Delta v_t}{\Delta v_i} \quad (11)$$

Solving (10) with the use of (11), (8), and (9) leads to the expressions

$$\begin{aligned}r &= \frac{\kappa \sigma^{1/2} - 1}{\kappa \sigma^{1/2} + 1} \\ \tau &= 1 - r\end{aligned}\quad (12)$$

where

$$\kappa = \sqrt{\frac{2\rho_0 c_0^2}{\beta^2}} \quad (13)$$

Hence reflection and transmission coefficients have been found for any incremental addition of stress by an oncoming spatially distributed stress wave. What is now different over the classical solutions for mismatched elastic materials as treated e.g. in [1] is the non-linearity introduced by the ambient stress level term $\sigma^{1/2}$. This now means that a total solution must be generated by adding up the incremental contributions to determine the next ambient stress level which determines the new r and τ coefficients, etc. This suggests the construction of rays in $X-t$ space in a Lagrangian diagram for the waves, and then doing the bookkeeping along the characteristics of the wave until the total solution is generated. One such example is given below.

SALIENT FEATURES

Most notable in this solution is the demonstration that shock mitigation is possible in passing from a "hard" to a "soft" material. To demonstrate this, numbers may be substituted in (13) for hard (elastic) aluminum and soft aluminum (e.g. $\beta = 5.60 \times 10^4$ psi) yielding a value of $\kappa = 8.04 \times 10^{-2}$ (psi)^{-1/2}. The values of $r(\sigma)$ and $\tau(\sigma)$ are plotted in Figure 2.

ANNEALED 1100 F ALUMINUM

• HARD ALUMINUM

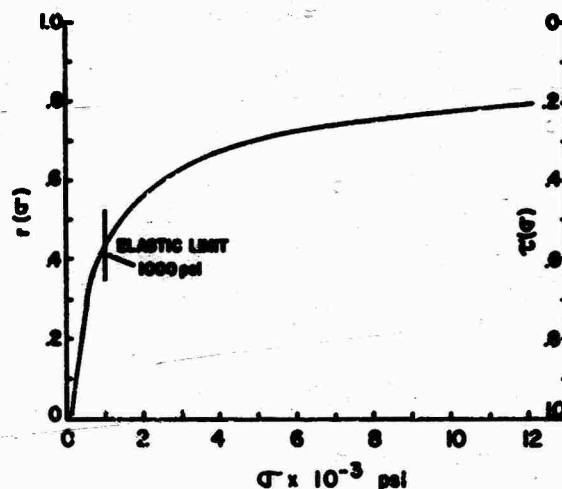


Figure 2. Reflection and Transmission Coefficients

Obviously, the stress increment carried forward is always less than the incident ($\tau < 1$) and that returned is a tensile one which lowers the oncoming. (For a free boundary, it would equal the oncoming and hence cancel.) On the other hand, absence of an interface would permit the high elastic stress pulse to continue on in the target, thus potentially inflicting damage at a deeper level. In this sense, an interface "reflects" back energy, keeping more of it at the front of the target, and thereby enhancing defeat possibilities. Obviously solutions to layered media problems require computational assistance of a computer, but the underlying philosophy is rather simple and may give reasonable answers in much shorter run times than other previous methods.

For completeness, a case is included which was calculated for a longitudinal stress wave in aluminum bars going from plastic to elastic (opposite from the case given here) which was compared with test data. In the absence of an interface, the maximum strain would have been 2.2%; data shown in Figure 3 rises to the higher maximum predicted of 3.5% caused by the total wave interaction. Again repeated, this is test data for the case opposite to that presented in the main body of this paper merely to demonstrate agreement of the analysis with experiment.

4. James F. Bell, *The Physics of Large Deformation of Crystalline Solids*, Springer Tracts in Natural Philosophy, Springer-Verlag, New York, 1968.

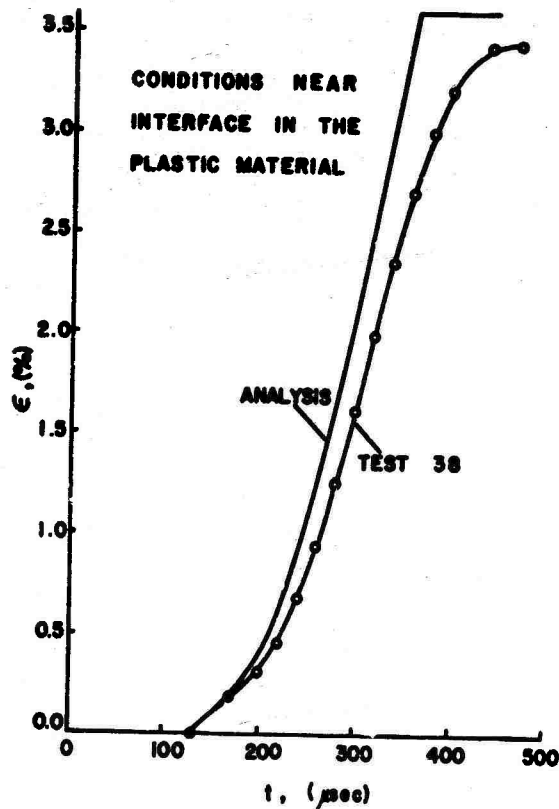


Figure 3. A Comparison of Technique and Test

REFERENCES

1. Ray Kinslow, "Stress Waves in Composite Laminates," AEDC Report TR-65-69, June 1965.
2. Yasuyuki Horie, "Designing an Optimum Thin Bumper on Armor Plates," Tech. Report 70-3, N. Carolina State Univ., AD 712074, August 1970.
3. Gordon L. Filbey, Jr., "Longitudinal Plastic Waves in Bars," Proc. Princeton Univ. Conf. on Solid Mech., pp 111-126, November 21-22, 1963.

STATISTICAL LOADS ANALYSIS TECHNIQUE FOR SHOCK AND HIGH-FREQUENCY EXCITED ELASTODYNAMIC CONFIGURATIONS

K. J. Saczalski and K. C. Park
Clarkson College of Technology
Potsdam, New York

A recently developed technique for describing deterministic and nondeterministic response characteristics of shock and high-frequency excited elastodynamic systems is extended, in a statistical sense, to determine reactive loads, and resulting stresses, at desired locations on structural elements within the system. The coupled transcendental elastodynamic equations include the elastic wave effects of continuous mass distributed structural elements as well as the inertial effects of arbitrary shaped rigid bodies. Depending upon the type of excitation imposed on the system, the calculated loads and stresses may be compared to known experimental and analytical failure criteria to establish limits of structural reliability.

INTRODUCTION

A large class of modern vibration problems, such as sonically induced fatigue, shock impact loading, and noise transmission, are of extreme practical significance, and are associated with high-frequency excitations of complex elastodynamic configurations. In general, an elastodynamic configuration consists of an assemblage of structural elements which include: straight and curved elastic members with continuous mass distribution along the length of the member, as well as the capability to resist stretching (compression), torsion, bending and shearing; arbitrary shaped rigid bodies; shear panel elements; plate elements; and arbitrary constraints. Attempts to mathematically model these complex systems usually culminate in the traditional models of lumped masses connected by massless elastic connectors, or the more recently popular consistent mass matrix model [1]. Unfortunately, use of the above simplified models for the more complex systems subjected to high-frequency excitation could lead to highly inaccurate results.

As an example consider the simple system of a wire fixed at the upper end and excited in the axial direction by a weight which is suddenly dropped to a massless platform attached to the

lower free end. If the assumptions are made that the mass of the wire is negligible in comparison to the mass of the exciting weight, and that uniform axial strain prevails through out the length of the wire for all time, then the maximum axial stress in the system will be calculated as approximately twice the static stress. If on the other hand the mass of the wire is not considered negligible, but is small in comparison to the mass of the exciting weight, then elastic stress waves will propagate along the wire, reflecting and refracting, and cause perturbations on the harmonic response of the exciting weight. As the ratio of the mass of the wire to the mass of the exciting weight becomes greater the assumption of uniform axial strain breaks down. The predominant effects of the elastic stress wave propagations in this case are to cause maximum tensile stresses which may be greater than the factor of two predicted by the elementary lumped mass model.

This problem was first examined experimentally by J. Hopkinson in 1872 and later by B. Hopkinson in 1905 [2]. G. I. Taylor, examining the same problem in 1946, verified the elastic wave effects observed by Hopkinson and showed that, in fact, the wave interactions could cause the ratio of dynamic to static tensile stress to be much

greater than that predicted by the lumped mass theory based on the assumption of uniform axial strain. From the results of the Hopkinson and Taylor studies, as well as investigations on the accuracy of the lumped mass and consistent mass methods [3,4], it may be concluded that any method which is to deal simply and effectively with predicting stresses and loads of high-frequency problems must include the elastic wave effects of the continuous mass distributed elements.

In a recent paper [5] a simplified technique was presented for describing deterministic and nondeterministic response characteristics of high-frequency excited, coupled, spatial vibratory configurations consisting of: continuous mass distributed elastic elements; point masses; arbitrary shaped rigid bodies; shear panel elements; plate elements [6]; and arbitrary constraints. In this paper the technique is extended, in a statistical sense, to determine the reactive loads (forces and moments), and resulting stresses, at any desired location of the individual elements in the system.

GENERAL FORMULATION OF RESPONSE EQUATIONS

The basis for developing the necessary Euler-Lagrange equations of equilibrium and compatibility of a given system is provided by the Lagrangian L , formed by the potential, kinetic and constraint energies of the system elements. The resulting set of equilibrium and compatibility equations are designated the elastodynamic equations of the complex configuration. Loadings may be in terms of forces (and moments) and/or displacements (and rotations). Unknown internal constraints, or reactive loadings, are represented by Lagrangian multipliers and are assumed to have harmonic solutions. Exclusion of the explicit time dependence of the elastodynamic equations, by operating in the frequency domain and using transform techniques, results in a reduced set of matrix equations which by their symmetry, and partitioned form, minimize the storage and ill conditioning problem of large order, sparse matrices normally associated with such systems. Applying steady state sinusoidal excitations of constant amplitude and varying frequency to the elastodynamic expressions yields frequency spectrums for the generalized coordinates $q(t)$ of the point and line intersections (nodes) of the structural elements.

The potential, kinetic, and constraint energies will be defined as functions of the generalized coordinates q_j , generalized velocities \dot{q}_j , and Lagrangian multipliers λ_i , respectively. Assembling the energies of the system into the Lagrangian L and then separating Lagrange's equation into two forms, for q_j and λ_i variables, gives

$$\frac{d}{dt} \left(\frac{\partial L}{\partial \dot{q}_j} \right) - \left(\frac{\partial L}{\partial q_j} \right) = f_j \quad (1)$$

$$\frac{d}{dt} \left(\frac{\partial L}{\partial \dot{\lambda}_i} \right) - \left(\frac{\partial L}{\partial \lambda_i} \right) = 0 \quad (2)$$

where Equation (1) yields equilibrium equations, some of which contain λ terms, and Equation (2) yields the compatibility equations for structural elements connected to the ground, rigid bodies, and plate elements.

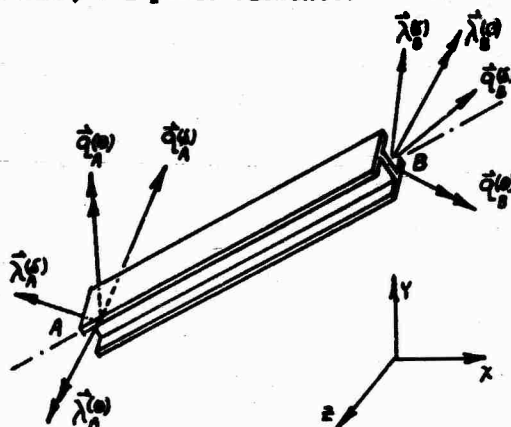


Fig. 1 Prismatic member element

In order to describe the physical contribution of a continuous mass distributed elastic member element, as shown in Fig. 1, it is convenient to take the scalar product of the average nodal loads vector λ at each end times their respective local response vectors q . The scalar product yields the potential energy of the continuous mass element as

$$U_e = \frac{1}{2} \{ \tilde{\lambda} \}^T \cdot \{ \tilde{q} \} \quad (3)$$

The load-response relationships, from modified theory, which describe the longitudinal, torsional, and flexural motion in the principal planes of the element are well known [7]. As an example the equations for longitudinal and torsional motion are given respectively as

$$AE \left(\frac{\partial^2 \eta_1(t)}{\partial s^2} \right) - \rho A \left(\frac{\partial^2 \eta_1(t)}{\partial t^2} \right) = 0 \quad (4)$$

$$GJ\left(\frac{\partial^2 \psi_1(t)}{\partial s^2}\right) - \rho I_P \left(\frac{\partial^2 \psi_1(t)}{\partial t^2}\right) = 0 \quad (5)$$

with similar, but somewhat more complex, relationships for bending in the two principal planes.

The time dependent solutions to the longitudinal, torsional, and bending equations of motion may be expressed in the normal mode form by

$$\eta_i(t) = \sum_{n=1}^{12} \eta_{in}^* C_n \delta_n(t) ; i=1,2,3 \quad (6)$$

$$\psi_i(t) = \sum_{n=1}^{12} \psi_{in}^* C_n \theta_n(t) ; i=1,2,3$$

where the C_n are the unknown nodal amplitudes of $\delta_n(t)$ and $\theta_n(t)$, and η_{in}^* , ψ_{in}^* are the shape functions of the normal modes. There are twelve C_n coefficients corresponding to the total number of degrees of freedom for both ends of the element. The solution to the equation of motion in the form of Eqs. (6) are also well known [7] and may be expressed by twelve scalar equations, representing the local coordinate response, at nodes A and B. These equations may be expressed in matrix form by the relationship

$$\{\hat{\eta}_A, \hat{\psi}_A, \hat{\eta}_B, \hat{\psi}_B\} = [G_{ij}] \{C_1, C_2, \dots, C_{12}\} \quad (7)$$

where the matrix $[G_{ij}]$ is a twelve by twelve non-symmetric matrix, containing terms represented by hyperbolic and trigonometric type functions.

The scalar components of the nodal load vector, in local coordinates, are given by relationships such as

$$\lambda_x(\delta) = AE \left(\frac{\partial \eta_1}{\partial s} \right) \quad (8)$$

$$\lambda_x(\theta) = GJ \left(\frac{\partial \psi_1}{\partial s} \right) \quad (9)$$

with similar relationships for shearing and bending. Taking the necessary derivatives of the vectors in Eqs. (6) and substituting into the equations of motion yields a column of twelve loads which are expressed in matrix form by

$$\{\hat{\lambda}_A(\delta), \hat{\lambda}_A(\theta), \hat{\lambda}_B(\delta), \hat{\lambda}_B(\theta)\} = [B_{ij}] \{C_1, C_2, \dots, C_{12}\} \quad (10)$$

The $[B_{ij}]$ matrix is a twelve by twelve non-symmetric matrix, similar to $[G_{ij}]$ matrix and also containing terms represented by hyperbolic and trigonometric type functions.

Solving for the C vector from Eq. (7), and substituting into Eq. (10), provides the loads as functions of the displacements and rotations in local coordinates

$$\{\hat{\lambda}_A(\delta), \hat{\lambda}_A(\theta), \hat{\lambda}_B(\delta), \hat{\lambda}_B(\theta)\} = [B_{ij}] [G_{ij}]^{-1} \{\hat{\eta}_A, \hat{\psi}_A, \hat{\eta}_B, \hat{\psi}_B\} \quad (11)$$

The matrix formed by $[B_{ij}][G_{ij}]^{-1}$ is defined as the symmetric, twelve by twelve, matrix of dynamic stiffness coefficients for the continuous mass element. Transforming η , ψ from the local coordinates to the inertial coordinates, and then substituting Eq. (11) into Eq. (3), provides the desired energy expression. The energy of a curved, prismatic, member element with a continuous mass distribution along the length is obtained by a procedure similar to the one used for the straight member element described above [8].

The kinetic energy K_m for a rigid body of arbitrary shape [9,10], shown in Fig. 2, may be expressed in matrix form as

$$K_m = \frac{1}{2} \{\dot{q}\}_m^T \cdot [M_m] \cdot \{\dot{q}\}_m \quad (12)$$

where M_m represents the mass and inertia tensor of the rigid body m , and \dot{q} implies time rate of change of q . If a rigid body is idealized as a point mass, with zero inertia tensor, then the kinetic energy may simply be expressed, in terms of the translational velocity of the node to which the mass is attached.

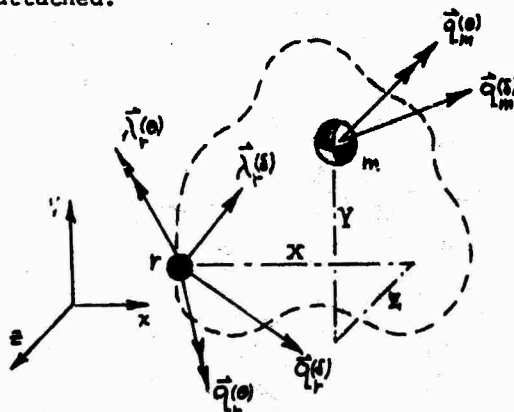


Fig. 2 A rigid body element

In addition to the potential and kinetic energies of the structural elements, there also exists a Lagrangian form of constraint energy [11] due to the internal loads acting at each node. Elastic compliance at an unconstrained node in space (i.e., a node free to displace and rotate within the bounds of the elastic properties of the structural elements connected to it), requires that the internal loads at the node be in equilibrium. Therefore, constraint energy is not required for the unconstrained node, and the normal six equations of equilibrium associated with displacement and rotation are sufficient to characterize the node properties. On the other hand, when a node is constrained to the ground, to the plates, or to the rigid bodies, it is essential to include the constraint energy which will yield unknown constraint load terms in the equilibrium equations, as well as in the associated compatibility equations for the node.

The form of constraint energy due to the load at node r on a rigid body as shown in Fig. 2, is given in terms of the local coordinates by

$$U_r = \{\vec{\lambda}\}_r^T \cdot \{[C_r][T_{mr}]^T\{\vec{q}\}_m + [C_r]\{\vec{q}\}_r\} \quad (13)$$

The matrix T_{mr} is a transfer matrix between the center of mass and node r , which relates the invariant distance components between the center of mass and node r . The constraint matrix C is given by

$$C = \begin{bmatrix} e(\delta) & | & \text{NULL} \\ \hline \text{NULL} & | & e(\theta) \end{bmatrix} \quad (14)$$

where each row of the two 3×3 submatrices $e(\delta)$ and $e(\theta)$ of Equation (14) contains the components of the local unit coordinate vector which is, preferably, in the direction of constraint. If a node is fully constrained, in the direction of inertial coordinates, then the constraint matrix C reduces to an identity matrix I . If a node is only partially constrained the rows of the 3×3 submatrices corresponding to the unconstrained local element directions become null or zero rows.

Another form of constraint energy, applied when a node A is constrained to ground g , is given by

$$U_g = \{\vec{\lambda}\}_A^T \cdot \{[C_g]\{\vec{q}\}_A - [I]\{\vec{w}\}_g\} \quad (15)$$

where w_g represents displacements and rotations of the ground in local

coordinates. A similar form of constraint energy for a node constrained to a plate element is given as

$$U_{ps} = \{\vec{v}\}_s \cdot ([I]\{\vec{q}\}_s - [C_s^*]^T\{\vec{w}\}_s) \quad (16)$$

where w_s represents the local displacements and rotations of the plate nodes, V_s represents the inertial coordinate components of the constraint loads λ_s , and C_s^* is a nonsymmetric constraint matrix made up of rows of direction cosine vectors whose components are in the direction of constraint normal to the plate or shell.

Assuming a harmonic solution, and employing the previous definitions of matrices, the coupled system of hybrid elastodynamic equations, derived from Equations (1) and (2) may be assembled in the following form

$$D_{uu}q_u + D_{ur}q_r + D_{us}q_s + D_{ug}q_g = f_u \quad (17)$$

$$D_{ur}^T q_u + D_{rr}q_r + D_{rs}q_s + D_{rg}q_g + C_r^T \lambda_r = f_r \quad (18)$$

$$D_{us}^T q_u + D_{rs}^T q_r + D_{ss}q_s + D_{sg}q_g + V_s = f_s \quad (19)$$

$$D_{ug}^T q_u + D_{rg}^T q_r + D_{sg}^T q_s + D_{gg}q_g + C_g^T \lambda_g = f_g \quad (20)$$

$$C_r q_r + C_r^T T_{mr}^T q_m = 0 \quad (21)$$

$$q_s = C_s^T w_s^* \quad (22)$$

$$C_g q_g = w_g \quad (23)$$

$$T_{mr} C_r^T \lambda_r - \omega_f^2 M q_m = 0 \quad (24)$$

where subscripts u, r, s, g, m represent unconstrained nodes, nodes constrained to the rigid bodies, nodes constrained to the plates, nodes constrained to the ground, and nodes located at the center of mass, respectively.

The symmetric M matrix is an uncoupled diagonal mass-inertia matrix, made up of the smaller 6×6 submatrices for each rigid body. The symmetric matrix D , consisting of dynamic stiffness coefficients, is obtained by differentiating the potential energy functions for prismatic members and is composed of $D_{uu}, D_{rr}, D_{gg}, D_{ur}, D_{ug}, D_{rg}$ in Eqs. (17) through (24) where D_{uu} represents coefficients for unconstrained nodes, D_{rr} represents

coefficients for nodes constrained to the rigid bodies, D_{gg} represents the ground constraints, and D_{rg} , D_{gg} , D_{rg} , represent the coupling matrices between the previous matrices. The transfer matrix T , is a non-symmetric matrix composed of smaller 6×6 non-symmetric transfer matrices (one for each node constrained to a rigid body). Finally, the C_r and C_g constraint matrices are non-symmetric matrices made up of smaller 6×6 submatrices as defined by Eq. (14), and pertain to nodes constrained to the rigid bodies and the ground, respectively.

Equations (17) through (24) provide the frequency response for any constrained spatial vibratory system. Viscous damping effects may be included through damping forces and will contribute imaginary elements to the elastodynamic equations. Applying steady state sinusoidal excitations of constant amplitude and varying frequency, ω_f yields the reduced frequency spectrum $H(\omega)$ of the generalized coordinates $q(t)$. The matrix reduction process is given in references [5] and [6]. Essentially the process consists of finding the $H(\omega)$ frequency response of the arbitrary shaped rigid body coordinates q_m and back substituting for the response of the q_u and q_r coordinates.

STEADY STATE, TRANSIENT AND RANDOM RESPONSE

Because of the transcendental nature of the elastodynamic equations, it becomes advantageous to operate in the frequency domain and use the Fourier integral approach rather than use the classical, and often popular, modal method to solve for general forced and random response. The frequency spectrum $H(\omega)$ of $q(t)$, obtained from the elastodynamic equation, acts as a transmissibility function and by the nature of its derivation, is generalized to any forcing function which may be obtained by the superposition of a number of harmonic forcing functions.

The transmissibility functions represent the coupled steady state solution for the complex structural configuration and are applicable to both the deterministic and nondeterministic areas. They include coupled elastic wave effects as well as the inertial effects of arbitrary shaped rigid bodies.

For the case of shock-impact loadings, the excitation spectrum $F(\omega)$ is obtained from the forward transform

of the forcing functions $f(t)$ by using a numerical "fast Fourier transform" technique. Multiplying the total transmissibility for a particular node by the force excitation spectrum yields the node response spectrum as

$$R(\omega) = H(\omega) \cdot F(\omega) \quad (25)$$

The time response $r(t)$ for a particular degree of freedom of a given node may be obtained by taking the reverse transform of $R(\omega)$ in Eq. (25) such that

$$r(t) = \frac{1}{2\pi} \int_{-\infty}^{\infty} R(\omega) e^{i\omega t} d\omega \quad (26)$$

Equation (26) therefore represents the transient response to any general forcing function $f(t)$, including shock-impact loadings. Numerous simple "fast Fourier transform" algorithms exist [12, 13, 14] which may be used to obtain the $F(\omega)$ and $r(t)$ functions. Determination of the velocity response $\dot{r}(t)$ requires only that the $R(\omega)$ transform be modified by the Fourier property for time differentiation which yields

$$\dot{r}(t) = \frac{1}{2\pi} \int_{-\infty}^{\infty} i\omega R(\omega) e^{i\omega t} d\omega \quad (27)$$

The velocity response provides a useful quantity for examining sound-structure interactions.

In describing the response characteristics of linear systems excited by random dynamic loadings, such as those encountered in random pressure fields, it is assumed that a given random excitation will have stationary and ergodic properties, and that a Gaussian random process will yield a Gaussian response. The response of such systems are most conveniently described by use of the power spectral density function. The power spectral density $P(\omega)$ of the elastodynamic configuration, at any frequency, is equal to the excitation spectral density $S_e(\omega)$ times the square of the absolute value of the transmissibility function $H(\omega)$, at that frequency, and is given by

$$P(\omega) = |H(\omega)|^2 S_e(\omega) \quad (28)$$

Integrating over the frequency range of interest yields the mean square displacement response of the structure as

$$\langle r^2(t) \rangle = \int_{\omega_1}^{\omega_2} P(\omega) d\omega \quad (29)$$

where ω_1 , and ω_2 represent the bandwidth limits of the system. In a manner similar to that used in the impact

excitation case, the mean square velocity response $\langle \dot{x}(t)^2 \rangle$ may also be obtained.

INTERNAL ELEMENT LOADS AND CORRESPONDING STRESSES

From the coupled frequency response $R(\omega)$ and transmissibility functions $H(\omega)$, it is possible to calculate spectrums of internal loads $V_i(\omega)$, and corresponding stresses, within the structural elements of the complex vibratory configuration by multiplying the static stiffness coefficient matrix S_{ij} of an individual element by its respective nodal response spectrums.

As an example consider the case of a prismatic member element with six degrees of freedom at each end (three translation and three rotation) whereby the resulting static stiffness coefficient matrix is a twelve by twelve array of constant coefficients. The relationship for the internal load spectrum is therefore given by

$$\{V_i'(\omega)\} = [S_{ij}] \cdot \{R_j(\omega)\} \quad (30)$$

Since the $R_j(\omega)$ is known from the solution of the elastodynamic equation, one may obtain $V_i(\omega)$ from Eq. (30). Similarly, by applying finite element techniques [15,16], one can obtain static stiffness coefficient matrices for plate elements and hence derive corresponding load-response spectral relationships for plate elements.

Transforming the load spectrums from inertial to local coordinates in the direction of the principal axes of the element, separates the loads into components which are parallel to the principal planes. In the case of a prismatic member element the transformed load spectrums represent the frequency dependent bending moments, shear forces, axial force and torque arising from the normal and shear stresses acting on plane cross-sections at the ends of the element. A treatment of the problem can therefore be given in terms of the stress resultants acting on each cross-section of the element rather than on unit stresses. A final transformation of the loads from the frequency domain to the time domain, via the numerical "fast Fourier transform" algorithm, provides the basis for recombining the bending moments, shear forces, axial force and torque to obtain the time dependent normal stresses and shear stresses acting on the cross-sections of the elements.

For the case of steady state excitations the maximum stresses obtained from the normal and shear stresses, may be compared to known experimental S-N (stress vs. number of cycles) curves to predict possible fatigue failure or damage. In general, however, the excitations which are of primary interest are those which are associated with the random, high-frequency, loading cases.

These cases normally include problems associated with sonically induced fatigue, noise transmission and the prediction of maximum likelihood, or probability, of first-excursion failures. An upper bound solution for the probability of a first-excursion failure can be obtained, by use of the generalized Chebyshev inequality, if the mean square values of the time dependant stresses or loads are known [17]. Employing a procedure similar to that used in determining the internal element loads for the steady-state case, and recalling the assumption that random excitations have stationary and ergodic properties, results in a set of spectral load, or stress, distribution functions which may be integrated over frequency range of interest to obtain the desired values of mean square loads or stresses. These values may then be compared to known failure criteria.

Another technique which was developed during recent years, and which provides a simple means for understanding and estimating significant properties of multimodal vibratory systems of the above nature, is the statistical energy analysis method [18, 19]. Basically, the method uses modal response and total average response properties to show that under certain conditions the steady-state mode to mode power flow is proportional to the difference between the time-average kinetic energies of the two modes. A primary reason for developing the statistical energy analysis method was that the use of classical methods, such as the modal method, for determining response of structures to broadband (high-frequency) excitation normally requires large amounts of computation due to the large number of modes that affect the total response in the band of interest. In addition, accurate determination of the shapes of the higher modes also presents difficulties along with other assorted problems, such as the inclusion of coupled wave and arbitrary shaped rigid body effects. Many of these problems have been minimized, or eliminated, by use of the elastodynamic statistical loads analysis technique.

CONCLUSION

To summarize, the hybrid elastodynamic formulation provides a consistent and effective technique for determining reactive loads and element stresses, as well as the steady state, transient, and probabilistic response characteristics, of complex structural configurations with general constraints. Symmetry and the partitioned

form of the elastodynamic matrices minimizes the storage and ill conditioning problem of large order, sparse matrices normally associated with such systems. Furthermore, the response to a general class of excitations has been greatly simplified by operating in the frequency domain and employing numerical fast Fourier transform techniques.

REFERENCES

1. J.S. Archer, "Consistent Mass Matrix for Distributed Systems," *Jl. of the Structural Division, A.S.C.E.*, Vol. 89, Aug. 1963, pp. 161-178.
2. H. Kolsky, *Stress Waves in Solids*, Dover Pub., New York, 1963.
3. R.M. Mains, "Comparison of Consistent Mass Matrix Schemes," *The Shock and Vibration Bulletin*, Bulletin 40, Part 4, Dec. 1969, pp. 1-16.
4. S.K. Tolani, R.D. Roake, "A Strain Energy Comparison of Discrete Modeling for Vibratory Continuous Systems," to be published in *ASME Trans. for Industry*, 1971.
5. K.J. Saczalski, T.C. Huang, "Elastodynamics of Complex Structural Systems," *Proc. of the 12th Midwestern Mechanics Conf.*, 1971, pp. 675-688.
6. K.J. Saczalski, T.C. Huang, "Coupled Response of Spatial Vibratory Structures Mounted to Isotropic Plate Elements," to be published in *ASME Trans. for Industry*, 1971.
7. T.C. Huang and C.L. Lee, "Free Vibrations of Space Framed Structures," *Proc. 11th Midwestern Mechanics Conf.* vol. 5, 1969, pp. 861-885.
8. L. Beitch, "Vibration Response of General Continuous Structures," *ASME Vibrations Conf.*, Paper No. 67 - VIRB - 44, 1967.
9. E.T. Whittaker, *A Treatise on the Analytical Dynamics of Particles and Rigid Bodies*, 4th Ed., Dover Pub., New York, 1944.
10. Yu Chen, *Vibrations: Theoretical Methods*, Addison-Wesley Pub., 1966.
11. C. Lanczos, *Variational Principles of Mechanics*, 3rd ed., Univ. of Toronto Press, 1966.
12. J.W. Cooley, et al, "The Finite Fourier Transform," *IEEE Trans. on Audio and Electroacoustics*, Vol. Au-17, No. 2, June 1969, pp. 77-85.
13. G.D. Bergland, "A Guided Tour of the Fast Fourier Transform," *IEEE Spectrum*, July 1969, pp. 41-51.
14. J.W. Cooley and J.W. Tukey, "An Algorithm for the Machine Calculation of Complex Fourier Series," *Math. Comput.*, vol. 19, Apr. 1965, pp. 297-301.
15. O.C. Zienkiewicz, *The Finite Element Method in Structural and Continuum Mechanics*, McGraw-Hill, New York, 1967.
16. J.H. Argyris, "Matrix Analysis of Three-Dimensional Elastic Media-Small and Large Displacements," *AIAA Journal*, January 1965, Vol. 3, No. 1, pp. 45-51.
17. Y.K. Lin, *Probabilistic Theory of Structural Dynamics*, McGraw-Hill, Inc., New York, 1967.
18. E.E. Ungar, "Statistical Energy Analysis of Vibrating Systems," *Trans. ASME J. Eng. Ind.*, Nov. 1967, pp. 626-632.
19. R.H. Lyon, "What Good is Statistical Energy Analysis, Anyway?" *Shock and Vibration Digest*, Vol. 2, No. 6, June, 1970.

STRUCTURAL ANALYSIS

NASTRAN OVERVIEW: DEVELOPMENT, DYNAMICS APPLICATION, MAINTENANCE, ACCEPTANCE

J. Phillip Rancy, Head, NASTRAN Systems Management Office and
Deane J. Weidman, Aerospace Engineer
NASA Langley Research Center
Hampton, Virginia

(U) The historical development of the NASTRAN system for structural analysis is briefly reviewed and NASTRAN's present capabilities for dynamic analysis are presented. Specific applications of NASTRAN to vibrations and dynamic response phenomena are illustrated, using typical engineering problems which were among those presented at the first NASTRAN Users' Colloquium, Langley Research Center, September 13-15, 1971. Finally, plans for the centralized maintenance and future development of NASTRAN are summarized. Emphasis is placed on NASA's intention to maintain NASTRAN as a valuable national capability.

INTRODUCTION

NASTRAN (NASA STRUCTURAL ANALYSIS) was developed by NASA to provide the capability for integrated analyses of complex aerospace structures. Until the NASTRAN concept emerged there was a proliferation of limited purpose, often proprietary, structural analysis programs. Usually these programs were not user oriented, were operational on only one type of computer, or were otherwise accessible to NASA only at high cost or unusual inconvenience or both. NASTRAN was designed to provide NASA with a complete, essentially machine-independent facility for detailed structural analysis encompassing statics, buckling, vibration, transient dynamics, and random response.

The purpose of this paper is to briefly review the development of NASTRAN, to highlight applications of NASTRAN in the area of vibration and dynamics, to discuss requirements and plans for maintenance and future development, and to summarize user acceptance of the NASTRAN system.

NASTRAN DEVELOPMENT*

NASTRAN was first conceived in 1965 when a committee of NASA specialists surveyed the existing structural computer programs in the aerospace industry. No reasonable overlay of existing programs met all of the NASA require-

*Most of the material presented in this section was borrowed from references 1 and 2 which should be consulted by the reader who desires more detail than given here.

ments so the committee recommended the development of a new state-of-the-art, applications program for integrated structural analysis of complex aerospace structures. After some preliminary analysis and technical evaluation, development of NASTRAN was begun in July 1966 by an industry team consisting of Computer Sciences Corp., the Baltimore Division of Martin-Marietta, The MacNeal-Schwendler Corp. and, later, Bell Aerosystems Company, all under the direction of the Goddard Space Flight Center.

A preliminary version of the statics portion of the program was delivered to NASA Centers in 1968 and delivery and installation of the complete system began in 1969. Release to industry came in November 1970.

Design Objectives

Since NASTRAN was intended for general use it had to satisfy a wide spectrum of requirements. In order to compete with other programs, it had to be efficient, versatile, and convenient to use. It had to be standardized to permit interchange of input and output among different users and structured to permit future modification and extension to new problem areas and to new computer configurations without major redevelopment. Specifically, NASTRAN was desired to be machine-independent for the user. Problem size was to be independent of machine size and a wide range of user-oriented features were required including plotting capability and well-organized documentation.

Most of the design objectives have been achieved. The program is machine independent from the user's standpoint; however, there are some system-dependent computer characteristics. The remainder of this section describes the design features of greatest interest to the vibrations and dynamics analyst.

System Capability

The range of application of the NASTRAN system extends to almost every kind of structure and to almost every method of fabrication. Structural elements are provided for the specific representation of the more common types of construction, including rods, beams, shear panels, plates, and shells of revolution. More general types of construction are treated by combinations of these elements and by the use of so-called general elements. Control systems, aerodynamic transfer functions, and other nonstructural features can be incorporated into the structural problem.

The range of analysis types in the program includes: static response to concentrated and distributed loads, to thermal expansion and to enforced deformation; dynamic response to transient loads, to steady-state sinusoidal loads, and to random excitation; determination of real and complex eigenvalues for use in vibration analysis, dynamic stability analysis, and elastic stability analysis. The system includes a limited capability for the solution of nonlinear problems, including piecewise linear analysis of nonlinear static response and transient analysis of nonlinear dynamic response.

Rigid Formats: Twelve prepackaged programs called rigid formats are presently available in NASTRAN and provide the desired capacity for integrated analysis; that is, the capability to compute the response of the same finite element model to every type of static and dynamic loading conditions. The rigid formats include the following capability:

- A. Static Analysis
 1. Basic static analysis
 2. Static analysis with inertia relief
 3. Static analysis with differential stiffness
 4. Piecewise linear analysis
- B. Elastic Stability Analysis
 5. Buckling
- C. Dynamic Analysis
 6. Normal modes analysis
 7. Direct complex eigenvalue analysis
 8. Direct frequency and random response analysis
 9. Direct transient response analysis
 10. Modal complex eigenvalue analysis
 11. Modal frequency and random response analysis
 12. Modal transient response analysis

Direct Matrix Abstraction Program (DMAP):

If an analyst wishes to conduct an analysis not provided for in the rigid formats, he can organize his own problem steps by using a language, called DMAP, contained within NASTRAN. Certain NASTRAN control features, namely the executive control, the input file processor, and the output file processor are made to operate automatically with the analyst's DMAP program, so that the user need not concern himself with core assignments and secondary storage assignments. The user need only specify the sequence of matrix operations and the module selections needed to solve the mathematical formulation of his particular case. He arranges for the forms of his input and output and makes provision for problem recovery and restart. In fact, DMAP need not necessarily pertain to structures; it can treat problems in any discipline so long as matrix formulation is employed. The other principle option in using DMAP is the instance of a user being essentially satisfied with a rigid format but wanting to modify or augment its operation. It is possible to make a DMAP alteration to a given rigid format.

Finite Elements: The structure to be analyzed is represented using elastic finite elements available in NASTRAN. At the present time the following elements are available:

One-dimensional
rod, tube, bar

Two-dimensional
shear panel, twist panel, membrane,
nonhomogeneous plate, homogeneous plate,
sandwich plate

Three-dimensional
conical shell, toroidal shell, solid of
revolution

General
general element, direct matrix input

Scalar
spring, mass, damper, nonlinear

The material properties associated with the above-listed elements are given in Table 1.

Eigenvalue and Dynamics Problems: Since NASTRAN is designed primarily for solving large-order matrices, several different situations in eigenvalue analysis arise in which the analyst wishes to obtain one or more of the following:

- (1) A few roots of a large-order matrix
- (2) All the roots of a large-order matrix
- (3) A few roots of a complex matrix

Procedures are included in NASTRAN for the preceding information to be obtained in solving buckling and vibration problems.

Various techniques are used to obtain eigenvalues. Root tracking techniques are used

TABLE 1

Material Properties Associated with NASTRAN Structural Elements

Elastic moduli	Thermal moduli	Mass
Isotropic Orthotropic Anisotropic Temperature dependent Stress dependent	Isotropic Orthotropic Anisotropic Temperature dependent	Structural density Nonstructural mass Lumped properties Coupled properties Weight Center of gravity

to obtain a few roots of large matrices - both real and complex. Two root tracking schemes are available. One is the well-established determinant method; the other is a method formerly used for refinement but now organized as a self-contained technique called the inverse power method with shifts. One advantage of this method is that a root can be obtained with high accuracy regardless of its order of appearance in frequency. It is well suited for the determination of bifurcation buckling loads and modes.

To obtain a large number of roots, a rotational method called the Givens/Q-R method is available wherein all roots are obtained simultaneously. The Givens method is used to tri-diagonalize real matrices only, and the Q-R method is used to extract the eigenvectors.

The methods of eigenvalue solution and type of output are listed in table 2.

There are several options available to the analyst when solving dynamics problems. Because dynamics problems usually require longer running times on the computer than statics problems the analyst will quite often want to reduce the number of degrees of freedom of his problem from that which was formulated for a statics solution.

The Guyan reduction method is one way of accomplishing this, or the analyst may choose to remodel his structure using fewer degrees of freedom. Solution of the dynamic differential equations can proceed by the Lagrangian modal approach if a sufficient number of modes were previously obtained from eigenvalue analysis, or direct integration can be carried out using finite differences in time.

There are essentially four different types of dynamics problems that can be solved - transient response, frequency response, random response, and elastic structure-control system stability. table 3 outlines NASTRAN structural dynamics problem analysis, it gives the NASTRAN options for solutions of dynamics problems, lists the basic types of dynamics problems and shows typical applications in each problem area together with list of inputs and the outputs available from the NASTRAN program.

Plotting: The NASTRAN program makes use of a broad variety of plotting capability on various types of plotters. The equipment for which NASTRAN was designed to interface are those routinely employed by the NASA Centers. Three types of plotters are included: table, microfilm, and incremental plotters. There is also a software package included in NASTRAN called

TABLE 2.- Eigenvalue Analysis

Root Tracking	Rotational
Determinant method Inverse power with shifts method	Givens/Q-R method
Output Obtainable from Eigenvalue Analysis	
Modal frequencies Generalized mass Mode shape normalization Generalized mass Maximum deflection Arbitrary component Modal plots	

TABLE 3
Structural Dynamics Problem Analysis

NASTRAN Options for Solution of Dynamics Problems Option to reduce degrees of freedom Option to augment with attached systems Option to specify damping Option for modal method or direct integration				
Basic Types of Dynamics Problems	Transient Response	Frequency Response	Random Response	Stability
Typical Application Type of input	DYNAMIC LOAD Grid point force amplitude Grid point force phase Time delay Initial conditions Integration time step Nonlinear scalar	SINUSOIDAL LOAD Amplitude Phase Frequency range	AUTO-SPECTRUM OF GRID POINT LOAD Frequency range TRANSFER FUNCTION	CONTROL SYSTEM Sensors Signal conditioners STRUCTURAL TRANSFER FUNCTION DYNAMIC LOAD Grid point force amplitude Grid point force phase Time delay Initial conditions Integration time steps Nonlinear scalar
Output Available	Grid point displacement, velocities, accelerations Grid point applied loads Element forces, stresses Deformation plot Curve plot	Displacement, velocity, acceleration, force, stress Transfer function General frequency response Curve plot	Frequency range Auto-spectrum Auto correlation Curve plot	Grid point displacements, velocities, accelerations Grid point applied loads Element forces, stresses Deformation plot Curve plot

the General-Purpose Plotter, which has reduced the commands to generic types. It needs only a small additional plotter-dependent translation of these generic commands to make it applicable to a plotter of any manufacture.

Two broad types of plots can be obtained - structure and curve plots.

Structure plotting: The pictorial representation of the structural analytical model can involve as large or as small a portion of the specimen as the analyst decides. He may call for any of orthographic, perspective, or stereoscopic projections. The orientation from which the essentials can best be viewed are selected and then automatically calculated. With deformed structures the scaling of the grid point displacements, which are ordinarily

in mils, is adjusted to give a size that will make the behavior quite evident.

Curve plotting: Instead of looking at total deformation of the structure, it may be more meaningful to explore time histories or frequency histories of element behavior and/or grid point behavior, such as stress, velocity, or autocorrelation. Coordinate lines can be arranged in almost any manner with regard to position, graduations, and labels.

More than one curve can be drawn on a given plot, and more than one plot can appear on a page.

Documentation: During the development of NASTRAN a deliberate attempt was made to assure that the program is well documented. As a result the documentation that is provided should

contain the answers to most of the questions that could be raised by the theoretician, programmer, and user, since each has a manual designed specifically for his needs. To provide for updating, the manuals are not bound but are punched for insertion in a three-ring binder. The separate manuals that are available are:

- (1) NASA SP-221, NASTRAN Theoretical Manual (ref. 3)
- (2) NASA SP-222, NASTRAN User's Manual (ref. 4)
- (3) NASA SP-223, NASTRAN Programmer's Manual (ref. 5)
- (4) NASA SP-224, NASTRAN Demonstration Problem Manual (ref. 6)

APPLICATIONS FOR DYNAMIC ANALYSIS

It is the purpose of this portion of the paper to introduce the potential user, particularly the dynamicist, to the capabilities of the NASTRAN system for dynamic analysis. The compendium of papers from the first NASTRAN Users' Colloquium (ref. 7) includes a typical subset of recent applications to dynamics problems. To this end the six typical applications which follow have been selected. All but the wave propagation problem are discussed in complete papers included in reference 7. The NASTRAN results for the wave propagation problem were computed by the authors to supplement data presented in reference 8. For convenience of the reader who may wish to refer to the original papers, physical units have been left as presented in references 7 and 8.

Wave Propagation

A schematic representation of the test apparatus is shown in figure 1. A clamped-clamped beam was loaded by the impulsive impact of 1/4 in. steel ball at its center. The actual displacements were measured by holographic means as described in Appendix D of reference 8. From a set of impact holograms, an experimental history of displacement was developed.

Essentially a "traveling wave" type of displacement pattern is evident, with an amplitude variation due to the time dependence of the actual loading. In figure 2, the transverse deflection shapes of the beam at $t = 51 \mu\text{sec}$ are shown. The time variation of the loading was assumed to be sinusoidal with a half-period of $30 \mu\text{sec}$ and an impulse of $2.92 \times 10^{-4} \text{ lb-sec}$. The displacement results were computed using both NASTRAN and a Drexel University developed computer code based on the method of characteristics called MCDIT 21. The NASTRAN results are nearly coincident with those produced by the method-of-characteristics approach with only slight differences near the wave front. Near the wave front the differences may be attributed to the fact that MCDIT 21 employs Timoshenko beam theory, whereas the NASTRAN model included transverse shear effects but neglected rotatory inertia. NASTRAN was found to be competitive with the special

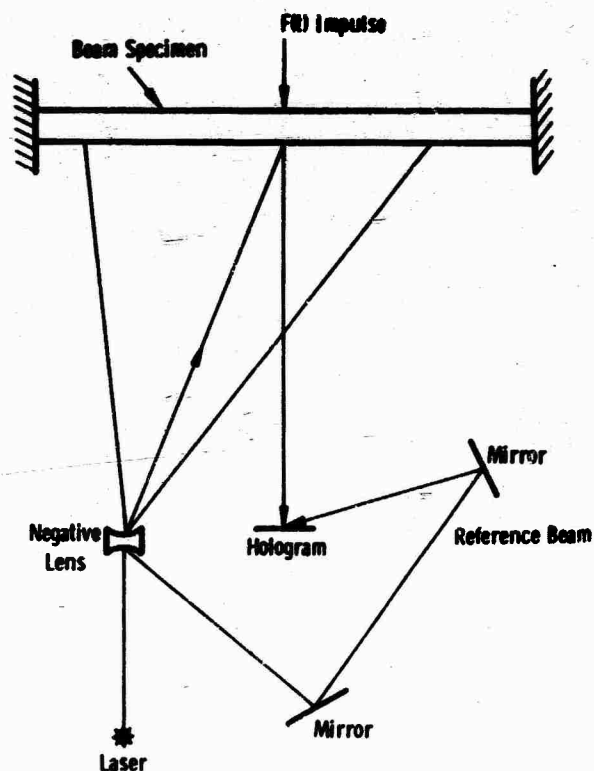


Figure 1.- Schematic of apparatus for transverse wave experiment

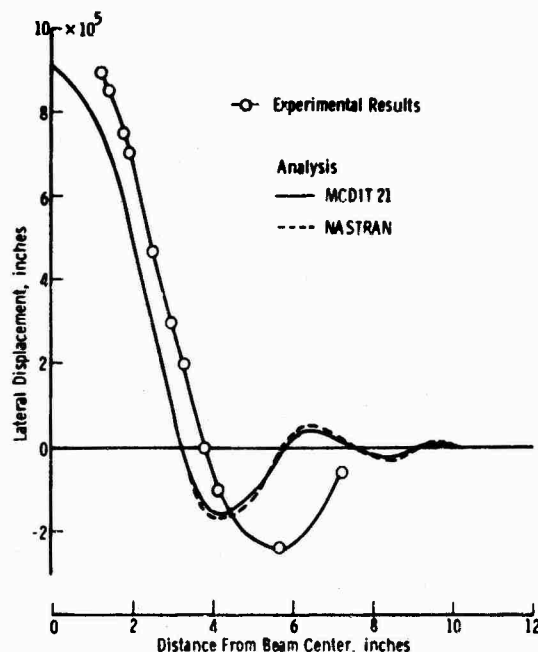


Figure 2.- Beam response at $t = 5.1 \times 10^{-5} \text{ sec}$ due to impact of 1/4-in. steel ball.

purpose program for this application and, in addition, the versatile plotting capability of NASTRAN allowed rapid interpretation of the results.

Space Shuttle Booster Analysis

The space shuttle structure has been analysed with NASTRAN through a series of changes in design and configuration. As the structure became better defined, more refined analytical models were developed and analyzed, thus allowing analytical results to keep pace with design alterations.

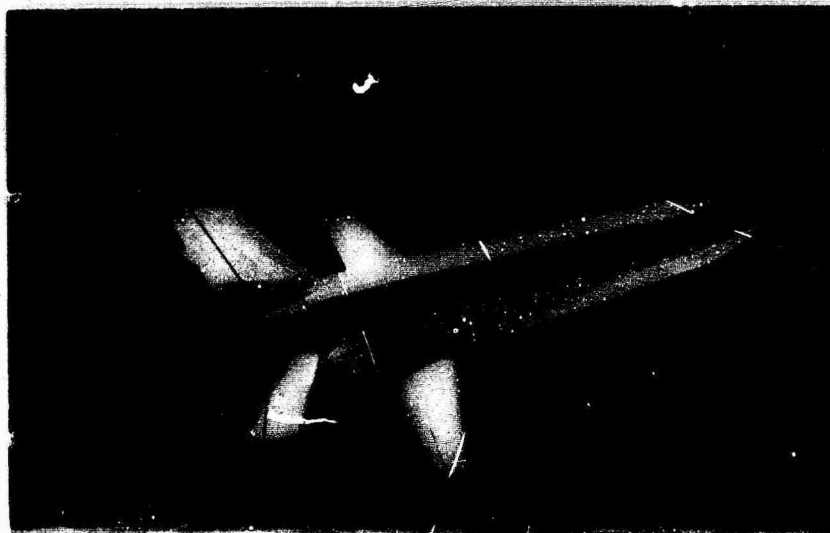
A typical space-shuttle, booster-vehicle design is shown in figure 3. This configuration has a large vertical tail and a relatively small tapered wing near the rear quarter-point of the fuselage. This structural design was idealized originally with beam elements, and eventually as a beam fuselage with plate-type aerodynamic surfaces, as shown in figure 4 which shows a wing-torsional mode shape, as well as showing a motion similar to the first bending mode of the horizontal tail. Note the rigid element definition of the orbiter and the flexible beam definition of the booster fuselage. From these results, an adverse coupling effect was found to exist. To evaluate the effectiveness of the fuselage structural redesign initiated to reduce this coupling, a detailed structural model of the booster fuselage was developed for the next configuration, a delta wing version as shown in

figure 5; it has a small canard forward on the fuselage as well as a large delta wing below the fuselage at the rear. Notice that no horizontal tail is needed in this design. While analyzing the static response of this structure, the design parameters became sufficiently defined to allow a detailed dynamic model as shown in figure 6, with a greatly increased booster grid definition. The orbiter is still defined as a simple beam structure and will be incorporated with this booster model for final analysis of the coupled configuration. Using this model, the dynamic response motions at each of the points on this model can be obtained similar to that shown in figure 5 for the simpler model. Additional information on these structures can be found in reference 7a.

Acoustic Analysis of the Pressures in a Rocket Motor Cavity

This application illustrates the use of NASTRAN for a nonstructural (acoustic) problem with a minimum of additional analysis (see ref. 7b for the theoretical derivation).

In solid fuel rockets an interior cavity is usually provided to allow the necessary optimum surface area of combustible material. In fact, a rather elaborate art of cavity and slot shaping has developed. Of important concern is the possibility of having pressure "instabilities" or pulses that will seriously affect the engine's operation. A typical example of a relatively simple slotting arrangement for the Minuteman II



Reproduced from
best available copy.

Figure 3.- Straight wing configuration.

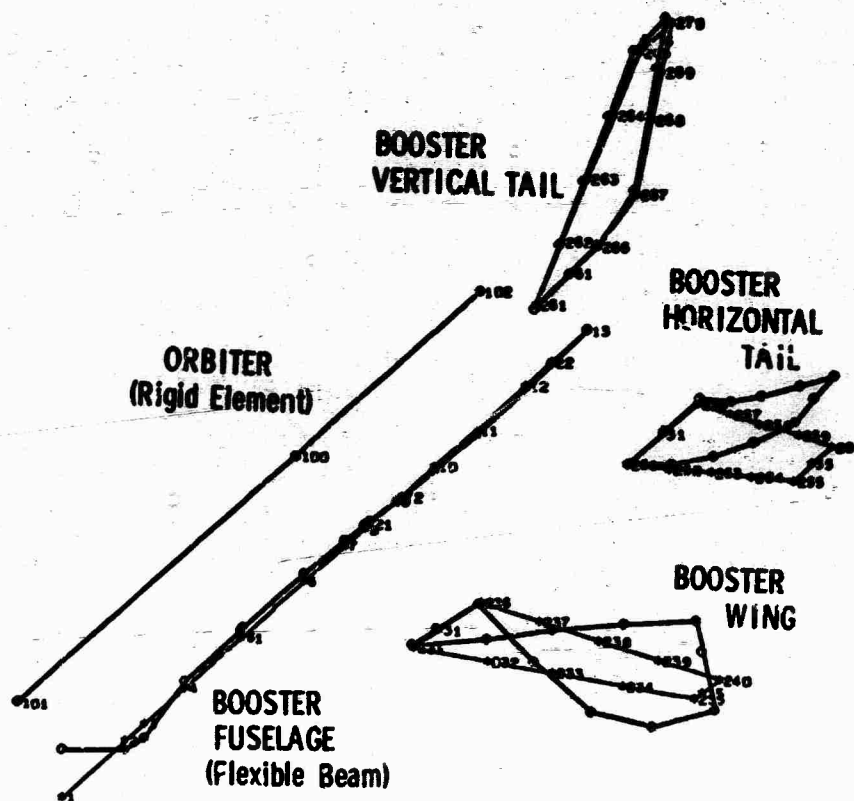


Figure 4.- Wing-torsion vibration mode shape for configuration of figure 3.

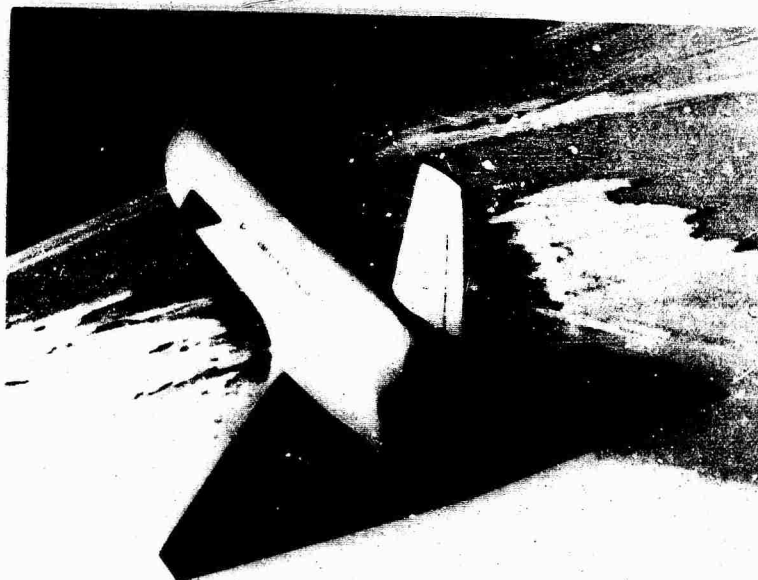


Figure 5.- Delta wing configuration.

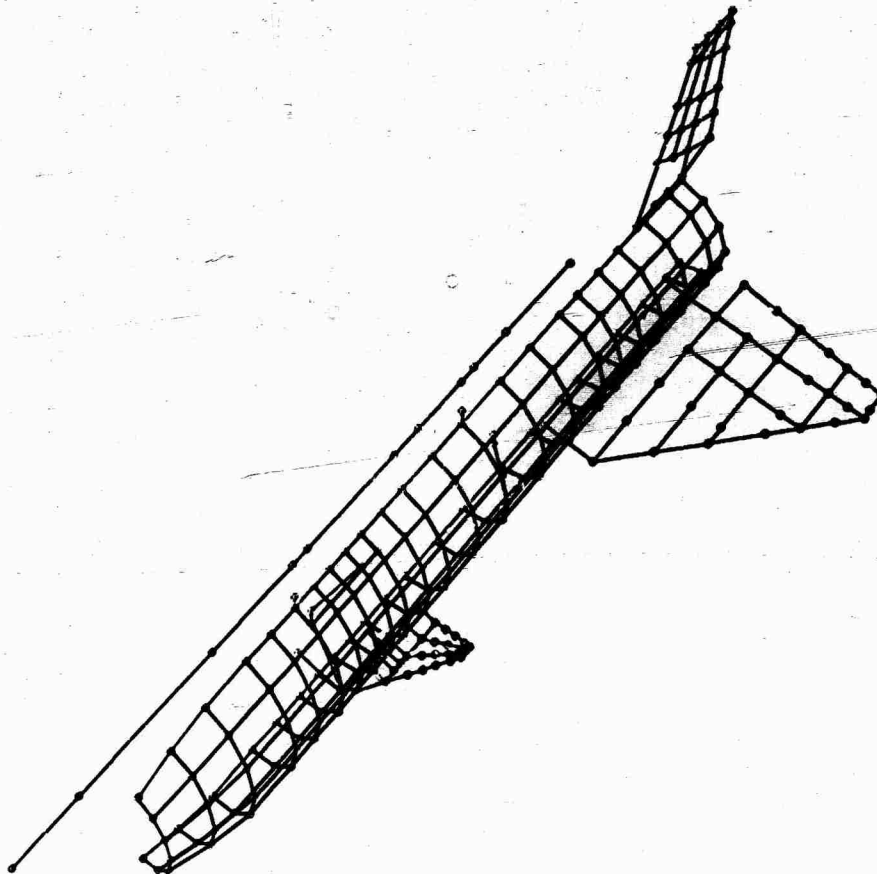


Figure 6.- Detailed dynamic model for delta wing version of figure 5.

missile is shown in figure 7. This figure shows a finite element model of the interior of the propellant cavity, which has a central cylindrical cavity. Four slots of constant width (shown shaded in the figure with conically flared cavities near the aft end) are spaced at 90° intervals around the central cavity. Another example of a more involved slotting geometry is shown in figure 8 for a Poseidon rocket motor with 12 slots spaced around a central cavity. The important fact to note is the large number of slots in this cavity, as well as the usual nonaxisymmetric character of these cavities. After a review of the basic equations for internal fluid flow, it was observed that they are similar to the equations for structural analysis, with the displacement and internal forces considered to be pressures and fluid accelerations, respectively. Thus, when the mode shapes and frequencies of these cavities are calculated, the mode shape becomes the pressure distribution in the cavity at that resonant frequency. The natural frequencies of the Poseidon rocket cavity as well as the pressure distributions or

"mode shapes" in the cavities at these frequencies are shown in table 4. The first six modes for each of the lowest two harmonics of the pressure distribution in the cavity have been calculated and compared with the experimental modes. Vibration modes are determined for two distinct times; one is the original rocket cavity before burn, and the other corresponds to 3 inches of propellant burned off of every exposed surface. The agreement in frequency between the NASTRAN results and the experimental values is very good, and NASTRAN further provides an insight into the character of the pressure distribution or mode shape associated with each natural frequency that was not observed experimentally.

Dynamic Analysis of an Electronic Assembly

The SKYLAB workshop structure includes an Experimental Support System (ESS) which contains several articles of electronic gear (see fig. 9 included from ref. 7c). This equipment must withstand a multitude of applied loads and accelerations. Therefore, the dynamic behavior of these

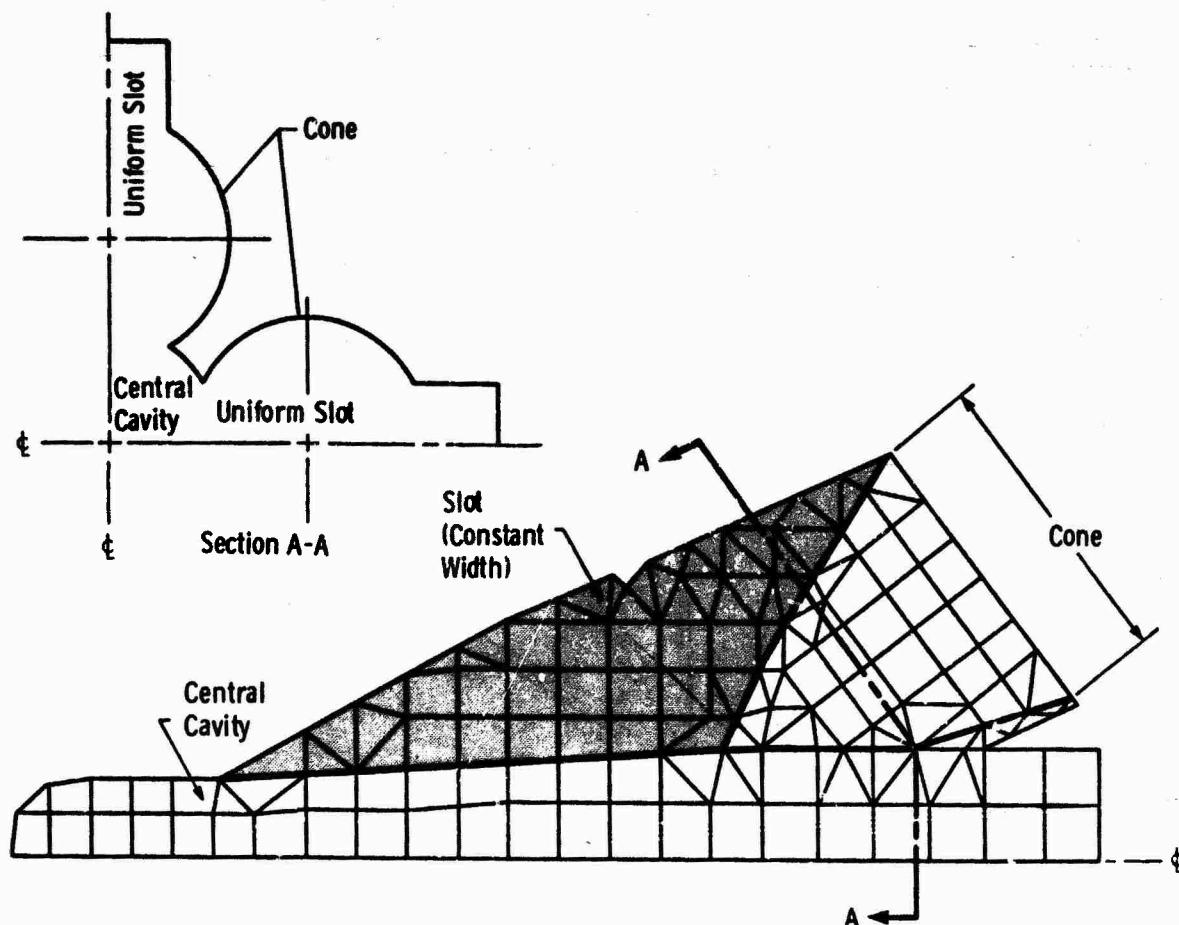


Figure 7.- NASTRAN model of propellant cavity of slotted segment of Minuteman II, Stage III, solid rocket motor.

electronic assemblies should be analyzed. A typical finite element model of one of the component parts is shown in figure 10. This structure is the primary power supply unit which is located in the lower left-hand corner of figure 9. In figure 10, the model consists of 156 plate elements that are numbered on this plot by the NASTRAN system. The dynamic response of the power supply was determined using a reduced number (39) of degrees of translational freedom as indicated by the 13 triangular symbols. Structure plots such as shown in figure 10 are very useful in verification of input data accuracy.

Using the structural model of the primary power supply as a typical example, the natural mode shapes for three typical modes are shown in figure 11. The mode shapes plotted by NASTRAN show the deformed mode shape superimposed on the undeformed shape for comparison. These plots can be used to check for mode shapes with large distortion for this assembly. The mode shapes were used to determine (by a modal method) a typical acceleration Power

Table 4.- Natural Frequencies of the Propellant Cavity for the Second Stage Poseidon Motor Cavity

		Frequency (Hertz)			
		0 Burn		3 in. Burn	
Harmonic (n)	Mode	NASTRAN	Experimental	NASTRAN	Experimental
0	1	308.1	398	324.0	322
	2	645.0	645	678.3	689
	3	962.0	962	1039.2	1051
	4	1422.0	1422	1430.8	1425
	5	1769.0	1728	1830.9	1831
	6	2010.8	2130	1994.4	
1	1	835.1		737.8	
	2	1313.4	1216	833.9	868
	3	1659.1	1620	1344.0	1349
	4	1832.8	1798	1558.2	1552
	5	2105.7		1812.5	
	6	2236.8		2130.1	2094

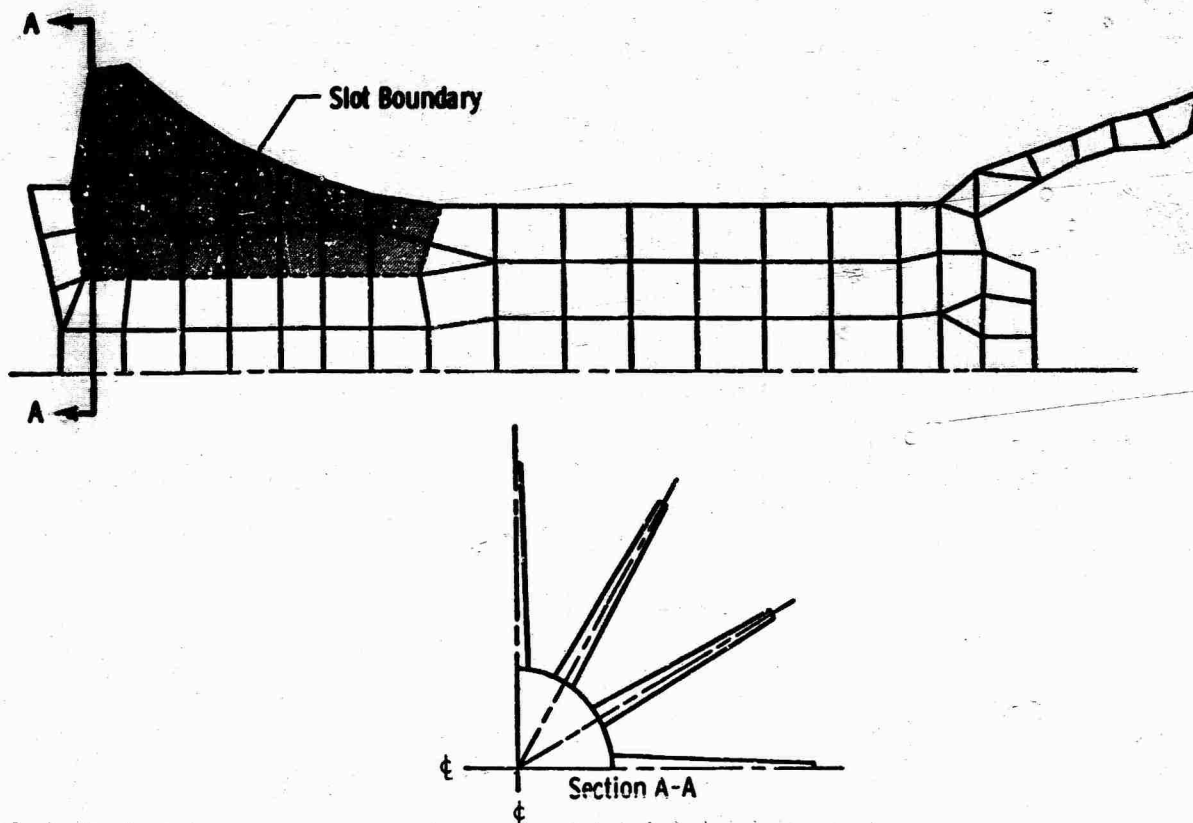


Figure 8.- NASTRAN model of propellant cavity of slotted segment of second stage Poseidon solid rocket motor.

Spectral Density (PSD) for a specific loading as shown in figure 12. From data of this type the response characteristics of all electronic packages can be determined and reviewed for possible undesirable dynamic response behavior.

Random Loading of Shells

The NASTRAN model of the structure analyzed in this example is shown in figure 13; this typical aerospace vehicle-type structure consists of a ring- and stringer-stiffened cylindrical shell with simply supported boundaries. Six degrees of freedom are associated with each interior grid point and three degrees of freedom with grid points which lie on the boundary, resulting in a total of 360 degrees of freedom.

Due to tenfold symmetry of the structure and its deflections under loading, only the location of grid points 2, 3, and 4 (see fig. 13) are needed to completely define the deflected mode shape of the structure at any specific time. The distributed random loading applied in this example was a simulated complex turbulent boundary layer pressure field and is fully discussed in reference 7d.

The natural mode shapes and frequencies for this structure were computed and are listed in table 5. Due to structural symmetry, only 7 distinct modes are present in the 12 that were found in the prescribed frequency range (100 to 300 Hz). Applying the desired random loadings, the power spectral density of the radial displacements were computed and are shown in figure 14. The peaks in these PSD's are all directly traceable to natural frequencies of the structure. Note the absence of the $m = 2$ modes (as shown in table 5) from the PSD of grid point 4. These modes have nodal lines that pass directly through this point exactly at the center of the shell and do not affect its response. The results of this analysis indicate the general applicability to dynamic response problems involving random loads.

Coupled Fluid-Structure Dynamical Modeling

An ingenious application to aircraft hydraulic system modeling has been demonstrated by Langley Research center personnel. A NASTRAN model of a portion of the F-14 hydraulic system (see fig. 15) was analyzed. The elastic properties of the piping wall were of major interest and could

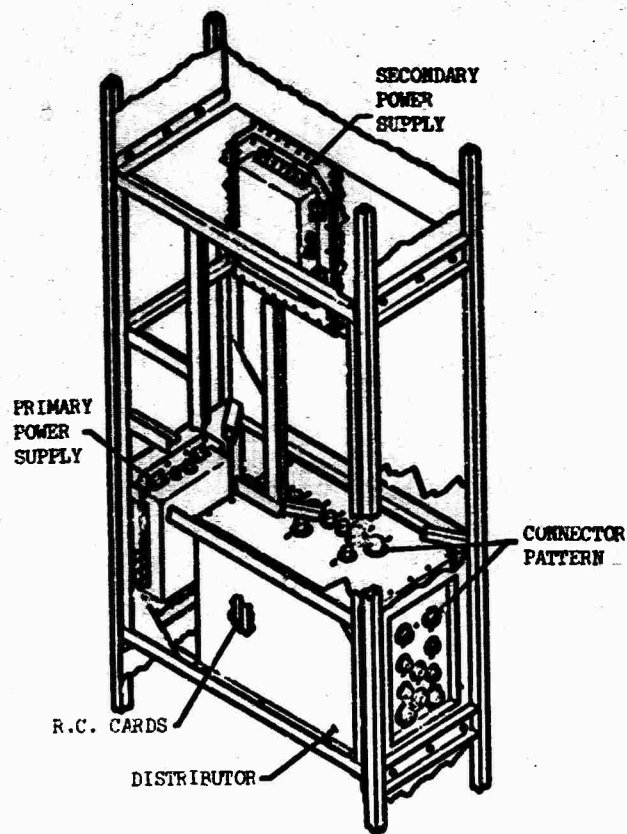
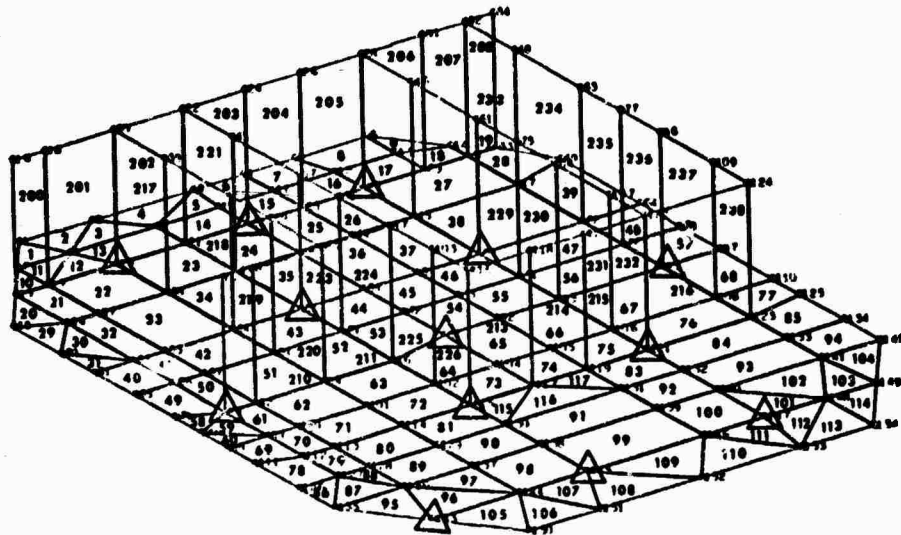
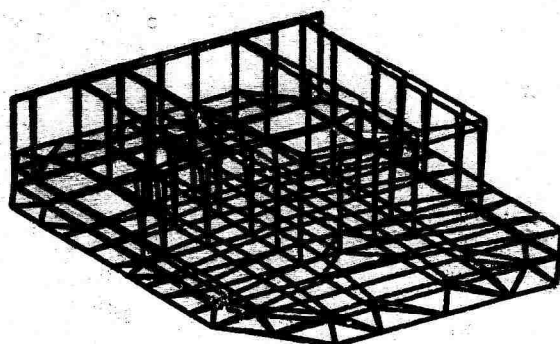


Figure 9. ESS side rails, enclosure, and electronic assemblies.

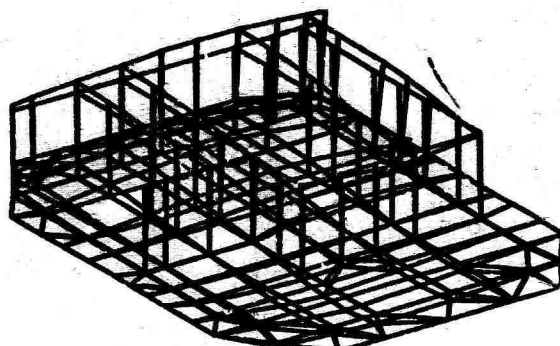


△ DYNAMIC COORDINATES - 3 Translational Degrees of Freedom

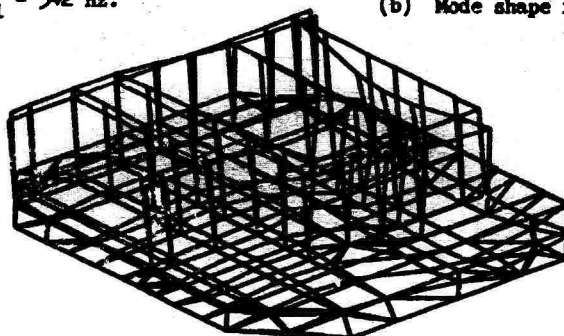
Figure 10.- Power supply finite element model with dynamic coordinates.



(a) Mode shape for $f_1 = 542$ Hz.



(b) Mode shape for $f_2 = 1295$ Hz.



(c) Mode shape for $f_3 = 1600$ Hz.

Figure 11.- Power supply mode shapes.

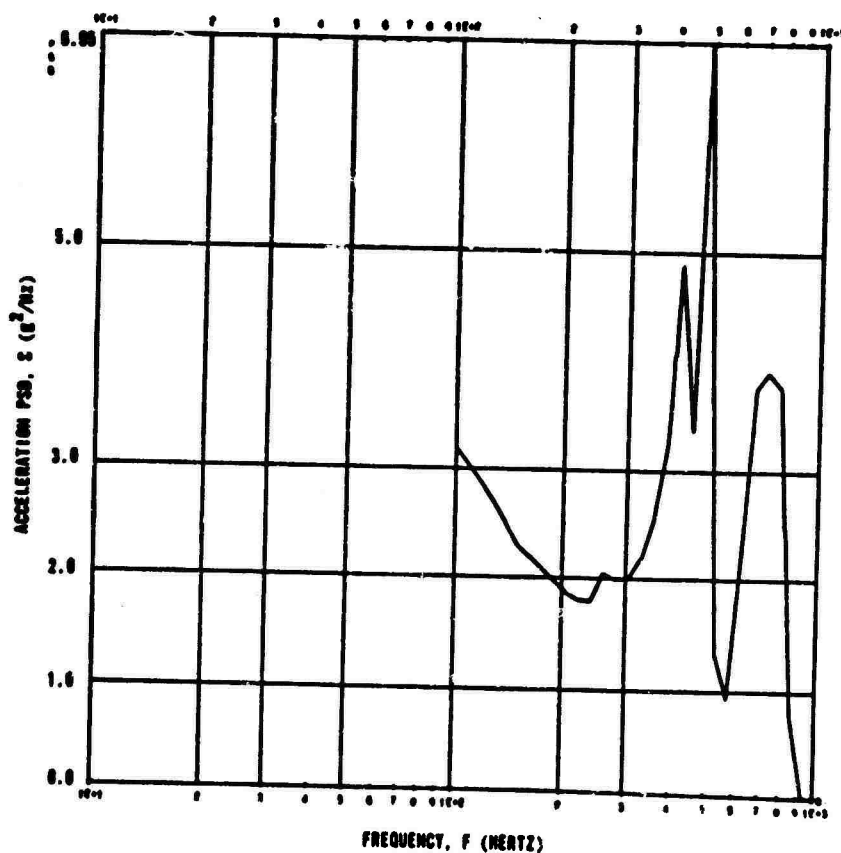


Figure 12.- ESS enclosure, PS No. 1 acceleration PSD response for HI random vibration criteria (flight axis).

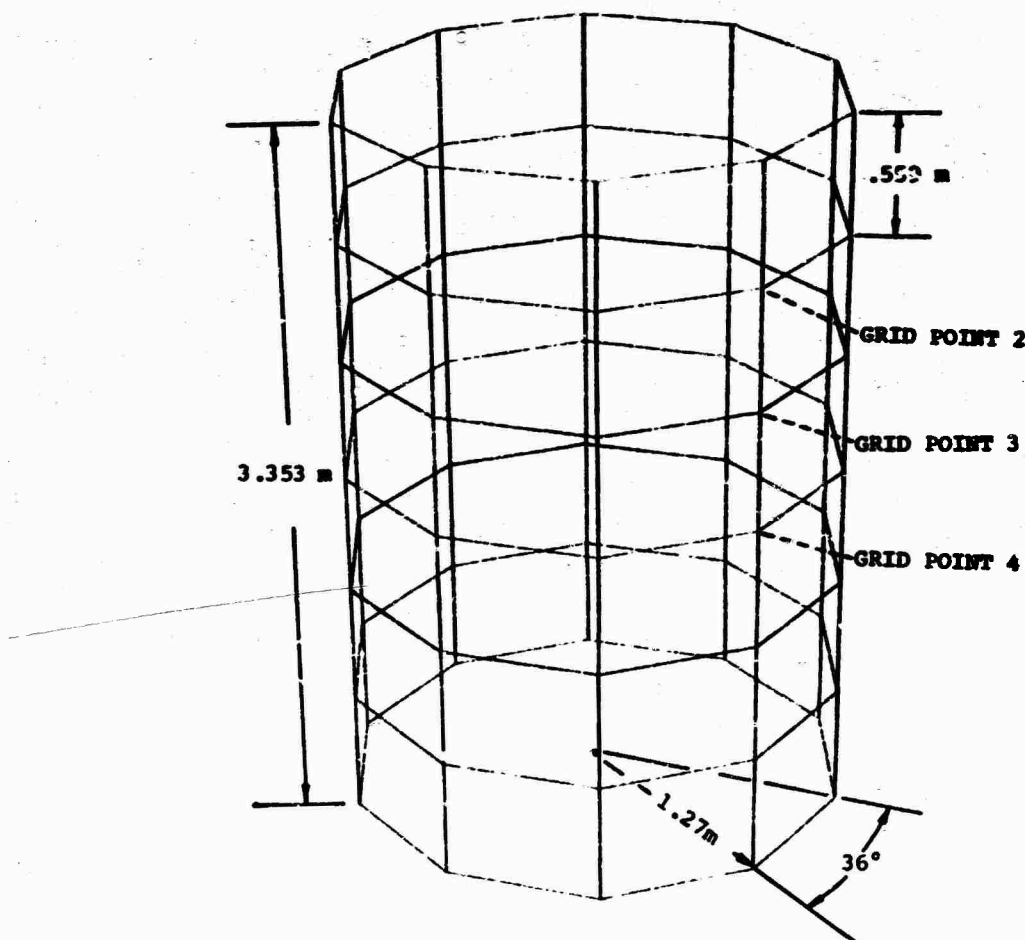


Figure 13.- Shell model for random loading analysis.

Table 5.- Modal Frequencies of Stiffened Simply Supported Cylindrical shell.

n	m	Frequencies
4	1	154.4, 154.4 Hz
3	1	149.8, 149.8 Hz
5	1	170.2 Hz -
2	1	187.5, 187.5 Hz
4	2	258.4, 258.4 Hz
6	1	- -
5	2	259.2 Hz -
3	2	- -
6	2	- -
1	1	280.4, 280.4 Hz

n number of circumferential waves
m number of axial half waves

not be neglected. The section of pipe shown at the top of figure 15 is idealized, as shown at the bottom of the figure, with the pipe itself defined as bar elements with bending stiffness and the fluid defined as a bar element with zero bending stiffness but possessing both a bulk modulus and a fluid density. Grid points 1-5 are references for the pipe elements and grid points 6-10 are references for the fluid elements. Constraint equations are written between corresponding grid points to keep the fluid constrained within the pipe, but allowing relative axial motion between the two. With this approach hydraulic systems can be analyzed as simple structures for a wide variety of analyses; that is, static load cases, normal mode cases, frequency response cases, etc. As an example of this general applicability, the standpipe structure shown in figure 16 was analyzed under a sinusoidally varying pressure pulse with a frequency of 485 Hz applied to the left-most end of the structure. The vertical standpipe shown has a natural frequency near 485 Hz, and the lateral displacement of the pipeline (as shown in fig. 16) is seen to be much larger for the

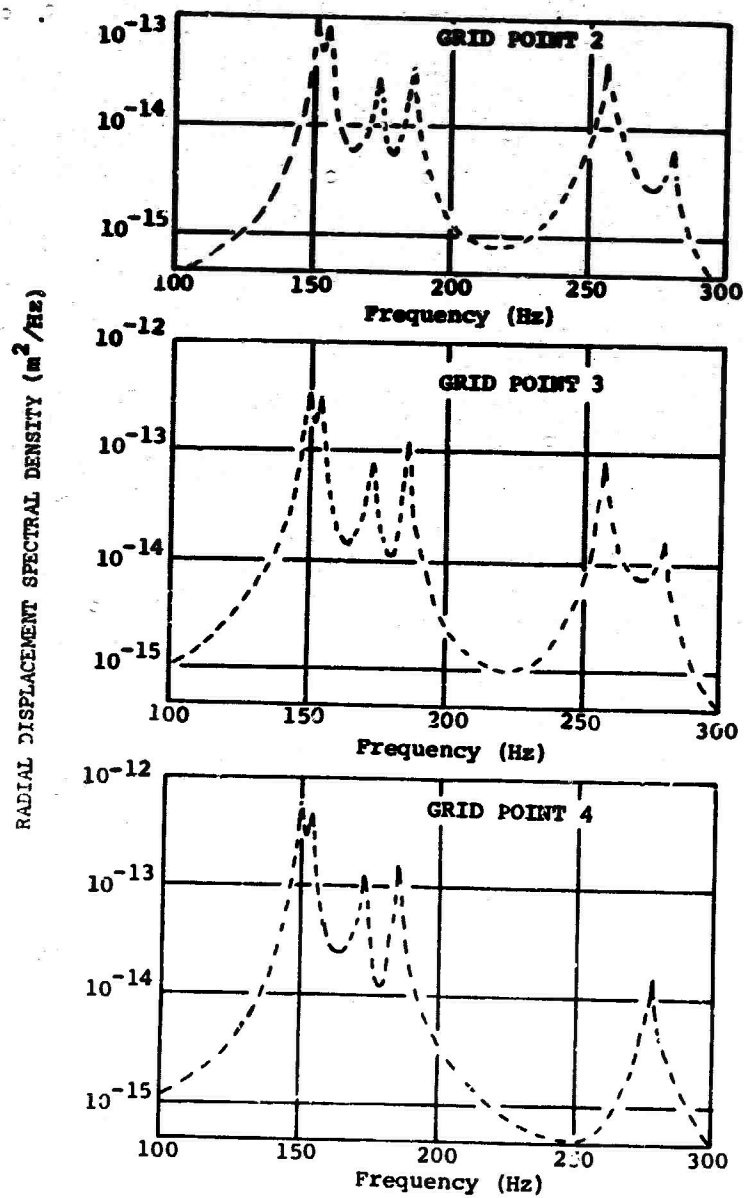


Figure 14.- Shell model displacement spectral density.

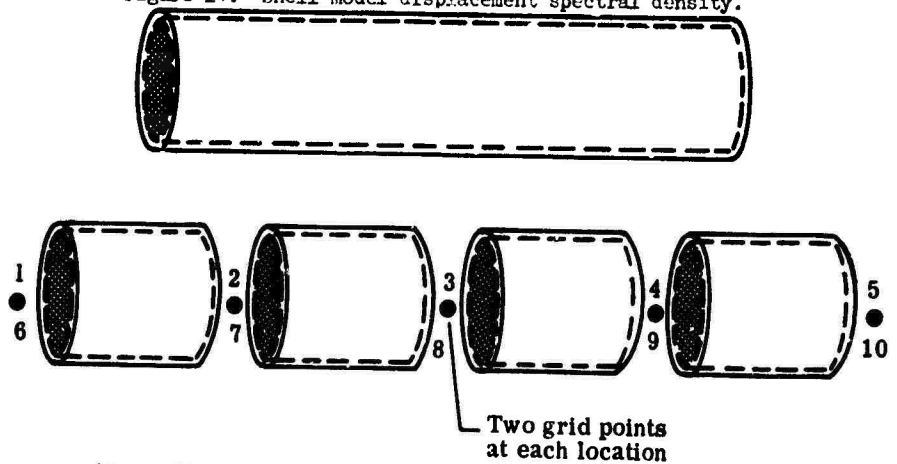


Figure 15.- NASTRAN model of fluid in a straight pipe.

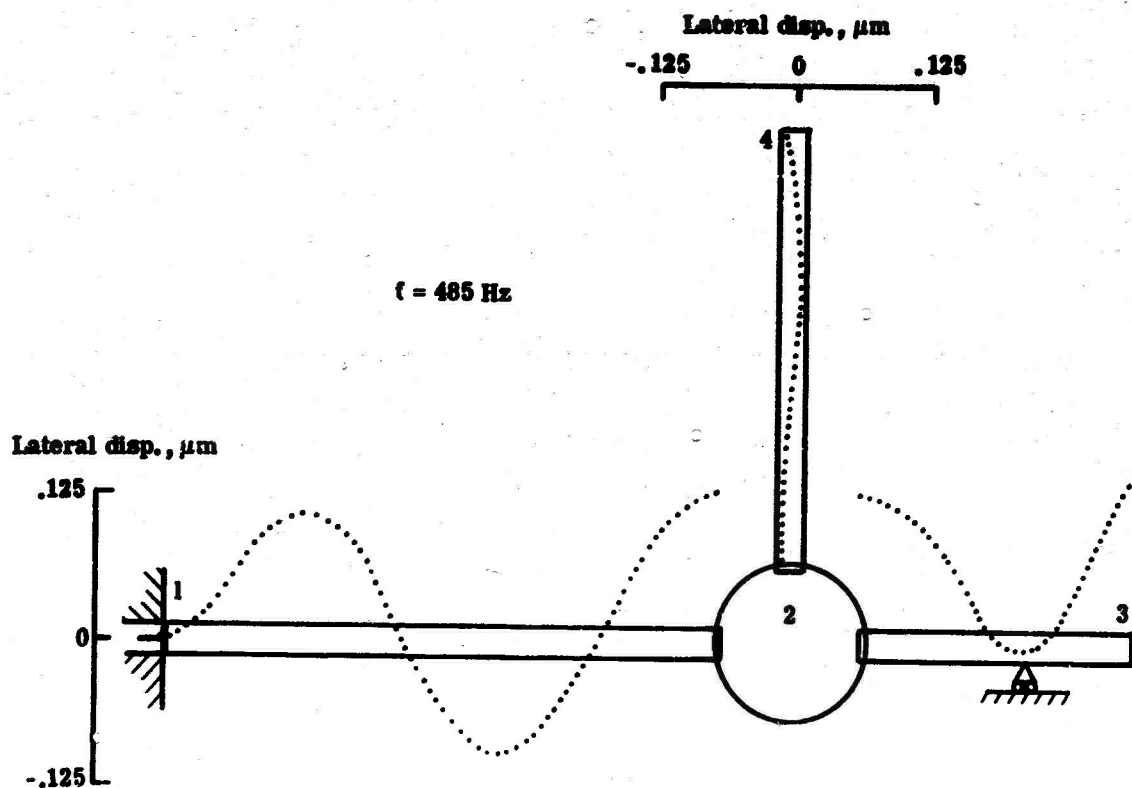


Figure 16.- Lateral response of standpipe structure.

horizontal members than for the standpipe. This fact indicates a significant coupling of pipeline wall deformation and the fluid motion. This coupling between pipeline wall deformation and the fluid motion is of great concern in such problems.

Table 6 shows the pressure ratios determined by both NASTRAN and an exact analysis for a variety of forcing frequencies. The grid points 1-4 referred to by pressures $p_1 - p_4$ are the numbers shown on figure 16. The results are in excellent agreement for all forcing frequencies. More involved examples of this type of analysis are presented in reference 7e.

Summary

The usefulness of NASTRAN as a comprehensive system for dynamic analysis has been illustrated by the six examples discussed above. Additional applications of NASTRAN for dynamic analysis may be found in reference 7.

NASTRAN MAINTENANCE AND FUTURE DEVELOPMENT

The requirement for centralized management of NASTRAN is dictated by its range of complex system software features and extensive capabilities. Maintaining NASTRAN together with its comprehensive user-oriented documentation as

Table 6.- Comparison of Pressure Ratios Predicted by NASTRAN to Those Predicted by Exact Theory for a Standpipe.

f, Hz	P_2/P_1		P_3/P_1		P_4/P_1	
	NASTRAN	Exact	NASTRAN	Exact	NASTRAN	Exact
375	-0.26	-0.26	-0.33	-0.38	-0.76	-0.76
400	-.21	-.21	-.32	-.32	-.77	-.76
450	-.1	-.1	-.18	-.18	-.9	-.89
485	0	0	0	0	-1.16	-1.16
500	.07	.07	.14	.14	-1.39	-1.38
550	1.28	1.27	3.35	3.39	-6.03	-6.04

a state-of-the-art system for structural analysis is a formidable task. Error correction, addition of new capability, enhancements for efficiency, and the documentation changes that are required as a result of these activities would impose an unbearable burden on NASTRAN's family of users and, eventually, would result in the disappearance of a truly standard NASTRAN system. NASTRAN

consists of over 151,000 Fortran statements which translate into over 1,000,000 machine language statements. It is currently operational on the IBM 360, CDC 6000 series, and the UNIVAC 1108 machine. Perhaps the most unique feature of NASTRAN is its executive system for data scheduling and overall systems control. Briefly, NASTRAN is as large and complex - in a computer software sense - as the operating systems for the three machines with which it interfaces. It is in fact, a facility with complete documentation which presently is in operation throughout the United States at over 70 different machine installations, with an estimated family of users numbering over 1,000 persons. The communal aspects of NASTRAN are obviously far-reaching.

The management of NASTRAN is the responsibility of the NASTRAN Systems Management Office (NSMO) located in the Structures Division at the Langley Research Center. The functions of this office span the spectrum of NASTRAN activities from maintenance to research and development.

Specifically, these functions include:

- Centralized Program Development
(Advisory Committee)
- Coordinating User Experiences
(NASTRAN Newsletter)
- System Maintenance
(Error Correction and Essential Improvements)
- Development and Addition of New Capability
- NASTRAN-Focused Research and Development

Significant Milestones

October 1970 - September 1971

When NSMO was established at Langley in October 1970 there existed a dire need for maintenance of the NASTRAN system. With the cooperation of Goddard Space Flight Center, an interim maintenance contract was negotiated with Computer Sciences Corporation through a contract in effect at GSFC. This contract provided for the essential function of error correction until a contract for full-time maintenance could be negotiated through an open competition. The interim maintenance activity was restricted to the correction of over 75 errors reported to NSMO, together with all associated documented changes. New thermal bending and hydro-elastic elements previously developed by the MacNeal-Schwendler Corporation under contract to GSFC were also installed. Levels 13 and 14 were created for Government testing and evaluation. The next version of NASTRAN to be released to the public through Computer Software Management Information Center (COSMIC), Barrow Hall, University of Georgia, Athens 30601, will be built upon the results of this interim maintenance activity and will be designated Level 15.

In June 1971, a contract for full-time maintenance of NASTRAN was awarded to the MacNeal-Schwendler Corporation. An offsite office near the Langley Research Center has been opened by MacNeal-Schwendler, and work on many items of maintenance and development has commenced.

In addition to the maintenance contract, a contract for the development of new elements and a thermal analyzer capability has been awarded to the Bell Aerospace Company.

Additional milestone accomplishments include the First NASA NASTRAN Users' Colloquium at the Langley Research Center, September 13-15, 1971, and publishing in August of the first issue of the NASTRAN Newsletter - a frequent publication of interest to the family of NASTRAN users.

Maintenance

Maintenance is defined herein to include error correction in both the NASTRAN code and documentation, support of all utility routines such as the linkage editor and conversion routines, and enhancements to the NASTRAN executive and matrix routines which will result in increased speed, efficiency, and convenience of operation. Maintenance is a systems activity rather than a new capability or element-oriented activity.

Utility Routines: Routines for creating new levels of NASTRAN as well as routines for converting NASTRAN from the CDC 6000 series (parent machine) to versions that will run on the IBM 360 and UNIVAC 1108 must be constantly updated as new or modified compilers and operating systems become available for any of the three NASTRAN machines. Automatic update routines are required to implement a patch to a given level. For example, a patch is presently available from COSMIC to update Level 12.0 to 12.1. The update routines are required to enable NASTRAN-type programmers to incorporate error corrections, supplied by the maintenance contractor, in a timely fashion.

Error Correction: Error correction is perhaps the single most important maintenance activity. Errors in either the code or the manuals for the standard level of NASTRAN are reported to NSMO, together with card decks and annotated output for evaluation and priority assignment. The maintenance contractor then diagnoses, isolates, and corrects the error and further validates the fix with appropriate demonstration runs. When fully corrected and validated, the correction card deck, together with card decks for other corrected errors, is made available by NSMO as a patch to the current level of NASTRAN. By faithfully reporting known and suspected errors, each member of the NASTRAN family of users benefits both himself and potentially many others. A constantly updated computerized data bank of all known NASTRAN bugs will be established, for NSMO, by the maintenance contractor. A sort may be performed at any time by rigid format, module, or some other significant system parameter to

determine the status of a previously reported bug or to determine the nature of any uncorrected error in a routine of interest. This coordinated, mutually beneficial, centralized error correction activity should result in a relatively trouble-free operation for NASTRAN users.

Enhancements for Efficiency: Several systems modifications to obtain greater operational speed and efficiency are presently in progress. These enhancements include:

- Substructuring capability to allow the solution of larger problems than is presently practical.
- Improved multiply/add (MPYAD) routines to reduce running time.
- User-specified single precision for the CDC machine.
- Much faster general input/output (GINO) routines.
- More efficient matrix packing routine.

It is anticipated that these and other system improvements will decrease average run times for the next public release of NASTRAN (Level 15) by as much as a factor of three in some analyses.

Dummy Element: A user-oriented dummy element capability is under development by the maintenance contractor. This important convenience will allow the incorporation of the mass, damping, and stiffness matrices for a new element for test, evaluation, and use in the NASTRAN environment.

NASTRAN Users' Newsletter: An important aspect of NASTRAN maintenance is timely communication with NASTRAN users concerning important developments and system improvements. The NASTRAN Users' Newsletter is designed to satisfy this requirement. Issued as often as necessary, it will contain a statement from NSMO, significant user notes, news of recently reported bugs, information on the next level to be released, and unique applications of NASTRAN.

Development of New Capability

Significant new capability is under development for NASTRAN in addition to the system-oriented activities of the maintenance contractor. The contract with Bell Aerospace previously mentioned provides for the development of several new elements and a comprehensive capability for thermal analysis. The evaluation and selection of new capability for NASTRAN requires the cooperation of NASA Centers, other Government agencies, and industry. For example, the system modifications, new elements, and thermal analyzer capability were selected from a prioritized compilation of items supplied by all of the NASA Centers. Preference has been given to the highest priority items, although some deviation is necessitated to achieve the greatest capability within a given cost constraint. The following list of new element capability is under development with public release planned for early 1973:

Nonprismatic Beam Element
Triangular and Trapezoidal Cross-Section
Rings with Nonaxisymmetric Deformation
General Element Defined by Stiffness Matrix
Multilayered Triangular and Quadrilateral
Plate Elements
Triangular and Quadrilateral Shell Elements
Rigid Body Element
Triangular and Quadrilateral Plates with
Membrane/Flexure Coupling
Curved Beam Element
Higher Order Shell of Revolution Element
for Nonaxisymmetric Deformation
Higher Order Triangular and Quadrilateral
Plate Elements
Isoparametric Solid Elements

In addition, a comprehensive heat-transfer capability is also planned to include the effects of both steady-state and transient conduction, convection, and radiation. Automatic conversion of the temperature history to displacement and stress history will be provided.

No attempt has been made to include with the new capability discussed above numerous other activities at other NASA Centers or within industry itself. Various nonstandard experimental or parochial versions of NASTRAN exist. When new capability tested in an experimental NASTRAN environment is found to be a valuable addition to the standard level of NASTRAN, it will be incorporated by NSMO.

Future Levels of NASTRAN

New levels of NASTRAN will be released when the number of error correction patches, system improvements, and new elements becomes excessive and dictates the generation of a complete new level. Ease and simplicity of bookkeeping and local management are prime drives in this situation. Although no firm commitment is possible, it is anticipated that future releases of NASTRAN will occur and will include new capability somewhat as follows:

1972 - Level 15

Error Corrections
Substructuring
Enhancements for Efficiency:

GINO
MPYAD
Single Optional Precision
(Limited)
Matrix Packing

Dummy Element
Thermal Analyzer
(Steady-State Conduction)

Error Corrections
Complete Single Precision
New Elements Developed by Bell
Complete Thermal Analyzer

Later levels will include additions to the comprehensive element capability and further enhancements for greater efficiency.

USER ACCEPTANCE

The NASTRAN Systems Management Office has attempted during the first year of operation to identify and classify the NASTRAN family of users. The sources of information include direct communications with users, the list of deliveries made by COSMIC, response to a questionnaire included in the first NASTRAN Newsletter dated August 20, 1971, and the NASTRAN Users' Colloquium held at the Langley Research Center September 13-15, 1971.

The NASTRAN Users' Colloquium was organized to provide a timely insight into the present status and rate of acceptance of NASTRAN throughout the Government and industry. The compendium of papers presented at the Colloquium and published as NASA TM X-2378 gives highlights of the experiences of NASTRAN users at over 25 different locations in the Government and private industry. The Colloquium was attended by nearly 300 persons including over 225 non-NASA attendees.

A survey of the as yet incomplete returns from the questionnaire in the first NASTRAN Newsletter indicates that NASTRAN is currently installed at over 70 different locations and that the average number of users per installation is about 13 persons. The most used rigid formats are 1 - basic static analysis, 3 - normal mode analysis, 5 - buckling, and 9 - direct transient response, in that order. These data indicate an approximate doubling of the number of NASTRAN installations and users during the past year. The demand for NASTRAN at commercial computer service bureaus and data centers indicates an increasingly significant utilization of NASTRAN's unique capabilities by aerospace and domestic industries both small and large. One data center already claims a potential of over 300 NASTRAN customers.

It is apparent that NASTRAN is rapidly becoming widely accepted as a comprehensive tool for a structural analysis. NASA's continued support for centralized maintenance and further development is an essential ingredient in sustaining user confidence in the NASTRAN system.

CONCLUDING REMARKS

A brief description of the development and capabilities of the NASTRAN system has been given with emphasis on application to dynamic analysis. Six illustrations of recently

conducted vibration and dynamic response computations which demonstrate the comprehensive character of NASTRAN have been presented. The functions of the NASTRAN Systems Management Office (NSMO) have been outlined. Improvements planned by NSMO including enhancements for efficiency, several new finite elements, and a complete heat-transfer capability together with tentative schedules for the release of new levels of NASTRAN were discussed.

NASTRAN has become a widely accepted facility for structural analysis. At present NASTRAN is installed on over 70 computers throughout the Government and industry and there are over 1,000 individuals in the NASTRAN family of users.

NASA has provided for the standardization and centralized management of NASTRAN by establishing the NASTRAN Systems Management Office in the Structures Division at the Langley Research Center and is firmly committed to maintaining and improving NASTRAN as a valuable national resource.

REFERENCES

1. R. H. MacNeal and C. W. McCormick, "The NASTRAN Computer Program for Structural Analysis," The MacNeal-Schwendler Corp., Paper No. 690612, presented at the National Aeronautic and Space Engineering and Manufacturing Meeting of the Society of Automotive Engineers, Los Angeles, Calif., Oct. 6-10, 1969.
2. T. G. Butler and D. Michel, "A Summary of the Functions and Capabilities of the NASA Structural Analysis Computer System," SP-260, NASA, Washington, D.C., 1971.
3. Richard H. MacNeal, "The NASTRAN Theoretical Manual," SP-221, NASA, Washington, D.C., September 1970.
4. Caleb W. McCormick, "The NASTRAN User's Manual," SP-222, NASA, Washington, D.C., September 1970.
5. Frank J. Douglas, "The NASTRAN Programmer's Manual," SP-223, NASA, Washington, D.C., September 1970.
6. NASA, "NASTRAN Demonstration Problem Manual," SP-224, NASA, Washington, D.C., October 1969.
7. "NASTRAN: Users' Experiences," TM X-2378, NASA, Washington, D.C., September 1971. The examples used from this reference are the following:
 - a. Paper 14 - "Modal Analysis of the Mated Space Shuttle Configuration," by R. K. Geiseke.
 - b. Paper 18 - "Acoustic Analysis of Solid Rocket Motor Cavities by a Finite Element Method," by David Herting, et al.

c. Paper 21 - "Structural Dynamic Analysis of Electronic Assemblies Using NASTRAN Restart/Format Change Capability," by Ronald P. Schmitz.

d. Paper 22 - "The Response of Shells to Distributed Random Loads Using NASTRAN," by Gary K. Jones.

e. Paper 23 - "Applications of NASTRAN to Coupled Structural and Hydrodynamic Responses in Aircraft Hydraulic Systems," by James Howlett.

8. D. A. Evensen and R. Aprahamian, "Application of Holography to Vibrations, Transient Response, and Wave Propagation," CR-1671, TRW Systems Group, Redondo Beach, Calif., December 1970.

DISCUSSION

Mr. Stirbis (Sandia Laboratories): Do you have any plans to install a mesh generation scheme in NASTRAN, and if so when?

Mr. Raney: We have not at the present time made firm plans to add any automatic data generation programs to NASTRAN. These are relatively easy for the individual user to develop and tailor expressly to his own needs. We know of several of these. The problem is getting a large number of individuals to agree that they all would like to have the same capability. To the extent we can get unanimity on automatic data generation or analysis of the output we will try to add this to NASTRAN. But at the present time we are in the position of looking at what can be done and searching for the necessary unanimity across a pretty wide range of users.

Mr. Pakstys (General Dynamics Corporation): What are your plans to get a three-dimensional finite element capability, such as the isoparametric hexahedron family?

Mr. Raney: We are now adding a family of isoparametric elements. I do not like to say when they will be available because I know I will be held to it no matter how I hedge myself. We are undertaking to add these and we hope to have them available to us in our own version of NASTRAN for checkout within about six months.

Mr. Monroe (Babcock & Wilcock Company): What is the difference between NASTRAN and ANSYS or ELAS? I understand they can handle similar problems.

Mr. Raney: That really would be the subject of one more talk, if not three. You might be interested in getting some of the papers from the ONR Symposium held in Urbana in September where they held a session comparing these programs. They are somewhat different. I am not familiar with the ANSYS capability. ELAS is a very nice program but it does not have the overall capabilities of NASTRAN.

Mr. Hurchalla (Pratt and Whitney Aircraft): Can anything be done to improve the errors notification process? I think very few errors have been sent out by COSMIC or NSMO compared to the number that seem to have been reported. I think CSC has a large number reported, but in the process of disseminating these we have not received any notifications of errors. Is anything being done about it?

Mr. Raney: Yes, our contractor is developing a comprehensive data base of all errors that have been reported and their exact status. That is, whether they have been corrected, what level of NASTRAN they have been corrected in, and the active ones. This information will be given to COSMIC very shortly and you should write to COSMIC to get it. COSMIC now has a limited list that gives the status of all the SPR's. We have worked real hard on this and we feel that it is better to have the communications suffer a little bit, but get the job done and actually get it in so the users will get the benefit of it, rather than to spend all of our time writing to people. We presently spend almost two hours a day just on the phone.

EXPERIENCE WITH NASTRAN AT THE NAVAL SHIP R&D CENTER AND OTHER NAVY LABORATORIES (U)

Petro Matula

**Naval Ship Research & Development Center
Bethesda, Maryland 20034**

(U) For the past three years NSRDC has been using the NASA Structural Analysis Program, NASTRAN, to solve a wide variety of Naval structural analysis problems. For the past 18 months other Navy and government organizations, utilizing NSRDC's background, have been applying NASTRAN in their projects.

(U) This paper summarizes the experience thus accumulated, the steps taken to acquaint the engineers in other Navy organizations with the program, and the current activity of the NASTRAN Project at NSRDC.

INTRODUCTION

(U) During the summer of 1966 a number of finite element programs were under development by NSRDC and other Navy laboratories for analysis of various naval structures. It was planned to integrate these separate capabilities into one general computer program for analysis of a wide variety of complex Navy structures. At about that time we became aware of the work on NASTRAN which, upon review of the design specifications, appeared to offer a set of capabilities suitable for our needs. Thus, rather than launching a parallel effort, NSRDC decided to follow NASTRAN's development and to adopt it for our own use as soon as it became available.

INITIAL APPLICATIONS OF NASTRAN AT NSRDC

(U) We began working with a pre-release partial version (containing only the static analysis capability) of NASTRAN in August 1968. Our initial applications of the program were to static problems and especially to those which had been solved before by other means.

(U) Our initial experience with NASTRAN was very favorable. We found that with a

judicious use of relatively simple elements in NASTRAN, we were able to obtain very good correlations between the NASTRAN results and the results by other programs and experiments [1]. In addition we found that the use of the program - both at the data preparation stage and at the output reading stage - was made relatively easy by very good documentation of the program and a very simple data input format.

(U) In the second half of 1969 the dynamic analysis capability of NASTRAN became available to us and we began to evaluate it with such "textbook" problems as a vibrating plate, a vibrating cylinder and others. The results of a normal mode analysis using NASTRAN for the plate and the cylinder are compared to the results obtained by several other means as shown in Tables 1 and 2 [1].

(U) In December 1969 NASA released a limited preliminary version of NASTRAN to the Aero-Space Industry and to selected government laboratories, including NSRDC, with a request for an evaluation report on the program and its documentation, noting merits, errors, deficiencies, etc.

Preceding page blank

TABLE 1
Natural Frequencies of Isotropic 6" Square Plate, 0.03"
Thick With Built-In Edges

Mode Shape (m,n)*	Experiment	Warburton	Classen & Thorne	NASTRAN
(1, 1)	340	349.3	347.831	347.3
(2, 1), (1, 2)	698	712.8	709.422	708.5
(2, 2)	1025	1052	1046.02	1039
(3, 1) - (1, 3)	1242	1276	1271.86	1273
(3, 1) + (1, 3)	1254	1283	1277.89	1279
(3, 2), (2, 3)	1578	1603	1594.89	1583
(4, 1), (1, 4)	2009	2043	2034.90	2044
(3, 3)	2102	2135	-	2097
(4, 2) + (2, 4)	2305	2358	2340.65	2326
(4, 2) - (2, 4)	2320	2358	-	2337
(4, 3), (3, 4)	2836, 2823	2876	-	2818
(5, 1) + (1, 5)	2943	2997	-	3013

*m,n - number of half-waves in X and Y directions, respectively.

TABLE 2
Natural Frequencies (Hz) of Simply-Supported Ring-Stiffened Cylinder
Cylinder Dimensions (Inches): Length - 18.54; diameter - 4.082; thickness - 0.047
14 Outside Stiffeners, Dimensions (Inches): Height - 0.1145; thickness - 0.086; spacing - 1.236

n	Galletly (inter-ring def.)	Galletly (no inter-ring def.)	Bleich (Galletly)	Wah	Wah and Hu	Basdekas	BOSOR (smeared rings)	BOSOR (discrete rings)	NASTRAN (plate elements)	NASTRAN (axisym. elements)
2	708	711	732	195	687	724	704	703	-	738
3	570	582	618	510	505	616	586	564	601	547
4	903	947	938	958	727	1042	957	889	896	771
5	1430	1514	1433	1525	1123	1592	1532	1393	-	1182

NAVY-NASTRAN PROJECT

(U) Almost simultaneously with NASA's request, the office of the Director of Laboratory Programs of the Navy sponsored an evaluation of the applicability of NASTRAN for Navy use. This led to the establishment of the NASTRAN Project at NSRDC.

(U) To acquaint other Navy installations with NASTRAN, to share NSRDC's NASTRAN experience with them, and to include as broad a base of Navy users as possible in the evaluation of NASTRAN, a two-day Navy-NASTRAN Colloquium was held at NSRDC in January 1970. It was attended by over 100 representatives from 20 Navy installations throughout the country.

(U) At the Colloquium, it became evident that interest in NASTRAN within the Navy was broad enough to warrant setting up some means of information exchange on NASTRAN throughout the Navy. As a result, the NASTRAN Project at NSRDC began publication of a quarterly newsletter in March 1970. The Newsletter, together with the Proceedings of the 1st Colloquium [1] and the NASTRAN Evaluation Report published in August 1970, made a significant contribution to dissemination of information among Navy NASTRAN users.

(U) To further improve the means of sharing NASTRAN experience among Navy users, to coordinate future improvements to NASTRAN as well as developments of various input/output interfaces, and to provide and coordinate training and consulting service for NASTRAN users, the Navy-NASTRAN Steering Committee was organized in September 1970. At the time of this writing 16 Navy installations are formally represented on the Steering Committee. Among them are nine laboratories, four shipyards, ONR, NAVORD, and the Naval Ship Engineering Center.

(U) In part, as a result of the NASTRAN Project's effort to make NASTRAN and the information on its use available to the Navy engineers, the use of NASTRAN increased significantly in the past year, especially among NSRDC engineers and also at the Naval Underwater System Center and the Naval Air Development Center. It has been estimated that in FY 71 the expenditure for NASTRAN computer runs alone at various Navy activities amounted to \$200,000.

(U) The 2nd Navy-NASTRAN three-day Colloquium was held in December 1970. As noted in the Proceedings of the 2nd Colloquium, the papers presented represented significant progress in the evaluation of the program as compared to the 1st Colloquium of one year earlier, especially the papers on "Static Structural Analysis, F-14 Horizontal Stabilizer," "Elasto-Plastic Analysis with NASTRAN," "Modal Analysis of Deckhouse," and "Transient Analysis: Direct vs. Modal by NASTRAN." Some other papers, such as "Data Generation for NASTRAN," "New Element Definition Capability for NASTRAN," and "New Elements for NASTRAN" represent some accomplished and some planned improvements to NASTRAN.

(U) For the complete text of the papers presented at both colloquia, the reader is referred to the Proceedings [1, 2].

(U) Our exploratory and production use of NASTRAN to date has enabled us to evaluate many options and capabilities of the program. Many more remain unexplored; others need further evaluation. However, as the number of users increases, bringing additional demands on the program, other capabilities will be evaluated.

(U) In addition to the Navy's use of NASTRAN, a considerable contribution to the evaluation of the program is continuously being made by other government activities who use NASTRAN in cooperation with the NASTRAN Project at NSRDC. Also, the NASTRAN User's Colloquium, scheduled by NASA for 13-15 September 1971 and expected to have the widest representation of users to date, should enrich considerably the general store of experience with NASTRAN.

SOME CURRENT WORK AT NSRDC

(U) A computer program such as NASTRAN, designed primarily for large problems and widely used, can realize considerable cumulative savings by improving its computer running time, however small such improvement may be. NSRDC's NASTRAN Project has made a significant contribution in this field. A computer program has been developed which automatically performs a permutation of user-assigned grid point numbers in order to reduce the bandwidth of the structural matrices arising in the finite element displacement method. Since computer running time is proportional to the square of the

matrix bandwidth, this results in substantial savings for many structural analyses. This capability has been operational as a preprocessor to NASTRAN for the past year and a half and is being used at Navy, NASA and other user centers. Most of our experienced NASTRAN users consider this preprocessor indispensable. Currently, NSRDC is working on improving the efficiency of the bandwidth minimization program.

(U) Another area of substantial savings in connection with the use of finite element computer programs is in data preparation. To use a program such as NASTRAN requires large quantities of data consisting of point-by-point and element-by-element geometric description of the structure being analyzed. NSRDC is currently completing a preprocessor to NASTRAN which will automatically produce the bulk of the data required for the analysis of submarine type structures taking into account such details as tapered stiffeners, cut-outs, and the like.

(U) It is probably safe to state that there is no finite element program in use today, including NASTRAN, whose library of finite elements satisfies every structural analyst. There will always be users who would like to add their own element to a program. In the case of NASTRAN, because of its wide use and of its excellent system design, a user-oriented capability for adding new elements to the program is doubly desirable. NSRDC is making a substantial contribution to this goal.

(U) To develop general expertise in adding an element into NASTRAN, a 3-degree-of-freedom triangle which solves the steady-state heat conduction problem has been added to the program and made operational [3]. To accomplish this, it was necessary to become thoroughly familiar with many aspects of NASTRAN's programming such as variables, tables, routines, structure, and restrictions. A number of NASTRAN tables had to be updated and a number of new subroutines written. These, then, had to be properly inserted into NASTRAN before the new element could be used.

(U) To be of practical use to the engineer, a facility for adding a new element to NASTRAN must not require the above tasks whenever a new element is to be added. NSRDC is currently completing a preprocessor which will generate the FORTRAN language tables and routines required by NASTRAN for a new element. The new element

definition capability is being tested and a report on the subject is being issued.

(U) In connection with the work on a new element definition capability, NSRDC has received a request from the Marshall Space Flight Center to incorporate into NASTRAN a three-dimensional transient thermal analysis capability which will interface directly with a three-dimensional structural analysis. This work is in progress.

CONCLUDING REMARKS

(U) The experience with NASTRAN at NSRDC and other Navy laboratories is based on three years of active use of the program. To many engineers NASTRAN was the only analysis tool suitable for their problems. Others, by the use of NASTRAN, were able to avoid costly experimentation and thus saved money on their projects. The overall consensus about NASTRAN is that it is the most comprehensive program available to the Navy engineers at this time for static and dynamic analysis of general 3-dimensional structures. The many considerations given to the user in the design of the program and the excellent documentation make it an easy program to use. The general nature of the program and its availability tend to create a broad base of users, and hence, a wide spectrum of experience with the program. This, coupled with a free exchange of information among the users through various media including the Navy and NASA Colloquia and publications, helps to accelerate and improve the mastering of the program by an individual user. In addition, the support of NASTRAN by NASA through the NASTRAN System Management Office (NSMO), with the objective of insuring the future usefulness of NASTRAN by maintenance and improvements, makes it an attractive program from the point of view of investing time and talent.

REFERENCES

1. "Proceedings of the 1st NSRDC-NASTRAN Colloquium," January 1970, NSRDC, NASTRAN Project, Code 1844.
2. "Proceedings of the 2nd Navy-NASTRAN Colloquium," December 1970, NSRDC, NASTRAN Project, Code 1844.
3. M. M. Hurwitz, "An Addition to the NASTRAN Element Library," NSRDC Report 3628, March 1971.

DISCUSSION

Mr. Macy (Supervisor of Shipbuilding, 3rd Naval District): Have you attempted to apply NASTRAN to DDAM type problems?

Mr. Matula: Not directly and no one has asked us to. Maybe some people did that but we do not know about it. The only shock application that I know about was done at the Naval Underwater Systems Center, New London Laboratory, but it did not apply directly to DDAM specifications.

Mr. Hurchalla (Pratt and Whitney Aircraft): Initially you mentioned the newsletter that you were thinking of publishing. Will it be strictly about NASTRAN, and what will its nature be?

Mr. Matula: We are not only thinking about publishing, we have published four issues of it already I think. It is a quarterly publication and it deals predominantly with NASTRAN subjects. While it is not restricted just to NASTRAN, so far, it has been predominantly NASTRAN.

Mr. Hurchalla: How does one get on the distribution list?

Mr. Matula: If you are with the government there is no problem. If you are a contractor, and if you can supply to us a sponsoring letter from a Navy customer we would put you on the mailing list.

RESULTS OF COMPARATIVE STUDIES ON REDUCTION OF SIZE PROBLEM

R. M. Mains
Department of Civil and Environmental Engineering
Washington University
St. Louis, Missouri

Comparative solutions have been made for a uniform cantilever beam represented by 20 linear plus 20 rotational coordinates, and for the beam represented by 10 linear coordinates obtained by kinematic condensation. The lower five or six frequencies, mode shapes, and modal effective masses were not altered appreciably by the kinematic condensation operation. An eyeball reduction of mass together with a static reduction of stiffness gave equally good results in the lower modes.

MOTIVATION

In the computer analysis of problems, the tendency is to model the system with enough coordinates so that each structural element is as simple as possible. Calculating the element stiffnesses and assembling them into the system stiffness matrix is the kind of operation which computers do readily, and about 3 minutes of computer time will produce a system stiffness matrix of order 150. It is not unusual to start with a matrix of order several hundred or even several thousand. The difficulties arise when the remainder of the calculations are performed, because static analysis requires matrix inversion and dynamic analysis requires either several inversions or the solution of the eigenvalue problem. The matrix of order 150 that took 3 minutes to assemble will require 60 minutes to invert (with conditioning and double precision), and 90 minutes for eigenvalues and eigenvectors. Because of this high cost of inversion and eigenvalue, the author has been investigating various schemes for reducing the size of problems, after stiffness assembly and before inversion or eigenvalue.

STATIC SIZE REDUCTION

For static problems, size reduction is simple and straightforward, but it does require at least one inversion at reduced size (1).^{*} First one rearranges the rows and columns of the stiffness matrix, K , such that the coordinates to be kept come first, as in K_{11} below, and the coordinates to be eliminated come last, as in K_{22} below.

^{*} Numbers in parentheses refer to the bibliography at the end of the paper.

$$K_{SYS} = \begin{bmatrix} K_{11} & K_{12} \\ K_{21} & K_{22} \end{bmatrix} \quad (1)$$

Then if there are no external forces to be applied to f_2 , with X = displacement vector and f = force vector,

$$\begin{bmatrix} K_{11} & K_{12} \\ K_{21} & K_{22} \end{bmatrix} \begin{bmatrix} X_1 \\ X_2 \end{bmatrix} = \begin{bmatrix} f_1 \\ 0 \end{bmatrix} \quad (2)$$

whence

$$X_2 = -K_{22}^{-1} K_{21} X_1 \quad (3)$$

and

$$[K_{11} - K_{12} K_{22}^{-1} K_{21}] [X_1] = [f_1] \quad (4)$$

If there are external forces to be applied at f_2 , then eq. (4) becomes:

$$[K_{11} - K_{12} K_{22}^{-1} K_{21}] [X_1] = [f_1] - [K_{12} K_{22}^{-1}] [f_2] \quad (5)$$

The reduced stiffness, K_{RED} is

$$K_{RED} = [K_{11} - K_{12} K_{22}^{-1} K_{21}] \quad (6)$$

and by successive partitions and reductions, any size stiffness matrix can be made small without any inversions larger than whatever size K_{22} is made. Usually about one digit of precision is lost with each successive reduction, so at double precision (IBM 360) about 6 successive reductions are a practical limit.

DYNAMIC SIZE REDUCTION BY IMPEDANCE

For dynamic problems, size reduction is complicated by the inertia terms, $M\omega^2$, in which M = mass and ω = frequency. As before, when there are no external forces applied in f_2 ,

$$\begin{bmatrix} Z_{11} & Z_{12} \\ Z_{21} & Z_{22} \end{bmatrix} \begin{bmatrix} X_1 \\ X_2 \end{bmatrix} = \begin{bmatrix} f_1 \\ 0 \end{bmatrix} \quad (7)$$

$$\text{and } [Z_{11} - Z_{12}Z_{22}^{-1}Z_{21}][X_1] = [f_1] \quad (8)$$

$$\text{but } Z = K + i\omega C - \omega^2 M \quad (9)$$

and for $C = 0$ (damping = 0) eq. (8) becomes:

$$[(K_{11} - \omega^2 M_{11}) - (K_{12} - \omega^2 M_{12})(K_{22} - \omega^2 M_{22})^{-1} (K_{21} - \omega^2 M_{21})][X_1] = [f_1] \quad (10)$$

For $\omega = 0$, eq. (10) is identical to eq. (4), as it should be; but for other ω 's there is no way to avoid a separate computation for each frequency. The number of frequencies to be used can be small if the eigenvalues are known, but that is the operation that is to be avoided.

DYNAMIC SIZE REDUCTION BY EIGENVECTORS

If the eigenvectors were known, then size reduction could be easily accomplished by a substitution of variables in the dynamic equation:

$$M\ddot{X} + C\dot{X} + KX = f(t) \quad (11)$$

$$\text{Let } X = X_0 Y \quad (12)$$

where X_0 = a small portion of the eigenvector set

Y = a substitute variable

and premultiply by X_0^T

$$\text{then } X_0^T M X_0 \ddot{Y} + X_0^T C X_0 \dot{Y} + X_0^T K X_0 Y = X_0^T f(t) \quad (13)$$

$$\text{which is } \ddot{Y} + 2\xi\omega_0 \dot{Y} + \omega_0^2 Y = X_0^T f(t) \quad (14)$$

Now eq. (14) is reduced in size, the equations are decoupled, and full detail is recoverable by eq. (12). This would be perfect if there were some way to get X_0 economically, but there is none known to the author.

KINEMATIC CONDENSATION

Mr. R. J. Guyan proposed a transformation(2) which he claimed (without supporting data) would reduce problem size without altering the lower frequencies. The proposal was: in eq. (11)

$$\text{set } \begin{bmatrix} X_1 \\ X_2 \end{bmatrix} = \begin{bmatrix} I \\ -K_{22}^{-1} K_{21} \end{bmatrix} \begin{bmatrix} Y_1 \end{bmatrix} \quad (15)$$

and premultiply by

$$[I \quad (-K_{12} K_{22}^{-1})] \quad (16)$$

to get

$$[(K_{11} - \omega^2 M_{11}) - (K_{12} K_{22}^{-1} K_{21}) + (\omega^2 K_{12} K_{22}^{-1} M_{21}) + (\omega^2 M_{12} K_{22}^{-1} K_{21}) - (\omega^2 K_{12} K_{22}^{-1} M_{22} K_{22}^{-1} K_{21})][Y_1] = [f_1 - K_{12} K_{22}^{-1} f_2] \quad (17)$$

If we expand eq. (10) with $f_2 = 0$, we get:

$$[(K_{11} - \omega^2 M_{11}) - K_{12}(K_{22} - \omega^2 M_{22})^{-1} K_{21} + \omega^2 K_{12}(K_{22} - \omega^2 M_{22})^{-1} M_{21} + \omega^2 M_{12}(K_{22} - \omega^2 M_{22})^{-1} K_{21} - \omega^2 M_{12}(K_{22} - \omega^2 M_{22})^{-1} M_{21} \omega^2] Y_1 = f_1 \quad (18)$$

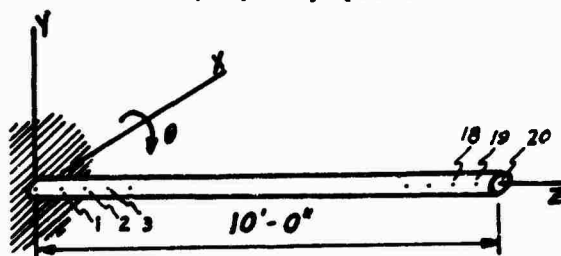
The difference between the rigorous equation, (18), and the approximation equation, (17), is that

K_{22}^{-1} replaces $(K_{22} - \omega^2 M_{22})^{-1}$ in terms 2, 3 and 4

the fifth terms are totally different.

NUMERICAL COMPARISONS

Since the comparison of equations 17 and 18 shows that Mr. Guyan's proposal is not mathematically correct, the question is then whether it gives acceptable numerical results despite the lack of rigor. The author had extensive data (3,4) on the cantilever beam shown in Fig. 1, so the various solutions for that beam were used to try Guyan's proposal.



A1. tube 6" O.D. x $\frac{1}{2}$ " wall

20 stations, Y and θ coordinates

40 degrees of freedom

Reduction to 10 linear coordinates,

2Y, 4Y, 6Y 20Y.

FIG. 1. CANTILEVER BEAM

Out of the stack of calculated values for the various numbers, three sets were selected as the most effective comparison of the reduction schemes. First, the frequencies for the odd numbered modes from first to ninth are listed in Table 1. In this table, row 1 is for the theoretical solution with bending but no shear or rotational inertia. Row 2 is the theoretical solution with shear and rotational

inertia as well as bending. Rows 3, 4 and 5 are for the 40-degree-of-freedom solution with shear and rotational inertia, for McCalley's consistent mass, Archer's consistent mass, and the author's diagonal mass. Rows 6, 7 and 8 are for the 20-degree-of-freedom solutions obtained by dropping rotational inertia terms from the mass matrices and using a stiffness matrix reduced according to eq. (6). Rows 9, 10 and 11 are similar to 6, 7 and 8 except that the stiffness was obtained from inversion of the deflection influence coefficient matrix for 20 linear degrees of freedom. Rows 12, 13 and 14 are for Guyan's kinematic condensation reducing 40 degrees of freedom to 10 according to eq. (15) and eq. (16). Row 15 is for stiffness reduced by eq. (6) and mass reduced by eyeball.

As one studies Table 1, it seems that modes 1 and 3 show little variation between row 2, which should be "correct," and all the other rows. By mode 7, the ordinary theory of row 1 is too high above row 2, and the "consistent" mass schemes are all above row 2 by about the same amount that the diagonal mass schemes are below row 2. In a 10-degree-of-freedom system, the author would not use more than 4 modes anyway, so the variations at mode 7 and higher are not significant for practical use.

The second comparison of results of kinematic condensation is shown in Table 2. These data were obtained by calculating the response of each mode to 100 in/sec step velocity at the base of the cantilever beam, and then summing the response for each coordinate across 10 modes. Column 1 is for McCalley's consistent mass and 40 degrees of freedom; columns 2, 3 and 4 are for kinematic condensation of 40 degrees to 10 for the various mass formulations; and column 5 is for the eyeball reduction of mass with stiffness reduced by eq. (6). The agreement is remarkably close, with most variations less than 0.1%. The root mean square was also calculated, and it showed even less variation. The implication is that deformations calculated for shock response will be little different whichever scheme of calculation is used. Since deformations vary but little, so will the stresses resulting from the deformations.

The third comparison of results of kinematic condensation is shown in Table 3. In this table, the members were obtained by calculating the modal effective mass for each mode, dividing by the total mass, and then accumulating the sum down the column of modes. The columns are the same as in Table 2. One criterion for determining the number of modes to include in a calculation uses this accumulated sum of effective mass ratios and some limit such as 0.90 or 0.95. Through the sum of the first five modes, there is little difference between the modal effective mass for any of the 10-degree solutions and the 40-degree solution. There is also little difference between the various 10-degree systems all the way through mode 10.

CONCLUSIONS

Kinematic condensation, as proposed by Guyan, as a means for reducing the size of a dynamic analysis without altering appreciably the lower frequencies and mode shapes, worked well on the straight, uniform cantilever beam reported herein. If it had not worked well on this beam, then it could not be expected to work on more complicated practical problems. The fact that it did work well on this beam is no guarantee that it will work well on a more complicated problem, but at least the scheme seems worth trying. One computer center (5) recently reported having used kinematic condensation to reduce 1783 degrees of freedom to 125 degrees of freedom before proceeding with dynamic analysis.

The data show that the eyeball reduction of mass with static reduction of stiffness is at least as good as any of the other schemes, and its lower cost is in its favor.

REFERENCES

1. R. M. Mains, "The Practical Problems of Generating Large Stiffness or Flexibility Matrices," ASME paper no. 63WA268, Nov. 1963
2. R. J. Guyan, "Reduction of Stiffness and Mass Matrices," AIAA Jour. v 3 n 2, Feb. 1965
3. R. M. Mains, "Comparisons of Consistent Mass Matrix Schemes," 39th Shock and Vibration Bulletin, Jan. 1969
4. R. M. Mains, "Further Comparisons of Consistent Mass Matrix Schemes," 40th Shock and Vibration Bulletin, Dec. 1969
5. "ENTRY," Newsletter of McDonnell-Douglas Automation Co., July & Aug. 1971.

TABLE 1
COMPARISON OF FREQUENCIES

		MODE NO.					Row No.
		1	3	5	7	9	
BENDING ONLY + SHEAR & ROTAT	THEORY 1	16.75	294.0	952.4	1937.1	3398.0	1
	THEORY 2	16.69	277.1	815.6	1518.6	2309.2	2
40 x 40 + SHEAR + ROTAT	MCCY	16.70	277.6	826.5	1576.1	2469.7	3
	ARCH	16.92	280.0	839.9	1603.7	2493.8	4
	RMM	16.68	275.4	805.0	1480.6	2205.0	5
20 x 20 K RED	MCCLIN1	17.54	282.1	855.7	1651.3	2604.6	6
	ARCLIN1	17.56	281.2	848.3	1621.9	2524.1	7
	RMMLIN1	17.67	277.9	819.8	1516.2	2259.1	8
20 x 20 FROM K ⁻¹	MCCLIN2	16.40	282.0	855.7	1651.3	2604.6	9
	ARCLIN2	16.42	281.2	848.3	1621.9	2524.1	10
	RMMLIN2	16.52	277.9	819.8	1516.2	2259.1	11
10 x 10 KINEMATIC CONDENS EYEBALL	MCCY	16.69	277.8	833.0	1632.3	2618.4	12
	ARCH	16.70	280.1	847.4	1664.2	2642.8	13
	RMM	16.67	275.8	817.5	1557.6	2382.3	14
	RME	16.63	272.4	785.2	1377.7	1848.2	15

TABLE 2
COMPARISON OF SUMS ACROSS ROWS OF RESPONSE TO 100 IN/SEC

COORD. NO.	MCCY40	MCCY10	ARCH10	RMM10	RME10
1	.06292	.05965	.05959	.05986	.06060
2	.16788	.16822	.16814	.16823	.16823
3	.30101	.30059	.30060	.30062	.30071
4	.44584	.44640	.44646	.44641	.44650
5	.59898	.59888	.59901	.59888	.59899
6	.75369	.75427	.75447	.75424	.75435
7	.91051	.91049	.91077	.91043	.91052
8	1.0662	1.0666	1.0670	1.0665	1.0666
9	1.2229	1.2225	1.2230	1.2223	1.2223
10	1.3798	1.3782	1.3789	1.3780	1.3779
	1	2	3	4	5

TABLE 3
ACCUMULATED SUMS OF MODAL EFFECTIVE MASS RATIOS

MODE NO.	MCCY40	MCCY10	ARCH10	RMM10	RME10
1	.6304	.6295	.6302	.6289	.6278
2	.8247	.8253	.8259	.8248	.8242
3	.8948	.8928	.8933	.8925	.8923
4	.9292	.9264	.9268	.9264	.9272
5	.9533	.9451	.9451	.9455	.9477
6	.9680	.9555	.9553	.9564	.9603
7	.9823	.9609	.9604	.9623	.9679
8	.9920	.9633	.9627	.9649	.9721
9	1.0048	.9642	.9635	.9660	.9739
10	1.0153	.9644	.9637	.9663	.9744

DISCUSSION

Mr. Pakstys (General Dynamics Corporation):

At the 36th Shock and Vibration Symposium we presented some results on Guyan's reduction problem on a three-dimensional beam. At that time we reported that we did it both ways. By one method we obtained all of the frequencies for the finite number of dynamic degrees of freedom, and then we reduced it by Guyan's reduction. We obtained good results but one of the lower predominant modes was missing, and this has happened on more complex systems. In general the results are good but some of the important modes just do not appear. Have you encountered this in your evaluation, or do you intend to look into this further?

Mr. Mains: No I was not aware that this phenomenon existed, and now that I am aware, I will certainly investigate further to see if I can make it occur and if so why. The fact that it worked in the problem that I used certainly does not mean that it is generally applicable. This is necessary that it work but it is not sufficient.

Mr. Koen (Bell Telephone Laboratories): We have been using this technique for quite a while and we have done a number of studies on cantilevered and simply-supported beams. We have added one more thing, and I think if you go through the process you described you could also write down the mass matrix. We applied the following criterion. The mass of the point eliminated must be at least two orders of magnitude less than the predominant mass. In other words one could eliminate rotary inertia in many cases. We found that it was necessary to reduce, because we did not have a complete double-precision program. That is, if we solved the complete 130 to 140 degrees of freedom problem, we found that we would get numerical inaccuracies, and it was necessary to reduce the rotary inertias. We found that we could obtain accurate low frequencies by doing this.

Mr. Mains: For 100 or 120 degrees of freedom it is not really necessary to reduce, but for 1000 degrees of freedom I am pretty sure you need to reduce. Now why?

Mr. Koen: If your problem is ill-conditioned, if you have very large conditioning numbers, even if you have 5 by 5 or 6 by 6 matrices, you still may not have enough precision in your computer.

Mr. Mains: These problems tend to be close to ill-conditioned in the first place. In fact a well designed structural system should be close to singular and so you have to be careful what you do to it.

Mr. Koen: When does one use static reduction? We found that it is necessary to look at the mass. And if you indeed just reduce those nodes which have very low mass I believe it can be shown rigorously that it will work.

Mr. Mains: In this problem that I used, the masses that I reduced were the same masses that I was keeping. So it was not a question of two orders of magnitude, but the same magnitude.

Mr. Koen: What was helping you was the frequencies, as you showed, which was interesting. But to get back to the former comment, I think they missed a mode because they may have eliminated the wrong mass.

Mr. Mains: That might be. When you do this form of elimination you work on the mass and you arrange it so that the total mass is still the same. It is just differently distributed throughout the system.

Mr. Koen: That is right. We take a look to see what modes have small mass.

Mr. Mains: Well apparently if you are going to miss a mode completely it means that you have loused up the system somehow by distributing the mass wrongly. If you put the mass in correctly you ought to be able to keep all of the lower modes. Isn't that right?

Mr. Koen: Yes, we eliminate the very very small mass terms which contribute to the very high frequencies.

Mr. Mains: That is very logical.

Mr. Koen: We have run many sample problems and found it to be good.

Mr. Gayman (Jet Propulsion Laboratory): We certainly agree with your concern about solving large order eigenvalue problems and we try to avoid these wherever we can and we have been fairly successful. This is one of the reasons we sponsored the development of the Component Mode Synthesis a few years back. We

wind up solving more smaller-order eigenvalue problems so we retain some physical sense of what we are doing with the smaller order problems.

Mr. Mains: I do not need to answer that. I agree.

Mr. Coale (Lockheed Missiles and Space Company): I am in the business of reducing problems just as Dr. Mains is and I am most interested in modal syntheses. But I do not really believe there is a panacea to be had in reduction for its own sake. We at Lockheed have had big problems, from one to 3000 or 4000 degrees of freedom, and we have actually had more problems with ill-conditioning and computation error in reducing than we have with direct solution of the eigenvalue problems. We happen to have two eigenvalue solvers that do a very good job with large problems.

Mr. Mains: But you only solve for a few of the eigenvalues.

Mr. Coale: That is all we want, and we check them against problems for which we know the answers. Anytime that you have a difficulty with a solution you do what you always did in school, before there were computers, you go back and work a problem that you think you know the answer to, and work with it until you get it to work before you go to problems where you do not know the answer. I believe that this is a good scheme, but so is direct solution. I have to say that because a little later this afternoon I will present a paper in which I solve large problems.

Mr. Mains: No need to reply to that either.

Mr. Workman (Battelle Memorial Institute): I take exception to your dim view of the state of the art in numerical analysis in computer application. We do not solve nearly as large problems as the aerospace industry. We have solved problems of up to 2000 by strictly Gaussian elimination with iterative improvement, in the static sense, and have found no numerical problems. We have a Control Data machine. Dynamically, by using Householder's method followed by the QR transformation and either inverse iteration or however you define the eigenvectors, we found total eigenvalues for systems, in our case 300 or 400, and have found no problems, no negative eigenvalues.

Mr. Mains: The Householder technique, tridiagonalization, and then forward elimination and back substitution is the scheme that I use for

my eigenvalue routine. When I switched that over to the IBM 360 at double precision I had to reset the gate on acceptance of the eigenvalue. If the difference between the last iteration and the present iteration were smaller than 10^{-8} I stopped and went on to the next root. On the IBM 360, in double precision, you get 14 digits. I started with 10^{-14} and the program just looped, so I backed up to 10^{-13} and it still looped, so when I got down to 10^{-10} it would just stay stable. So I run with 10^{-10} for my criterion. But if I had a bigger problem than my present limit of 80 I am not sure that I could get away with 10^{-10} . I might have to go to 10^{-8} or 10^{-7} . This is what concerns me. The computational accuracy is limited because of the physical capabilities of the computers.

Mr. Workman: That is true that the work side is certainly a critical factor besides conditioning number in numerical solution. But the Control Data in single precision is the same as the IBM 360 in double precision. We have experienced no problems in 300 or 400. Of course we used the QR transformation after the tridiagonalization process.

Mr. Mains: Do you get all positive roots? Everytime?

Mr. Workman: Yes. We have never had any problem.

Mr. Mains: Will your program tell you if you get a negative root?

Mr. Workman: Yes, it prints out all of the roots.

Mr. Mains: Yes, and you can fix it up so that it prints out all of the roots and prints them out in any order you want and without a negative sign too, but does the solution really give you no negative roots?

Mr. Workman: Well they are printed out that way. As you know the Householder method will put the roots on the diagonal in ascending order followed by the QR transformation. We never have had any problems with it. I notice that NASTRAN uses this Guyan reduction and they use Givens transformations to find their eigenvalues. I would be interested to know if people who have used NASTRAN have had any problems.

Mr. Mains: You are the first man I have ever met who does dynamic analysis and who says he gets all positive roots every time. It never happened to me before.

Mr. Coale: It just occurred to me that we have a check on our program which tells us at any stage of the calculation of eigenvalues, and we calculate them starting with the lowest, how many eigenvalues of that matrix are below a certain level. It would seem to me that it would eliminate the possibility of negative eigenvalues.

Mr. Mains: Well if it told you how many were below zero it would certainly tell you.

Mr. Coale: That is counted; it does.

Mr. Mains: Good.

STRUCTURAL DYNAMICS OF FLEXIBLE RIB

DEPLOYABLE SPACECRAFT ANTENNAS

B. G. Wren, W. B. Haile, Jr. and J. F. Hedges

Lockheed Missiles and Space Company
Sunnyvale, California

This paper will discuss the structural dynamic technology problems unique to flexible rib deployable spacecraft antennas. As such, it will cover the analysis and testing attendant to deployment and on-orbit configurations. In the analysis, due to the physical symmetry of the pertinent configurations, some unique problems arise. Symmetric eigenvalue problems arise and lead to a number of identical roots of the frequency equation. The solution of these multiple eigenvalue problems and current results are presented. This is meant to be a discussion type paper of the various technology problems. Detailed mathematical aspects of the analysis have not been included. However, limited test results are compared with analytical predictions. As antenna structures become large and more flexible, their analysis is growing in interest, complexity and necessity.

INTRODUCTION

In general, antennas (e.g., Fig. 1) obtain higher electrical gains as the diameter (aperture) increases. However, as the antenna diameter grows, it becomes necessary to stow it in a compact shape such that it will both fit within a given shroud envelope and withstand the launch and ascent loads. A current design that achieves this function is the flexible rib deployable antenna. This can be graphically demonstrated with reference to Figs.(2-4). The antenna structure in these figures is used for demonstration purposes only. In its fully open or deployed configuration the structure has a circular paraboloidal shape, e.g., Figs.1 and 4. The main structural elements are (1) a central hub structure, (2) parabolically curved ribs projecting from the hub and uniformly spaced and (3) a lightweight reflecting mesh stretched between the upper edges of the ribs to form an approximately paraboloidal electrical reflecting surface. The cross section of the ribs can be of complex structural shape (either open or closed section).

In the ascent (stowed) configuration, the ribs and mesh are wrapped around the hub and restrained. In space, the rib restraint is removed (e.g., by a pyrotechnical separation event) and the strain energy stored in the ribs powers the deployment. Schematically this is illustrated in Figs. (2-4).

Since antenna size is growing (e.g., Applications Technology Satellites F & G have 30 foot diameter parabolic reflectors) the problems during orbital operations are mainly concerned with attitude stability and control rather than high dynamic loads (as was the case during launch and ascent). A possible exception is the actual deployment sequence itself.

The deployment of the antenna can induce high dynamic loads throughout the entire antenna structure and also transfer a significant amount of torque to the spacecraft.

The dynamics of the deployed configuration (during on-orbit operation) induces rather low loads into the antenna structure and spacecraft if the antenna motions are small and if there is sufficient spectral separation between the open loop control system frequencies and the open loop structural dynamic frequencies of the antenna. However, for the on-orbit configurations, as well as the deployment configuration, of symmetric antenna structures some unique problems arise. A symmetric eigenvalue problem arises and leads to a number of identical multiple roots of the frequency equation (i.e., the so called "multiple eigenvalue" problem). A "brute force" approach does not work for this problem. That is, entering the "primitive" or "global" mass and stiffness matrices

into standard computer eigenvalue programs will result in numbers that are meaningless. The computer simply cannot distinguish the essential features of the type and degree of structural symmetry.

The solution is to decompose the "primitive" or "global" problem into a number of smaller "wave" sized problems. This is accomplished by a Fourier decomposition in the circumferential direction. The "wave" sized problems are solved and then are transferred back to obtain the "primitive" or "global" solution. The basic theory for this Fourier decomposition method can be found in Refs. 1 and 2.

The paper concludes with some recent results of analysis and testing. Emphasis will be given to the results attendant to the deployment and on-orbit configurations.

DEPLOYMENT DYNAMICS

The deployment of a flexible rib antenna is initiated by release of the circumferential restraint which keeps the ribs and interfolded mesh in place around the hub. A typical design uses a number of circumferentially spaced doors, separately hinged to the hub structure, and held in place against the furled antenna by a circumferential cable. Deployment is initiated by pyrotechnic cable cutters. Several distinct phases of motion follow.

Unfurling Phase

During the first, or unfurling phase, the ribs progressively unwrap from the hub. Examination of high speed movies of the deployment indicates that, in plan view, the unfurled portion of each rib approaches a straight line tangent to the hub. As the ribs unwrap from the hub, the "straight" portion of each rib becomes longer until the points of tangency reach the roots of the ribs (e.g., Figs. 2 and 3). At this time, essentially all of the strain energy stored in wrapping the ribs around the hub has been converted to kinetic energy of the ribs and spacecraft. Since angular momentum is conserved, a small retrograde motion is imparted to the hub of the spacecraft.

In the analysis of the unfurling phase, it is assumed that all ribs unfurl in phase. The unfurled portion of each rib is assumed to remain rigid and tangent to the hub. The hub and spacecraft is assumed to be a single rigid body. Angular momentum of the system is conserved and the relative motion between ribs and hub results from release of the bending energy stored in wrapping the ribs. A sketch of a partially unfurled rib, as assumed in the analysis, is shown in Figure 5.

Coast Phase

The second phase of motion is termed the coast phase. During the coast phase, each rib rotates about the line hinge at its root, from a position approximately tangent to the hub to a fully-deployed radial orientation. This phase ends when the rib strikes its alignment stop. Until the last 10-20% of the coast phase the motion is primarily planar. During the last portion of this phase, mesh tension increases and "untwists" the ribs, pulling them into their dished shape.

In the numerical analysis of the coast phase, only the planar motion is considered, and the ribs are assumed to remain straight through this final 90° of travel. There is no further release of stored energy during this phase since the ribs are rotating freely about the hinges. Due to the changing geometry, however, the angular velocities of the ribs and the hub/spacraft will vary.

Impact Phase

The final phase of motion is the impact phase. The ribs strike the stops at the roots, and rebound is limited by individual rib latches or hinge torsion springs. The kinetic energy of the system at lockup produces transient oscillations of the antenna and spacecraft. For an antenna whose axis lies along one of the spacecraft principal inertial axes, the resultant vibrations involve "torsional" modes of the antenna.

Analysis of this phase of motion is based on conventional linear modal response and superposition, using as initial conditions the velocity profile of the rib and hub at the end of the coast phase. Only the wave number zero modes of the system are excited as a result of this pattern of initial velocity (see next section).

Deployment loads at lockup typically are design loading conditions for rib hinges and latches and portions of the hub structure. A typical deployment history, showing the variation of total torque on the hub is shown in Figure 6.

DYNAMICS OF THE DEPLOYED CONFIGURATION

Flexible rib antennas are modelled as finite element systems where each rib and the hub are treated as a number of elemental beams and the mesh as a number of string panels. Rib modelling accounts for their structurally complex shape in that they are, in general, curved, tapered and of open section with offset section shear center, offset section centroid, and offset mesh attachment (e.g., Fig. 7). Mesh to rib attachment is along the concave edge of the rib. In motion, then, rib bending and twisting are coupled and constitute a major feature of the structural behavior. Local Cartesian coordinates were selected at each

analytical point on the structure to define the displacements with all six degrees of freedom being allowed at each point.

From a structural dynamics standpoint flexible rib antennas are difficult to analyze for three important reasons. First, and most obvious, a finite element analysis leads to an extremely large degree of freedom system. Imagine an antenna with 50 ribs, each rib divided into five finite beam segments, and each analytical point allowed six local degrees of freedom. Then, the system will have 1800 total degrees of freedom. Secondly, and less obvious, orders of magnitude in the elemental stiffness and mass coefficients are extreme. In general, the hub is stiff and heavy, the ribs are less stiff and less massive, and the mesh is weak and lightweight. Computer analysis of such a system requires double precision in all calculations, and, even then, may be subject to troublesome round off errors if the system is large. Thirdly, and least obvious but most difficult to analyze is the symmetry of the flexible rib design leading to a high degree of redundancy and multiplicity of roots. Computationally, eigensolutions for problems with multiplicity greater than about six are impossible on computers with programs as they exist today.

All three major problems may be avoided by taking advantage of the structural symmetry in a consistent and logical manner. Such was done by analytically expanding the displacement vector in a finite (finite because the number of ribs is finite) Fourier series in the circumferential direction so that the Fourier coefficients remain undetermined, but the Fourier trigonometric arguments are selected to decouple the problem. Furthermore, the solution obtained will be exact. Mathematics of the technique are fully described in reference 1 and 2 and will not be repeated herein.

The Fourier transformation produces a set of new, smaller size, uncoupled eigenproblems which are solved one at a time and each of which has, at most, a multiplicity of only two. Results are then back transformed to assemble the solution for the primitive antenna. Each transformed problem set describes a "wave number" of the antenna. That is, the rib mode shape patterns occur as wave 0 - all ribs displace identically; wave 1 - rib displacements are coefficients of $\sin \theta$; wave 2 - rib displacements are coefficients of $\sin 2\theta$; etc. θ is the circumferential angle, 0 to 2π measured around the antenna.

Graphic results obtained (for a free-free structure) from this technique follow in Figures 8 (8a-8l) where the wave number and mode shape number (for that wave) are labeled on each figure.

A side benefit of this type of analysis is that many "almost multiple roots" are avoided. That is, since the mesh is usually weak compared to the ribs and constitutes the element which joins the ribs, a given mode in each wave number will have an almost identical natural frequency but a very different mode shape. However, by solving the problem in wave numbers, it is unlikely that, in a single wave number type, there will be closely spaced natural frequencies. Computer solutions favor widely separated and distinct eigenvalues (frequencies) in structural problems.

Once the natural frequencies and mode shapes of the antenna are known, it is possible to build the modal equation of motion using as many modes of as many types as desired. The result is then used in a modal superposition analysis where other parts of the spacecraft assembly may be added, and/or in a forced response analysis by applying modal forces and including modal damping parameters. The methods used follow the usual structural dynamics techniques except that the analyst must remember that the flexible rib antenna problem has already been through one transformation so that its modal properties represent not the physical antenna but the transformed one.

For the time conscious reader, using the method described herein, 50 mode shapes were found for a 48 rib reflector complete with hub assembly in a 4 minute 1106 computer run.

RESULTS AND CONCLUSIONS

This paper has presented the essential features of the structural dynamic technology problems associated with flexible rib deployable spacecraft antennas. Typical results have been presented that indicate very good correlation with limited tests results.

Mathematically modelling two antennas for which test results were available and predicting natural frequencies and mode shapes for the structure with a fixed hub produced the following correlation:

	First Natural Frequency, Hz	
	Test	Analysis
30' ATS antenna	1.13	1.12
14' test antenna	2.60	2.68

Test results were produced during deployment of the structure in a one g environment by averaging values of the "cup up" deployment and the "cup down" deployment. Once high frequency modes had essentially been attenuated by damping, only the first natural frequency torsional mode remained. This mode was used for analytical correlation.

Even without test results for comparison, indications of flexible rib antenna behavior may be inferred from the computed mode shapes. Though not clearly shown on the modal plots of Figure 8, coupling of all degrees of freedom is pronounced since the ribs have offset elastic axes and the typical rib is weak in torsion. Among the modes presented, Figures 8(b-1) show a significant amount of coupling. Also notice the clearly spaced frequencies of wave 2, mode 3; wave 3, mode 3; and wave 4, mode 3. These closely spaced frequencies continue through all wave number sets. So, if the designer wishes to know all modes with frequencies below a certain value, he is likely to be presented with an immense amount of data; say, the first six or eight modes from each possible wave number. For the 48 rib example shown, $6 \times (48/2 + 1) = 150$ modes with natural frequencies below 20 Hz.

REFERENCES

- a. M. L. Gossard and W. B. Haile, Jr.,
"Structural Dynamics of a Paraboloidal Antenna", The Shock and Vibration Bulletin No. 41, Part 6, pp. 103-114, Dec. 1970.
- b. M. L. Gossard and W. B. Haile, Jr.,
"Structural Dynamics of Flexible Rib Antennas", LMSC-A983874, Lockheed Missiles and Space Company., Sunnyvale, California, Sept. 15, 1971.

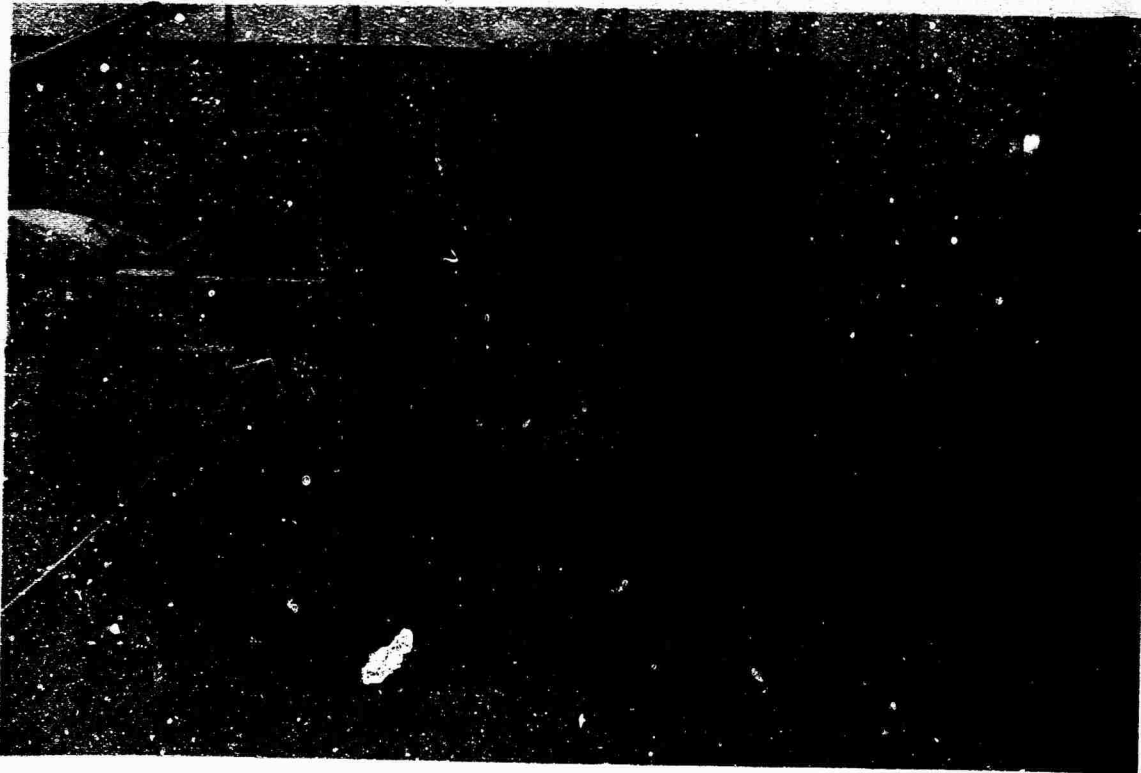
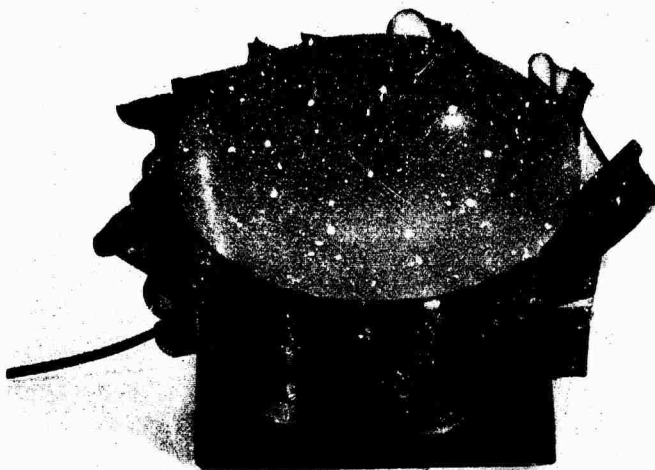


FIG.1 20 FOOT DIAMETER FLEXIBLE RIB ANTENNA



Reproduced from
best available copy.

FIG. 2 ANTENNA MODEL (INITIATION OF DEPLOYMENT)

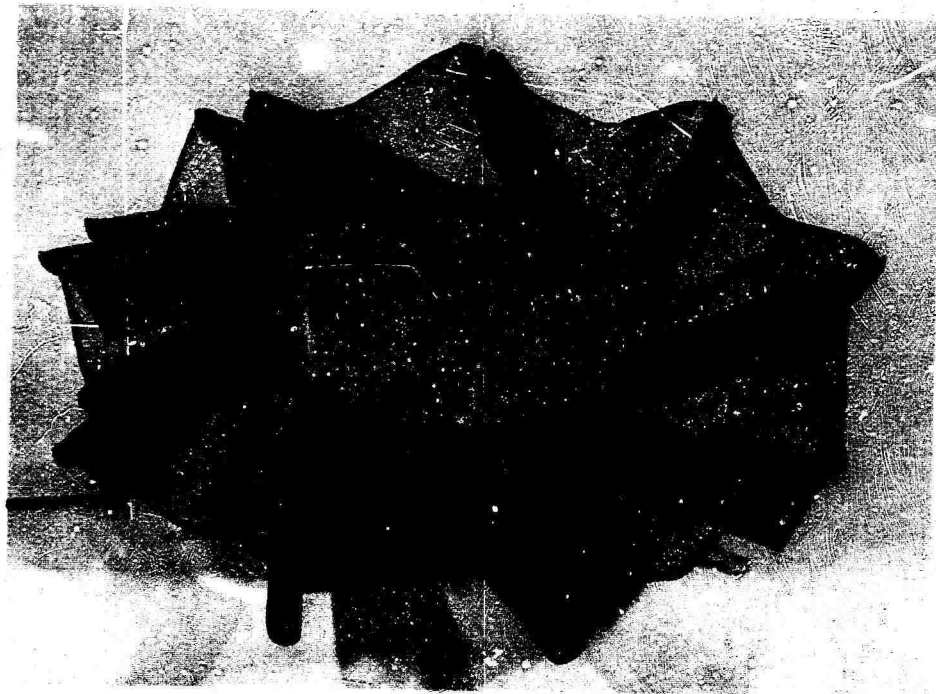


FIG. 3 ANTENNA MODEL (PARTLY DEPLOYED)

Reproduced from
best available copy.

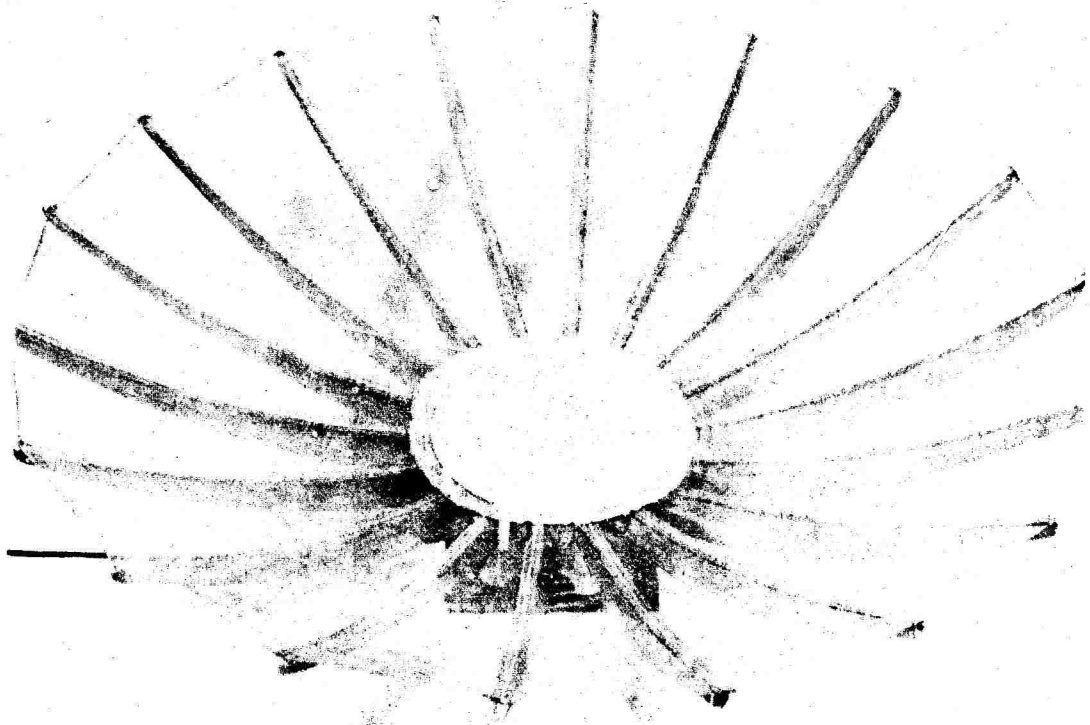


FIG. 4 ANTENNA MODEL (FULLY DEPLOYED)

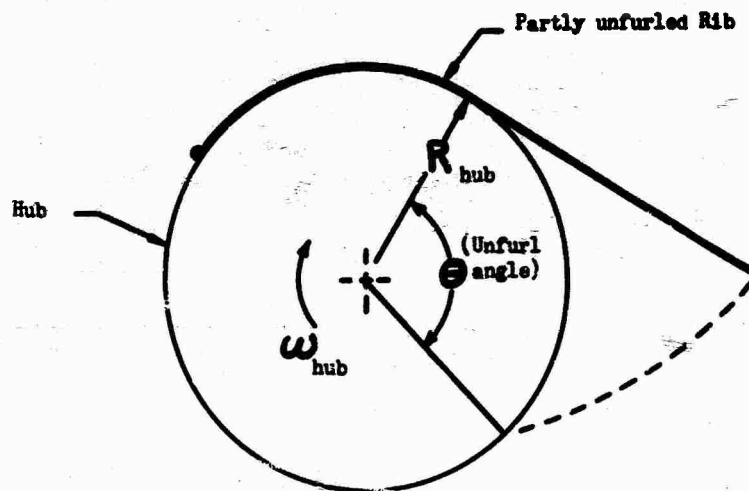


FIG. 5 DYNAMIC MODEL OF UNFURLING PHASE

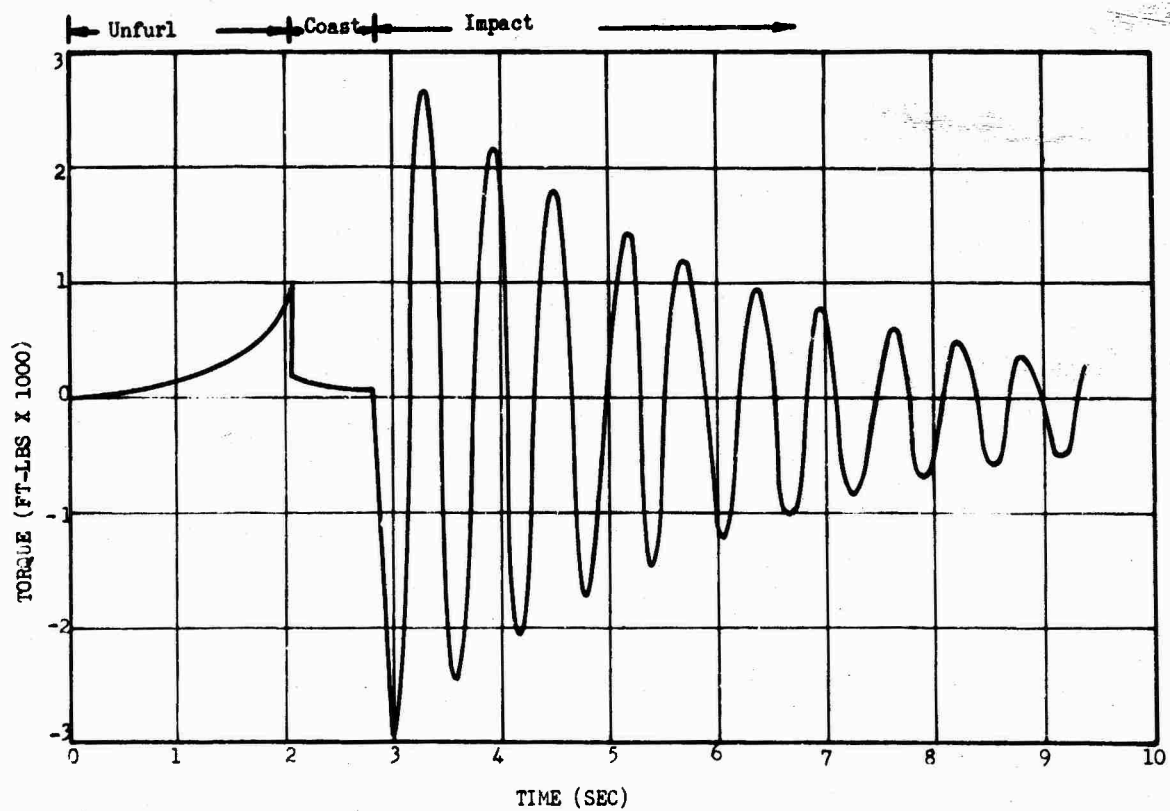


FIG. 6 DEPLOYMENT TORQUE HISTORY

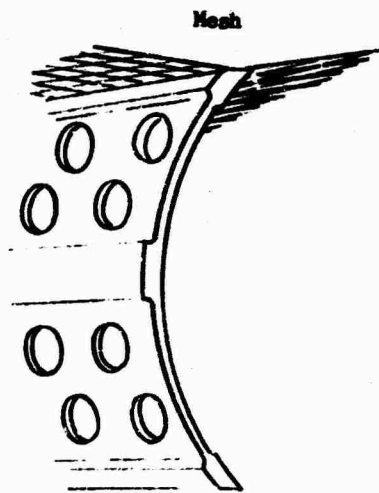
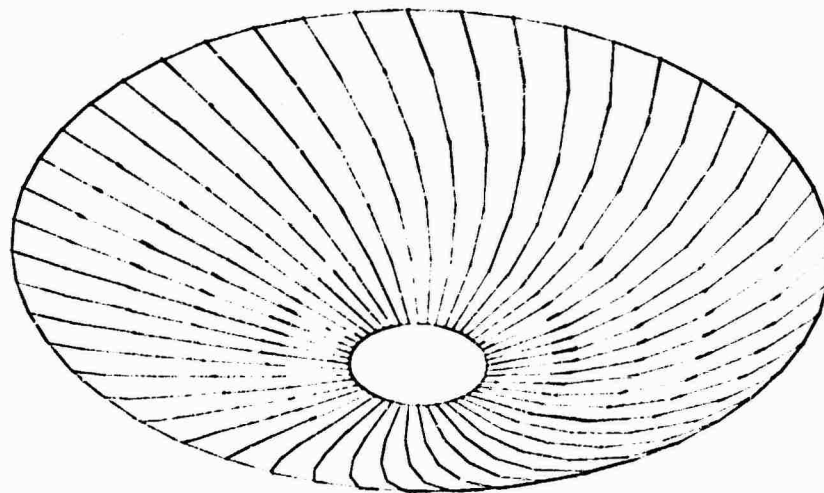


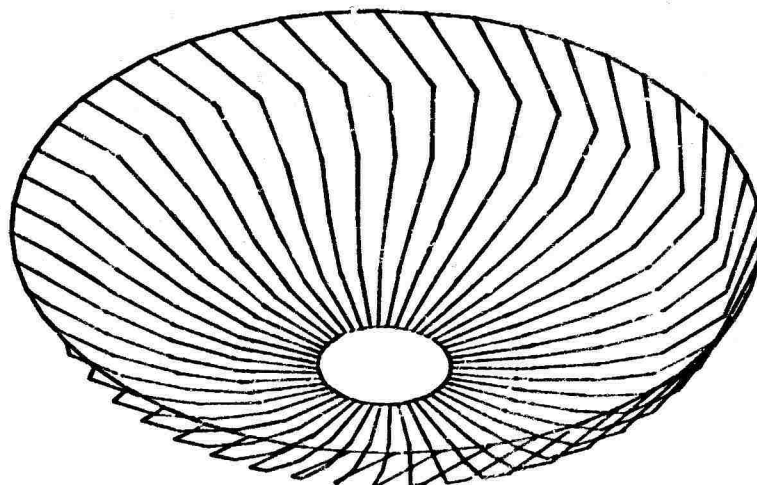
FIG. 7 TYPICAL RIB SECTION



WAVE 0, MODE 3, 2.17 Hz

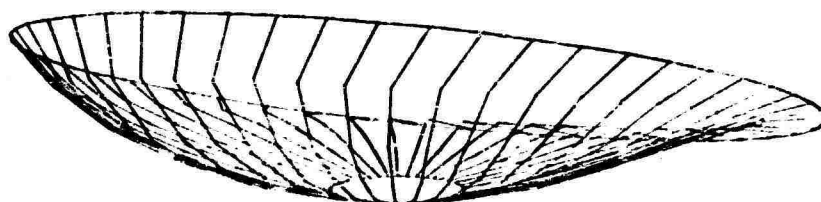
(a)

FIG. 8 TYPICAL ANTENNA MODE SHAPE



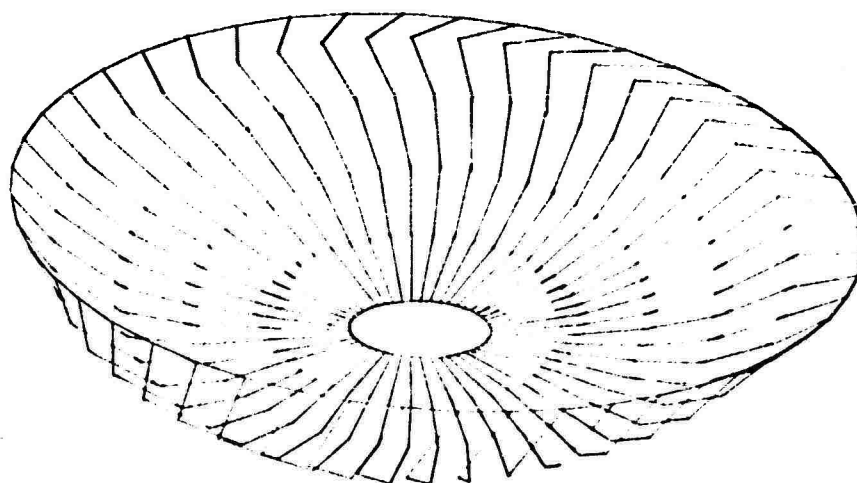
WAVE 0, MODE 4, 7.24 Hz

(b)



WAVE 1, MODE 5, 9.54 Hz

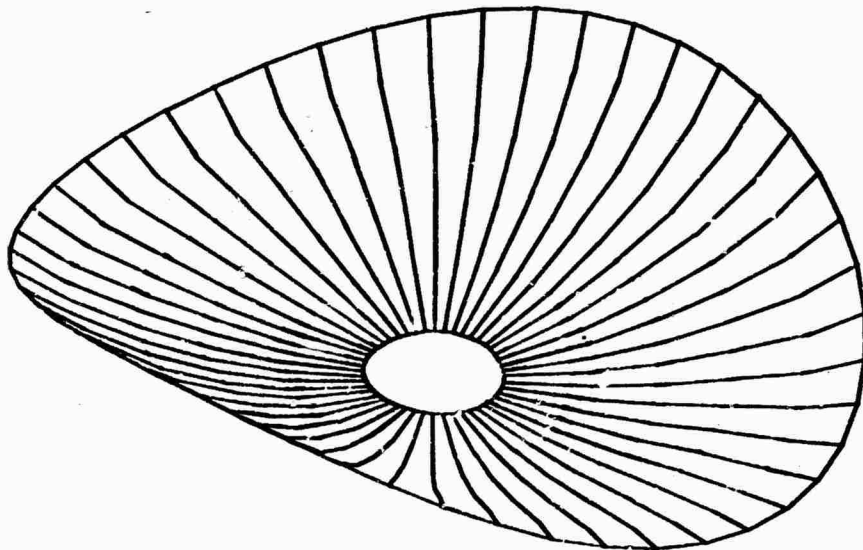
(c)



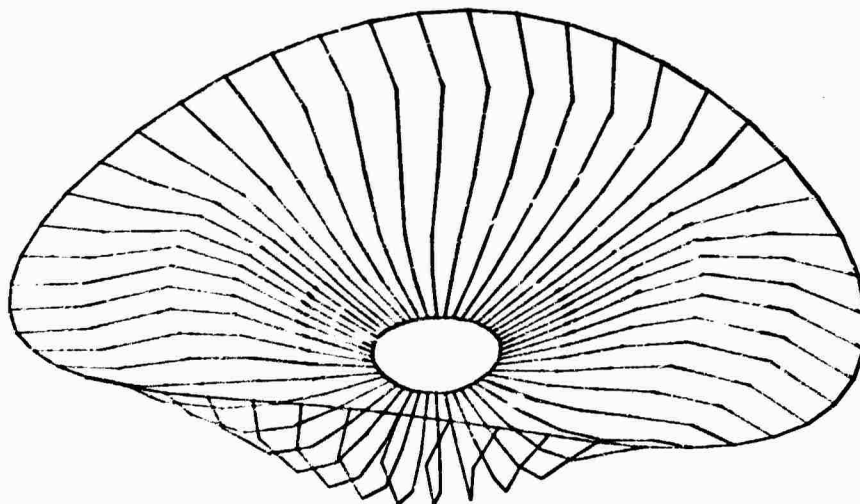
WAVE 1, MODE 7, 11.27 Hz

(d)

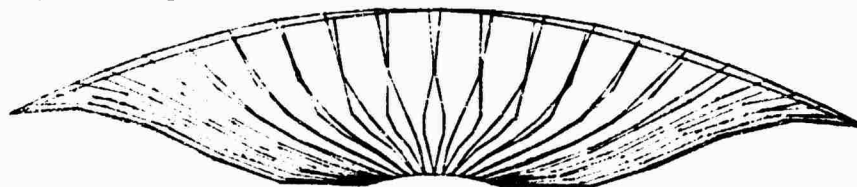
FIG. 8 (CONT'D) TYPICAL ANTENNA MODE SHAPE



WAVE 2, MODE 1, 4.17 Hz
(e)

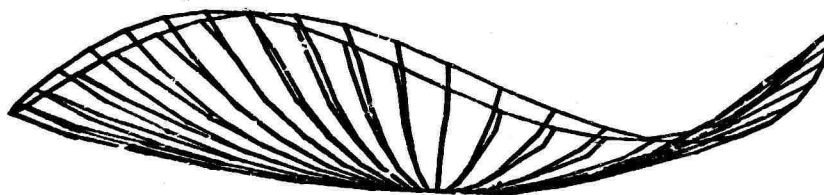


WAVE 2 MODE 3, 10.05 Hz
(f)

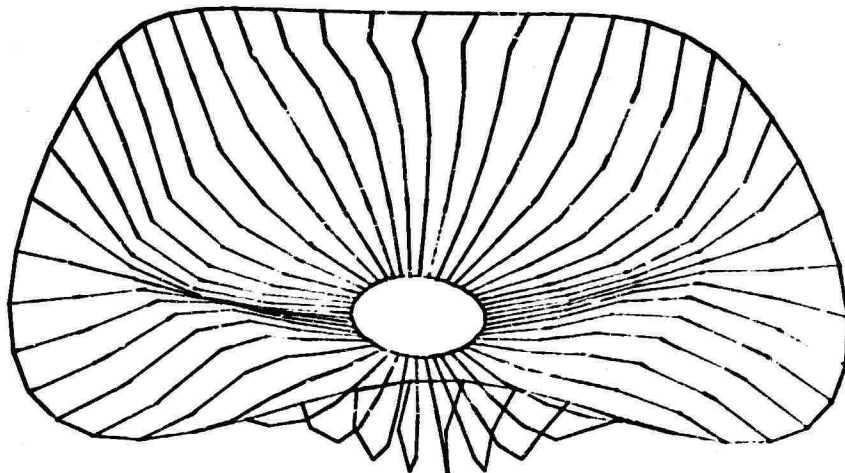


WAVE 2, MODE 5, 12.84 Hz
(g)

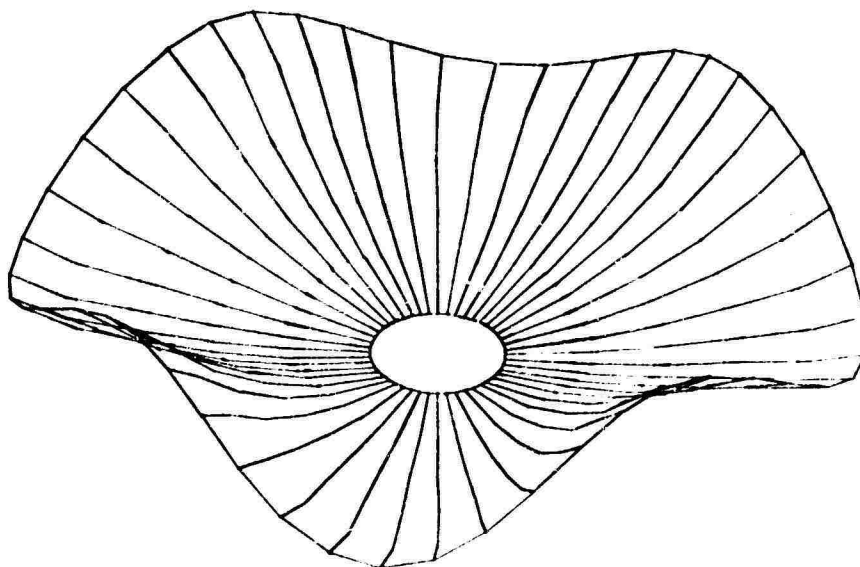
FIG. 8 (CONT'D) TYPICAL ANTENNA MODE SHAPE



WAVE 3, MODE 1, 6.02 Hz
(h)

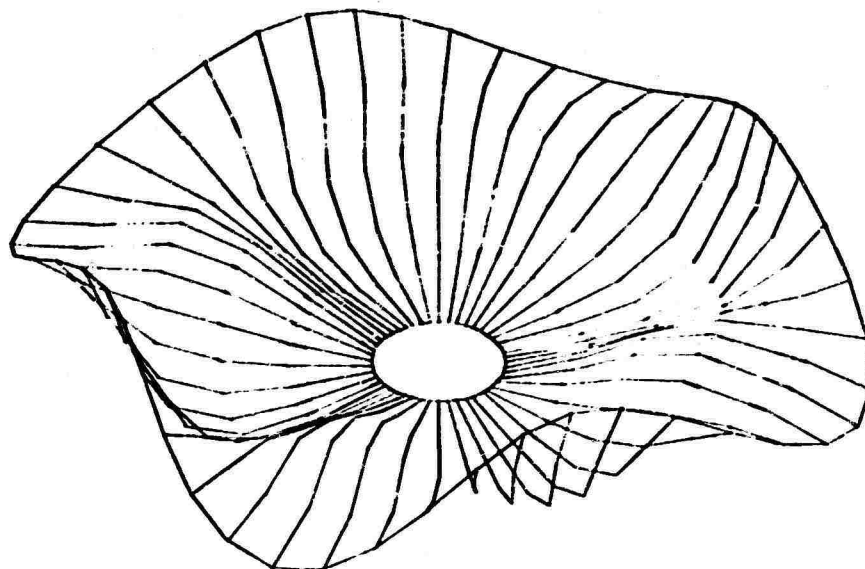


WAVE 3, MODE 3, 10.54 Hz
(i)

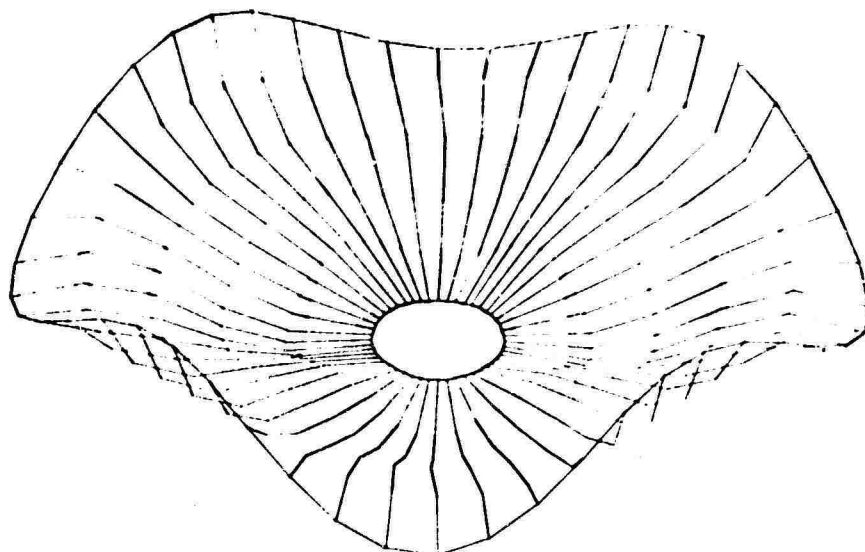


WAVE 4, MODE 1, 6.80 Hz
(j)

FIG. 8 (CONT'D) TYPICAL ANTENNA MODE SHAPE



WAVE 4, MODE 3, 10.68 Hz
(k)



WAVE 4, MODE 5, 13.77 Hz
(l)

FIG. 8 (CONT'D) TYPICAL ANTENNA MODE SHAPE

INFLUENCE OF ASCENT HEATING ON THE SEPARATION DYNAMICS OF A SPACECRAFT FAIRING

C. W. Ccale, T. J. Kertesz
Lockheed Missiles & Space Company, Inc.
Sunnyvale, California

The problems created by buildup of thermal prestresses in a separable spacecraft fairing are considered in this paper. These prestresses are produced by ascent heating of the fairing. When the fairing is cut pyrotechnically above the atmosphere into two halves and jettisoned the thermal prestresses seriously affect the early post-separation dynamic response of the fairing and can cause the fairing to hang up or to bump the enclosed spacecraft. The problem is evaluated and approaches to both thermal static and structural dynamic analysis are outlined. Some results of actual calculations for a large fairing are presented.

INTRODUCTION

This paper treats the clamshell-like jettisoning of a space vehicle fairing in the presence of thermally-induced prestresses. Unprotected spacecraft, designed to operate in orbit or on a space trajectory, are frequently too fragile to survive ascent through the atmosphere. For protection, the spacecraft is enclosed in a fairing which is designed to withstand the ascent environment (Fig. 1a). Once above the sensible atmosphere the fairing is separated by means of pyrotechnic joints into two halves, rotated away from the main vehicle by compressed helical springs, and at about a 60° angle from the vehicle axis, separated from the vehicle completely and jettisoned (Fig. 1b).

The fairing in addition to surviving the ascent in good condition, must be built to separate reliably and cleanly. If the fairing does not separate or if there is a delay in separation the entire launch may be a failure. Likewise, if the fairing intrudes into the spacecraft envelope during separation and strikes the spacecraft unacceptable damage may occur. Even if damage or failure is avoided, flexible fairing oscillations may produce unacceptable excitation of the booster during separation. Full scale ground tests are used to evaluate separation behavior of the fairing. However, these tests are costly and cannot cover the full range of conditions to which the fairing may be exposed. A parallel engineering analysis is therefore necessary. This paper describes such an analysis and some of the results obtained.

Before discussing the problem in more detail a brief description of fairing geometry and construction is in order. The fairing considered in this paper is a light, ring-stiffened corrugated shell structure composed of a long cylinder, a double cone and a spherical cap. Some details of the shell construction are shown in Figure 2. Because of the longitudinal separation joint the pre-separated fairing is not axisymmetric. The joint itself has no moment carrying capability. Along each side of the joint runs a stringer to provide edge stiffening. Thus after separation the fairing halves are composed of ring-stiffened half shells with longitudinal edge stiffeners. The base ring at the open end of the cylinder is made relatively stiff both to prevent excessive motion of the bottom corner of the fairing and to distribute the hinge loads. Both bending and torsional stiffness of the post-separated fairing halves are rather low because of the open cross section.

SOURCES OF FAIRING EXCITATION

A number of loadings combine to produce fairing dynamic response after initiation of separation. The primary driving force acting on the fairing halves is produced by the prestressed thruster springs. The sudden release of the stored energy produces breathing and twisting motions in the fairing halves.

A contained pyrotechnic explosive which separates the fairing from the booster and "cuts" it into two sections produces an impulsive loading. This loading may be radial or tangential depending on the joint design.

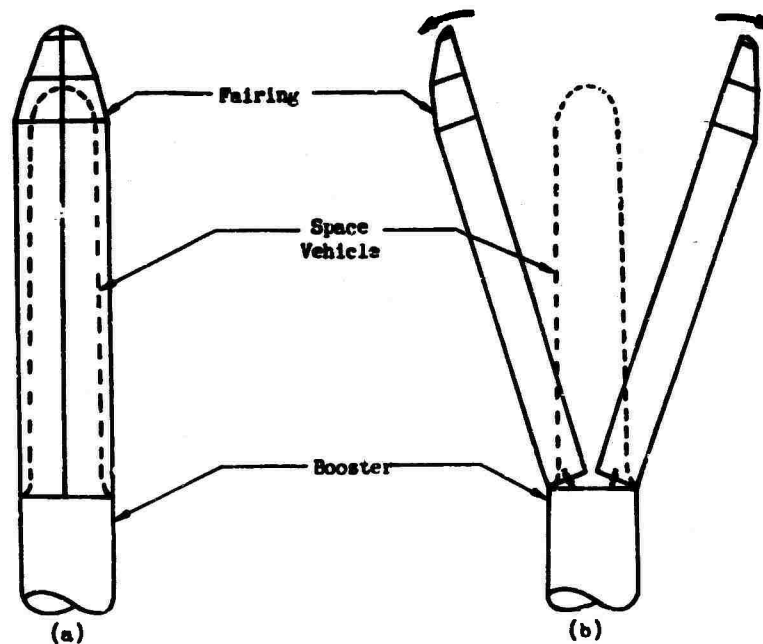


Fig. 1. Space Vehicle with Separable Fairing

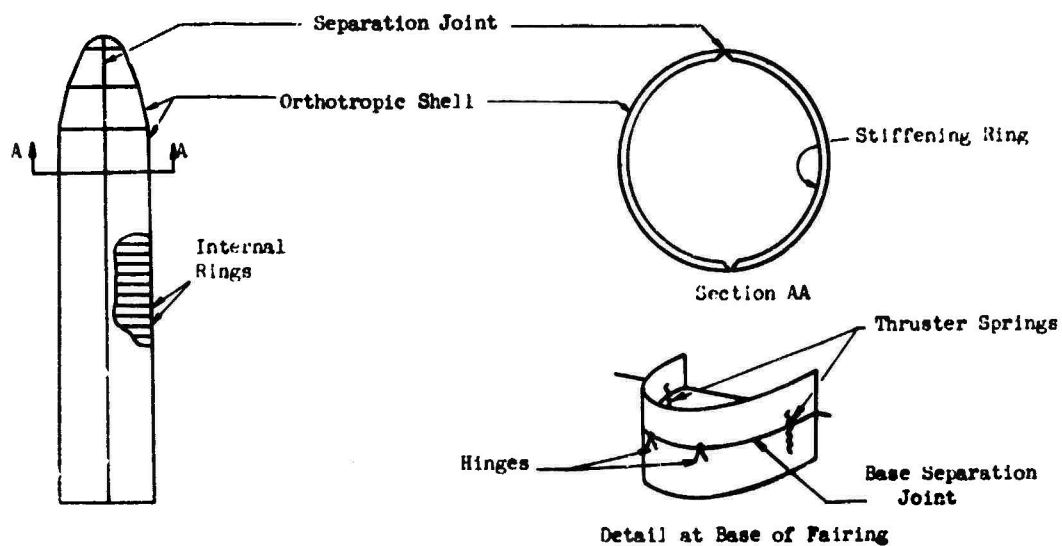


Fig. 2. Space Vehicle Fairing - Construction Details

Any appreciable amount of oscillatory or transient motion of the booster during separation is transmitted through the hinges to produce a "foundation excitation" acting on the fairing halves. Such a vehicle excitation may be caused by residual oscillation after engine ignition or by control system limit cycling.

In addition to the above, a more subtle excitation of the fairing can occur. During ascent the launch vehicle reaches supersonic velocity through the atmosphere. As a result a strong bow shockwave is produced at the nose of the vehicle. Across this shockwave a large rise in temperature occurs. Because the trajectory is curved and because of steering maneuvers, the vehicle moves at an angle of attack through the atmosphere causing the heating to vary significantly around the circumference of the vehicle. The resultant temperatures in the fairing are a function of the mass and conductivity of metal involved in any one area, thermal resistances between assembled parts, and surface reflectivity of the fairing surface. In addition to varying longitudinally and circumferentially the temperature of the fairing varies radially between the outer skin and the inner flange of the rings creating gradients across the ring-skin combination.

Heating produces deflections and distortions in the fairing as well as internal prestresses. When the fairing is separated into two halves the sudden release of the thermal prestresses produces significant dynamic excitation.

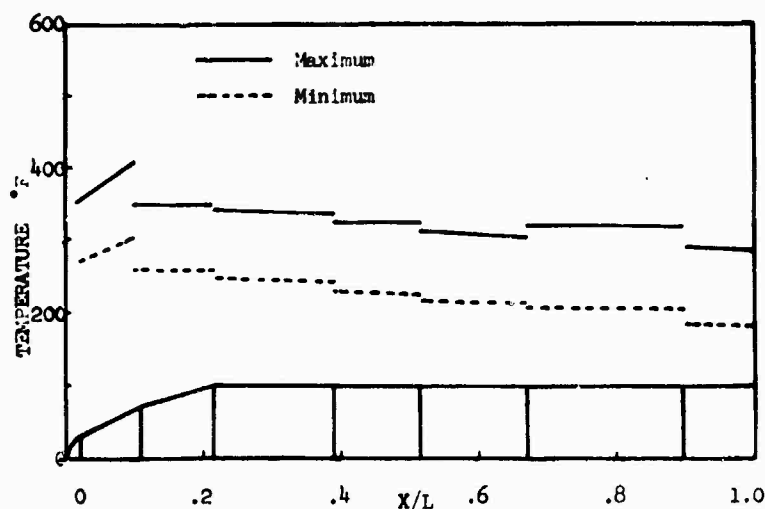
Prestressing can also occur because of manufacturing imperfections and assembly procedures. This type of prestress is largely controllable or correctable.

FAIRING ANALYSIS

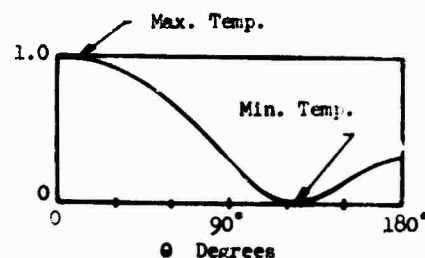
Significant information concerning fairing behavior during separation can be obtained through analysis of rigid fairing models and non-thermal flexible fairing models.

However, for large fairings (diameters of 8 feet or larger) all of the previously mentioned effects must be considered. For this purpose a finite element model of the fairing is most suitable. Such a representation is capable of taking into account various features of the fairing configuration and construction as shown in Fig. 2. The model can be used to determine modal behavior of the complete, pre-separated fairing. More importantly the modal behavior of the post-separated fairing halves (Fig. 1b) on hinges and springs can be calculated. These modes include nearly-rigid rotation about the hinge line, beam motion, torsional motion, and shell modes of the half cone-cylinder.

The influence of ascent heating which produces deflections and internal stresses in the fairing requires a further, more sophisticated analysis. For this problem the finite element model of the fairing is altered to permit thermal static calculations. Deflections of both the pre-separated, complete fairing and the post-separated fairing halves must be considered. Once the thermal static deflections of the fairing have been calculated it is possible to formulate a thermal initial condition for use in the postseparation dynamic analysis. This analysis and the results obtained are discussed in the following sections.



(a) Longitudinal Temperature Distribution



(b) Circumferential Temperature Distribution Function

Fig. 3 - Fairing Temperatures at Separation

PAIRING THERMAL STATIC BEHAVIOR

As previously mentioned, because of angle of attack histories and steering maneuvers, the fairing experiences asymmetric heating circumferentially. Due to the existence of localized heat sinks, i.e., rings, and thermal resistances between the corrugation sheet, face sheet, and ring flanges, there are also temperature differences between the shell and ring inner flanges at the time of separation. Typical longitudinal and circumferential temperature distributions are shown in Figure 3.

The longitudinal distribution changes radically at the cone-cone and cone-cylinder junctions and varies gradually along the length of the cylinder. The circumferential distribution is specified by a maximum and minimum at each longitudinal station. A normalized circumferential distribution function which may vary at different axial stations can be used to describe the skin temperature variations at any circumferential location.

Radial temperature gradients can be specified by defining a second layer of temperatures over the entire fairing in the same manner.

A circumferential distribution of temperatures is shown in Fig. 4. In Fig. 4a the maximum temperature point (windward point) lies in the separation plane of the fairing. Note that although there is only one maximum, two minimums occur at about 120° from the windward side. Fig. 4b shows a case where the windward maximum temperature point occurs at an angle to the separation plane of the fairing. This is termed a skewed temperature distribution at skew angle ϕ .

The temperature distributions shown in Fig. 3 cause thermal deflections and stresses which in large part are relieved at separation. To limit the scope of this paper, dynamic response due to circumferential skin temperature distributions only will be treated. Radial temperature gradients will be assumed to be zero. Dynamic response due to gradients is equally important and can be treated in a similar manner.

Without considerable experience with behavior of structures under non-uniform heating conditions, it is difficult to predict or to evaluate the behavior of the fairing under the temperatures of Figs. 3 and 4. However, considerable insight into static behavior of the fairing subjected asymmetric heating can be gained by decomposing the circumferential temperature distribution of Fig. 4 into Fourier component distributions and considering the effect upon the fairing of these individual simplified distributions. Because the problem is assumed to be mathematically linear the deflections produced in the fairing by the individual Fourier component temperatures can be recombined to yield the fairing response to the original temperature distribution. Any arbitrary

circumferential distribution of temperature can be expanded in a series of sine and cosine distributions.

$$F(\theta) = a_0 + a_1 \cos \theta + b_1 \sin \theta + a_2 \cos 2\theta + b_2 \sin 2\theta + \dots$$

These component distributions are shown in Fig. 5. The first or zeroth cosine component is a constant temperature rise circumferentially. Fig. 3 shows this to be the major part of the elevated temperature. In the case of a constant circumferential temperature, the fairing (assuming a uniform coefficient of thermal expansion) grows radially and longitudinally without other distortion and without buildup of internal stresses. This component distribution therefore has negligible effect upon the separation process.

The $\cos \theta$ and $\sin \theta$ components each produce a transverse bending of the fairing as a beam. This bending always occurs away from the maximum temperature point. In spite of the fact that the fairing is distorted, no internal stresses are built up. Therefore, if the pre-separated fairings were heated with either of these two temperature components and then separated, the fairing halves would not be excited dynamically. Thus while this is the most visible part of the pre-separated thermal response, it has no significance in determining post separated dynamic behavior.

The $\cos 2\theta$ component is symmetric with respect to both the separation plane and the perpendicular "backbone" plane. If the coefficient of the $\cos 2\theta$ component is positive, the separation edges of the half fairings are raised in temperature while the backbones are cooled. Because of differential expansion and contraction longitudinally, the post separated half fairings would like to bend away from each other, as shown in Fig. 5. However since prior to separation the two halves are attached, they react on each other and essentially no distortion occurs. Sizeable internal prestresses however do build up. If the complete fairing were heated with this component and then suddenly separated, the fairing halves would vibrate about their post-separated static equilibrium positions.

The $\sin 2\theta$ component shows similar behavior except that this component represents a distribution skewed 45° with respect to the separation plane. In fact this distribution is antisymmetric with respect to both the separation and backbone planes. Because of the two planes of symmetry of the fairing, the response is also antisymmetric with respect to both planes. Before separation the two halves of the fairing react on each other to effectively prevent distortion. The separated halves under this distribution move sideways and twist as shown in Fig. 5. This Fourier component is particularly significant in reducing clearance between the fairing and the enclosed spacecraft. Higher order Fourier components show similar characteristic behaviors which become more localized and less significant for overall fairing motion.

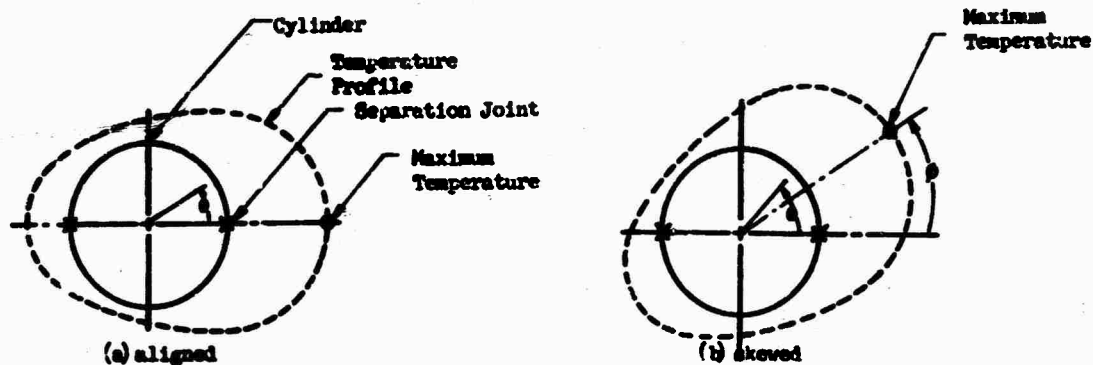


Figure 4 - Circumferential Temperature Distributions

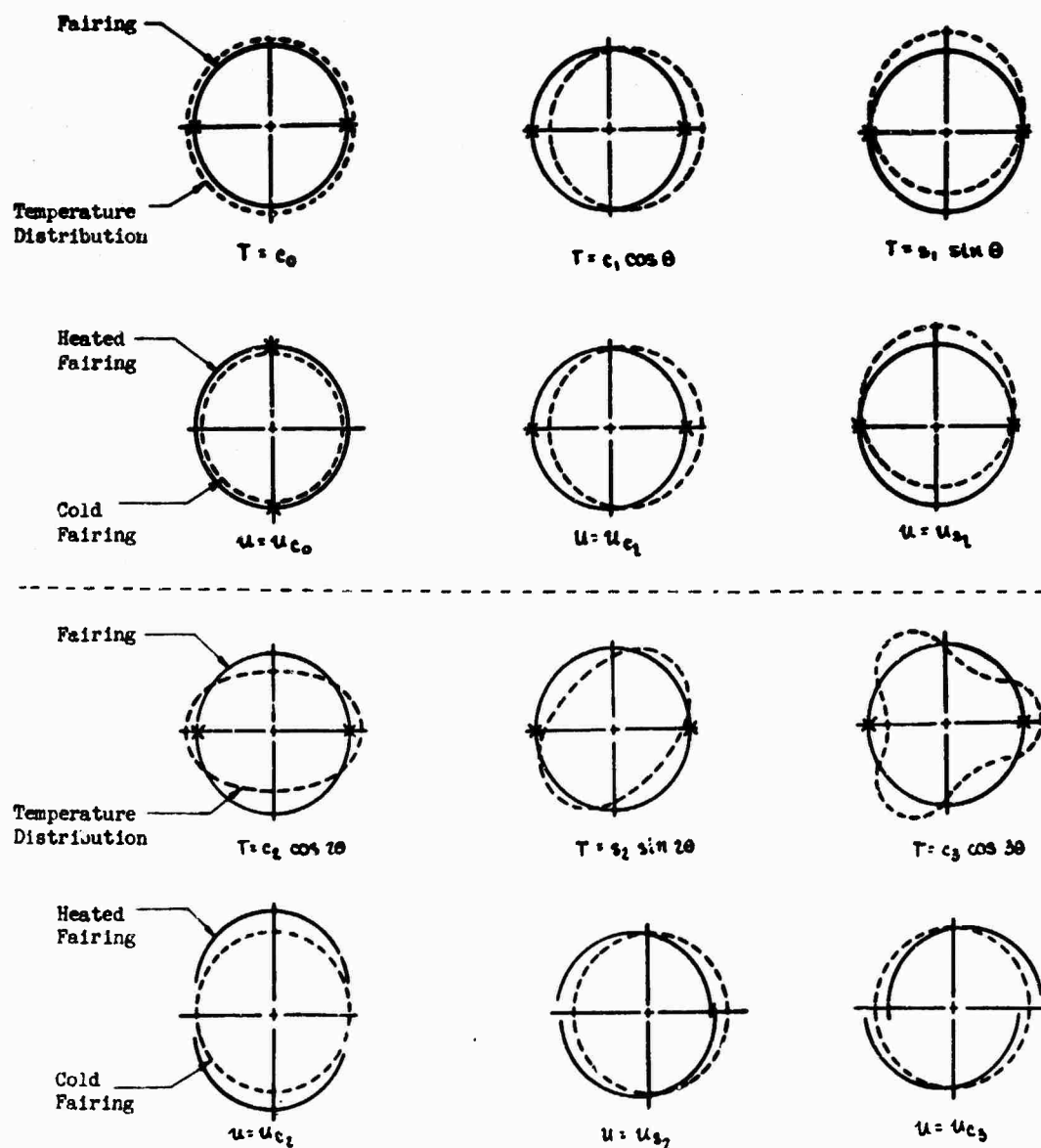


Figure 5 - Fourier Component Temperatures & Deflections

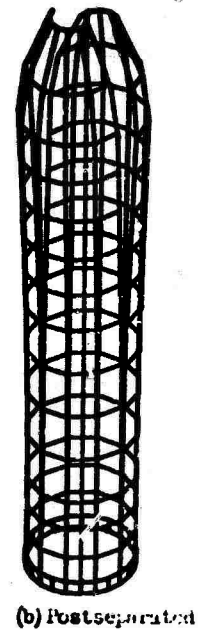
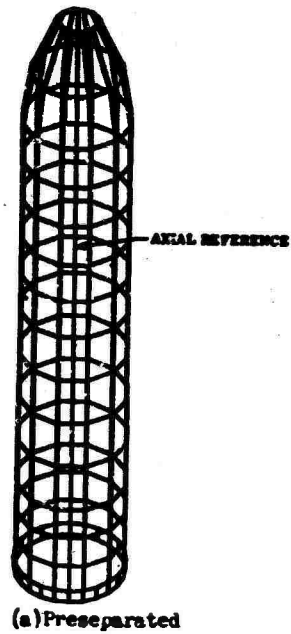
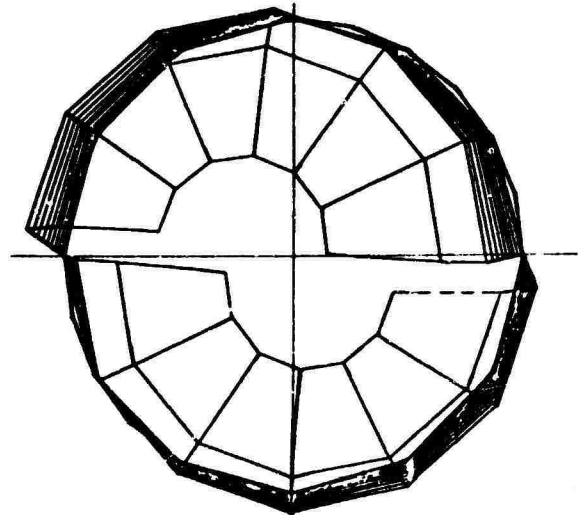
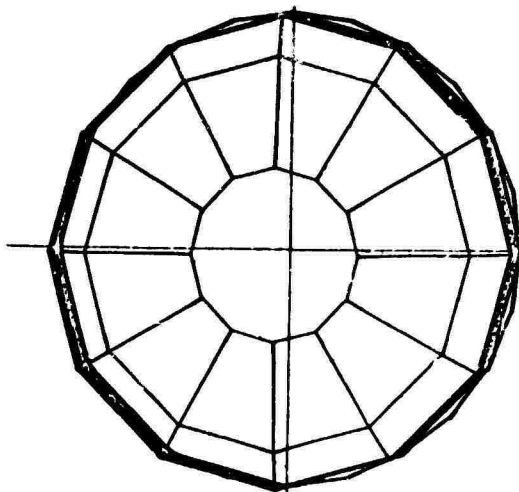


Figure 6 Fairing Thermal Static Deflection - Isometric View



(a) Pre-separated

(b) Post-separated

Figure 7 Fairing Thermal Static Deflection - Top View

Consider now the thermal static deflection of the fairing under the asymmetric temperature distribution of Fig. 3 acting at a 20° skew angle. In Figure 6a a three-dimensional schematic drawing of the fairing is shown. When this pre-separated fairing is subjected to asymmetric heating, the principal deflections are longitudinal growth and a "hotdog" type of bendover away from the hot, windward side. In addition, internal prestresses are created in the fairing. This is graphically illustrated in Fig. 6b. This figure shows the static equilibrium of the two post-separated fairing halves under the same temperatures. These two halves could be brought back into juxtaposition by application of edge forces equivalent to the internal joint stresses in the pre-separated fairing. Figures 7a and 7b show an end view of the pre and post-separated fairing under the same temperature distribution. It is further possible to look at the deflections at any cross-section of the fairing as in Fig. 8. This figure shows the original position of the cross section of the cold fairing, the corresponding position of the heated pre-separated fairing and the positions of the two post-separated fairing halves. Additionally, the spacecraft envelope at this cross-section is shown. All of the deflections as well as the spacecraft clearance have been multiplied by a factor of 2 in the figure.

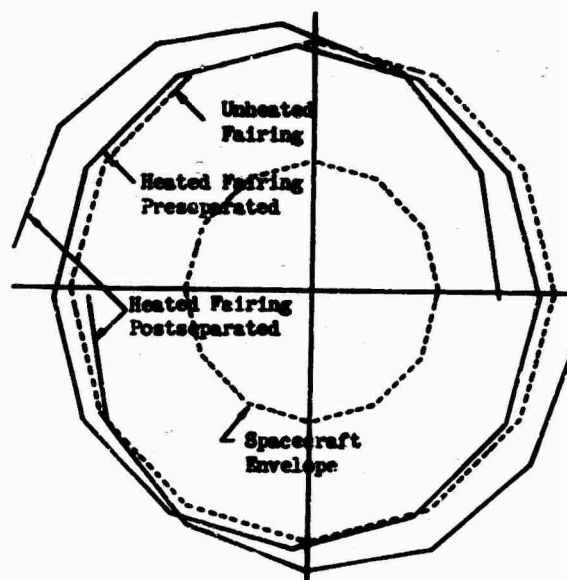
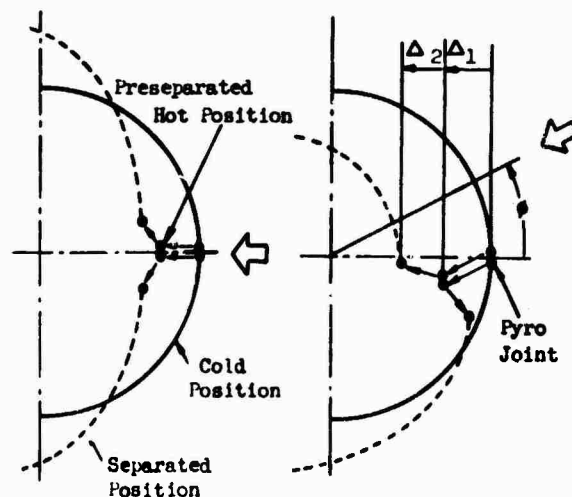


Fig. 8 - Fairing Thermal Static Deflection Crosssectional View

Figure 9 illustrates more clearly the influence of the skew angle. This figure shows the displacement cross section before and after separation under two different heating conditions. In Figure 9a the static deflection of pre and post-separated fairing sections are shown when the effective windward generator is in the fairing separation plane. Figure 9b depicts the corresponding deflected positions when the windward generator is rotated out of this plane. With the skew angle zero the symmetric temperature distribution is aligned with a plane of symmetry of the fairing and the displacements are also symmetric as shown. Note that the windward edges of the fairing move inward toward the spacecraft before separation and move in slightly farther after separation as well as springing outward tangentially.



- Δ_1 = Preseparation Deflection
- Δ_2 = Postseparation Deflection
- ϕ = Skew Angle
- \leftarrow = Maximum Temperature

Fig. 9 - Influence of Skew Angle on Fairing Deflections

The behavior of the fairing under the skewed temperature distribution of Figure 9b is more serious. Here the heated pre-separated fairing moves away from the maximum temperature point as expected. Upon separation one separated edge moves inward, the other outward. The edge which moves inward can cause serious loss of spacecraft clearance.

POSTSEPARATED DYNAMIC RESPONSE OF THE HEATED FAIRING

The basic approach to the dynamic response analysis of the fairing under the thermal prestress consists of considering the problem as primarily a linear, free vibration problem with specified initial displacement and velocity conditions, and with time-varying excitation provided only by booster transient motions.

This is accomplished as follows: Displacements $\{u(t)\}$ of the fairing, measured with reference to a fixed coordinate system, are decomposed into three parts

$$\{u(t)\} = \{u_r(t)\} + \{u_s\} + \{\tilde{u}(t)\} \quad (1)$$

Here $\{u_r(t)\}$ represents rigid body motion of the fairing produced by "base motion" of the booster. During separation this motion is transmitted through the hinges and thruster springs. The second component $\{u_s\}$ is measured from the unloaded static equilibrium configuration of the postseparated fairing with no "base motion" present. In this equilibrium position the thruster springs are not prestressed and the fairing is at a non-elevated reference temperature. To obtain displacements $\{u_s\}$, the lower end of the thruster springs are moved to the prestress position. Since the fairing halves are free to move, this does not prestress the springs but causes the fairing halves to rock backward on the hinges to a new equilibrium position. The fairing is now heated to the separation temperatures and additional deflection of the fairing occurs. The resulting combined deflection configuration of the fairing from its original equilibrium position is designated as $\{u_s\}$.

Consider next that the edge forces are applied to the longitudinal and base separation edges to bring the fairing halves together in their heated, pre-separated equilibrium position. This displacement configuration is designated as $\{u_A\}$ and is the same configuration as is obtained by heating the pre-separated fairing and prestressing the thruster springs.

The vibration problem in terms of the unknown flexible dynamic component $\{\tilde{u}\}$ of Eq(1) can now be expressed as

$$[M]\{\ddot{\tilde{u}}\} + [D]\{\dot{\tilde{u}}\} + [K]\{\tilde{u}\} = -[M]\{\ddot{u}_r\} \quad (2)$$

$$\{\tilde{u}(0)\} = \{u_A\} - \{u_s\} \quad (3)$$

$$\{\dot{\tilde{u}}(0)\} = \{\dot{u}_c\} \quad (4)$$

In these equations $[M]$, $[D]$, and $[K]$ are the mass, damping, and stiffness matrices respectively, of the fairing finite-element model. The time-dependent excitation which appears on right hand side of the differential equation is the result of specified base motion of the fairing. The displacement initial condition

includes, as described above, the effects of both thruster spring prestress and thermal prestress. The velocity initial condition is produced by the impulsive loading of the pyrotechnic shock applied at the separation edges of the fairing.

The equations above can be transformed to modal coordinates. We have

$$\{u_r(t)\} = [\phi_R] \{\eta_R(t)\} \quad (5)$$

$$\{\tilde{u}(t)\} = [\phi] \{\eta(t)\} \quad (6)$$

$$[R]\{\ddot{\eta}\} + 2[R][\zeta][\omega^2]\{\dot{\eta}\} + [\omega^2]\{\eta\} = -[S]\{\ddot{\eta}_R\} \quad (7)$$

$$\{\eta(0)\} = [R]^{-1}[\phi]^T[M]\{\{u_A\} - \{u_s\}\} \quad (8)$$

$$\{\dot{\eta}(0)\} = [R]^{-1}[\phi]^T[M]\{\dot{u}_c\} \quad (9)$$

In these equations $[\phi_R]$ represents the matrix of rigid body modes of the fairing while the normal modes are designated by $[\phi]$. The corresponding generalized coordinates are η_R and η .

In the differential equation, $[R]$ and $[\zeta]$ and $[\omega^2]$ represent the generalized mass, damping, and frequency matrices where

$$[R] = [\phi]^{-T} [M] [\phi] \quad (10)$$

$$[\zeta] = [\phi]^{-T} [D] [\phi] \quad (11)$$

Matrix $[S]$ is defined as

$$[S] = [\phi]^{-T} [M] [\phi_R] \quad (12)$$

and represents the inertial coupling between the constrained normal modes and the rigid body modes.

With the required information concerning the structure, the initial conditions, and the base motion available, Equations (7-9) can be solved for the modal response of the fairing. The displacement response then can be obtained from Eqs. (1), (5), and (6). Internal stresses and constraint forces (in particular, hinge loads) can be post-calculated utilizing the finite element model.

This is a straight forward procedure that works in certain cases. However, there is a major complicating factor. The complication can be seen by considering Fig. 10. This figure shows fairing separation at three different temperature skew angles (cf Fig. 4). Consider first separation at a 90° skew angle (Fig. 10a.)

In this case, the postseparated equilibrium of the fairing under heating and with the thruster

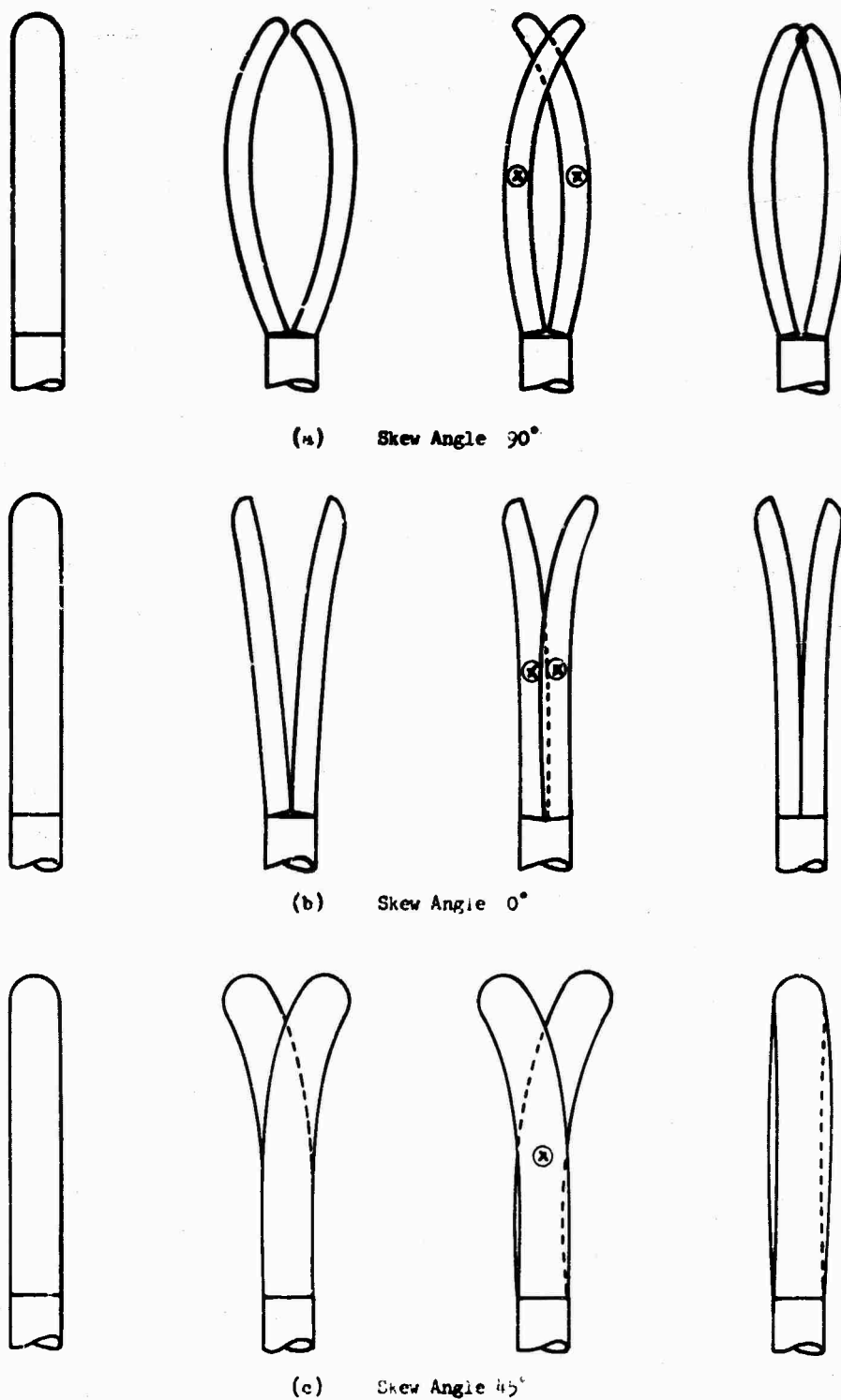


FIG. 10 Firing Separation Interference Problems

prestress relaxed would be as shown in sketch (2) of Fig. 10a. The base of the fairing halves is rocked backward on the hinges but the fairings are bowed inward by the heating. However, when the pre-separated fairing is suddenly released and begins to move dynamically, the contribution of the modes associated with bowing predominate initially (being higher in frequency than the rocking frequency on thruster springs). The fairing halves would like, therefore, to behave as in sketch (3) with their centers of mass relatively stationary. However, the two halves interfere with each other at the forward end and the result is an initial motion similar to sketch (4). The equilibrium for this motion is not that shown in sketch (2). Eventually the rocking mode comes into play sufficiently to separate the fairing halves, but the subsequent motion may be quite different than if no interference between the fairing halves had occurred.

At a 0° skew angle the post-separated equilibrium position is as shown in sketch (2) of Fig. 10b). The fairing has a banana-peel appearance--just the opposite bowing from the 90° case. The post-separated dynamic motion of the fairing without interference would involve motion as shown in sketch (3). Because of interference between the two halves and also at the base of the fairing, the initial motion is more as pictured in sketch (4), with an unzipping of the fairing, starting at the tip and proceeding toward the base. This may occur rather rapidly followed by base interference of longer duration (all relatively of short duration, of course). Again the subsequent motion about the equilibrium of sketch (2) can be drastically affected by the interference.

Finally, consider the case of a 45° skew angle. The sketches of Fig. 10c show in this case a view of the fairing with the separation plane in the plane of the paper. In their post-separated equilibrium position, the fairing halves are rocked forward toward and backward away from the viewer. In addition the fairing halves are bowed sideways, as shown in sketch (2). As in the other cases, upon separation the fairing halves initially would like to move toward the positions of sketch (3). They are prevented from this by an interlock ring at the forward end of the fairing and interference occurs as in sketch (4). Eventually because of the rocking motion of the fairing the forward end of the fairing comes unlatched and motion toward the equilibrium of sketch (2) occurs.

Because of the interference just described, the boundary conditions on the fairing halves vary during the separation process. The fairing, at any instant will move toward an equilibrium position corresponding to the current boundary conditions. For example, in Fig. 10a, the fairing first moves toward the equilibrium associated with a nose tip constraint. At a certain time, termed the transition time, the fairing suddenly starts moving toward a new tip free equilibrium condition.

The approach used to solve this problem is to utilize Equations (1) - (12) presented previously but to monitor certain of the constraint forces. When the transition time occurs, as signaled by a change in sign of these forces, the calculation is stopped and the problem reinitialized, using new fairing modes and a new equilibrium condition. The calculation is then resumed. This process can be repeated several times, if several transitions occur or to simulate a continuous variation in the constraints on the fairing.

The equations for the i^{th} phase of the motion can be expressed as follows:

For time interval $t_{i-1} < t < t_i$

$$\{u(t)\} = \{u_F(t)\} + \{u_B(t)\} + \{\tilde{u}(t)\} \quad (13)$$

$$\{u_F(t)\} = [\phi_R] \{\eta_i(t)\} \quad (14)$$

$$\{\tilde{u}(t)\} = [\phi_i] \{\eta_i(t)\} \quad (15)$$

$$[R_i] \{\ddot{\eta}_i\} + [R_i] [\xi_i] [\omega_i^2] \{\eta_i\} + [\omega_i^2] \{\eta_i\} = -[S_i] \{\ddot{\eta}_i\} \quad (16)$$

$$\{\eta_i(t_{i-1})\} = [R_i]^{-1} [\phi_i]^T [M] (\{u(t_{i-1})\} - \{u_B(t_{i-1})\}) \quad (17)$$

$$\{\dot{\eta}_i(t_{i-1})\} = [R_i]^{-1} [\phi_i]^T [M] \{\dot{u}(t_{i-1})\} \quad (18)$$

The notation in these equations is the same as used previously, except that subscripts i have been added to indicate the particular phase of the separation process being considered.

As can be seen in Fig. 10, which considers only three illustrative cases, a variety of interference problems may require evaluation. For many of these, the transition time is not immediately obvious. In particular, when a continuous change of constraints occurs, only an approximation to the actual motion can be obtained.

Consider the case of Figure 10b where fairing interference with the base occurs. To establish an analytical basis for boundary condition change and to have a single criteria to monitor it can be assumed that when the moment produced by the base reaction forces about the axis connecting the hinges changes sign, the base boundary conditions should be switched from constrained to free.

The base moment can be calculated directly by determination of the base constraint forces and integration of their moment about the hinges. Alternatively, and perhaps more conveniently, the moment equilibrium about the hinges shows that this base moment M_B is equal to the moment of the inertia forces acting on the fairing minus the moment of the thruster spring forces.

Time

$$M_{\theta_i} = - \int_{m_T} y \ddot{u}_i dm - F_p h_p \quad (19)$$

or in matrix rotation

$$M_{\theta} = - \{ \phi_{R_i} \}^T [M] \{ \ddot{u}_i \} - F_p h_p \quad (20)$$

Here $\{ \phi_{R_i} \}$ is the rigid body rotation mode about the hinge line. Making use of Eqs (14) and (15), we can obtain for the base moment

$$M_{\theta} = - I_{RX} \ddot{\eta}_{\theta_i} - \{ S_{\theta_i} \}^T \ddot{\eta}_i - F_p h_p \quad (21)$$

where

$$I_{RX} = \{ \phi_{R_i} \}^T [M] \{ \phi_{R_i} \} \quad (22)$$

and

$$\{ S_{\theta_i} \}^T = \{ \phi_{R_i} \}^T [M] \{ \phi_i \} \quad (23)$$

This form for the base moment is more directly suitable for determination in connection with the dynamic response calculation.

PAIRING RESPONSE EVALUATION

In the previous section, several special cases of fairing separation were considered. As illustrated by Figure 10, these included temperature distribution skew angles of 0°, 45°, and 90°. In practice these precise conditions seldom occur. Typically, on an ascent trajectory, because of dispersion the windward generator may lie anywhere within 15° of the nominal location, which is usually itself skewed. The motion at arbitrary skew angle resembles a combination of those cases discussed previously, with the influence of the sin 2θ and cos 3θ components dominating the response from the point of view of clearance reduction. A typical case might be a 5° nominal skew angle, with a maximum possible skew of 30° on a dispersed trajectory.

Consider then the case of a 20° skew angle. Figures 6 through 8 have already shown the corresponding pre and postseparated fairing thermal deformations. Figure 11 displays the

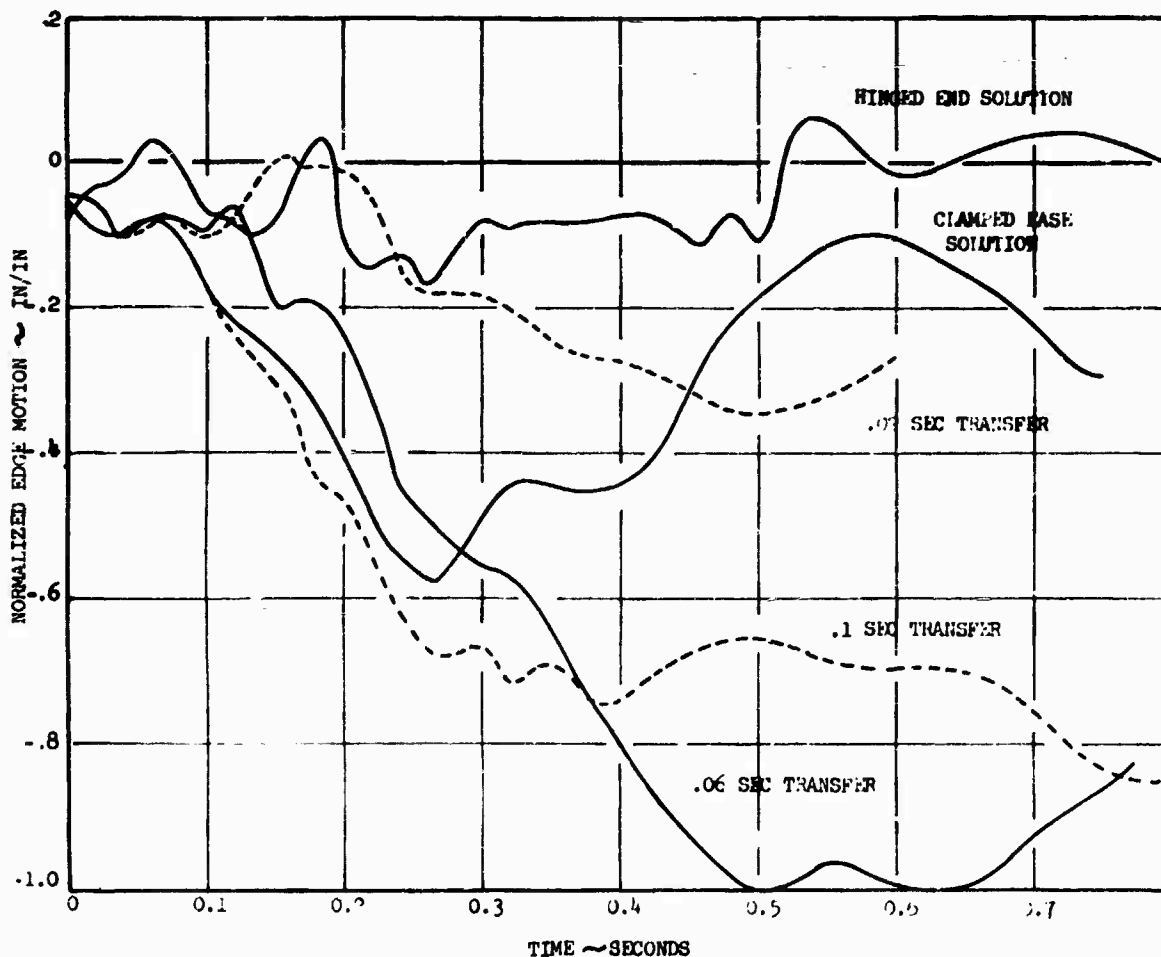


Fig. 11 Post Separated Radial Motion of a Pairing Edge Point

radial motion of an edge point of the post-separated fairing. This point is located roughly at the midpoint of the fairing's cylindrical section. The response considered in this figure is due to thermal effects and thruster prestress only (no base motion or pyrotechnic shock).

The five displacement histories of Figure 11 represent two linear and three bi-linear dynamic response cases. The linear cases correspond to the two extreme base conditions. These are (1) the fairing is free of interference constraints throughout the motion, and (2) the base is permanently constrained against translational displacements.

The three bi-linear cases represent response with transition from constrained to free-base conditions, occurring at different transition times. As explained in the previous section, the moment of the base constraint forces is monitored for a change in sign. If the time at which this occurs is designated as t_p , the three bi-linear cases of Figure 11 correspond to transition times of t_p , $0.3 t_p$, and $1.6 t_p$. Several transition times are considered because basing transition on the total base moment is only an approximation. The post-separated base joint can take compression but not tension. Because of the skew angle, the fairing is excited in torsion. Consequently, the fairing upon separation first pushes against the base on both sides, then lifts off on one side, followed by liftoff of the other side, and complete separation from the base. The base moment is therefore only an approximate measure of the base constraint. In Figure 11, t_p occurs at 0.06 second.

It is remarkable that while the first phase motion lasts less than 0.1 second (compared to a time of nearly 1 second considered in Figure 11) it produces dramatic changes in the overall response. The explanation of this lies in two facts: (1) the base-constraint causes more of the stored potential energy to be fed into the low-frequency antisymmetric, torsional and side-way modes than is the case for a 'free-base' initial condition and (2) the frequencies of the lowest antisymmetric modes for a free-base condition are lower by a factor of six than the corresponding modes for the base-constrained fairing. Thus in the bi-linear case, where the base of the fairing is initially constrained, more energy is fed into the antisymmetric modes of the fairing, which contribute most heavily to the radial edge motion shown in Figure 11. During first phase motion the velocity of these modes builds up rapidly. At transition a further amplification occurs. The kinetic energy of the low-frequency antisymmetric modes is transferred primarily to the corresponding modes of the fairing with an unconstrained base. However, because these modes have much lower frequencies, the same energy is reflected in much higher amplitudes.

To illustrate this point, a review of an actual example is convenient. For a specific fairing the lowest two antisymmetric modes contain 1.5 and 7.3 in-lb of potential energy when the linear assumption is used for the dynamic response computation. That is to say, the fairing base is assumed to be free at the instant of separation. Most of the stored energy goes into higher modes which may be symmetric or antisymmetric with respect to the fairing's planes of symmetry. On the other hand, when the same fairing starts its motion with a constrained base, the lowest antisymmetric mode contains 140 in-lb of potential energy. When boundary-condition transition occurs, this energy is fed into antisymmetric post-transition motion of the fairing.

Moreover, since the expansion of the first constrained-base antisymmetric mode in terms of unconstrained antisymmetric modes is primarily a linear combination of the first two of the latter modes, a substantial part of the energy goes into these two modes. Specifically, in the example under consideration, the transferred energies are 23.5 and 39 in-lb. This is, respectively, 17 and 5.5 times the energy that is stored in these antisymmetric modes in the linear case. Thus the bi-linear response computation shows an 'overshoot' factor of about five with respect to the linear response.

These dynamic response studies indicated that since the base constraint condition has such a dramatic effect on clearance between the fairing and spacecraft, it is advantageous to fly trajectories where the windward generator has a 90° skew angle with respect to the separation plane. While this condition, as was described before, produces interference near the tip of the fairing with the potential of binding, it causes very little reduction in spacecraft clearance. Knowing about the interference forces allows one to design for them. Small assist springs placed at the tip of the fairing and low friction sloping surfaces at the contact point are used to eliminate the possibility of permanent binding.

DYNAMIC WAVE PROPAGATION IN TRANSVERSE LAYERED COMPOSITES

C. A. Ross, J. E. Cunningham, and R. L. Sierakowski
Acrospace Engineering Department
University of Florida
Gainesville, Florida

A method is developed for experimentally determining stress pulse attenuation across a single composite lamina in a solid epoxy rod. The attenuation factor is found to be a function of the initial pulse shape and amplitude. Experimental results are compared with an analytical model. The practical implications of the initial results provide an insight into the prospective fracture/failure damage occurring within composite materials subject to dynamic load.

INTRODUCTION

One of the principal problems encountered in dynamic loading conditions is that of determining how short duration pulses are propagated through solid materials. That is, in impact processes, energy can be transmitted large distances from the point of impact by stress waves which can produce considerable damage at remote distances from the impact point. Thus, in order to predict and control the type and extent of the fracture phenomenon, as well as other forms of damage occurring during impact and impulsive loading processes, knowledge of the behavior of stress waves in the material is of importance.

In recent years, considerable attention has been focused on the potential use of composite type materials for various design applications due to the wide flexibility offered for materials selection to fit a particular design application. While considerable investigation of the behavior of composites subjected to static loadings has been reported on, less attention has been devoted to studies associated with predicting the behavior of composites under dynamic loadings. Thus, while such questions as speed, attenuation, and dispersion of stress waves in homogeneous metals have been

investigated, less knowledge is available on the behavior of such waves in composites. Some initial investigations into the behavior of stress pulses in axially reinforced rods have been studied experimentally by [1,2], in layered plates by [3,4] and in bonded rods using dissimilar materials in [5].

In previous investigations the attenuation/dispersion of stress pulses due to impact in long uniaxial composite rods has been found to be dependent on many parameters such as pulse length, specimen geometry, initial pulse amplitude, initial pulse shape, and volume fraction of the reinforcing constituent [6]. For monolithic materials, where internal friction is low, pulse height may decrease due to dispersion of the pulse and in materials where internal friction is significant, pulse height change can be attributed to energy loss as well as geometric dispersion. In composite materials the effects of the constituents as well as the overall synergistic effects can be of importance. Further, stress pulse propagation in transversely reinforced composites is further complicated by the reflection and transmission of the pulse at the interfaces of the matrix and composite lamina.

In the present paper studies of the attenuation/dispersion due to impact generated pulses as opposed to dispersion of ultrasonics with changes in frequency is investigated. The basic objective of the present research is to study the effect of a single transverse lamina on a stress pulse propagating in a monolithic material. This objective was accomplished by observing pulse amplitude attenuation in long rod specimens containing a single transverse composite lamina. An analytical prediction based on one dimensional stress pulse propagation is developed and graphical as well as tabular results are presented.

SPECIMEN FABRICATION

Based upon previous experimental work and experience in fabricating a stainless steel filament epoxy matrix composite system [2,6,7,8], this type of composite was chosen as the basic experimental model. The long bar specimens were cast in a mold designed to accommodate a gate with attached wire grid as shown in Fig. 1. The grids

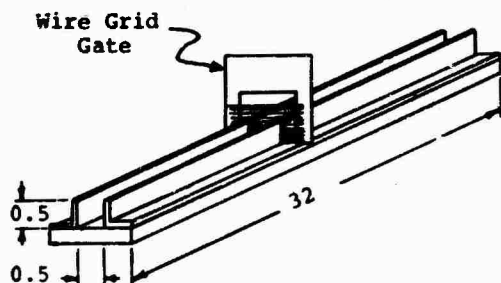


Fig. 1 MOLD ASSEMBLY

consisted of continuous strands of type 304 soft stainless steel wire. [The grid was wound on the gate using a lathe assuring proper spacing of filaments. This procedure resulted in a known volume fraction of filaments within the given lamina.] Further, the grid and mold were cleaned and degreased using trichlorethylene vapor before casting. A mold release agent was applied to the mold and additional cleaning of the grid was accomplished using a dilute acid solution followed by a neutralizing agent.

The epoxy used as the rod material was Shell Epon 828 resin mixed with 12 parts of shell 400-A hardener to 100

parts, by weight, of resin. The resin was preheated to 150°F then thoroughly mixed with hardener and degassed in a vacuum (one inch Hg) for twenty minutes. The mixture was then placed in the mold and cured at 150°F for 3 hours. Upon removal from the mold the specimen is machined to a 0.35 x 0.35 inch square cross section rod. A schematic of a finished specimen is shown in Fig. 2.

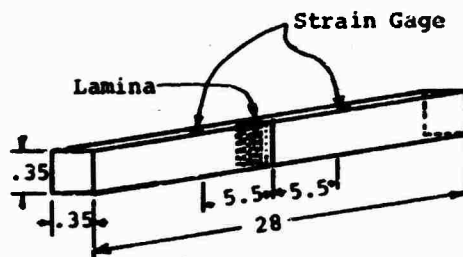


Fig. 2 FINISHED SPECIMEN

EXPERIMENTAL PROCEDURE

The finished specimens were instrumented using BLH FAE-06J-1236 etched foil strain gages, as shown in Fig. 2. The active gage was placed in a bridge circuit as shown in Fig. 3. It was found necessary to limit the current in the strain gage to less than five milliamperes due to the low conductivity of the epoxy. Small amplitude square pulses were generated in the specimens by impacting it with a three inch long epoxy projectile of the same cross sectional dimensions as the specimen. Pulse shape and wave

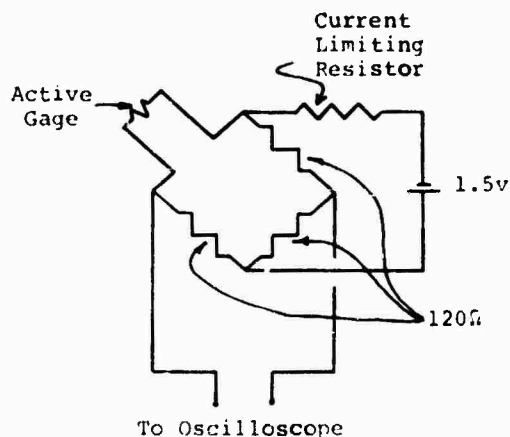


Fig. 3 STRAIN GAGE BRIDGE CIRCUIT

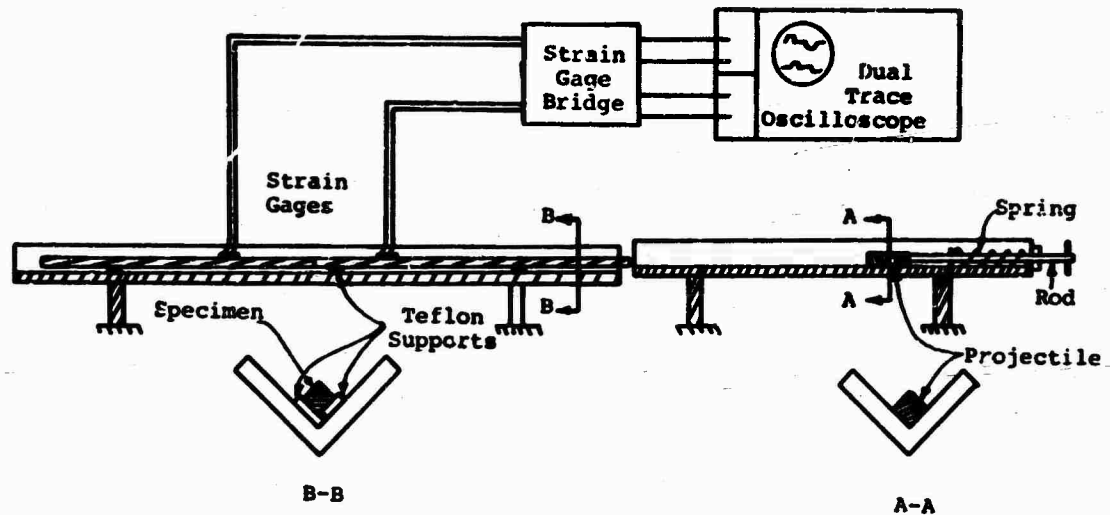


Fig. 4 SCHEMATIC OF TEST APPARATUS

propagation speed were monitored using the strain gage output connected to an oscilloscope. A schematic showing the test apparatus is shown in Fig. 4. Preliminary tests were performed using a gas gun, as described in [7], to propel a round projectile against a round specimen; however, the simpler system shown in Fig. 4 permitted the use of a square projectile and a square cross section rod. Most specimens were instrumented with two equally spaced strain gages located at both sides of the lamina. In these cases the first pulse was used to trigger the oscilloscope by the internal trigger mode and with proper adjustment the major portion of the pulse was recorded. The second strain gage was then recorded on the other beam and in turn gave pulse shapes both before and after the lamina. Typical pulse shapes showing the initial compressive pulse and the first reflected tensile pulse are shown in Fig. 5. Many reflections showing pulse height attenuation are also shown in Fig. 6. The oscilloscope traces were recorded using a Polaroid camera attachment.

RESULTS AND DISCUSSION

The pulse propagation speed was calculated using the data shown in Fig. 6. Selecting the initial compressive peak as a reference, and by accurately measuring the rod length and time between peaks the pulse propagation speed was calculated for the second, fifth, and tenth traverses of the rod. These results are given in Table I.

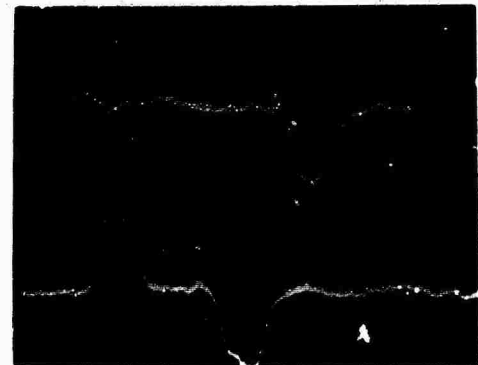


Fig. 5 INITIAL COMPRESSIVE AND TENSILE PULSES. BEFORE AND AFTER LAMINA.

Reproduced from
best available copy.

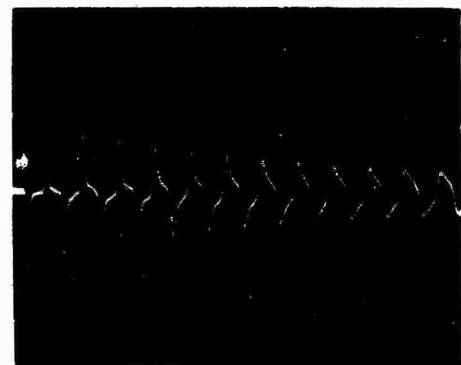


Fig. 6 ATTENUATION CURVE

TABLE 1

Vol. Fraction of Lamina and Fibers/Inches	n	Wave Speed in/sec	$D \times 10^2$ 1/in	$\alpha \times 10^2$ 1/in	$\alpha_j \times 10^2$ 1/in	$\delta \times 10^2$
0%	2	72,200	0.181			
0	5	72,900	0.162	0.147	0	0
	10	73,900	0.149			
20%	2	71,900	0.203			
	5	72,800	0.175	0.159	0.012	0.336
32	10	73,800	0.162			
30%	2	71,800	0.221			
	5	72,500	0.185	0.164	0.017	0.475
48	10	73,600	0.168			
50%	2	71,700	0.234			
	5	71,500	0.192	0.169	0.023	0.645
80	10	72,300	0.173			
78.5%	2	71,100	0.241			
	5	71,400	0.201	0.178	0.031	0.870
125	10	72,100	0.182			

The amplitude attenuation D is defined as the natural log of the pulse amplitude ratio divided by the rod length traversed between the two pulses. Using the rod length and the initial pulse amplitude the attenuation is defined as

$$D = \frac{1}{2nl} \ln \frac{A_0}{A_n} \quad (1)$$

Amplitude attenuation values as defined by Eq. (1) were also calculated for $n = 2, 5, 10$ and are given in Table I. This same data is shown in graphical form of Fig. 7. These data points may be fitted to an analytical curve given as

$$D(n) = \gamma e^{-\beta n} + \alpha \quad (2)$$

Calculated values of α are given in Table I and indicated on the right side of Fig. 7. The variation of the amplitude attenuation factor D with n is considered to be related to the dispersion occurring in the high frequency components of the square pulse during the first few reflections. This dispersion may account for the increased pulse propagation speed with increasing number of reflections as seen in Table I. The aforementioned dispersion phenomena has been obtained experimentally in the boron epoxy specimens

described in [9].

The differences between the attenuation numbers (D and α) of the monolithic rod and rods having composite lamina are assumed to be attributed solely to the lamina, i.e. any attenuation due to geometry and end effects would be present in both type specimens. Based on this assumption the attenuation of the pulse upon passage through the lamina is defined as

$$\delta = (\alpha_j - \alpha_e)l \quad (3)$$

The attenuation factor δ is defined in this manner in order to eliminate any dependence on the reflection number n . Using the values of α for $n \rightarrow \infty$ eliminates the first term of Eq. (2) and δ may be redefined as

$$\delta = \ln \frac{P_0}{P} \quad (4)$$

Values of δ are given in Table I and P/P_0 as a function of the number of filaments per lamina are shown in Fig. 8. The value of δ should be independent of the number of reflections for a given equal initial pulse amplitude and this may be shown to be reasonably true, within experimental error, by subtraction of the curve obtained for the epoxy rod from the curves of the rods containing a lamina. These results are omitted from Fig. 7 for clarity.

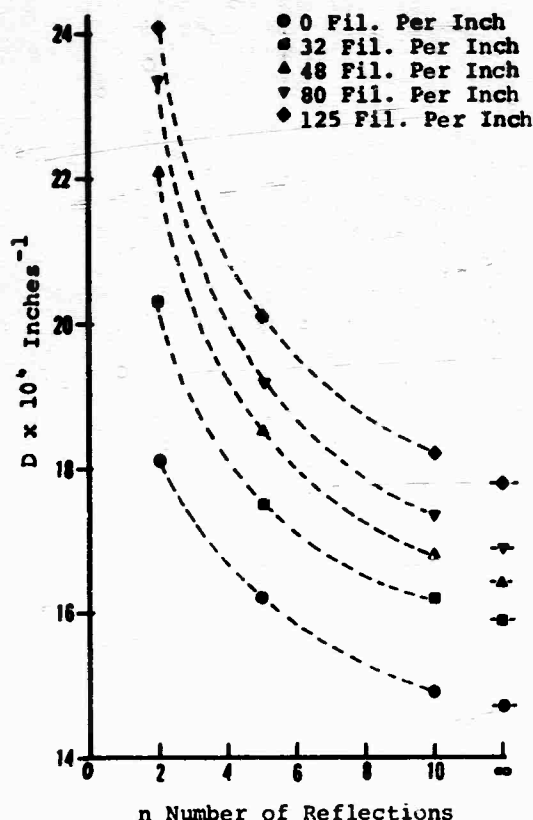


Fig. 7 ATTENUATION FACTOR D AS A FUNCTION OF n.

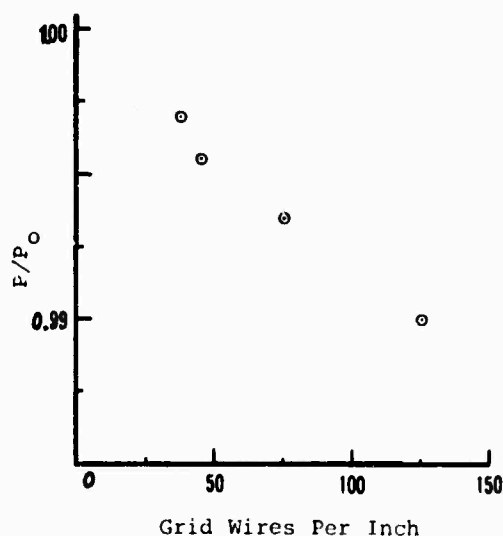


Fig. 8 PERCENT OF STRAIN AMPLITUDE TRANSMITTED THROUGH LAMINA

An analytical model based on one dimensional pulse propagation theory is shown as the solid curve in Fig. 9. This derivation is omitted from the present paper for brevity. The model takes into account the reduction of pulse propagation speed with increasing filament content of transversely reinforced composites as shown analytically by [10] and verified experimentally for steel epoxy composites [11]. The preceding observation accounts for the analytical prediction of zero attenuation for a lamina having an area fraction of approximately 65%. Due to the difficulty in fabricating a specimen with this type lamina this point has not been verified experimentally. However, experimental data for axial reinforced specimens [6] tends to show a minimum value at approximately this same volume fraction.

CONCLUSIONS

In the current study it has been found possible to fabricate a simple single lamina specimen which can be used to yield useful data for investigation of combined system effects on pulse propagation in transverse layered composites.

The one dimensional analytical model, advanced on the basis of experimental data obtained, appears to give reasonable results for the specimens tested and may be used to predict attenuation effects for composite materials such as plates and transversely reinforced rods or beams.

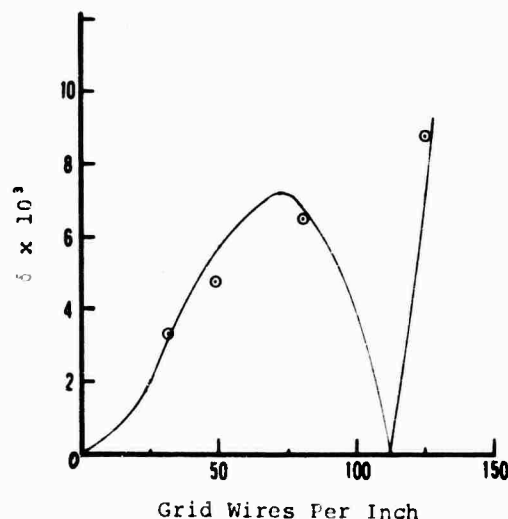


Fig. 9 ATTENUATION NUMBER FOR A SINGLE LAMINA VS. NUMBER OF WIRES PER INCH.

However, additional study and research is necessary before one may adapt this method to composites having closely packed lamina.

The practical implications of the initial results obtained here provide insight into the prospective failure/fracture damage occurring within composite type materials subjected to dynamic loading.

REFERENCES

- [1] T. R. Tauchert and F. C. Moon, "Propagation of Stress Waves in Fiber-Reinforced Composite Rods," Proceedings of AIAA/ASME 11th Structures Structural Dynamics, and Materials Conf., Denver, Colorado, April, 1970.
- [2] R. L. Sierakowski, G. E. Nevill, Jr., C. A. Ross, and E. R. Jones, "Follow-On Studies on the Ballistic Impact of Composite Materials," Tech. Rept. AFATL-TR-70-87, August, 1970.
- [3] R. Kinslow, "Stress Waves in Laminated Materials," AIAA Paper No. 67-140, 1967.
- [4] I. M. Daniel and R. L. Marino, "Wave Propagation in Layered Model due to Point-Source Loading in Low-Impedance Medium," Experimental Mechanics, No. 5, May, 1971.
- [5] J. D. Achenbach, J. H. Hermann, and F. Ziegler, "Tensile Failure of Interface Bonds in a Composite Body Subjected to Compressive Loads," AIAA Journal, October, 1968.
- [6] G. E. Nevill, Jr., R. L. Sierakowski, C. A. Ross, and E. R. Jones, "One Dimensional Wave Pulses in Steel-Epoxy Composites," accepted for publication in Experimental Mechanics, 1971.
- [7] R. L. Sierakowski, G. E. Nevill, Jr., C. A. Ross, and E. R. Jones, "Studies on Ballistic Impact of Composite Materials," Tech. Rept. AFATL-TR-69-99, July, 1969.
- [8] R. L. Sierakowski, G. E. Nevill, Jr., C. A. Ross, and E. R. Jones, "Dynamic Compressive Strength and Failure of Steel Reinforced Epoxy Composites," Jnl. of Comp. Mtl., Vol. 5, July, 1971.

- [9] T. R. Tauchert and A. N. Guzelsu, "An Experimental Study of Dispersion of Stress Waves in a Fiber-Reinforced Composite," J. of Appl. Mech., ASME preprint paper no. 71-APM-27.
- [10] J. E. Ashton, J. C. Halpin, and P. H. Petit, "Primer on Composite Materials: Analysis," p. 77, Technomic Pub. Co., Stamford, Conn., 1969.
- [11] R. L. Sierakowski, et. al., AFATL Tech. Rept. to be published February, 1972.

NOMENCLATURE

A_0	peak to peak amplitude of the initial compressive pulse and first tensile reflection, arbitrary units
A_n	peak to peak amplitude of nth compressive pulse and nth reflected wave, arbitrary units
D	amplitude attenuation value, inches ⁻¹
l	length of specimen, inches
n	number of reflected pulses
P_0	amplitude of pulse before passing through the lamina, arbitrary units
P	amplitude of pulse after passing through the lamina, arbitrary units
α	value of attenuation number D after many reflections ($n \rightarrow \infty$), inches ⁻¹
α_e	number for solid epoxy rod
α_j	number for rod with lamina
β, γ	arbitrary constants
δ	attenuation number for a single lamina.

R-W PLANE ANALYSIS FOR VULNERABILITY OF TARGETS TO AIR BLAST

Peter S. Westine
Southwest Research Institute
San Antonio, Texas

This paper suggests the use of a general equation for defining the vulnerability of any target to an air blast wave. Engineers often determine a charge weight versus standoff distance isodamage curve for complex targets by conducting many experiments. Because the form of this equation is now known, many less experiments are needed. This simple, but yet reliable, formula could also be used as a code for storing explosives in the vicinity of houses, highways, aircraft, etc. Test data from a variety of different targets including aircraft, cantilever beams, trucks, antennae, cylinders, and houses are used to demonstrate the validity of this equation.

INTRODUCTION

Whenever an explosive charge is detonated in the vicinity of an airplane, house, antenna, truck, or other structure, an air blast wave is emitted which is capable of causing significant damage. Complex analytical structural analysis procedures do exist which can be used to estimate the level of damage imparted to a target by an air blast wave; however, the use of these procedures requires numerous engineering assumptions with the inevitable consequence that they are used only to predict damage to rudimentary structural components such as plates and beams. Provided that a complex target can be idealized as a plate or beam, the intensity of a blast wave which initiates permanent damage can usually be estimated by using analytical computer programs for structural response. Whenever these programs are extended to predict the magnitude of permanent deformation, they become very unwieldy and generally offer only the crudest of damage intensity estimates when the structure is complex.

To circumvent these difficulties, engineers often resort to experimental techniques. Tests are generally conducted by placing a charge in the vicinity of a target and detonating it to create an air blast wave which damages the structure. Usually a team of "assessors" looks at the target and decides if it has been

damaged so that it can not function. If the assessors are evaluating the damage imparted to a house, they classify the damage according to different categories. For example, the British [1] refer to such classes of damage to brick houses as: A damage - complete demolition; B damage - 50% to 75% of brickwork destroyed or unsafe; C damage - partial collapse of roof, partial demolition of one or two walls, load bearing members damaged; D damage - minor structural damage, partitions and joinery wrenched; and E damage - 10% of glass broken. A similar technique for characterizing the damage imparted to aircraft [2] has been used, the A through K kill categories. If the assessors feel the target has not been adequately damaged to prevent it from performing a mission or functioning, another charge is detonated at a location several paces closer to the target so that a more severe level of damage can be evaluated.

The data obtained in these damage assessment experiments are usually plotted on a graph of standoff distance, R , versus charge weight, W . Ideally, if enough data can be obtained, the R - W curve has isoclines of constant levels of damage, isoclines for A, B, C, D and E damage to a house or for A through K damage to an aircraft.

Obviously, cost is a serious drawback to this empirical approach. A new target must

be damaged each time another charge weight is tried so one can obtain an additional data point on the R-W curve. Because the target is usually a complex structure such as an airplane, truck, or antenna, the costs escalate rapidly as additional data points are obtained.

The purpose of this paper is to present an equation which can be used to define the entire R-W curve for any structure, provided that three or more experimental data points exist which define a constant level of damage in the target's R-W plane. Under certain limiting conditions, less than three data points can exist. This equation has the form

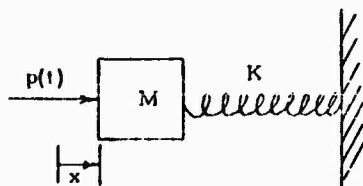
$$R = \frac{A W^{1/3}}{\left(1 + \frac{B^6}{W} + \frac{C^6}{W^2}\right)^{1/6}} \quad (1)$$

where A, B, and C are coefficients to be determined from three or more experimental data points.

In subsequent discussion, we will show that Eq. (1) and special variations on it (such as when B^6 and/or C^6 are very small or when B^6/W or C^6/W^2 is very large relative to the other terms in the denominator) can be used to accurately define air blast isodamage curves in the R-W plane for complex targets.

THEORETICAL BASIS FOR R-W RELATIONSHIP

To understand why Eq. (1) is appropriate, one must understand the concept of the pressure-impulse diagram (P-I diagram) as applied to the determination of isodamage curves for structures loaded by an air blast wave. This concept can be illustrated simply by considering a qualitative model such as a single-degree-of-freedom elastic system loaded with an air blast wave. Figure 1 illustrates this rudimentary model. A mass M is attached to



a rigid support by a spring with a linear spring rate, K . At some time which we arbitrarily will call time zero, a transient force, $p(t)$, as shown in Fig. 1, is applied to the mass. The force will be characterized by its maximum amplitude, P , and a duration of characteristic time, T . We will assume that the maximum damage imparted to this system will be associated with the maximum deflection of the spring, X_{max} . One obtains a solution for X_{max} as a function of the other four parameters (M , K , P , and T) by (1) writing the second-order differential equation which defines the motion of the mass, (2) solving this differential equation for its complementary and particular solutions, (3) substituting the boundary conditions for the mass being initially at rest into the equation, (4) differentiating the resulting expression to obtain the velocity which, when set equal to zero, gives the time when the deflection is a maximum, and (5) substituting the time of maximum deflection into the transient expression for displacement to determine X_{max} as a function of M , K , P , and T .

Unfortunately, an explicit expression for X_{max} can not be written because this problem can not be solved by a closed form solution; nevertheless, Fig. 2 graphically presents a two-dimensional space which is a complete solution to this problem.

In Fig. 2 the solution for the maximum deflection is a two-parameter space of non-dimensional numbers. The ordinate is a normalized deflection obtained by dividing the maximum deflection, X_{max} , by the static deflection, P/K . The abscissa in Fig. 2 is a nondimensional time obtained by dividing the duration of the load, T , by the response time of the structure, $\sqrt{M/K}$. For both very long and very short nondimensional times, the solution approaches two different asymptotes. The asymptote for long durations of loading is illustrated by a dashed line in Fig. 2 and has

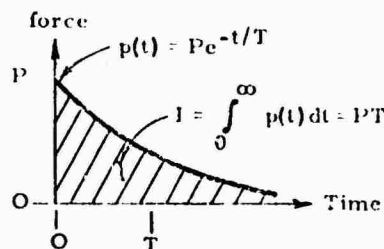


Figure 1. Single-Degree-of-Freedom Elastic Model Loaded With an Air Blast Wave

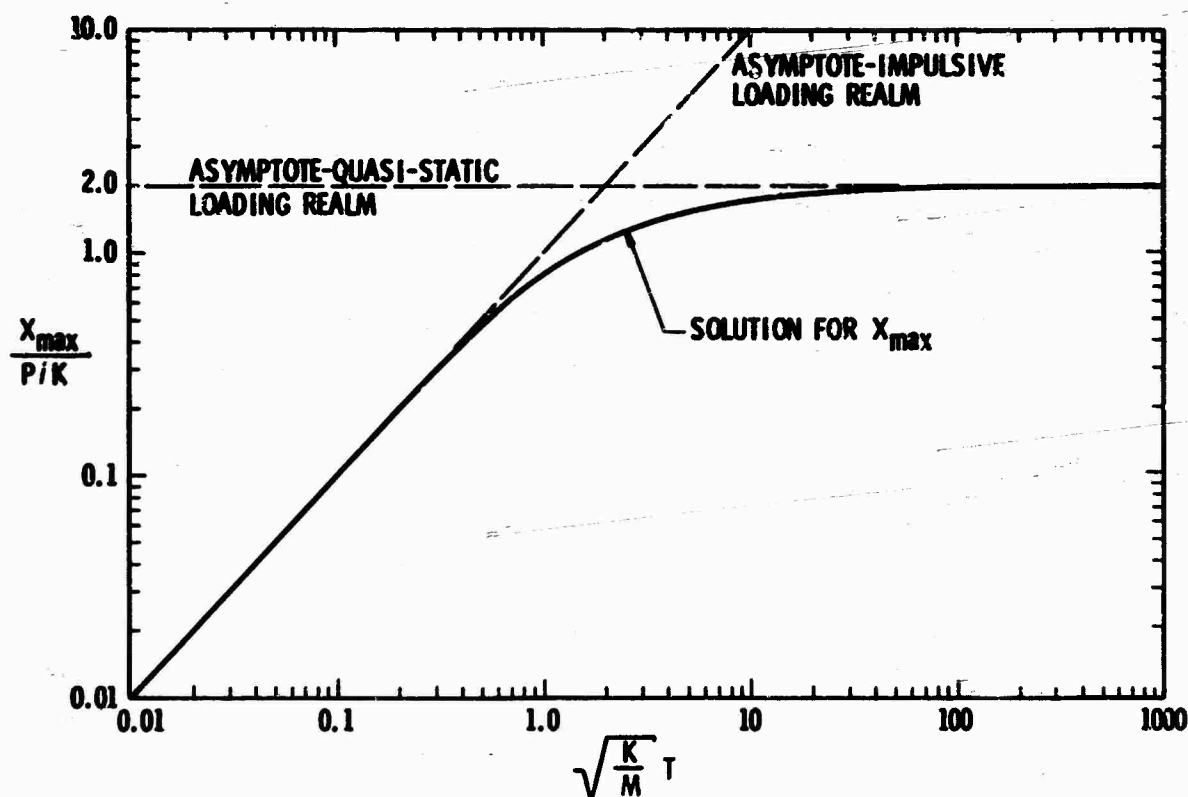


Fig. 2. Maximum Response to Force Pulse

been labeled the asymptote for the "quasi-static loading realm". The equation for this asymptote is

$$X_{\max} = 2 \frac{P}{K} \quad (2)$$

We call this loading realm the quasi-static loading realm because the maximum deflection is independent of the duration of loading. This deflection does not equal the static deflection; however, it is directly proportional to the static deflection.

On the other hand, the response of this system to a blast load asymptotically approaches a different limit whenever the duration of loading is very short relative to the period of structure. The equation for this asymptote is

$$X_{\max} = \frac{(PT)}{\sqrt{KM}} \quad (3)$$

because the nondimensional deflection increases linearly with the nondimensional time in this loading realm. We term this loading realm the "impulsive loading realm" because

the response of a system depends upon the impulse imparted to the structure, PT , and is independent of either the peak applied load or the duration of loading.

This concept whereby maximum deflection is dependent upon the peak applied load for long durations of loading and upon the impulse for short durations of loading is more than a theoretical concept. Many different investigators, the earliest of whom was apparently J. Sperrazza [3], have applied this concept to numerous studies determining the vulnerability of complex targets to air blast waves. We shall show that Eq. (1) for the vulnerability of targets in the R-W plane approaches the appropriate asymptotes for both the quasi-static and impulsive loading realms.

QUASI-STATIC LOADING REALM

The duration of a blast wave is longer for large explosive charges than for small explosive charges. If W in Eq. (1) becomes very large relative to the coefficients B and C , the denominator in Eq. (1) approaches unity. This observation demonstrates that Eq. (1) becomes Eq. (4) for blast waves from extremely large

explosive charges.

$$R = A W^{1/3} \quad (4)$$

We have already demonstrated that for large explosive charges the response of a structure can be given by Eq. (2). For any given structure (a constant value of K), Eq. (2) shows that a constant level of deformation implies a constant intensity of peak applied pressure. Those who are familiar with Hopkinson's Law [4] for scaling the peak applied pressure imparted to a target realize that, under sea-level ambient conditions, peak pressure is a function of a single parameter, the standoff distance divided by the charge weight to the 1/3 power, as shown in Eq. (5).

$$P = f \left(\frac{R}{W^{1/3}} \right) \quad (5)$$

Because we are developing isodamage curves in the quasi-static loading realm, the peak pressure is a constant for any given target undergoing a constant magnitude of deformation. Hence, Eq. (5) is actually Eq. (6).

$$\frac{R}{W^{1/3}} = f^{-1}(P) = \text{constant} \quad (6)$$

However, Eq. (6) is identically Eq. (4), if the constant equals A. This in turn, is the limiting case of Eq. (1) for large explosive charges. Thus, we observe that Eq. (1) approaches the appropriate asymptote for the quasi-static loading realm which, in turn, is the appropriate asymptote for large explosive charges.

IMPULSIVE LOADING REALM

Short durations of loading relative to the period of a structure are caused by small explosive charges. We have already seen in Eq. (3) that for short durations of loading, the magnitude of deformation for any given structure (constant values of K and M) is dependent upon only the impulse. Eq. (1) is capable of approaching one of two different limits for small values of charge weight. Either the term B^6/W or C^6/W^2 predominates in the denominator of Eq. (1) whenever W becomes small. If B^6/W predominates, Eq. (1) becomes Eq. (7).

$$R = \left(\frac{A}{B} \right) W^{1/2} \quad (7)$$

Eq. (7) is the appropriate limit for very strong targets. By strong targets, we imply that the target is very close to the explosive charge,

so close that the loading is caused by momentum in the explosive products from the charge rather than by a shock wave propagated in air. W. E. Baker [5] has shown that normally reflected impulse imparted to a target which is very close to an explosive charge is directly proportional to charge weight divided by the standoff distance squared as shown in Eq. (8)

$$I \propto \frac{W}{R^2} \quad (8)$$

However, Eq. (8) is Eq. (7) whenever I is a constant as it would be in the impulsive loading realm. Hence, we observe that, for very strong targets in the impulsive loading realm, Eq. (1) approaches the appropriate limits.

If C^6/W^2 predominates in the denominator of Eq. (1) for small explosive charges, Eq. (1) becomes Eq. (9).

$$R = \left(\frac{A}{C} \right) W^{2/3} \quad (9)$$

Eq. (9) is the limit for a very weak target in the impulsive loading realm. This limit is the same as the limit for the impulse in an acoustic wave which is given by Eq. (10).

$$I \propto \frac{W^{2/3}}{R} \quad (10)$$

The impulse in an air blast wave approaches the acoustic limit whenever the wave is far from the source. Very weak structures will be located at a large distance from the explosive source; therefore, Eq. (10) is valid for very weak structures in the impulsive loading realm. We have already indicated that a constant level of damage in the impulsive loading realm implies a constant value of impulse. Setting the impulse I equal to a constant in Eq. (10) makes Eq. (10) equal to Eq. (9). Thus, we see that Eq. (1) is also capable of approaching the appropriate limit for a very weak target in the impulsive loading realm.

EQUATION (1) APPLIED TO THE VULNERABILITY OF TARGETS

We have demonstrated that Eq. (1) approaches the appropriate theoretical limits for small explosive charges and for large explosive charges. We are now ready to see this equation applied to specific problems where insufficient experimental data exist on a complex target to define an isodamage curve in the R-W plane. All experimental data come from a report by O. T. Johnson [6]. Johnson accumulated data on thirteen different targets;

we will demonstrate the applicability of Eq. (1) by applying it in detail to five of these targets. Usually air blast vulnerability data are classified "Confidential"; however, to keep this paper unclassified, we will delete such information as the type of target being attacked (other than to mention an aircraft, antenna, truck, etc.), the degree of damage being considered, and the direction of the attack on the target. These and other classified details are superfluous information which can be deleted from our discussion without compromising the validity of the results.

The first problem being considered is the vulnerability of a truck to air blast damage. This problem illustrates the use of Eq. (1) in its most general form. Included in Table I for this problem is Eq. (1) where A is equal to 6.481, B^6 is equal to 45.06, and C^6 is equal to 6045. Four experimental data points were used to determine this target's coefficients. Also shown in Table I are comparisons of observed and calculated standoff distances for this target. We observe that the average error is apparently random in sign and only equal to 5.5%. Because Eq. (1) is valid for both smaller and larger explosive charges, it should define the entire R-W plane for this target.

Special cases of Eq. (1) occur whenever the coefficients B^6 or C^6 equal zero. Table II presents experimental data for an aircraft which has been damaged by an air blast wave. Note that the C^6 coefficient equals zero in this illustrative example. This result indicates that the aircraft is a strong structural target whose vulnerability in the impulsive loading realm approaches a limit established by Eq. (7). There have been six experimental data points used to determine the two coefficients in Table II. Very little scatter occurs when one compares calculated standoff distances to observed standoff distances; the average error is only 0.52%.

In Table III, we present data for an antenna whose vulnerability is defined by the special case in which the B^6 equals zero in Eq. (1). This target is obviously a weak structure whose standoff distance relationship in the impulsive loading realm is determined by Eq. (9). Four experimental data points were used to compute the two coefficients in Table III. Very little error can be noted in any of the results when one compares calculated and observed standoff distances.

Under some conditions, one may have experimental data on the vulnerability of a target

which was obtained only in the quasi-static loading realm or only in the impulsive loading realm. When this situation arises, one must modify Eq. (1) by using either Eq. (4) if the data are in the quasi-static loading realm or Eq. (7) or (9) if the data are in the impulsive loading realm. The fourth target is one of these cases. This target is an aluminum right circular cylinder 3 inches in diameter, 9 inches long, and 0.022 inch thick. Such a shell structure has a very high natural frequency, or conversely a very short natural period, which causes the response of this structure to fall in the quasi-static loading realm even though the energy release is relatively small. Under this circumstance, a single coefficient, A , defines the vulnerability of this target to any charge weight larger than the smallest charge found in Table IV. We observe that the scatter in experimental results is relatively small, especially when one realizes that the crushing of cylinders usually exhibits large experimental scatter. The equation presented in Table IV to define the vulnerability of this cylinder is Eq. (4) which should not be used for explosive charges less than 8.5 pounds, as the response of this structure to smaller charges would eventually fall into other loading realms.

In Table V, we present vulnerability data for another aircraft. These data fall exclusively in the impulsive loading realm. Because this aircraft is a strong structure, Eq. (7) with its single coefficient, A/B , defines the R-W plane for any charge weight less than the maximum charge weight found in Table V. Once again, very little scatter is observed in experimental results whenever one compares calculated to observed standoff distances. The results presented in Table V can be used for any charge weight less than 3,000 pounds, but should not be used for larger explosive charges as the response of this system to larger charges will eventually be placed in another loading realm.

One obtains a curve fit to Eq. (1) by solving for the A , B^6 , and C^6 coefficients, using a least-squares curve fit. A least-squares curve fit is obtained by rearranging Eq. (1) to form Eq. (11).

$$\left(\frac{W^3}{R^6}\right)A^6 - (1.0)B^6 - \left(\frac{1}{W}\right)C^6 = W \quad (11)$$

In matrix form, Eq. (11) may be written as Eq. (12).

$$\begin{bmatrix} \frac{W^3}{R^6} & -1.0 & -\frac{1}{W} \end{bmatrix} \begin{bmatrix} A^6 \\ B^6 \\ C^6 \end{bmatrix} = [W] \quad (12)$$

TABLE I - TRUCK

$$R = \frac{6.481 W^{1/3}}{\left(1 + \frac{45.06}{W} + \frac{6045}{W^2}\right)^{1/6}}$$

<u>W (lb.)</u>	<u>R_{obs} (ft.)</u>	<u>R_{cal} (ft.)</u>	<u>Percent Error</u>
8.0	6.0	5.992	0.133
64.0	20.0	21.34	6.70
222.0	35.0	37.37	6.77
512.0	55.6	50.84	8.18
Avg.			5.45

TABLE II - AIRCRAFT

$$R = \frac{3.748 W^{1/3}}{\left(1 + \frac{2498}{W}\right)^{1/6}}$$

<u>W (lb.)</u>	<u>R_{obs} (ft.)</u>	<u>R_{cal} (ft.)</u>	<u>Percent Error</u>
8.0	7.0	7.02	0.285
20.0	10.5	10.55	0.476
38.0	14.5	14.35	1.045
100.0	23.0	23.02	0.130
450.0	47.5	48.01	1.073
3000.0	115.0	114.9	0.087
Avg.			0.516

TABLE III - ANTENNA

$$R = \frac{6.295 W^{1/3}}{\left(1 + \frac{103.8}{W^2}\right)^{1/6}}$$

<u>W (lb.)</u>	<u>R_{obs} (ft.)</u>	<u>R_{cal} (ft.)</u>	<u>Percent Error</u>
10.0	12.0	12.03	0.250
50.0	23.0	23.00	0.000
300.0	44.0	42.00	4.76
900.0	59.0	60.64	2.78
Avg.			1.948

TABLE IV - 3x9x.022-inch CYLINDER

$$R = 4.60 W^{1/3}$$

<u>W (lb.)</u>	<u>R_{obs} (ft.)</u>	<u>R_{cal} (ft.)</u>	<u>Percent Error</u>
8.5	9.0	9.55	6.1
115.0	26.0	22.3	16.6
900.0	45.0	44.3	1.6
2200.0	60.0	59.8	0.3
Avg.			6.2

TABLE V - AIRCRAFT

$$R = 1.728 W^{1/2}$$

<u>W (lb.)</u>	<u>R_{obs} (ft.)</u>	<u>R_{cal} (ft.)</u>	<u>Percent Error</u>
8.0	5.0	4.90	2.04
20.0	7.5	7.75	3.33
38.0	10.2	10.65	4.41
100.0	16.5	17.28	4.73
450.0	37.0	36.65	0.95
3000.0	103.0	94.7	8.76
Avg.			4.04

If one uses a shorthand notation to the effect that Eq. (12) is Eq. (13),

$$[A] [C] = [W] \quad (13)$$

then a least-squares fit for the coefficients in the C matrix can be obtained from Eq. (14)

$$[C] = [A^T A]^{-1} [A^T] [W] \quad (14)$$

where the superscript T implies the transform matrix and the superscript -1 implies the inverse matrix. This procedure was used to obtain the coefficients in the preceding examples. The curve fit can be weighted towards either the impulsive loading realm or the quasi-static loading realm by respectively dividing Eq. (11) or multiplying Eq. (11) by W to obtain Eq. (15) for a least-squares fit in the impulsive loading realm or Eq. (16) for a least-squares fit in the quasi-static loading realm.

$$\left[\frac{W^2}{R^6} \right] A^6 - \left(\frac{1}{W} \right) B^6 - \left(\frac{1}{W^2} \right) C^6 = 1.0 \quad (15)$$

$$\left[\frac{W^4}{R^6} \right] A^6 - (W) B^6 - (1.0) C^6 = W^2 \quad (16)$$

Least-squares fits to Eqs. (11), (15) and (16) were obtained in addition to least-squares fits to these equations with the B and C coefficients equal to zero in order to obtain the most accurate curve fits for these targets.

If significant scatter occurs in a limited number of experimental data points, curve fitting Eq. (1) to the experimental data can result in negative B or C coefficients. Eq. (17) for the data from Table IV is an example of such a result.

$$R = \frac{4.600 W^{1/3}}{\left(1 - \frac{78.68}{W} + \frac{689.7}{W^2} \right)^{1/6}} \quad (17)$$

Unfortunately, an equation such as (17) has vertical asymptotes or specific positive values of W at which the denominator of the equation goes to zero and the standoff distance approaches infinity. For example, Eq. (17) has an infinite R for a positive W of approximately 10. Obviously, such a result is meaningless. Although one might conclude that the curve fit was excellent if one only compared calculated values of R to experimental values of R, the conclusion would be invalid. Whenever these

negative coefficients arise from a least squares fit to Eq. (1), we have to realize that more experimental data points are needed if we are to have a three-parameter fit, or we must try various one- or two-parameter fits to the existing data.

Table VI presents curve fits using Eq. (1) and variations thereon to experimental data from all thirteen targets studied by O. T. Johnson [6]. In addition to the results presented in the previous five tables, Table VI

presents curve fits from Eq. (1) and variations thereon to experimental data on more aircraft, wire gages, various tip deflections on aluminum cantilever beams, overturning data on a cylinder, and additional crushing data on cylinders. The last column in Table VI presents the average percentage error for the experimental data on these targets. We can observe that the overall average accuracy for these errors on thirteen targets equals 5.8%.

TABLE VI - SUMMARY OF RESULTS FROM 13 DIFFERENT TARGETS

Structure Number	Type of Structure	Vulnerability Equation	Average Percentage Error
1	Aircraft	$R = 2.03 W^{1/2}$	5.89
2	Aircraft	$R = 1.728 W^{1/2}$	4.04
3	Aircraft	$R = \frac{8.748 W^{1/3}}{\left(1 + \frac{2498}{W}\right)^{1/6}}$	1.98
4	Aircraft	$R = 1.720 W^{1/2}$	4.26
5	Wire Gauge	$R = \frac{11.45 W^{1/3}}{\left(1 + \frac{145.5}{W}\right)^{1/6}}$	9.10
6	Cantilever Al. Beams (5" deflection)	$R = \frac{8.859 W^{1/3}}{\left(1 + \frac{756.9}{W^2}\right)^{1/6}}$	10.95
7	Cantilever Al. Beams (10" deflection)	$R = \frac{8.868 W^{1/3}}{\left(1 + \frac{77.17}{W}\right)^{1/6}}$	11.11
8	Trucks	$R = \frac{6.481 W^{1/3}}{\left(1 + \frac{45.06}{W} + \frac{6045}{W^2}\right)^{1/6}}$	5.45
9	Antennas	$R = \frac{6.295 W^{1/3}}{\left(1 + \frac{103.8}{W^2}\right)^{1/6}}$	1.95
10	Overturning Cylinders	$R = \frac{7.995 W^{1/3}}{\left(1 + \frac{112.2}{W}\right)^{1/6}}$	2.15
11	Crushing Cylinders (3" x 8.62" x .019")	$R = \frac{4.633 W^{1/3}}{\left(1 + \frac{423.0}{W^2}\right)^{1/6}}$	3.70
12	Crushing Cylinders (3" x 9.00" x .006")	$R = \frac{17.16 W^{1/3}}{\left(1 + \frac{286.9}{W}\right)^{1/6}}$	8.70
13	Crushing Cylinders (3" x 9.00" x .022")	$R = 4.60 W^{1/3}$	6.20
			Avg. 5.81

MEANING OF PREVIOUS STUDIES

O. T. Johnson [6] made an empirical observation in which he suggested that the R-W plane might be defined by a one-parameter curve fit given by Eq. (18).

$$R = A W^{0.435} \quad (18)$$

This study indicates that the 0.435 exponent on W in Eq. (18) is a compromise exponent falling between the 0.333 exponent that is valid in the quasi-static loading realm [see Eq. (4)] and the 0.500 exponent for strong structures in the impulsive loading realm [see Eq. (7)] or the 0.667 exponent for weak structures in the impulsive loading realm [see Eq. (9)]. Because there are only moderate differences in the 0.435 exponent and these other exponents, Johnson concluded that Eq. (18) could be used without causing large errors. Table VII is Johnson's procedure applied to the target in Table IV.

TABLE VII - JOHNSON'S PROCEDURE APPLIED TO TARGET IN TABLE IV

$$R = 2.82 W^{0.435}$$

W (lb.)	R_{obs} (ft.)	R_{cal} (ft.)	Percent Error
8.5	9.0	7.16	25.7
115.0	26.0	22.23	16.9
900.0	45.0	54.42	20.9
2200.0	60.0	80.28	33.8
		Avg.	24.3

Notice that in Table VII the error is significantly greater than in Table IV, even though both targets are for a one-parameter curve fit. In addition, the largest error in Table VII occurs for the smallest and largest charge weights. This result indicates that, if Johnson's equation were extended to even smaller or larger charges, the error would become greater and greater. One can also see a systematic error in Table VII rather than the random error which is apparent in Tables I through V. Johnson's procedure averages the standoff distance for a charge weight in the middle of his experimental test results, but it gives less and less accurate results as one moves further away from the average charge weight. If Johnson's procedure is applied to data from the "knee" of the R-W curve, that is, from the region where both pressure and impulse apply, it can give fairly accurate results; however, the error will compound as one then enters the impulsive or quasi-static loading

realms.

A second criticism of Johnson's procedure is that it is incapable of predicting a change in failure modes in any target. For example, the wing of an airplane will fail as a beam when loaded by a blast wave from very large nuclear explosive charges. On the other hand, this same wing loaded by a blast wave from small chemical explosive charges will fail locally by shredding panels and damaging stiffeners. Because Johnson's procedure has the same numerical exponent on W, he can not change failure modes. Even if Johnson concluded that he could have two separate coefficients in front of W for different failure modes, his solutions would give parallel lines on a log-log plot of R vs. W. These parallel lines could never intersect; hence a structure according to his solution could not change from one failure mode to another failure mode. Eq. (1) can be used to determine different failure modes in the same structure. Separate groups of coefficients

would be needed for each failure mode; nevertheless, the solutions are capable of intersecting so that different modes of failure are critical for different magnitudes of energy release.

Our criticism of Johnson's approach is not intended to mean that his technique should never be used. If one only has a single data point, and wishes to make only a small extrapolation in experimental results, Johnson's approach can be used without causing large errors. But, whenever three or more data points exist, Eq. (1) should be used as it is more accurate and approaches appropriate theoretical limits.

The Armed Services Explosive Safety Board has the mission of determining what are safe standoff distances around all explosive storage facilities. This organization [7] uses Eq. (4) for the quasi-static loading realm to

compute the maximum quantity of explosives that can be stored in a facility close to a road, runway, oil storage tank, house, etc. Obviously, the use of Eq. (4) by this organization should be criticized because it is only valid for one of the loading realms. In all fairness to the ASESB, this writer recognizes that they are aware of this limitation in using Eq. (4); nevertheless, the present U. S. codes on the storage of explosives have never been changed. Eq. (1) or a variation thereon would be far superior for determining what constituted appropriate standoff distances for various complex targets in the vicinity of explosive storage facilities.

The British [1] use a code which is a variation on Eq. (1) to determine how much explosive can be stored in the vicinity of brick houses. The British possess a large amount of air blast damage data on structures as a consequence of their being under bombardment during World War II. These data were used to empirically obtain Eq. (19) which is valid for brick house isodamage curves on the R-W plane.

$$R = \frac{K W^{1/3}}{\left[1 + \left(\frac{7000}{W}\right)^2\right]^{1/6}} \quad (19)$$

Eq. (19) is a special case of Eq. (1), when B equals zero. A brick house is probably a weak structure; hence, Eq. (19) should be valid. The British insert different values of K into Eq. (19) for different levels of damage. For example, a K of 9.5 is used to define complete demolition of the house, Class A damage, and a K of 140 is used when only 10% of the glass is broken, Class E damage.

Although the British use only one value of C for all levels of damage in Eq. (19) we should not presuppose that all targets would have a single B or C coefficient for different levels of damage. Targets 6 and 7 in Table VI are curves for data from identical cantilever aluminum beams which have been loaded to give different intensities of response. Structure 6 is for an isodamage level with 5 inches of permanent tip deflection, whereas structure 7 is for an identical beam undergoing 10 inches of residual tip deformation. These structures do not have the same B and C coefficients in their denominators. This observation indicates that we should not presuppose that a given structure has a constant value of the coefficients B or C for all levels of damage.

SUMMARY

In this paper, an equation which can be used for determining the form of the R-W plane for constant levels of damage from air blast waves imparted to complex targets has been presented. This equation has three coefficients in it which must be determined from experimental data. We have shown that a theoretical basis exists for using an equation with this format. The equation has been applied to vulnerability data from a variety of targets to demonstrate its applicability.

This charge weight-standoff equation can not be used to define the vulnerability of targets at altitude from data obtained at sea level. The P-I diagram must be used to determine vulnerability under altitude conditions. When used at sea level conditions, Eq. (1) will define isodamage curves for complex targets. Under certain special conditions, the three-parameter fit becomes a two-parameter fit. If all experimental data for a target lie completely in the impulsive loading realm or completely in the quasi-static loading realm, a one-parameter curve fit can be used to determine the vulnerability of a target over a limited range in charge weights.

Presently, the U. S. code for the storage of explosives uses a one-parameter fit which applies only to the quasi-static loading realm. Experimental data could be used to redefine the quantity distance tables in terms of the three coefficients, A, B and C in Eq. (1) to present a more accurate relationship for relating charge weight and standoff distance in the storage of explosives.

ACKNOWLEDGEMENTS

The work reported in this paper is unsponsored research performed by individual initiative. The writer is indebted to two St. Mary's University of San Antonio students, Messrs. Joe Martinez and Richard Guntz, for assisting in curve fitting Eq. (1) to experimental data. Dr. Wilfred E. Baker of SwRI reviewed the text of this paper, Mr. O. T. Johnson of BRL urged publication of this work, Mr. Michael Sissung of SwRI edited this transcript, and Mrs. Mary Ann Stark typed all drafts of this paper. All of their assistance is appreciated.

REFERENCES

1. D. E. Jarrett, "Derivation of the British Explosives Safety Distances." Prevention of and Protection Against Accidental Explosions of Munitions, Fuels, and Other Hazardous Mixtures, Annals of the New York Academy of Sciences, New York, October 28, 1968.
2. W. E. Baker, Damage to Aircraft by External Blast, Ballistic Research Laboratories Report Number 741, October 1950 (Confidential).
3. J. Sperrazza, Dependence of External Blast Damage to A-25 Aircraft on Peak Pressure and Impulse, Ballistic Research Laboratories Memorandum Report Number 575, September 1951 (Confidential).
4. B. Hopkinson, British Ordnance Board Minutes 13565, 1915.
5. W. E. Baker, "Prediction and Scaling of Reflected Impulse From Strong Blast Waves," International Journal of Mechanical Sciences, Vol. 9, pp. 45-51, 1967.
6. O. T. Johnson, A Blast Damage Relationship, Ballistic Research Laboratories Report Number 1389, September 1967 (Confidential).
7. DoD Contractor's Safety Manual for Ammunition Explosives, And Related Dangerous Materials, DoD 4145, 26M October 1968.

**PERFORM: A COMPUTER PROGRAM TO DETERMINE THE LIMITING PERFORMANCE
OF PHYSICAL SYSTEMS SUBJECT TO TRANSIENT INPUTS**

**Walter D. Pilkey and Bo Ping Wang
Department of Aerospace Engineering and Engineering Physics
University of Virginia, Charlottesville, Virginia 22901**

PERFORM is a user-oriented computational capability for the evaluation of the limiting performance of multi-degree-of-freedom dynamic systems. Appropriate systems are those for which certain maximum response variables, e.g., peak accelerations, stresses, or displacements, are to be minimized while other maximum response variables are bounded. The user provides system equations of motion in which those portions, e.g., isolators, of a system to be evaluated have been replaced by functions of time. Sets of constraints, objective functions, and possible transient inputs are also user prescribed. PERFORM then automatically computes the limiting performance characteristics. These characteristics can be employed in the evaluation phase of systems design by informing the systems engineer whether or not his preliminary design scheme is feasible and will guide him in appropriate modifications as the design proceeds and in the selection of optimal hardware.

INTRODUCTION

This paper describes the computational capability, PERFORM, for the evaluation of the limiting performance of transient dynamic systems. With this computer program the designer is able to determine on the basis of response specifications alone the feasibility of his proposed design; moreover he can monitor and measure his success during the design process itself. This is possible because the capability provides characteristics of the theoretically best, that is, the limiting, design concept. Without the characteristics of the limiting design, the evaluation of proposed designs can be made only by performing a multitude of analyses for each candidate design.

The development of PERFORM has been an effort to place one aspect of real-world systems design on an analytical basis. This is needed because so much of the physical design process is an art rather than a science. PERFORM makes it possible in certain areas of transient-loaded mechanical, structural, and control systems to approach a design directly from the design criteria with

no commitment to a particular design concept. Naturally design implies optimal design since the ultimate aim of the system designer should be to attain the wherewithal to deduce and implement concepts so that the design criteria are met in an optimum fashion.

PERFORM is designed for use in an engineering problem-oriented form. The user need only prescribe system equations of motion, sets of constraints, objective functions, classes of possible inputs, and desired limiting performance characteristics.

CAPABILITIES OF PERFORM

PERFORM is a computer program that can be used to determine the limiting performance characteristics of a dynamic system subject to transient loading. The concept and formulation of the limiting performance problem is considered in detail in Ref. 1, wherein particular emphasis is given to shock isolation systems. The example problems mentioned in this paper provide an indication of the range of applications of PERFORM.

The dynamic system can be described and input to PERFORM using the first or second order equations

$$\begin{aligned} \dot{\bar{s}} &= \underline{A}\bar{s} + \underline{B}\bar{u} + \underline{D}\bar{f}_k \\ \underline{M}\ddot{\bar{q}} + \underline{C}\dot{\bar{q}} + \underline{K}\bar{q} + \underline{U}\bar{u} &= \underline{F}\bar{f}_k \end{aligned} \quad (1)$$

in which \bar{u} is a vector of time varying functions, called control or isolator forces, that have replaced portions of the physical system. \underline{A} , \underline{B} , \underline{D} , \underline{M} , \underline{C} , \underline{K} , \underline{U} , \underline{F} are coefficient matrices. \bar{s} and \bar{q} are vectors of response variables, e.g., displacements, stresses, accelerations. \bar{f}_k is a forcing function vector where the subscript indicates the k^{th} set of forcing or loading functions. This allows the system to encounter alternate sets of disturbances which might occur with equal probability.

The acceptable equations of motion appear to be linear. In fact, however, they are "quasilinear" since those portions of the system replaced by \bar{u} can be linear, nonlinear, active, or passive. The remainder of the system must be linear as must the overall kinematics.

The user must place his equations in one of the forms of Eqs. (1). The non-zero elements of the matrices \underline{A} , \underline{B} , \underline{D} or \underline{M} , \underline{C} , \underline{K} , \underline{U} , \underline{F} are then entered as inputs. This is accomplished by identifying the matrix, e.g., \underline{M} MATRIX, and then specifying an element and its value, e.g., i , j , and M_{ij} . Elements not entered are assumed to be zero.

PERFORM finds the characteristics, including \bar{u} and tradeoffs between optimal response variables, of the dynamic system such that bounds on some of the response variables \bar{s} or \bar{q} or control forces \bar{u} are not violated while the maximum (or minimum) in time of other elements of \bar{s} or \bar{q} are minimized (or maximized).

Regardless of the form (first or second order) used to describe the equations of motion, the formats for the objective function and constraints are the same. In the case of the second order equations, a state variable vector \bar{s} is established as

$$\bar{s} = \begin{bmatrix} \bar{q} \\ \dot{\bar{q}} \\ \ddot{\bar{q}} \end{bmatrix} \quad (2)$$

Any linear combination of state variables, derivatives of state variables, or control forces can be used as an objective function. In the case of the system described by second order equations, these become linear combinations of accelerations, velocities, displace-

ments, and control forces. The objective function is input to PERFORM as

$$\underline{PX1}\bar{s} + \underline{PX2}\bar{u} + \underline{PX3}\bar{f}_k \quad (3)$$

where $\underline{PX1}$, $\underline{PX2}$, and $\underline{PX3}$ are coefficient matrices. If more than one row of the matrices of Eq. (3) contains non-zero elements, then the peak values in time of the vectors resulting from the meaningful rows are to be compared. PERFORM minimizes (maximizes) the maximum (minimum) of the peak values.

Constraints may be placed on state variables, derivatives of state variables, and control forces. The general form, which is again linear, is

$$\underline{YL} \leq \underline{Y1}\bar{s} + \underline{Y2}\bar{u} + \underline{Y3}\bar{f}_k \leq \underline{YU} \quad (4)$$

where $\underline{Y1}$, $\underline{Y2}$, $\underline{Y3}$ are coefficient matrices and \underline{YL} , \underline{YU} are lower and upper bound vectors. Constraints can be imposed at every time of the response or at specific times.

In summary, PERFORM accepts system equations of the form of Eq. (1). For prescribed initial conditions, PERFORM then computes the \bar{u} vector such that the

$$\max |\underline{PX1}\bar{s} + \underline{PX2}\bar{u} + \underline{PX3}\bar{f}_k| \quad (5)$$

is minimized (or $\min | |$ is maximized) while the constraints of Eq. (4) are satisfied. Any linear combination of \bar{s} , \bar{u} , and \bar{f}_k can be tabulated or plotted versus time. A tradeoff curve between the maximum objective function and any particular constraint can be generated by varying the bounds on that constraint.

PERFORM SYSTEM DESCRIPTION

PERFORM is a system of several programs, the functions, inputs, and outputs of which are outlined here. Figure 1 is the PERFORM system flowchart. Detailed descriptions and documentation for PERFORM are given in Ref. 2. The three separate system programs PREPROC (Pre-processor), MPS/360 (linear programming system), POSTPROC (Post-processor) are represented by rectangular boxes.

●PREPROC

The pre-processor program (PREPROC) places the problem as specified by the user in a linear programming format. The outputs of this program include the data necessary to get the results from the post-processor, the MPS/360 linear programming problem input, and a report on the pre-processor itself. PREPROC is written entirely in FORTRAN.

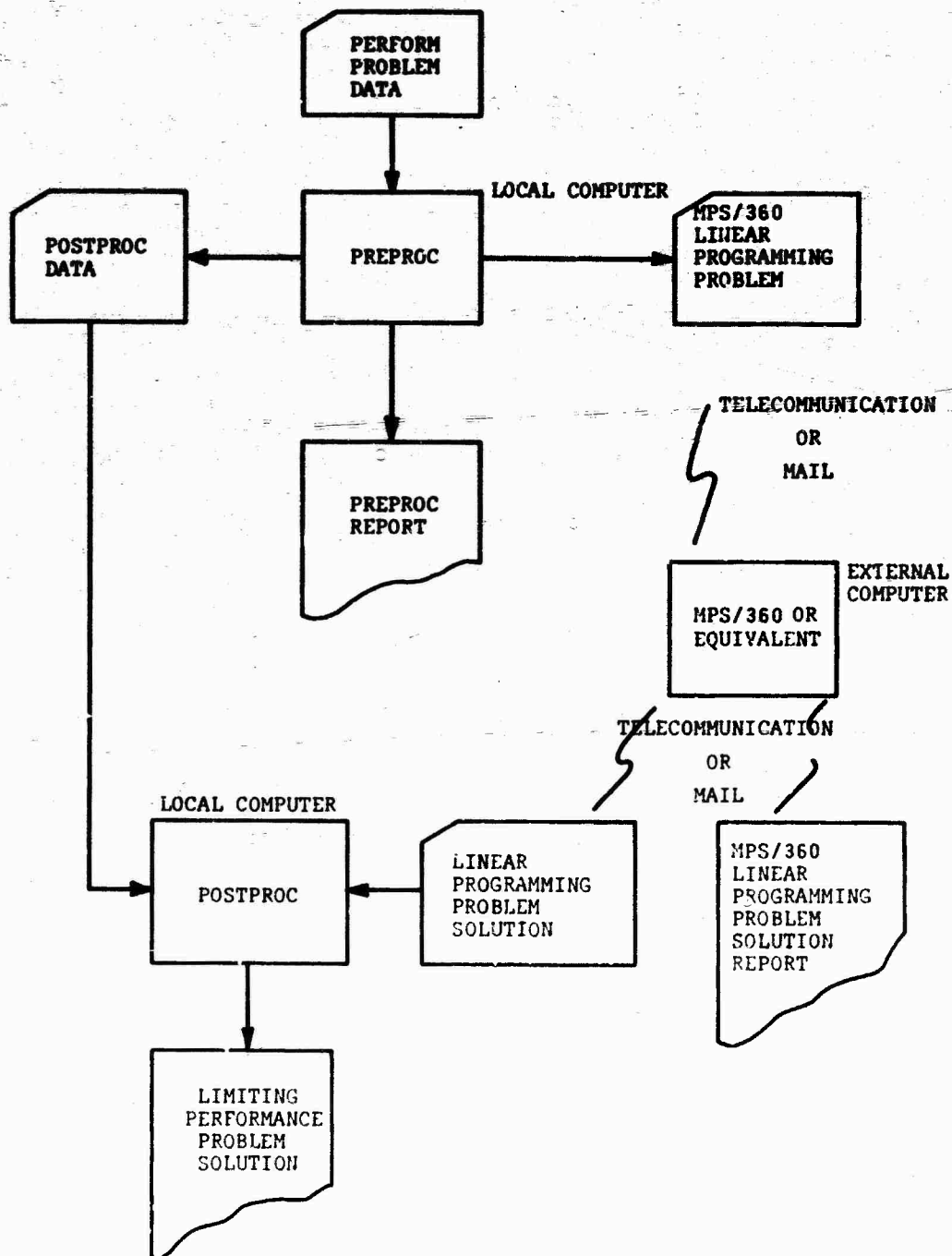


Fig. 1 - PERFORM system flowchart

•MPS/360

Mathematical Programming System (MPS)/ 360 is an IBM software package capable of efficiently solving extremely large linear programming problems. Most other commercially available linear programming systems accept MPS/360 input and hence are compatible with PERFORM. The input to MPS/360 is the linear

programming problem output of PREPROC. As indicated in Fig. 1, PERFORM is organized such that PREPROC and POSTPROC are to be run on local computers while MPS/360 can be run at the most convenient computer center where MPS/360 or an equivalent linear program is available. Naturally all of PERFORM can be run on the same computer if MPS/360 is available locally.

•POSTPROC

The post-processor program produces the final report of the problem solution. The tradeoff diagrams and trajectories requested by the user are tabulated or plotted in appropriate form. This program is written entirely in FORTRAN.

TECHNICAL DESCRIPTION

The limiting performance problem is formulated as a linear programming problem. The details of the formulation are given in Ref. 2. The unknown control forces are discretized in time. Integration of the equations of motion for known disturbances yields the response (state) variables as linear combinations of the control forces. The objective functions and constraints are then formed from these response variables and hence are also linear functions of the discretized control forces. The limiting performance problem then can be formulated as a linear programming problem.

A single solution of the system equations suffices to establish the linear programming problem. This is in contrast to most structural optimization schemes which involve multiple analyses of the system dynamics. The dimension of the linear programming problem depends on the number of controllers, the number of time intervals, and the number of sets of forcing functions. It is independent of the degrees of freedom of the system.

APPLICATIONS

PERFORM is designed to be used to establish the limiting performance characteristics of a variety of dynamic systems. It is particularly appropriate for the study of shock isolation systems [1]. Several applications of PERFORM are outlined in this section.

•Single-Degree-of-Freedom System

Consider a single-degree-of-freedom shock isolation system (see Fig. 2). Since this system has been so thoroughly explored elsewhere, e.g., Ref. 1, it is included here only to illustrate the use of PERFORM in the study of the limiting performance of a familiar system. The equation of motion is given by

$$m\ddot{z} + u = 0 \quad (6)$$

with initial conditions $\dot{z}(0)=\dot{z}(0)=0$. The kinematic relation is $z=x+y$. This gives

$$m\ddot{x} + u = -m\ddot{y} \quad (7)$$

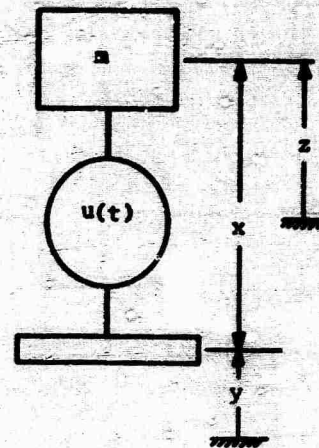


Fig. 2 - Single-degree-of-freedom shock isolation system

If $-m\ddot{y}$ is set equal to f , this is in the format (Eq. (1)) accepted by PERFORM.

Suppose the lowest possible peak acceleration of the mass (\ddot{z}) is sought if the relative displacement (x) between the mass and the base is bounded. Then the objective function (Eq. (3)) is given by $\ddot{z} = u/m$, with

$$\bar{s} = \begin{bmatrix} \ddot{z} \\ x \end{bmatrix} \quad (8)$$

The constraints are of the form of Eq. (4), that is,

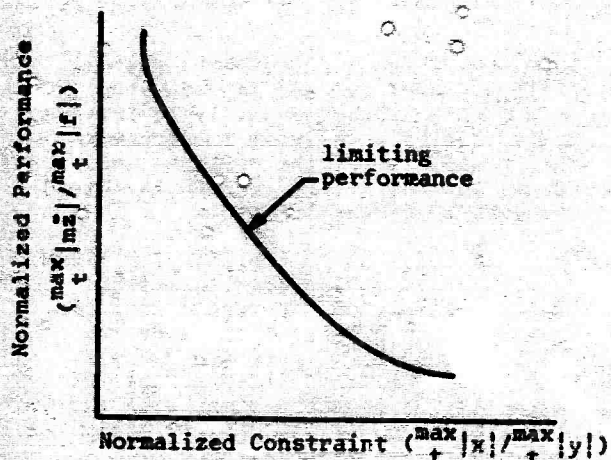
$$-X_{\max} \leq x \leq X_{\max} = YU \quad (9)$$

with X_{\max} prescribed.

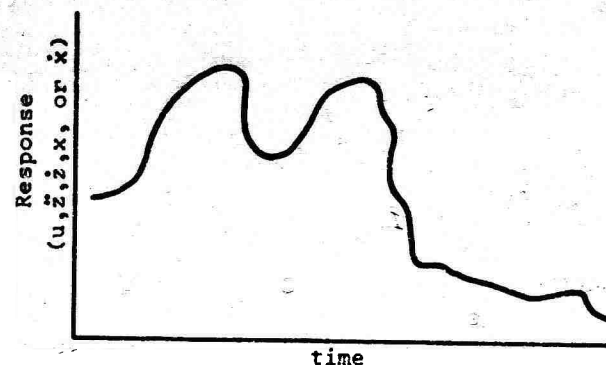
Typical results appear as in Fig. 3. At the users request, PERFORM automatically computes and plots the limiting performance or tradeoff curve of Fig. 3a. Details of the interpretation and use of this type of curve are discussed at length in Ref. 1. For a given constraint value, it is not possible for an isolator to be designed for the prescribed disturbance that exhibits a peak acceleration less than that on the limiting performance curve. Fig. 3b shows a time response history for an optimal isolator at a designated constraint level.

•Multi-Degree-of-Freedom Shock Isolation System

Using quite nonrestrictive assumptions, systems of the sort shown in Fig. 4 can be treated using PERFORM. Here the goal is to compute the limiting performance in terms of peak accelerations while several relative displacements are bounded. This problem



a. Limiting performance--A tradeoff diagram



b. Optimal time trajectories

Fig. 3 - Typical output of PERFORM

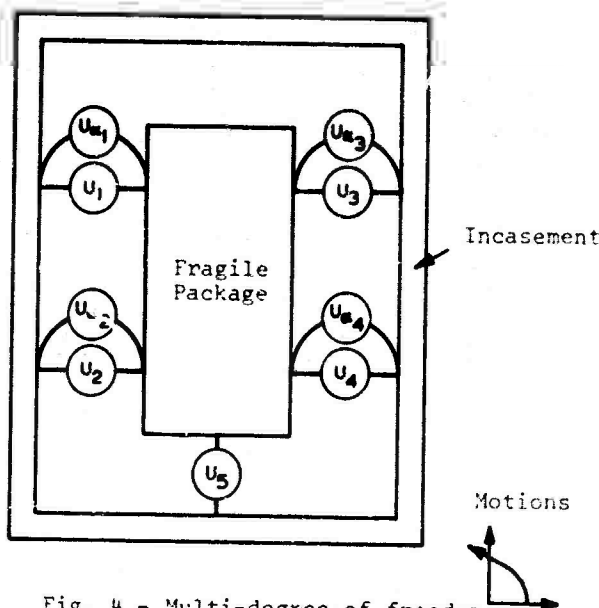


Fig. 4 - Multi-degree-of-freedom isolation system

was considered in Ref. 3 and extended in Ref. 2, where numerical results are given for a multi-degree-of-freedom

system with multiple objective functions.

• Other Applications

The applications of PERFORM to the design of mechanical systems are numerous. The following descriptions are of typical applications, all of which are treated in detail in Ref. 2.

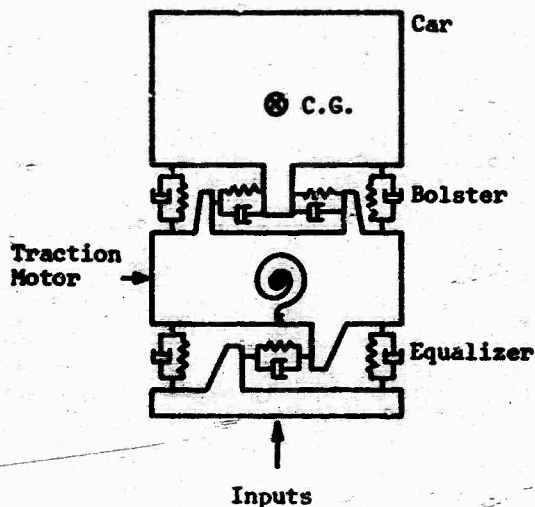
The Sewall-Parrish-Durling ten-degree-of-freedom model [4] for the lateral response of a high speed train subject to lateral or rolling inputs is formulated in Ref. 2 in terms of limiting performance by replacing some or all of the suspension configurations (Fig. 5a) by general isolator forces. Both three-isolator and eleven-isolator models are considered. The objective is to minimize lateral accelerations while bolster spring deflections are bounded.

The helicopter rotor isolation problem of Ref. 5 is also suitable for a limiting performance study (Fig. 5b). Here the multiple isolator system DAVI for vertical transient loadings can be replaced by four control forces to give four equations of motion in the PERFORM format. Here the control force definitions include the mass of the isolators themselves. The optimal isolator behavior can be computed to minimize the peak linear and angular accelerations of the fuselage while bounds on the motion across the isolator system are not violated.

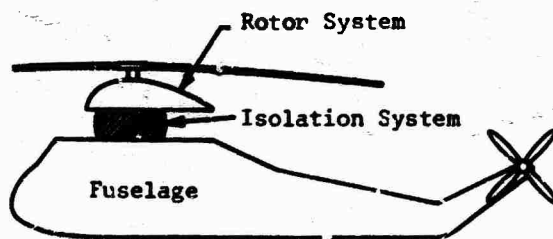
Another design problem that should be treated from a limiting performance standpoint is the question of lading protection in freight cars (Fig. 5c). The usual approach to this problem is that of analyzing the system response for a particular cushion or absorber configuration [6]. With PERFORM the potential protection given the lading by the cushion is computed regardless of the cushion configuration. In particular, the problem of minimizing the peak force transmitted to the lading while the cushion travel distance is bounded can be treated from the standpoint of limiting performance.

Such control problems as that of minimizing the lateral drift of a launch vehicle from a reference trajectory along a flight path can be approached as a limiting performance problem. The formulation of Ref. 7 for this problem, including bounds on the magnitude of bending moments, can be placed in a PERFORM format.

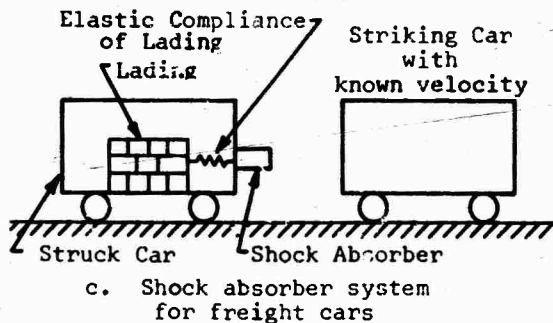
Finally, a max-min, rather than a min-max, problem is considered in Ref. 8.



a. High-speed train suspension system



b. Helicopter rotor isolation



c. Shock absorber system for freight cars

Fig. 5 - Various suspension system situations

The problem, control of a pressurized-water nuclear power plant, as given is suitable for solution by PERFORM. Specifically, the goal is to maximize the minimum pressure of a pressurizer while constraints are placed on maximum pressure and several responses. Also, terminal constraints are given on temperature and its rate of change.

CONCLUSIONS

A computational capability, PERFORM, for the evaluation of the limiting per-

formance of transient dynamic systems has been developed and is described in this paper. This capability is intended to be used by a designer to determine the feasibility of the proposed design specifications. Thus PERFORM is intended to be a design tool.

In addition to the use of PERFORM to scrutinize design specifications, this capability can be used during the actual design process to measure the relative success of proposed designs. This is accomplished by comparing the response of proposed designs with the characteristics of the theoretically best design provided by PERFORM.

ACKNOWLEDGMENTS

The helpful suggestions of J. L. Sewall and R. V. Parrish of NASA Langley Research Center were appreciated. This investigation was supported by NASA Langley Research Center (NGR 47-005-145).

REFERENCES

1. E. Sevin and W. Pilkey, Optimal Shock and Vibration Isolation, Shock and Vibration Information Center, Washington, D. C., 1971.
2. W. Pilkey, B. P. Wang, Y. Yoo, B. Clark, "Limiting Performance Capability for the Design of Dynamic Systems Subject to Transient Loading," Final Report NASA Grant NGR 47-005-145, 1971.
3. G. H. Klein, "Optimization of Linear, Nonlinear and Active Multi-Degree-of-Freedom Shock Isolation Systems," Ph.D. Dissertation, University of California at Los Angeles, 1971.
4. J. L. Sewall, R. V. Parrish, and B. J. Durling, "Rail Vehicle Dynamic Studies," Shock and Vibration Bulletin, Vol. 40, 1969.
5. E. Schuett, "Passive Helicopter Rotor Isolation Using the Kaman Dynamic Antiresonant Vibration Isolator (DAVI)," USAAVLABS Technical Report 68-46, 1968.
6. F. Freudenstein, "Dynamic Analysis of Long-Travel, High Efficiency Shock Absorbers in Freight Cars," J. of Engr. for Industry, ASME Paper No. 70-RR-1, 1970.
7. K. J. Davis and D. A. Ford, "Studies in Minimax Control," NASA TM-X-53189 1964.
8. M. R. Evans, "Optimal Control of Multivariable Dynamic Systems thru Linear Programming," Ph.D. Dissertation, University of Pittsburgh.

STRUCTURAL DYNAMIC ANALYSIS AND TESTING OF A SPACECRAFT DUAL TRACKING ANTENNA

D. D. Walters, R. F. Heidenreich, A. A. Woods and B. G. Wynn

Lockheed Missiles and Space Company
Sunnyvale, California

This paper will discuss the dynamic characteristics of flexible dual tracking antenna structures subjected to gimbal motor stepping torques. The structural dynamic technology problems encountered are approached from both the analysis and test point of view. The analytical techniques and assumptions are thoroughly delineated. The correlation and application of this analysis was then used to determine the most relevant test data assimilation, test techniques, and instrumentation requirements. This study will point out some of the typical problems encountered in the design, analysis and test of deployable antennas (fixed or flexible rib) that are mounted from spacecraft on rather large flexible booms and are excited by control forcing functions to accurately position the system. Some of the problems that are encountered in the analysis and test such as gear backlash, backup structure flexibility, zero "g" simulation, instrumentation noise, gear stress and fatigue, etc. are discussed.

INTRODUCTION

Preliminary analysis of antenna structures is presented showing the techniques used to size booms and antennas and the restrictions imposed on the analysis such as weight limitations, stowed space limitations, motor torques, and step-force torque frequency ranges. Based on these preliminary analysis the antenna and support structure sectional properties are determined. Also, the natural frequencies and modes shapes are defined and the structural response levels are determined for purposes of stress analysis and test information.

Antennas are complicated structures whose dynamic response can not be completely defined by analysis. Therefore, the analysis must be supported by a comprehensive test program. This paper will fully define the test set up required to accurately determine the structural oscillations that are encountered during antenna positioning. Considerations made in antenna suspension such as attach cable lengths and c. g. locations to best simulate zero "g" are explained. The selection of the type of instrumentation and data recording devices used and the considerations that were made in choosing them is presented. Both accelerometer and photographic measurements were obtained for a typical configuration and excellent correlation exists between these measurements. Some of the

problems encountered with accelerometers and their respective integrating devices are described. Photographic techniques, their applications for this structure and their results and shortcomings are also described.

Due to the antenna's oscillatory motion and impact loads from gear backlash, the stepper motor gear train is subjected to repeated loads and stresses. These repeated loads, the manner in which they were measured during test and their statistical distribution and number of cycles are described. Because of this cyclic motion, a gear fatigue analysis was conducted and considerations and effects of tooth surface finish, load applications, etc. are elaborated upon. To determine the lifespan of this particular antenna stepper motor gear, a simulated extended life test was conducted. The test set up, torque simulator, and gear wear versus time will be described.

ANALYSIS

Prior to the final design of structures (in this case an antenna structure) that are exposed to periodic forcing functions, an analysis of the expected frequencies and responses is conducted. Since this antenna system is positioned by stepping torque motors that apply short duration,

periodic square wave pulses, a dynamic modal analysis was necessary to determine the dynamic loads imposed on the structure. These loads were then used to arrive upon a feasible preliminary design. This design was then employed to study the dynamic properties of such systems.

When the antenna system stepper motors position the antennas, short duration pulses are applied in the pitch and roll direction. There were seven pitch rates that varied from 0.5 to 11 pulses per second and three roll rates of 0.80, 1.5, and 2.0 pulses per second. Because antenna systems have weight limits, the modal analysis of the antenna showed that in order to tune the natural frequencies to exceed the pulsing frequencies by a reasonable margin the weight would become excessive. Therefore, the antenna could not be designed to exceed the gimbal pulsing frequencies. The resonant frequencies were determined by analysis and the resulting loads, deflections and stresses were low and not design critical. However, because the gear train tolerances of the pulsing motor could not be represented accurately in the dynamic model, the actual displacements of the antenna assembly could not be determined prior to the dynamic response test.

A finite element model for the modal analysis was made as shown in Figure 1. The model consisted of 11 node points (6 degrees of freedom each) connected by 10 straight beams. The beams have flexibility in both bending axes, torsional and axial flexibility. The stiffness properties for beams connecting node 1-2, 2-3, 3-4 and 4-5 were derived from the cross-sectional properties of the hardware. The stiffness properties of the beams connecting node 1 with nodes 10 and 11 reflect the same flexibility as obtained from static tests.

A step force test was made on the platform assembly (the beam connecting the antennas) to determine the individual frequencies of the 3 foot dish and its feed assembly and the 2 foot dish and feed. The frequencies obtained from the tests are shown in Table I. The frequencies were used to determine the stiffness of the beams connecting nodes 5 through 9 in the finite element model.

A parameter study was made to determine the effect of varying the boom stiffness on the frequency of the system. The results are shown in Table II. Case I is the actual value of the boom. Cases III and IV were selected to determine the stiffness necessary to raise the frequency above 15 Hz in order to exceed the highest pitch pulsing frequency of 11 Hz by a factor of 1.5. The increased size and weight of the boom necessary to obtain this frequency was considered prohibitive.

The tolerance of the gear train (backlash) of the pulsing motor could not be adequately represented in a linear dynamic model. The actual time histories of the acceleration and displacement of the dishes could not be accurately

determined by this analysis. Although the actual deflections could not be determined, the effects on maximum deflections expected due to changes in mass and stiffness could be ascertained.

The pulsing motor torque was applied to the gimbal point of the dynamic model and maximum displacements were computed for various mass and stiffness changes. Since the largest displacements were obtained with a pitch input torque, this input torque was used in the parameter study. The changes in maximum deflections due to changes in platform stiffness and boom stiffness are shown in Table III. Deflections were computed with the 3 foot antenna both closed and open to determine the effect on the deflection. The change is shown in Table II.

The modal analyses indicated that the antenna assembly pulsing frequencies were in the saw range as the structural resonant frequencies. Further analysis also revealed that with the existing weight constraints of the antenna these resonant frequencies could not be significantly increased. The modal deflections were computed and were found to be no more than several minutes of arc. These facts were all well borne out during dynamic response testing and it was concluded that the modal analysis was an extremely valuable tool throughout the study and early design phase.

TEST SUSPENSION SYSTEM

To determine the approximate amount of oscillatory response of the antenna system to the gimbal motor input pitch and roll torques, a preliminary test setup was devised and instrumented to determine the highest response pulsing frequency. This setup was done in such a manner that the pitch axis was parallel to the floor. When this test was conducted, the accelerometer and photographic data clearly revealed that the gravity force had an adverse effect on the dynamic oscillation of the antenna system (i.e., as the unit pitched farther over the magnitude of the oscillations increased). However, this data indicated that the maximum oscillations occurred in the pitch direction at or near the pitch rate of 4 Hz and the roll pulse rates did not contribute significantly to the oscillations.

Based on the preliminary test data, it was determined that a more sophisticated test minimizing gravity effects should be conducted. This was accomplished by suspending the antenna system in such a manner that the pitch axis would be perpendicular to the floor to minimize the effect of gravity on the dynamic oscillations. This allowed pulsing only in the pitch direction, which the preliminary test showed to be more severe than the roll pulse response. In addition, a much more complete and accurate instrumentation and photographic technique was devised. Gimbal gear torque loads were also required from this test because of questions that were raised concerning gear tooth failure and wear.

The suspension system that was used for the system dynamic response test is shown in Figure 2. Careful study of this illustration shows that the point B ceiling attachment needs to be directly over the gimbal pitch axis or a torque load is applied. Obviously, the higher the ceiling attach point becomes, the smaller the torque component is if the system is misaligned. It was agreed that with very careful alignment and center of gravity location by transits, a thirty-five foot ceiling height would be adequate. To keep the natural frequencies of the attach cables as low as possible (0.50 Hz or less) a 0.25 pound per inch spring was installed to the cable near the ceiling. A detail step by step procedure was devised that used transits to accurately determine the c.g. of the antenna system.

ACCELEROMETER TEST DATA ACQUISITION

Ten accelerometers (Kistler type 818) were installed on the antenna system at the locations shown in Figure 2. These locations were chosen to determine various critical oscillation amplitudes and resultant torque loads due to gimbal pitch motion.

The torque load on the gimbal gear was determined by summing the accelerations of various accelerometers as follows:

$$\vec{T} = \sum_{i=1}^{10} \vec{F}_i \cdot l_i = \sum_{i=1}^{10} m_i \cdot \ddot{x}_i \cdot l_i$$

Thus, the total moment about the pitch axis was derived from the various mass accelerations and moment arms of the antenna structure. This was achieved by channeling the accelerometer response through a sum and difference network.

The antenna deflection data was determined by the use of integration and sum and difference networks. For example, to determine the relative rotation of the 3 foot dish feed with respect to the 3 foot dish, the accelerometer signal given below was twice integrated through the integration network.

$$\ddot{\theta}_B = g \left\{ \left(\frac{\ddot{x}_1 - \ddot{x}_2}{l_1} \right) - \left(\frac{\ddot{x}_4 - \ddot{x}_7}{l_2} \right) \right\}$$

where θ_B = Min. of Arc of Channel B

$g = 386 \text{ in/sec}^2$

subscript numbers refer to accelerometer location
(See Figure 2)

The angular excursions of all the other critical locations on the antenna were integrated in a similar manner.

Following a specific test procedure, the test specimen was pulsed at seven different pitch rates and oscillograph and magnetic tape data was recorded. The measurements that were recorded on the oscillograph are shown in

Table IV.

Analysis of the oscillograph recordings consisted of reading the maximum peak value encountered during each plus and minus pitch direction for each of the seven pitch rates resulting in a total of fourteen values for each channel of data. The axis in minutes of arc for the various pitch rates are small even though these values contained a considerable amount of electrical noise in all data channels except Channel A.

The maximum peak value of each channel and its respective pitch rate is summarized in Table V. It can be seen by comparison of signal to noise levels that the noise level may contribute significantly to the measured rotations.

This analysis of the oscillograph data shows that the dynamic oscillations encountered during tracking operations are small even when the noise level is included in the peak rotation values.

The torque loads on the sector gear were obtained from the accelerometer data by reading a sample of pitch axis torques over an extended time span. The Poisson Approximation method was then used to arrive at a distribution of the number of cycles of different torque levels that the antenna system is expected to experience during its use. These torque distributions and cycles (Table VI) were used for the sector gear fatigue analysis.

PHOTOGRAPHIC TEST DATA ACQUISITION

To obtain additional dynamic response data, high speed motion pictures were taken of the specimen during the dynamic response test. The photographic information was also to be used for comparative purposes with the accelerometer data because of the known noise problems with the amplification of low accelerometer voltages encountered during the small antenna oscillations.

During the alignment of the antenna system, high speed cameras were installed in the ceiling loft in such a manner that pitch rate dynamic oscillations could be photographed. Several targets were located on the specimen to photographically record the various motions of the antenna system. The optical target locations, and their respective numbers, that were used for the analysis of the dynamic oscillations are illustrated in Figure 3. The film speed used for analysis was one hundred frames per second to be assured enough points would be measured to define the complete cyclic motion of the specimen. This frame speed was based on a maximum expected specimen oscillation frequency of 20 Hz.

The test was conducted according to a detailed procedure with the high speed cameras recording the pulse rate data. After a cursory look at the accelerometer data, the pulse rates that were considered to be the most critical were selected and the photographic data of these rates was analyzed. The pulse rates that were

selected for analysis were 4, 7, and 11 Hz. The machine used to read the photographic data was a Gerber Film Analyzer which measures distances from the reference target to the moving targets (i.e., targets #1, #2, and #3) in the X and Y plane. Based on the geometry of the distances from the pitch axis of rotation to the various targets, the equations of the angular rotations of each target were derived. These equations were written so that the angle change per frame (i.e., $\Delta\theta$), as well as the cumulative angle (i.e., θ_c) for each target, was determined. Also, the relative angular change per frame was ascertained for the 3 foot dish with respect to its feed and for the 3 foot dish feed with respect to the 2 foot dish.

A computer program was written and the angular oscillations of the various targets were printed in the standard computer format. Eight different angular measurements were printed for each picture frame read. A description of the print-out data for the various targets is shown in Table VII. A plot routine of this data was also made to show a time history of the angular movement of the antenna system. One example of the time history plots of photographic data for a pulse rate of 4 pulses per second is shown in Figures 4 and 5. The first plot (i.e., Figure 4) shows the change in angle of each target versus time. Due to reader error and lens distortion some cumulative data error occurs. This cumulative error is well illustrated after 2400 milliseconds in Figure 4. Ideally, if there were no cumulative errors all three targets would very nearly be the same value after 2400 milliseconds. The total angular rotations of each target are not identical but the important magnitudes of oscillations for each pitch pulse are very well described. The relative angular rotations of targets 1, 2 and 3 (i.e., Figure 5) describe the angular differences between critical antenna structural locations.

The maximum peak angular oscillations measured from the photographic data for pulse rates of 4, 7, and 11 Hz are listed in Table VIII. This shows that the highest angular rotation measured occurs on the 3 foot dish at a pulsing frequency of 4 Hz.

In order to obtain an overall comparison of the photographic and accelerometer test data, refer to Table IX. This data shows some of the variations of angular rotation in the two data gathering techniques. Because of the electrical noise observed from the accelerometer data, it was decided that it was less accurate than the photographic data. This comparison of both data techniques shows the worst single amplitude oscillation that was measured was 9.26 minutes of arc and the highest relative rotation was 9.51 minutes of arc at a pulse rate of 4 Hz.

FATIGUE ANALYSIS AND EXTENDED LIFE TEST

Due to the many variables that may influence fatigue failure such as surface finish, load application, environment, etc., any fatigue

analysis of even the simplest parts is an approximation at best. Therefore, the fatigue analysis defining the specified life of a very complicated antenna system gear train under impact load conditions is extremely difficult to achieve with any reasonable accuracy. For this reason, simulated service testing or actual service testing will provide the most reliable data for particular applications.

A simulated service test prior to the design of a gear system may be more accurate but it is not only impractical but in many cases may be impossible because of schedule commitments, budget restrictions, etc. Even though the fatigue analysis is an approximation, it is most certainly an essential part of any preliminary design of this nature. To best illustrate these differences between the analysis and the test data, both a fatigue analysis and an extended life test was conducted on the antenna gear train system. The particular gear of concern was the aluminum alloy (7075-T6511) sector gear.

The calculated gear root static stresses, based on the torque loads determined from the dynamic response test, are shown in Table VI. These stresses included variables such as impact factors, scatter factors, stress concentration factors, and contact ratios that either have to be assumed or based on some prior experience. The values of these variables are primarily determined by the individual doing the analysis and his evaluation of the gear loading conditions and service requirements. By the application of the Minor theory of linear cumulative fatigue damage to an appropriate S-N plot, the expected service life of the antenna sector gear was determined.

This analysis showed that the sector gear would exceed its spectrum life of 3,500 cycles by approximately 170 per cent.

After fabrication of the sector gear system a life test fixture was made in such a manner that the sector gear would experience similar inertias and frequencies as seen on the actual system.

Accelerometers were placed on the inertia simulators and the pulse rate was varied until the maximum torques were obtained. These maximum torques were recorded at the pitch pulse rate of 9 Hz. The torque values were then recorded on the oscillograph for a long enough period to achieve enough data points for a suitable torque distribution. This data was then analyzed and the number of stress reversal cycles for various torque ranges was determined. (See Table X).

The extended life test was then conducted. Periodic checks of the amount of wear was recorded after 40, 80, 120, and 160 hours of testing. A comparison of the amount of the gear backlash wear is tabulated in Table XI. As shown, the life test of the sector gear after

160 hours of testing showed an increase in backlash of only 2.6 minutes of arc. Most of this wear occurred in the first 40 to 80 hours of test which leads one to believe that most of the wear is in smoothing the rough points and high spots on the gear teeth.

After 160 hours (approximately 5×10^6 pulsing cycles) of simulated service testing, the test was stopped. The sector gear was then inspected and there was no evidence of fatigue damage, cracks, fretting, etc. Thus, it more than exceeded its requirements of 3500 pulsing cycles. The extended life test data was then analyzed in the same manner as described in the fatigue analysis discussion.

The fatigue analysis data indicated gear failure after approximately 5×10^5 applied cumulative cycles and the life test data analysis showed that the sector gear was subjected to 1.8×10^6 cumulative cycles without failure. Thus, the fatigue analysis was very conservative and resulted in a conservative design for this application. Conservative design for the antenna gear train was desirable in this case because the additional reliability was achieved with an insignificant weight penalty, and low gear wear and backlash requirements imposed some conservatism in the design.

This study revealed that gear wear may be examined in great detail. The determination of the torque loads and life cycle testing was relatively easy to perform. However, interpretation and application of these results was a more difficult task. This gear train analysis emphasizes the fact that present day knowledge of fatigue of complicated systems is not sufficiently advanced to permit design for a specified life within close limits. It must be noted that simulated service testing and actual service testing may provide the most reliable data for particular applications.

CONCLUSIONS

This paper has described the pertinent structural dynamic aspects of analyzing, designing and testing of a typical boom mounted spacecraft tracking antenna system. Analysis and tests to define dynamic structural perturbations from stepper motor forcing functions, instrumentation and data gathering problems and techniques, and the effects of cyclic loading on stepper motor gear wear and fatigue characteristics were delineated. As the use and concepts of flexibly mounted tracking antennas increase, these structural dynamic problems are of significant importance to the overall mission and performance of spacecraft antenna systems.

TABLE I

STEP FORCE PLATFORM FREQUENCY DATA

Location	Step Force Direction	Direction of Measurement	1st Mode f_n (Hz)
2' Dish & Feed	Pitch	Pitch	6-7
2' Dish & Feed	Pitch	Roll	8
2' Dish & Feed	Roll	Pitch	20
2' Dish & Feed	Roll	Roll	7
3' Dish & Feed	Pitch	Pitch	12-14
3' Dish & Feed	Roll	Roll	42
3' Dish Feed Tip	\perp to feed	\perp to feed	18-19

TABLE II
BOOM STIFFNESS VS. FREQUENCY

Case	Frequency (Hz)	EI_1 (lb-in ²) (1)	EI_2 (lb-in ²) (2)	J_0 lb-in ²)
I	3.27	.722 X 10 ⁶	.287 X 10 ⁷	.505 X 10 ⁶
II	3.7	.916 X 10 ⁶	.253 X 10 ⁷	.612 X 10 ⁶
III	17.7	.50 X 10 ⁸	.50 X 10 ⁸	.124 X 10 ⁸
IV	18.2	.10 X 10 ⁹	.10 X 10 ⁹	.124 X 10 ⁸

(1) EI_1 - Bending stiffness in plane of nodes 1, 2, and 3

(2) EI_2 - Bending stiffness normal to plane determined by nodes 1, 2 and 3

TABLE III
STIFFNESS PARAMETER STUDY

CASE	PITCH AXIS RESPONSE CHANGE	
	2' DISH	3' DISH
OPEN ANTENNA	0	0
CLOSED ANTENNA	-3%	-8%
50% INCREASE PLAT. STIFFNESS	+1%	-7%
100% INCREASE PLAT. STIFFNESS	-7%	-.5%
50% INCREASE BOOM STIFFNESS	-16%	-22%

INPUT - 4 PULSES/SECOND

TABLE IV
OSCILLOGRAPH MEASUREMENTS RECORDED DURING
THE ANTENNA DYNAMIC RESPONSE TESTS

Measurement Channel	Units	Value Measured	Symbol
A	in-lbs	Total Moment about Pitch Axis	$\sum_1 (m_1 \ddot{x}_1) l_1$
B	Min. of Arc	Relative Rotation of 3 ft Dish Feed to 3 ft. Dish	3' F/D
C	Min. of Arc	Relative Rotation of 2 ft Dish Feed to 2 ft. Dish	2' F/D
D	Min. of Arc	Absolute Rotation of 3 ft Dish Feed	3' F
E	Min. of Arc	Absolute Rotation of 3 ft Dish	3' D
F	Min. of Arc	Absolute Rotation of 2 ft Dish	2' D
G	Min. of Arc	Absolute Rotation of 2 ft Dish Feed	2' F
H	Min. of Arc	Relative Rotation of 3 ft Dish Feed to 2 ft Dish Feed	3' F/2' F
I	Min. of Arc	Relative Rotation of 3 ft Dish to 2 ft Dish	3' D/2' D

TABLE V

MAXIMUM PEAK VALUE AND AVERAGE NOISE LEVELVERSUS PITCH PULSE RATE

<u>Measurement Channel</u>	<u>Max. Peak Value Pulse Rate</u>	<u>Maximum Peak Value</u>	<u>Mean Peak Noise Level</u>
A $\sum_1 (n_1 \bar{x}_1) l_1$ (in-lbs)	7 Pulses/Sec.	54	Insignificant
B 3' F/D (Min)	4 "	6.76	4.05
C 2' F/D "	7 "	8.46	4.06
D 3' F "	5 "	5.52	1.41
E 2' D "	4 "	6.75	3.99
F 2' D "	4 "	5.53	3.54
G 2' F "	4 "	4.50	2.63
H 3' F/2' F (Min)	4 "	5.40	2.32
I 3' D/2' D "	4 "	7.80	5.28

TABLE VI

DYNAMIC RESPONSE TESTPITCH AXIS TORQUE LOAD DISTRIBUTION

<u>TORQUE (In-Lb)</u>	<u>CYCLES</u>	<u>STRESS (psi)</u>
0-8	3,664	5,820
9-16	6,668	11,650
17-24	3,568	17,450
25-32	1,114	23,300
33-40	417	29,100
41-48	95	34,900
49-56	18	40,750
57-64	4	46,600

TABLE VII

ANTENNA SYSTEM COMPUTER PRINT-OUT FORMAT PER FRAME

Symbol	Value Measured Per Frame (Min. of Arc)	Target No. Read (See Fig. 3)
$\Delta \theta_1$	Angular Rotation of 3' Dish	1
$\Delta \theta_2$	Angular Rotation of 3' Dish Feed	2
$\Delta \theta_3$	Angular Rotation of 2' Dish Feed	3
θ_{1C}	Total Cumulative Rotation of 3' Dish	1
θ_{2C}	Total Cumulative Rotation of 3' Dish Feed	2
θ_{3C}	Total Cumulative Rotation of 2' Dish Feed	3
$\Delta \theta_1 - \Delta \theta_2$	Relative Rotation of 3' Dish Feed to 3' Dish	1 & 2
$\Delta \theta_2 - \Delta \theta_3$	Relative Rotation of 3' Dish Feed to 2' Dish	2 & 3

TABLE VIII

MAXIMUM PEAK VALUES OF PHOTOGRAPHIC DATAFROM ANTENNA RESPONSE TEST

Pulse Rate (Pulses/Sec)	Maximum Peak Value (Min.)				
	$\Delta \theta_1$	$\Delta \theta_2$	$\Delta \theta_3$	$\Delta \theta_1 - \Delta \theta_2$	$\Delta \theta_2 - \Delta \theta_3$
4	9.26	2.86	2.10	9.51	3.21
7	4.74	2.99	5.25	4.89	4.81
11	3.54	3.91	7.13	3.80	5.83

$\Delta \theta_1$ = Target #1 angular rotation - 3' Dish

$\Delta \theta_2$ = Target #2 angular rotation - 3' Dish Feed

$\Delta \theta_3$ = Target #3 angular rotation - 2' Dish Feed

TABLE IX

MAXIMUM PEAK VALUES OF PHOTOGRAPHIC AND
ACCELEROMETER DATA FROM ANTENNA DYNAMIC

RESPONSE TEST

Pulse Rate Pulses/Sec	Value Measured (See Table V)	Maximum Peak Value (Min. of Arc)		
		Photo (See Table VIII)	Accel. (See Table V)	Highest Values
4	3' D	9.26	6.75	9.26
	3' F	2.86	4.0	*4.0
	2' F	2.10	4.5	*4.5
	3' F/D	9.51	6.76	9.51
	3' F/2'F	3.21	5.4	*5.4
7	3' D	4.74	4.28	4.74
	3' F	2.99	2.72	2.99
	2' F	5.25	3.0	5.25
	3' F/D	4.89	5.14	*5.14
	3' F/2'F	4.81	3.78	4.81
11	3' D	3.54	5.63	*5.63
	3' F	3.91	3.20	3.91
	2' F	7.13	2.70	7.13
	3' F/D	3.80	5.94	*5.94
	3' F/2'F	5.83	3.78	5.83

* Indicates the accelerometer data gave the highest value

TABLE X

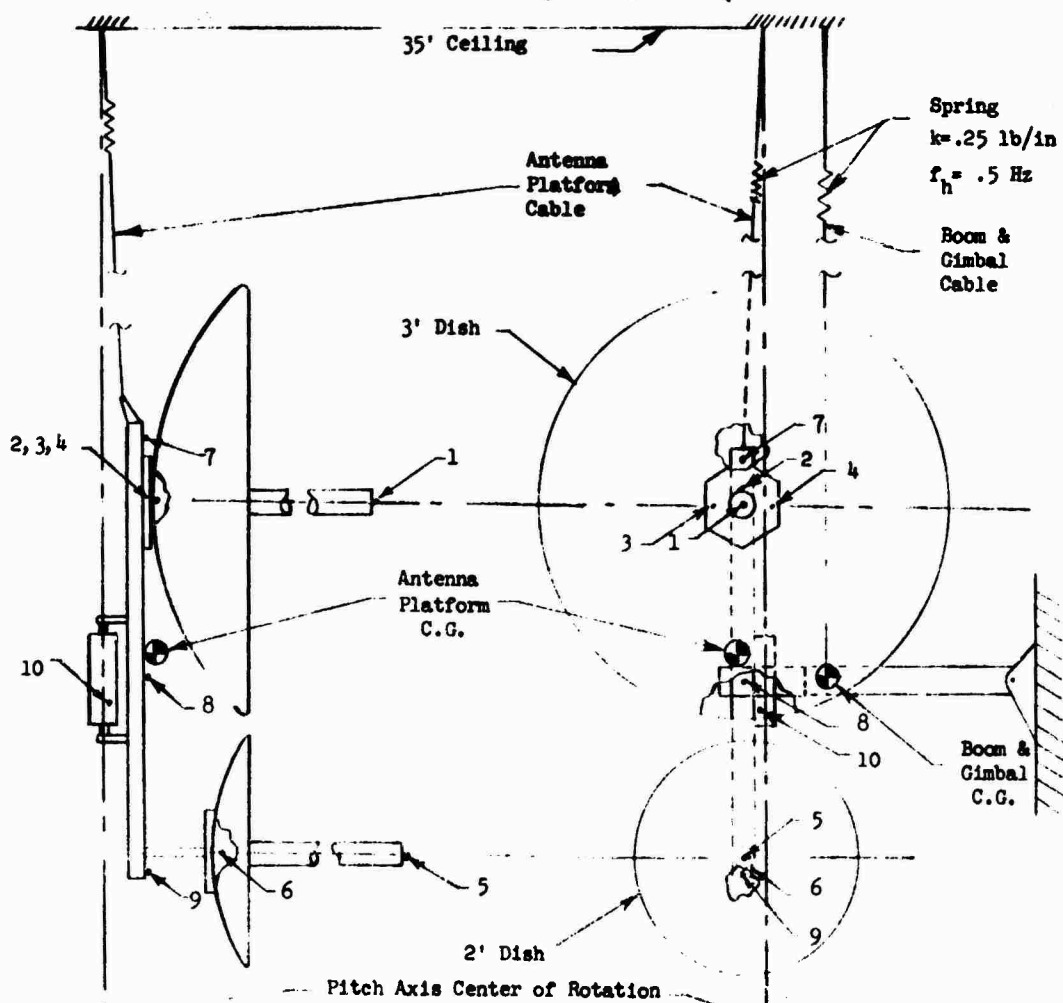
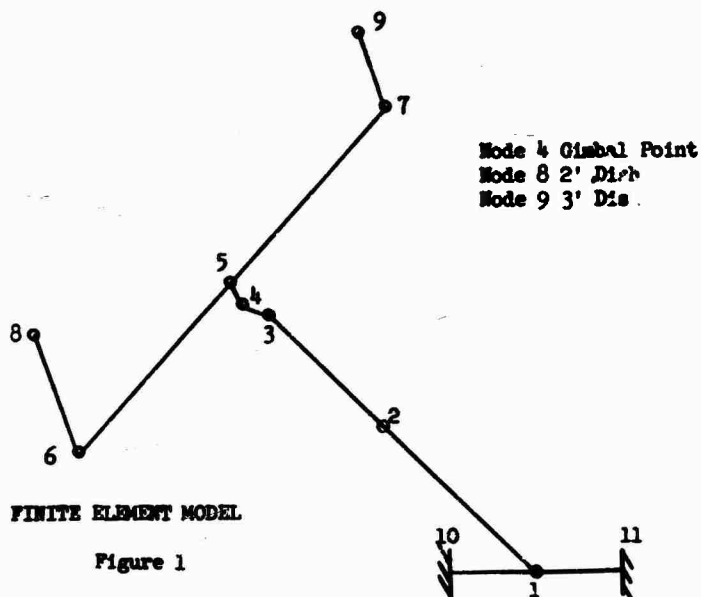
EXTENDED LIFE TEST PITCH
GIMBAL SECTOR GEAR TORQUES

Torque Range (in-lb)	Complete Reversals Per Hour
0 - 10	7,250
11 - 15	1,350
16 - 20	2,670
21 - 25	180

TABLE XI

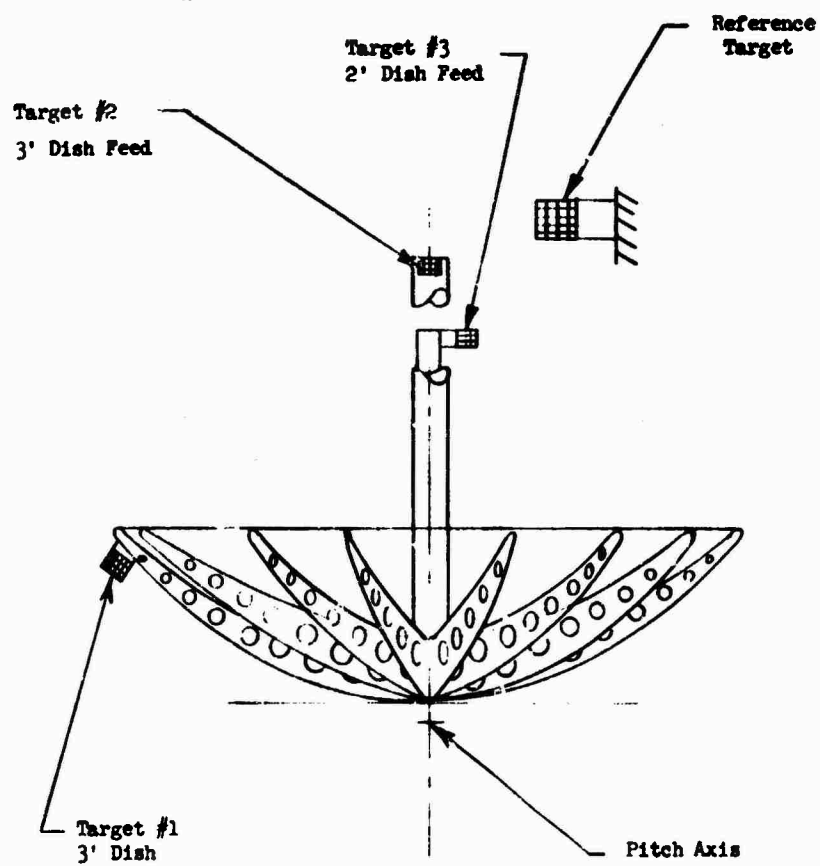
EXTENDED LIFE TEST PITCH SECTOR
GEAR BACKLASH MEASUREMENTS

Pitch Position (Degrees)	Gear Backlash Measurement (Minutes of arc)				
	Start	After 40 Hrs.	After 80 Hrs.	After 120 Hrs.	After 150 Hrs.
0	8.3	10.3	10.5	10.8	10.9
15	8.3	9.2	9.9	10.8	10.8



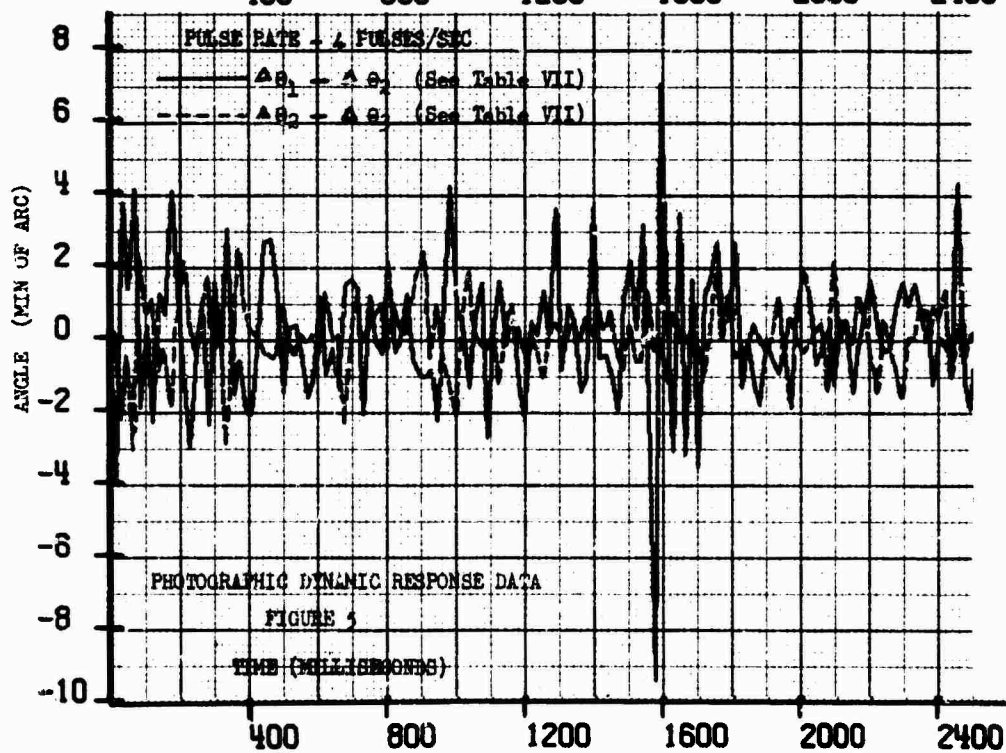
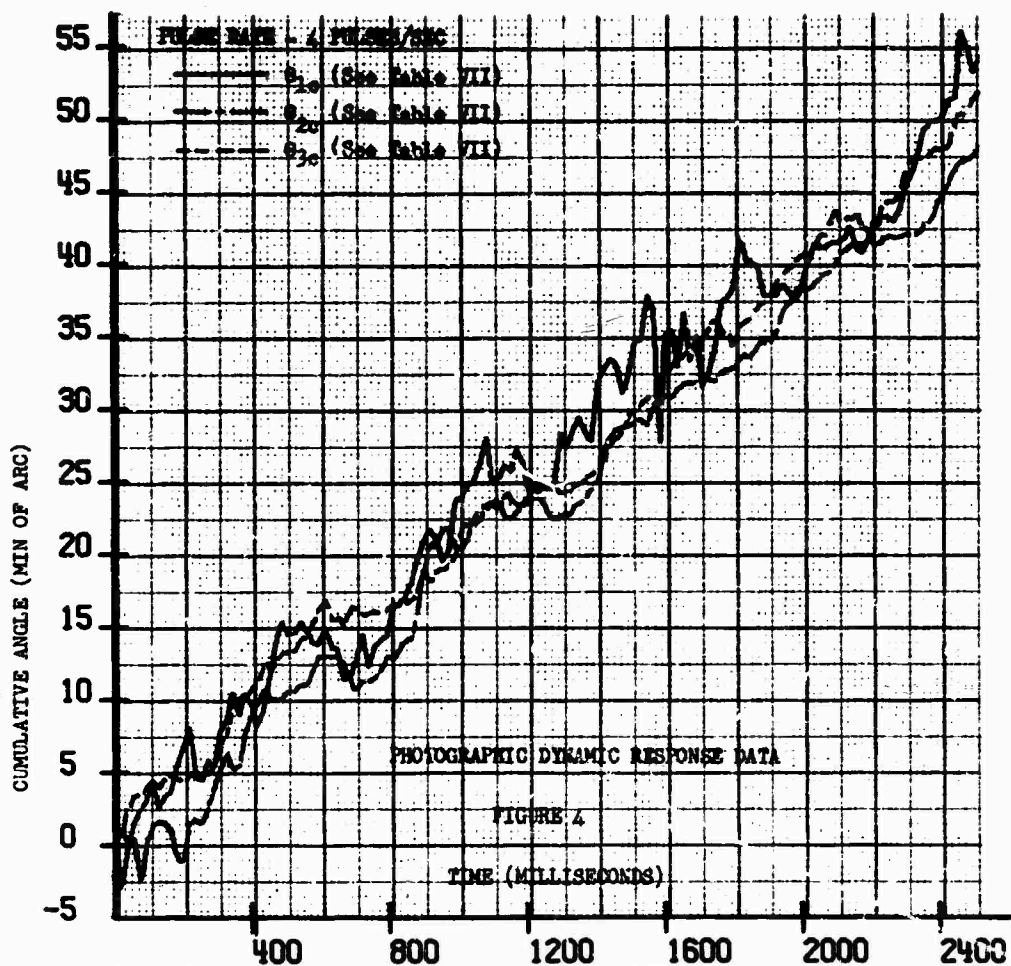
ACCELEROMETER LOCATION NOS. AND SUSPENSION SYSTEM FOR THE DYNAMIC RESPONSE TEST

Figure 2



OPTICAL TARGET LOCATIONS FOR
DYNAMIC RESPONSE TEST

Figure 3



SHIP'S PROBLEMS

DETERMINATION OF FIXED-BASE NATURAL FREQUENCIES OF A COMPOSITE STRUCTURE OR SUBSTRUCTURES (U)

C. Ni, R. Skop, and J. P. Layher
Naval Research Laboratory
Washington, D.C.

A general technique for determining the fixed-base natural frequencies of an in situ or laboratory mechanical structure or substructure is presented. These frequencies are obtained semianalytically through a series of response measurements and by utilizing the invariance properties of the mobility elements of the structure under investigation. The analysis is based on an arbitrary conceptual lumped mass model of an n degree-of-freedom, undamped linear time-invariant system, but the technique derived from this analysis is also applicable to continuous structures. An extension of the method to damped linear time-invariant systems is made to study the feasibility of its application in real structures. The fixed-base natural frequencies of the lowest two modes of a beam on three supports are determined by theoretical calculations, a standard resonance test, and the semianalytical technique presented in this paper. A comparison of the results shows the applicability and usefulness of the method described herein.

INTRODUCTION

As a result of recent developments, the application of matrix analysis to the solution of dynamic problems of large composite structures has become widespread. The division of a composite structure into mutually coupled substructures with constraints, is one of the essential steps in this analysis. These constrained substructures are, in turn, treated separately to produce results that are then synthesized to obtain the dynamic properties of the total composite structure. Methods of structure synthesis are categorized according to the applied internal boundary conditions among the divided substructures: the displacement method primarily emphasizes the matching of internal boundary displacements, and the force method basically considers the equilibrium of interaction redundant forces. Among the developed methods reported to date, a displacement method treated by Hurty [1] is particularly interesting in certain engineering applications. In his method, a composite structure is divided into fixed-base (or fixed-constraint) substructures. The dynamic problem of the total composite structure is then reduced to the solution of two separate problems:

- (1) The dynamic problem of the fixed-base substructures.
- (2) The mechanical coupling between the adjacent substructures.

This division is advantageous in the treatment of composite structures consisting of functional substructures. Normally, the spatial configuration of a functional substructure is well defined, and the imposed fixed-base constraint isolates the particular substructure from its surroundings. Consequently, the obtained dynamic properties of this substructure are independent of space and time, and such data can be of permanent value in engineering practice. Parallel but independent to this treatment, the determination of fixed-base natural frequencies has been studied both theoretically and experimentally [2]-[5] at the U.S. Naval Research Laboratory.

In order to design a structure which undergoes dynamic loading, a knowledge of the natural frequencies of free vibration of the structure is required. Two commonly used approaches for determining the fixed-base natural frequencies of a structure are:

- (1) **Analytical approach:** This approach requires modeling the structure under study. In general, the modeling problem is very complicated and virtually relies on individual experience and intuitive judgment.
- (2) **Experimental approach:** This approach is essentially a structure resonance method. By sweeping a range of exciting frequencies, the resonance mode of the structure is actually excited by the applied oscillatory force at the given fixed-base supporting condition. The fixed-base natural frequencies of the structure are identified by the resonance frequencies. This method fails when the supporting base becomes flexible.

The acquisition of information concerned with the fixed-base natural frequencies is made difficult by the induced uncertainties and the limitations of these two methods.

These limitations are overcome by a semi-analytical method for determining the fixed-base natural frequencies of composite structures which has recently been developed [6]. The structure dynamic response measurements at the constraints of the substructure, and the invariance properties of the total structure, are used to determine the substructure's true fixed-base natural frequencies. The mathematical analysis is based on a "Conceptual Lumped Mass Model" to derive expressions for special functions in terms of measurable physical quantities. These quantities are the appropriate dynamic responses of the structure and the applied forces. Such special functions contain the information of the fixed-base natural frequencies of the divided substructures and the natural frequencies of the total structure. By proper deduction from those special functions, the fixed-base natural frequencies of the substructure under consideration can be concluded.

A "Conceptual Lumped Mass Model" is a lumped mass model without actually modeling the real structure. The advantage of this concept is to by-pass the complicated modeling problem and allow us to approach a continuous model with ease. Furthermore, in doing this, point-wise measurement in experiment become rigorously justified. The results derived from this method are actual physical quantities of the substructures or the total structure considered as a whole.

The experimental verification of this semi-analytical method not only provides a definite way to obtain the fixed-base natural frequencies desired, but also proves the applicability of the lumped mass model itself, in general. Such proof consolidates the matrix analysis of composite structures on its basic theoretical ground.

THEORETICAL ANALYSIS

A steady state solution is used to develop a semi-analytical method for the determination of fixed-base natural frequencies by shake test. Generalized coordinates in configuration space and matrix representation of a dynamic structure are used in this theoretical treatment. The analysis is based on an arbitrary undamped, linear time-invariant, conceptual lumped mass model. An extension of this method to cases of small linear damping is then validated (Appendix).

The governing differential equation of an n degree-of-freedom dynamic structure has the general form

$$[M]\{\ddot{q}\} + [K]\{q\} = \{F(t)\} \quad (1)$$

For an applied sinusoidal force

$$F(t) = \bar{f} \sin \omega t \quad (2)$$

the steady state solution of equation (1) has the general form

$$\{q\} = \{\bar{q}\} \sin(\omega t + \phi) \quad (3)$$

where ϕ is the relative phase of the associated response with respect to the applied force. For undamped systems, ($\phi = m\pi$, $m = 0, 1, \dots$) equation (3) becomes

$$\{q\} = \{\bar{q}\} \cos \phi \sin \omega t \quad (4)$$

and the spatial part of equation (1) becomes

$$(-\omega^2[M] + [K])\{\bar{q}\} \cos \phi = \{\bar{f}\} \quad (5)$$

or

$$\left(-\omega^2[M] + \frac{1}{\cos \phi}[K]\right)\{\bar{q}\} \sin \phi = \{\bar{f}\} \quad (6)$$

where

$$\omega \bar{q} \cos \phi = \bar{q} \sin \phi$$

for steady states.

The linear operator in equation (6)

$$[Z] = \left(-\omega[M] + \frac{1}{\omega} [K] \right)$$

is defined as the mechanical impedance matrix.

For a nondegenerate system, the impedance matrix has a rank n and its inverse exists

$$[Z]^{-1} [Z] = [Z] [Z]^{-1} = [I] \quad (7)$$

By a linear transformation, equation (6) can be written as

$$(\ddot{q} \sin \phi) = [W] (\ddot{r}) \quad (8)$$

where

$$[W] = [Z]^{-1} \quad (9)$$

is defined as the mobility matrix of the system.

Any mechanical structure can be described by three coupled main substructures:

- Equipment: The substructure under investigation.
- Support: The substructure supporting the equipment.
- Base: The remaining part of the total structure other than the equipment and support.

According to the above subdivision, equation (6) can always be arranged to have the partitioned form

$$\begin{bmatrix} [Z^e] & (C_s^e) & (0) \\ \dots & \dots & \dots \\ (C_s^e)^T & [Z^s] & (C_b^s) \\ \dots & \dots & \dots \\ (0) & (C_b^s)^T & [Z^b] \end{bmatrix} \begin{Bmatrix} \{\ddot{q}^e\} \\ \dots \\ \{\ddot{q}^s\} \\ \dots \\ \{\ddot{q}^b\} \end{Bmatrix} = \begin{Bmatrix} \{\ddot{r}^e\} \\ \dots \\ \{\ddot{r}^s\} \\ \dots \\ \{\ddot{r}^b\} \end{Bmatrix} \quad (10)$$

It is noticed that there is no direct coupling between the equipment and the base substructure because of definition.

From equation (8), the elements of the mobility matrix

$$m_{ij} = \frac{\ddot{q}_i}{\ddot{r}_j} \sin \phi_{ij} \quad (11)$$

can be calculated from directly measurable physical quantities, i.e., the response and force amplitudes and the relative phase between them. Equation (9) shows that the elements of the mobility matrix can be expressed in terms of cofactors of the impedance determinant and the impedance determinant itself

$$m_{ij} = \frac{Z_{ji}}{|[Z]|} \quad (12)$$

It is evident that, for a given structure, the mobility elements are functions of the exciting frequency alone. In other words, the mobility elements are invariant physical quantities of the dynamic structure with respect to space and time. They are independent of the condition whether the resonance modes of the equipment substructure are excited or not. Therefore, one may obtain the necessary mobility elements experimentally and construct the resonance condition for the determination of the fixed-base natural frequencies of a substructure.

Consider a system composed of an ℓ degree-of-freedom equipment substructure, an $m - \ell$ degree-of-freedom support substructure and an $n - m$ degree-of-freedom base substructure. The condition for the excitation of a resonance mode of the equipment substructure at one of its fixed-base natural frequencies requires

$$\ddot{q}_{\ell+1} = \ddot{q}_{\ell+2} = \dots = \ddot{q}_n = 0 \quad (13)$$

From equation (8), one may single out the part containing the generalized velocities of the support substructure and apply the equipment substructure resonance condition in equation (13)

$$\begin{aligned} m_{\ell+1\ell+1} \ddot{r}_{\ell+1} + m_{\ell+1\ell+2} \ddot{r}_{\ell+2} + \dots + m_{\ell+1n} \ddot{r}_n &= 0 \\ \vdots \\ m_{m\ell+1} \ddot{r}_{\ell+1} + m_{m\ell+2} \ddot{r}_{\ell+2} + \dots + m_{mn} \ddot{r}_n &= 0 \end{aligned} \quad (14)$$

The existence of a solution of this set of simultaneous homogeneous algebraic equations depends on

- (1) $n - \ell > m - \ell$ There are infinite number of solutions for various given forces.
- (2) $n - \ell = m - \ell$ There exists a non-trivial solution. It becomes an eigenvalue problem.
- (3) $n - \ell < m - \ell$ There is no solution.

By controlling the shaking forces, one always can restrict himself to the second case, i.e., $n = t = m - t$. The secular equation of this case is defined as the mobility function

$$\begin{vmatrix} m_{t+1,t+1} & \dots & m_{t+1,m} \\ \vdots & \ddots & \vdots \\ m_{m,t+1} & \dots & m_{mm} \end{vmatrix} = \Omega(m_{ij}; \omega) . \quad (15)$$

The matrix corresponding to this mobility function in equation (15) is a square mobility submatrix, $[\Omega]$, associated with the dynamic responses of the support substructure. Equation (15) shows that all the forces are applied on the support substructure, and we shall continue to limit ourself to this particular case throughout the derivation. In practice, the forces can be applied any where except on the equipment substructure as is shown in [6].

It is important to show explicitly that the mobility function does contain the information of the fixed-base natural frequencies of the equipment substructure. Equation (7) shows that the impedance matrix and the mobility matrix are commutative and they can be written in a partitioned form according to the substructures.

$$\begin{bmatrix} [Z^a] & (C_s^a) & (0) \\ (C_s^a)^T & [Z^a] & (C_b^a) \\ (0) & (C_b^a)^T & [Z^b] \end{bmatrix} \begin{bmatrix} m_{11} & \dots & m_{1m} \\ \vdots & \ddots & \vdots \\ m_{m1} & \dots & m_{mm} \end{bmatrix} = \begin{bmatrix} [I] & (0) & (0) \\ (0) & [I] & (0) \\ (0) & (0) & [I] \end{bmatrix} \quad (16)$$

The matrix multiplication in equation (16), by summation convention, may be written as

$$\begin{aligned} z_{ij} m_{jk} &= 1 \quad i = k \\ z_{ij} m_{jk} &= 0 \quad i \neq k . \end{aligned} \quad (17)$$

Suppose the mobility matrix is replaced by a nonsingular matrix

$$\begin{bmatrix} [I] & m_{11} & \dots & (0) \\ (0) & [\Omega] & & (0) \\ (0) & m_{m1} & \dots & [I] \end{bmatrix} \quad (18)$$

Equation (16) becomes

$$\begin{bmatrix} [Z^a] & (C_s^a) & (0) \\ (C_s^a)^T & [Z^a] & (C_b^a) \\ (0) & (C_b^a)^T & [Z^b] \end{bmatrix} \begin{bmatrix} [I] & m_{11} & \dots & (0) \\ (0) & [\Omega] & & (0) \\ (0) & m_{m1} & \dots & [I] \end{bmatrix} = \begin{bmatrix} [Z^a] & (0) & (0) \\ (C_s^a)^T & [I] & (C_b^a) \\ (0) & (0) & [Z^b] \end{bmatrix} \quad (19)$$

Taking the determinant of both sides of equation (19) and applying Laplace's expansion, equation (19) becomes

$$|[Z]| \cdot \Omega(m_{ij}; \omega) = |[Z^*]| \cdot |[Z^b]|$$

or

$$\Omega(m_{ij}; \omega) = \frac{|[Z^*]| \cdot |[Z^b]|}{|[Z]|} \quad (20)$$

Equation (20) shows explicitly that the mobility function not only carries information of the fixed-base natural frequencies of the equipment substructure, $|[Z^*]| = 0$, but also the fixed-base natural frequencies of the base substructure $|[Z^b]| = 0$, and the natural frequencies of the total structure $|[Z]| = 0$.

Since our main interest is to determine the fixed-base natural frequencies of the equipment substructure, it is desirable to devise a function which eliminates the extraneous information involved in the mobility functions. Suppose an additional shaking force is applied at one location on the equipment substructure, then by following the same procedure of deriving a mobility function, the corresponding mobility function may be written

$$\Omega'(m_{i+1, j+1}; \omega) = \left| \begin{matrix} m_{11} & \dots & m_{1t} \\ \vdots & & \vdots \\ m_{it} & \dots & m_{tt} \end{matrix} \right| = \frac{|[Z'^*]| \cdot |[Z^b]|}{|[Z]|} \quad (21)$$

Comparing equation (20) and (21), the impedance determinants of the base substructure and the total structure are the common factors. This suggests that the extraneous information can be excluded by taking the ratio of these two mobility functions. For this purpose, a resonance function is defined as

$$\psi(m_{ij}; \omega) = \left| \frac{\Omega'(m_{i+1, j+1}; \omega)}{\Omega(m_{ij}; \omega)} \right| = \left| \frac{|[Z'^*]|}{|[Z^*]|} \right| \quad (22)$$

Here, a double line designates absolute value. The absolute values are chosen to be used in the resonance function so that its graphical representation conforms to the conventional concept of "resonance peak." For a physical system, $|[Z'^*]|$ is finite for a finite exciting frequency ω ; thus the singularities of the resonance function $\psi(m_{ij}; \omega)$ corresponding to $|[Z^*]| = 0$ give the identity of the fixed-base natural frequencies of the equipment substructure.

It is important to point out that the resonance function is not defined when

$$|[Z^b]| = 0 \quad \text{and} \quad |[Z]| = 0 \quad (23)$$

although the analytical form in equation (22) shows that the resonance function is independent of the impedance determinants $|[Z^b]|$ and $|[Z]|$. The reason is that we are not measuring the impedance elements but the mobility elements indirectly through force and response measurements according to equation (11). It is then evident from equation (22) that, when $|[Z^b]| = 0$ and $|[Z]| = 0$, the resonance function becomes 0/0 and 00/00 respectively. Such induced ambiguities can be eliminated by data analysis and present no real problem.

EXPERIMENT AND APPLICATION

The success of this method in computer simulations [6] was followed by laboratory experiments conducted at the random vibration laboratory, NRL. A detailed report on experimental procedures and results is being prepared as an NRL Report.

Physical quantities as well as theoretically derived special functions pertaining to the practical application of this method are summarized here:

Mobility elements (for acceleration response)

$$m_{ij} = -\frac{\ddot{q}_i}{\dot{f}_j} \cos \phi_{ij}$$

Mobility functions

$$\Omega(m_{ij}; \omega) = |[m_{ij}]| = \frac{|[Z^*]| \cdot |[Z^b]|}{|[Z]|}$$

$i, j = 1, 2, \dots, t$

t - total number of support points.

$$\Omega'(m_{ij}; \omega) = |[m'_{ij}]| = \frac{|[Z'^*]| \cdot |[Z^b]|}{|[Z]|}$$

$i, j = 1, 2, \dots, t+1$

$(t+1)$ th point on equipment substructure.

Resonance function

$$\psi(m_{k1}; \omega) = \left| \frac{\Omega(m_{ij}; \omega)}{\Omega'(m_{ij}; \omega)} \right| = \left| \frac{|[Z^*]|}{|[Z'^*]|} \right|$$

The measurable quantities \ddot{q}_i , \dot{T}_i , ϕ_{ij} are obtained by a series of shake tests. Since the shake test itself is well known in structure dynamic response studies, only a few important aspects which are essential to conclude meaningful results are presented in this paper. It is understood that the natural frequencies of a structure are linear dynamic properties of the structure. The corresponding mathematical model used in the theoretical analysis is linear time-invariant and deterministic. Therefore, the key governing rule of the experimental or test measurements is to confine the operation within the range of linearity. In practical terms, the noise from all sources must be kept low. It is noticed in the theoretical analysis that the relative phase of the responses with respect to the applied force are necessary in the mobility and resonance function calculation, even in an undamped linear time-invariant case. In practice, the measured responses always involve frequency components other than the exciting frequency, in spite of the fact that the exciting frequency can be a well defined and controlled value. The main sources of these undesirable frequency components are of electrical and mechanical origin. Contribution due to electrical distortion are often negligible. The mechanically induced distortion is mainly due to the nonlinear dynamic behavior of the total structure, which is an inherent property of the structure under test and cannot be removed without altering the structure itself. However, such nonlinear responses are avoidable if a specific experimental procedure is established so that the test is conducted within the dynamic range where the linear time-invariant mathematical model is valid. Within this dynamic range, the mobility elements of a given structure are independent of space and time, but functions of the exciting frequency alone. By utilizing this invariance property of the mobility elements as a guide line, the determination of fixed-base natural frequencies of a substructure becomes possible.

For the very reason described above, preparatory work is needed before taking useful data. This work is described below.

(1) Force amplitude determination: Either too small or too large a force amplitude will cause increasing noise to signal ratio, consequently reducing the reliability of mobility element calculation. Although the mechanisms are different for these two cases, the former is believed due to harmonic instability ([7], [8]) and the latter is more likely due to the inelastic property of the structure, their effect on this particular method is the same. To avoid this difficulty, an appropriate magnitude of the force

amplitude has to be first selected. This is done by varying the force amplitude applied on the structure while response measurements, taken at a given constant exciting frequency are recorded by oscillograph. The mobility elements corresponding to each force amplitude setting are calculated and plotted against force amplitudes. A typical plot is shown in Figure 1. Within the range designed by R_f in the plot, the mobility element is force amplitude independent for a given exciting frequency ω . Responses due to forces within this dynamic range are essentially governed by the linear time-invariant analytical model.

(2) Narrow band filter application: One is aware that nonlinear responses of varying degree are always present in real structures. Only structures with small nonlinear dynamic behavior are considered here because dominantly nonlinear systems certainly cannot be described by a linear analytical model. Direct measurement of relative phase angle by a zero crossing type of phase meter or lissajous type of measurement on oscilloscope is very difficult at times. This difficulty is overcome, for slightly damped cases, by using a narrow band filter and comparing the phase difference between the two fundamental components.

After the preparatory work is done, the remaining task of the experiment or test is rather routine and will not be discussed here. The necessary data is collected and then used to calculate the value of the mobility functions and the resonance function corresponding to each exciting frequency. This is a straightforward routine on any digital computer, and no special program is needed.

In order to draw conclusions about the fixed-base natural frequencies of the equipment substructure, the possible ambiguities mentioned in the theoretical analysis have to be eliminated. The technique for doing this task is illustrated in the schematic diagram given in Figure 2.

The mechanical system used in a laboratory experiment to test the validity and applicability of the method presented in this paper is shown in Figure 3. The structure is essentially composed of three substructures:

Equipment: The equipment substructure consists of a 1" x 2" x 4' steel beam with three simple supports at the quarter points along its length.

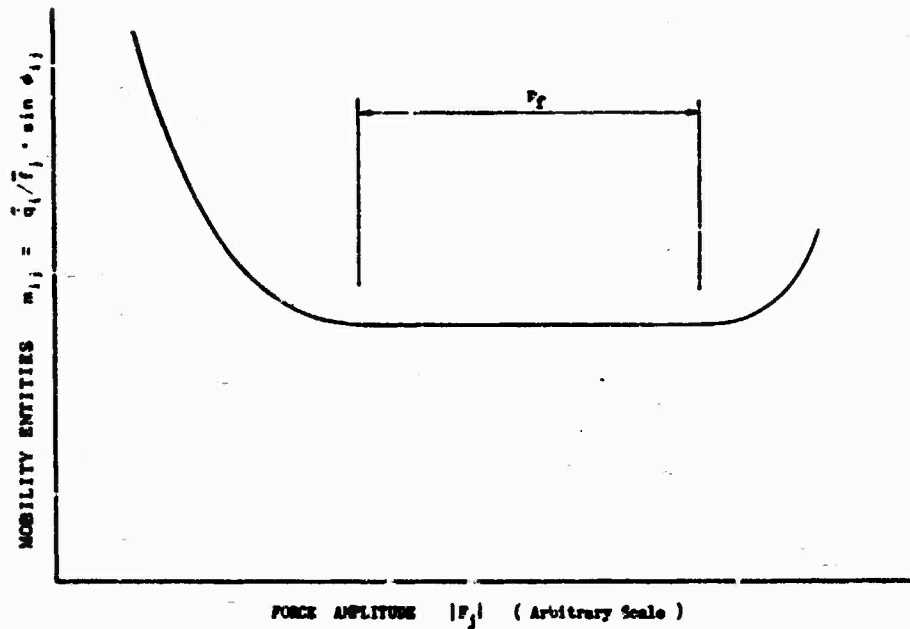


Fig. 1 - Schematic drawing for selection of shaking force amplitude (U)

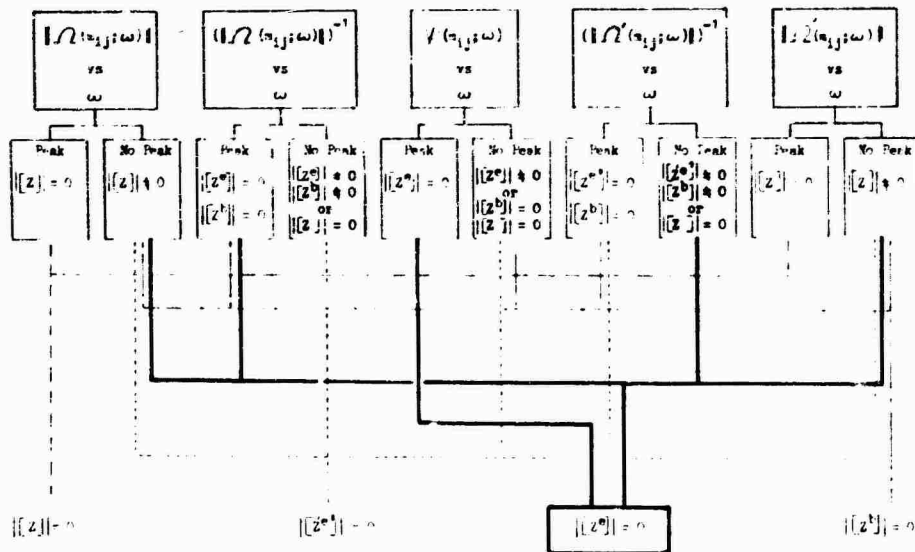


Fig. 2 - Result interpretation diagram (U)

Support: The support substructure consists of all the common points of the equipment and the base.

truss-like frame constructed partially of steel frame and partially of aluminum channels.

Base: The base is the remaining part of the total structure other than the equipment and the support. The base consists of a metallic

The results obtained from the semianalytical method developed here reveal fixed-base natural frequencies of the lowest two modes of the test beam of 125 Hz and 140 Hz as shown in Figure 4. These results are compared below

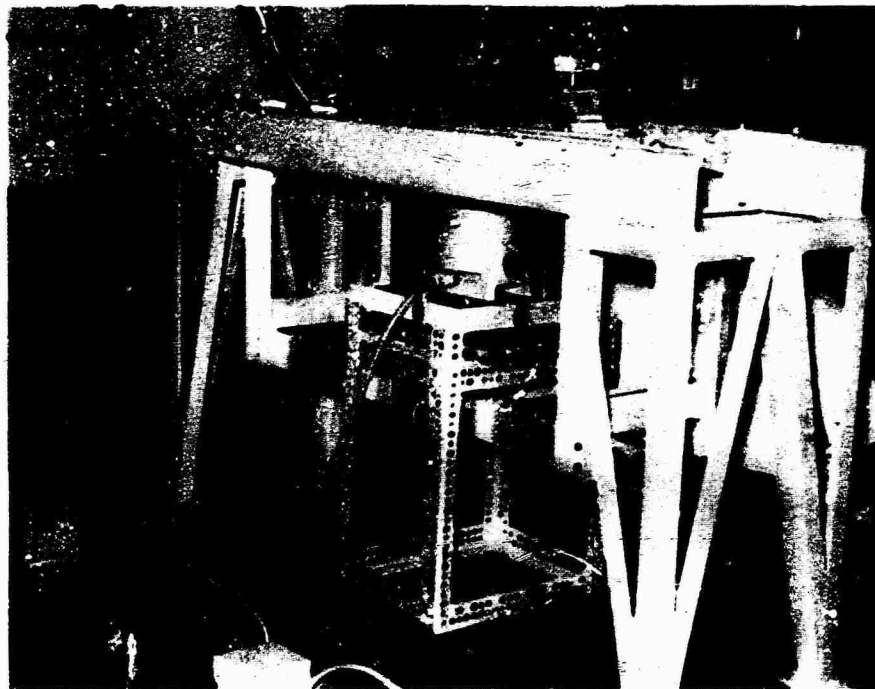


Fig. 3 - Test structure (U)

with theoretically calculated values as well as experimental results, shown in Figure 5, from a standard resonance test:

	f_1	f_2
Theoretical calculation	138 Hz	148 Hz
Standard resonance test	120 Hz	(140 Hz) not conclusive
Semianalytical method	125 Hz	140 Hz

One observes that the discrepancies between the experimental results are smaller than those between either experimental result and the calculated theoretical value.

DISCUSSION AND CONCLUSION

There is a discrepancy of less than five percent between the results of the two experimental methods. Figures 4 and 5 show that, in this case, the semianalytical method gives a better resolution of the fixed-base natural frequencies than the standard resonance test method. The discrepancies between the experimental results and the theoretical results calculated from Bernoulli-Euler beam theory

amount to ten to fifteen percent. An examination of the possible causes of the higher theoretically predicted natural frequencies reveals that they are most likely due to neglecting viscous damping. When viscous damping is taken into consideration, the calculated frequency values are lowered and the discrepancy gap is narrowed. This implies that the semianalytical method yields quite accurate results. Therefore it is concluded that:

1. The semianalytical method gives accurate structural dynamic information.
2. The semianalytical method provides a simple means to determine fixed-base natural frequencies of a composite structure in situ. Such measurement cannot be done by any existing standard test method.
3. The semianalytical method overcomes the induced uncertainties and the limitations of the analytical and conventional experimental approaches.

REFERENCES

1. Hurty, W.C., "Dynamic Analysis of Structural Systems Using Component Modes," J. AIAA, Vol. 3, No. 4, April, 1965, pp. 678-685

2. O'Hara, G.J., "Mechanical Impedance and Mobility Concepts," J. Acoust. Soc. Am. Vol. 41, No. 5, 1967, pp. 1180-1184
3. Petak, L.P. and O'Hara, G.J., "Determination of Fixed-Base Natural Frequencies of Dual Foundation Shipboard Equipments by Shake Test," NRL Report 6451, Aug. 1966
4. Petak L. P. and Kaplan, R.E., "Resonance Testing in the Determination of Fixed-Base Natural Frequencies of Shipboard Equipment," NRL Report 6176, Dec. 1964
5. Remmers, G.M., "Experimental Technique for Determining Fixed-Base Natural Frequencies of Structures on Single Non-Rigid Attachment Points," The Shock and Vibration Bulletin 38, Part 2, Aug. 1968
6. Ni, Chen-chou and Skop, R., "Determination of Fixed-Base Natural Frequency of Multiple Foundation Mechanical Systems by Shake Test," NRL Report 7300 (to be published)
7. Tseng, W.T. and Dugundji, J., "Nonlinear Vibrations of a Beam under Harmonic Excitation," J. Appl. Mech., Vol. 37, No. 2, Trans. ASME, Vol. 92, Series E, June 1970, pp. 292-297
8. Mettler, E., "Schwingungs- und Stabilitätsprobleme bei mechanischen Systemen mit harmonischer Erregung," Z. angew. Math. Mech., Vol. 45, 1965

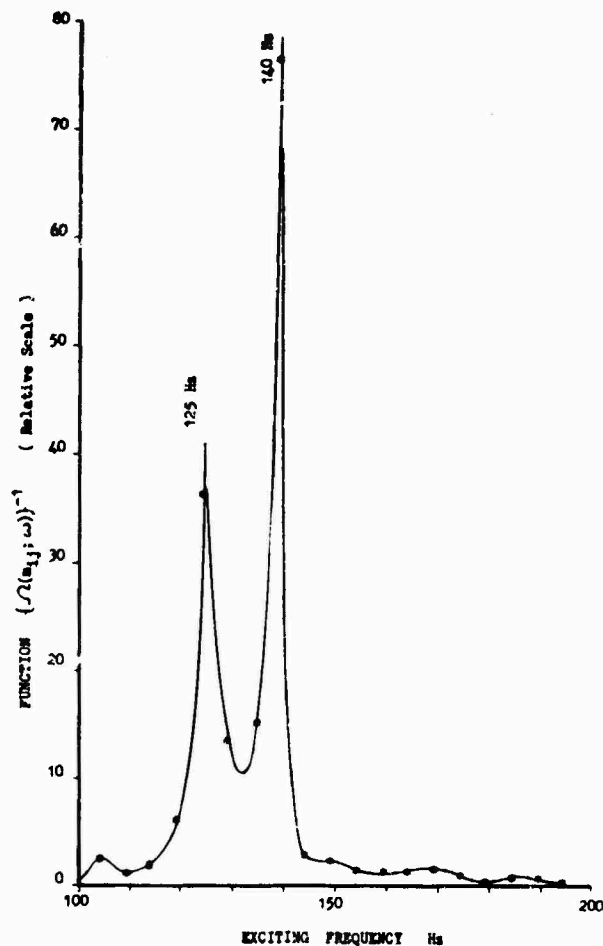


Fig. 4 - Experimental result (semi-analytical method) (U)

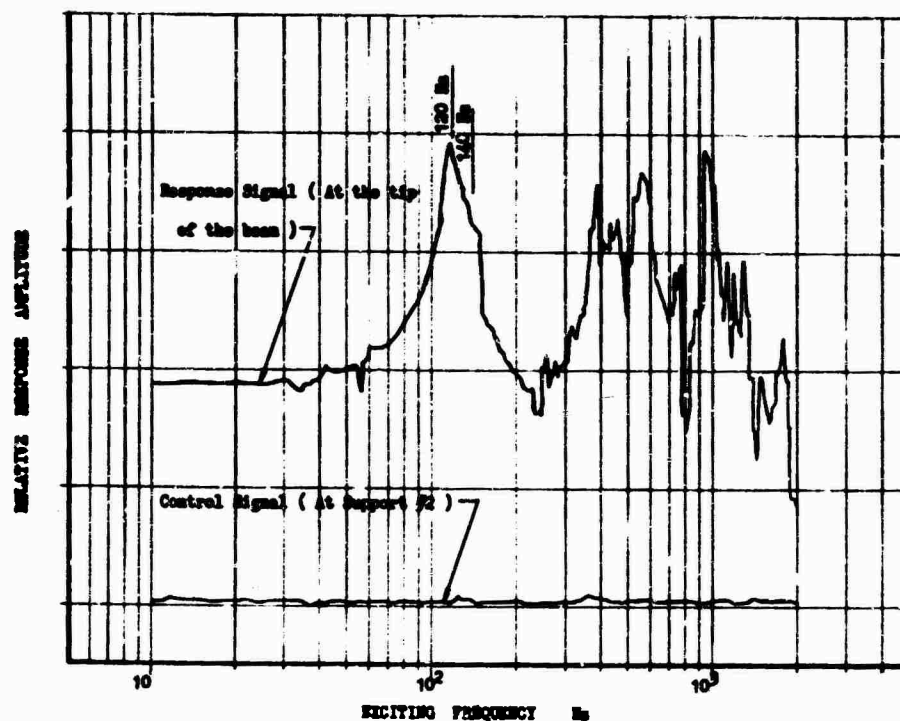


Fig. 5 - Experimental result (standard resonance test method) (U)

Appendix

DAMPED LINEAR TIME-INVARIANT SYSTEM

Assume the dissipative energy of a damped linear time-invariant system can be described by the Rayleigh dissipation function

$$R = \frac{1}{2} \dot{q}^T [R] \dot{q} \quad (A1)$$

The elements r_{ij} of the damping matrix $[R]$ are real and positive. The governing differential equation of such a dynamic system is

$$[M] \ddot{q} + [R] \dot{q} + [K] q = \{F\} \quad (A2)$$

The general solution of equation (A2) is

$$\{q\} = \{\bar{q} \cos \phi \sin \omega t + \bar{q} \sin \phi \cos \omega t\} \quad (A3)$$

for a sinusoidal force input $\{F\} = \{\bar{f} \sin \omega t\}$. The spacial part of equation (A2) becomes

$$\begin{aligned} -\omega^2 [M] \{\bar{q} \cos \phi\} - \omega [R] \{\bar{q} \sin \phi\} \\ + [K] \{\bar{q} \cos \phi\} &= \{\bar{f}\} \\ -\omega^2 [M] \{\bar{q} \sin \phi\} + \omega [R] \{\bar{q} \cos \phi\} \\ + [K] \{\bar{q} \sin \phi\} &= \{0\} \end{aligned} \quad (A4)$$

or

$$[Z] \{\bar{q} \sin \phi\} - [R] \{\bar{q} \cos \phi\} = \{\bar{f}\} \quad (A5)$$

$$[R] \{\bar{q} \sin \phi\} + [Z] \{\bar{q} \cos \phi\} = \{0\} \quad (A6)$$

by substituting $\bar{q} \sin \phi = -\bar{q} \cos \phi$. Here, $[Z]$ is the impedance matrix as if the system is undamped. Equation (A6) determines the relative phase of the responses with respect to the applied forces. For small damping, $r_{ij} \ll 1$. By eliminating the response vector component $\{\bar{q} \cos \phi\}$, equation (A5) becomes

$$\{\bar{q} \sin \phi\} = ([I] + [Z]^{-1} [R] \cdot [Z]^{-1} [R])^{-1} [Z]^{-1} \{\bar{f}\} \quad (A7)$$

or in terms of the mobility matrix of the corresponding undamped system

$$\{\bar{q} \sin \phi\} = ([I] + [W] [R] \cdot [W] [R])^{-1} [W] \{\bar{f}\} \quad (A8)$$

For certain real structures, m_{ij} and r_{ij} are normally very small. Considering a first approximation

$$([I] + [N][R] \cdot [N][R])^{-1} \rightarrow [I]^{-1} = [I]$$

equation (A8) can be written as

$$\{\bar{q} \sin \phi\} \doteq [N]\{\bar{f}\} \quad (A9)$$

This is exactly the expression of equation (8) in the main text for the corresponding undamped system. Therefore, we conclude the applicability of the method to slightly damped linear time-invariant systems.

EQUIVALENT SPRING-MASS SYSTEM: A PHYSICAL INTERPRETATION*

Ben K. Wada, Robert Bamford, and John A. Garba
Jet Propulsion Laboratory
Pasadena, California

Large finite element computer programs and/or comprehensive modal tests are used to obtain the eigenvalues and eigenvectors of structures that have many degrees of freedom. The large quantity of data often masks the physical implications of the results, and these implications are invaluable for proper data usage.

This paper describes a technique that generates an equivalent spring-mass model for each eigenvector of the structure when the generalized mass and stiffness matrices are available.

The physical significance of the equivalent spring-mass system and its application in modal testing, identification of eigenvectors, extraction of a lower-order model, comparison of similar models, selection of significant eigenvectors, and usage with limited computer programs are discussed.

INTRODUCTION

Large finite element structural analyses computer programs and/or large modal tests are used to evaluate dynamic solution of structures with many degrees of freedom. Often the degrees of freedom of the structure are reduced by use of selected eigenvalues and eigenvectors as generalized coordinates for a dynamic response solution. The large quantity of data representing the eigenvalues and eigenvectors often masks the physical implications of the results, and these implications are invaluable for proper data usage.

This report uses well-known concepts to develop a technique of obtaining an equivalent spring-mass system for each eigenvector when the dynamic characteristics of the structure are available as a generalized mass matrix and associated eigenvalues. The technique is equally applicable to test data or data from analyses of continuous structures or analyses of discrete structures.

The procedure is to renormalize each eigenvector such that its reaction is equal to that of a corresponding equivalent single-degree-of-freedom (spring-mass) system. Incremental inertia properties must be added in the model to represent the rigid-body contribution of the truncated eigenvectors. In order to illustrate the concept, a simple model of a cantilevered beam is described (Figs. 1 and 2).

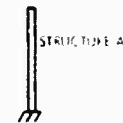


Fig. 1. Initial structure



Fig. 2. Cantilever eigenvectors of structure A

The equivalent single-degree-of-freedom system (Fig. 3) for each eigenvector of Structure A (Fig. 2) is normalized and represented such that each reaction R_i is properly simulated. The "rigid mass" in Fig. 3 represents the rigid-body mass properties of Structure A contributed by the truncated eigenvectors.

The procedure to define equivalent single-degree-of-freedom systems is developed for the general case wherein six base reactions are represented by three orthogonal force components and three orthogonal moment components.

* This paper presents the results of one phase of research carried out at the Jet Propulsion Laboratory, California Institute of Technology, under Contract No. NAS 7-100, sponsored by the National Aeronautics and Space Administration.

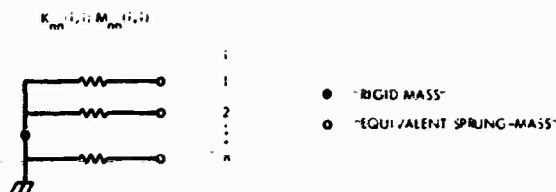


Fig. 3. Structure A represented as equivalent spring-mass systems

The primary objective is to indicate the physical significance of the equivalent spring-mass system and its application in modal testing, identification of eigenvectors, extraction of lower-order model, comparison of similar models, selection of significant eigenvectors, and usage with limited computer programs.

ANALYSIS

The Equilibrium Equation*

The unrestrained equilibrium equation of a discrete undamped structure is

$$[m]\{\ddot{u}\} + [k]\{u\} = \{f\} \quad (1)$$

where

$[m]$ = mass matrix corresponding to each degree of freedom with mass

$[k]$ = stiffness matrix corresponding to each degree of freedom

$\{u\}$ = displacement vector representing each degree of freedom (includes translation and rotation)

$\{f\}$ = force vector

The eigenvalues and eigenvectors of the structure defined by Eq. (1) after restraints are imposed and obtained from the solution of

$$[-\omega^2 [m_u] + [k_u]]\{U_u\} = \{0\} \quad (2)$$

where $u = u_0 e^{i\omega t}$ and $\{f\} = 0$ are substituted into Eq. (1). Subscript u refers to the matrices after the restrained degrees of freedom are eliminated. The i th eigenvalue and arbitrarily normalized eigenvectors are represented as ω_i^2 and $\{\phi_i\}$.

The order of Eq. (1) can be reduced when the structural characteristics exhibited by the lower eigenvalues and eigenvectors are most significant. The total motion of each degree of freedom $\{u\}$ is represented as a linear combination of displacement functions

$$\begin{aligned} \{u\} &= [\{\phi_r\}^T \{\phi_1\} \{\phi_2\} \dots \{\phi_n\}] \begin{Bmatrix} \{P_r\} \\ \{P_n\} \end{Bmatrix} \\ &= [\phi] \begin{Bmatrix} \{P_r\} \\ \{P_n\} \end{Bmatrix} \end{aligned} \quad (3)$$

where

n = number of retained eigenvectors

$\{\phi_r\}$ = displacement of $\{u\}$ associated with six rigid-body motions at the restraint point

$\{P_r\}$ = generalized displacements associated with rigid-body motions at the restraint point

$\{P_n\}$ = generalized displacements associated with the eigenvectors

Substitution of Eq. (3) into Eq. (1) and premultiplication by $[\phi]^T$ results in

$$\begin{Bmatrix} [M_{rr}] & [\overline{M}_{rn}] \\ [\overline{M}_{nr}] & [\overline{M}_{nn}] \end{Bmatrix} \begin{Bmatrix} \{\ddot{P}_r\} \\ \{\ddot{P}_n\} \end{Bmatrix} + \begin{Bmatrix} 0 & 0 \\ 0 & [\overline{K}_{nn}] \end{Bmatrix} \begin{Bmatrix} \{P_r\} \\ \{P_n\} \end{Bmatrix} = \begin{Bmatrix} \overline{F} \\ \{F\} \end{Bmatrix} \quad (4)$$

where

$[M_{rr}]$ = mass matrix, rigid-body modes

$[\overline{M}_{rn}] = [\overline{M}_{nr}]^T$ = essential coupling matrices, rigid-body modes and eigenvectors

$[\overline{K}_{nn}] = [\omega_n^2 \overline{M}_{nn}]$ = diagonal generalized stiffness matrix

$\{\overline{F}\}$ = generalized force vector

The generalized mass and stiffness matrices are diagonal because the eigenvectors are orthogonal with respect to their mass and stiffness matrices [2].

Equation (4) may apply to a structure with inertia relief in some rigid-body degrees of freedom, in which case the related terms in the matrices $[\overline{M}_{rn}]$ and $[\overline{M}_{nr}]$ are zero.

It is recognized that since all eigenvectors are orthogonal with respect to each other, each eigenvector can be represented as a single-degree-of-freedom system. Each single degree of freedom corresponds to a generalized displacement. A unique normalization factor for each eigenvector exists that satisfies the proper

* Reference (1) expands upon the analyses presented herein.

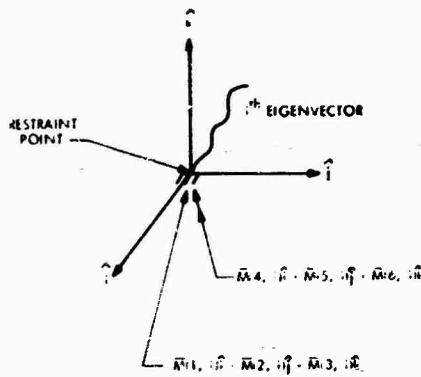


Fig. 4a. Physical system

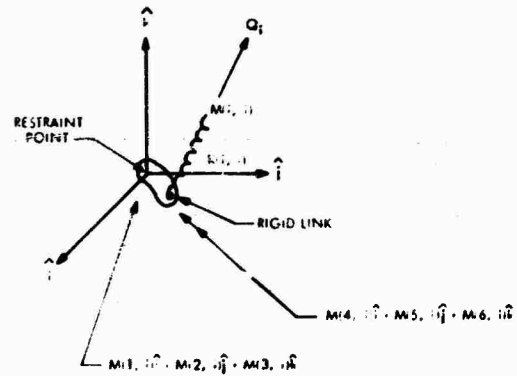


Fig. 4b. Equivalent spring-mass system of the physical system of Fig. 4a

inertial reaction at the restraint point represented by $[M_{rn}] \{\bar{P}_n\}$. The normalization factor will be developed from physical deduction.

The Mass Matrix

The following discussion is applicable for any eigenvector i . For the i th eigenvector, the inertial reaction caused by a unit acceleration of the i th generalized mass $M(i,i)$ at the restraint is the i th column of $[M_{rn}]$

$$\begin{Bmatrix} \bar{M}(1,i) \\ \bar{M}(2,i) \\ \vdots \\ \bar{M}(6,i) \end{Bmatrix}$$

The physical representation is shown in Fig. 4. Indices 1, 2 and 3 represent translation along the overall coordinates defined as \hat{i} , \hat{j} and \hat{k} , and indices 4, 5 and 6 represent rotation about \hat{i} , \hat{j} and \hat{k} axes.

The objective is to evaluate a renormalization factor q_i that, applied to the physical system of Fig. 4a, results in a single-degree-of-freedom system defined by generalized displacement Q_i , where a unit acceleration of $M(i,i)$ results in the reactions shown in Fig. 4b when the appropriate orientation and location of the line of action are used.

For translation, a unit acceleration of $M(i,i)$ in the \bar{P}_i direction must result in reaction components $\bar{M}(1,i)$, $\bar{M}(2,i)$ and $\bar{M}(3,i)$. Defining q_i as the renormalization factor gives

$$q_i^2 \bar{M}(i,i) = \left(q_i^2 \bar{M}^2(1,i) + q_i^2 \bar{M}^2(2,i) + q_i^2 \bar{M}^2(3,i) \right)^{1/2} \quad (5)$$

where q_i is the unique renormalization factor for eigenvector i . Note that the terms of $\bar{M}(i,i)$ are multiplied by q_i^2 . Solution of Eq. (5) results in

$$q_i = \frac{[\bar{M}^2(1,i) + \bar{M}^2(2,i) + \bar{M}^2(3,i)]^{1/2}}{M(i,i)} \quad (6)$$

The renormalized mass terms are:

$$M(i,i) = q_i^2 \bar{M}(i,i)$$

$$M(k,i) = q_i \bar{M}(k,i) \text{ where } (k=1, \dots, 6) \quad (7)$$

It follows that

$$M(i,i) = (M^2(1,i) + M^2(2,i) + M^2(3,i))^{1/2} \quad (8)$$

Note that this mass is directional, unlike a physical mass.

The line of action of Q_i in Fig. 4b can be located to result in inertial moments $M(k,i)$, where $k = 4, 5, 6$, corresponding to unit angular acceleration of mass $M(i,i)$ about the restraint point. The above requirements are satisfied when the moment arms about \hat{i} , \hat{j} and \hat{k} axes to the line of action of Q_i are

$$r_{4i} = M(4,i) / (M^2(2,i) + M^2(3,i))^{1/2}$$

$$r_{5i} = M(5,i) / (M^2(3,i) + M^2(1,i))^{1/2}$$

$$r_{6i} = M(6,i) / (M^2(1,i) + M^2(2,i))^{1/2} \quad (9)$$

Each equivalent spring mass system i for eigenvector i contributes to the rigid-body inertial matrix $[M_{rr}]$. The contributions to $[M_{rr}]_i$ by the i th eigenvector is

$$[M_{rr}]_i = [u_{li} M(i,i) u_{im}] \quad (l, m = 1, 2, \dots, 6) \quad (10)$$

where u_i = motion of mass $M(i, i)$ in the Q_i direction corresponding to rigid-body motion in the i th direction at the restraint point. From Eqs. (7) and (9), Eq. (10) reduces to

$$\begin{bmatrix} M_{rr} \end{bmatrix}_i = \begin{bmatrix} M(l, i) M(m, i) / M(i, i) \end{bmatrix} \quad (l, m = 1, 2, \dots) \quad (11)$$

The total generalized mass matrix for the i th eigenvector or i th equivalent spring-mass system is

$$[M]^{(i)} = \begin{bmatrix} \frac{M(l, i) M(m, i)}{M(i, i)} & M(l, i) \\ M(m, i) & M(i, i) \end{bmatrix} \quad (12)$$

where $(l, m = 1, 2, \dots, 6)$.

The Stiffness Matrix

The stiffness matrix is also renormalized by q_i and can be represented as

$$K(i, i) = q_i^2 \bar{K}(i, i) = \omega_i^2 M(i, i) \quad (13)$$

Renormalized Equilibrium Equation

The renormalized equilibrium equation that results from the substitution of Eq. (7) and (13) into (4) is

$$\begin{bmatrix} [M_{rr}] & [M_{rn}] \\ [M_{nr}] & [M_{nn}] \end{bmatrix} \begin{Bmatrix} \{\ddot{P}_r\} \\ \{\ddot{O}_n\} \end{Bmatrix} + \begin{bmatrix} 0 & 0 \\ 0 & [K_{nn}] \end{bmatrix} \begin{Bmatrix} \{P_r\} \\ \{O_n\} \end{Bmatrix} = \{F\} \quad (14)$$

$$\begin{bmatrix} [M_{rr}] & [\bar{M}_{rn}] \\ [\bar{M}_{nr}] & [\bar{M}_{nn}] \end{bmatrix} =$$

$$\begin{bmatrix} 0.3519E4 & 0 & 0.1233E5 & -0.1531E3 & 0.2152E1 & 0.2509E2 & -0.3738E0 & 0.2496E1 \\ & 0.3519E4 & -0.1233E5 & 0 & 0.4823E2 & -0.2603E2 & 0.2221E1 & 0.3937E1 & 0.5312E-1 \\ & & 0.3519E4 & 0.1532E3 & -0.4854E2 & 0 & -0.6654E-1 & 0.1046E0 & -0.1139E-1 & -0.6532E-1 \\ & & & 0.4975E5 & -0.1171E2 & -0.1867E3 & 0.9485E2 & -0.7966E1 & -0.8215E1 & -0.6134E-1 \\ & & & & 0.4946E5 & -0.3848E3 & 0.6780E1 & 0.7923E2 & -0.1471E1 & 0.2096E+2 \\ & & & & & 0.2593E4 & -0.4202E1 & -0.1683E1 & -0.7533E1 & 0.2653E+0 \\ \hline & & & & & & 0.2150E0 & 0 & 0 & 0 \\ & & & & & & & 0.1982E0 & 0 & 0 \\ & & & & & & & & 0.5402E-1 & 0 \\ & & & & & & & & & 0.2871E-1 \end{bmatrix} \quad (16)$$

where the units are kg, kg-m, kg-m².

Residual Mass Matrix

As noted in Eq. (12), each eigenvector contributes to the total rigid-body mass matrix $[M_{rr}]$. Consequently, if the dynamic system is represented by a set of spring-mass systems representing a truncated set of eigenvectors, then a residual mass matrix or the rigid-body contribution of the truncated eigenvectors must be accounted for. Residual mass matrix is defined as

$$[M_{RES}]^{(i)} = [M_{rr}] - \sum_{i=1}^{i=n} [M_{rr}]^{(i)} \quad (15)$$

when n = number of eigenvectors retained. Reference (1) shows that $[M_{RES}]^{(i)}$ approaches 0 as i approaches the total number of eigenvectors of the structure. The following discussion uses the definition of $[M_{RES}]^{(i)}$ and its physical significance.

APPLICATION

Definition of Problem

As the various applications are described, examples are presented for clarification. The data used for the example are obtained from a 139-dynamic-degree-of-freedom model of a typical spacecraft. Data for only the first four eigenvectors from a total of 139 are listed.

The arbitrarily normalized generalized mass data for four eigenvectors are:

The arbitrarily normalized generalized stiffness data for four eigenvectors are:

$$\begin{bmatrix} \begin{bmatrix} 0 & 0 \end{bmatrix} \\ \begin{bmatrix} 0 & \bar{K}_{nn} \end{bmatrix} \end{bmatrix} = \begin{bmatrix} \begin{bmatrix} 0 & 0 \end{bmatrix} \\ \begin{bmatrix} 0 & \begin{bmatrix} 0.1206E3 \\ 0.1158E3 \\ 0.6045E2 \\ 0.4406E2 \end{bmatrix} \end{bmatrix} \quad (17)$$

where the units are N/m.

The first four frequencies corresponding to elements of the generalized mass and stiffness matrices are:

$$f_i = \frac{1}{2\pi} \sqrt{\frac{\bar{K}(i,i)}{\bar{M}(i,i)}} \quad (18)$$

Eigenvector	Frequency, Hz
1	3.7707
2	3.779
3	4.3274
4	6.4871

The above data were obtained from a finite element model of a spacecraft; however, the data could equally have been obtained from modal test data or solution of a continuous structural system.

The generalized mass and stiffness matrices of Eqs. (16) and (17) renormalized by (6) result in

$$\begin{bmatrix} \begin{bmatrix} M_{rr} & M_{rn} \\ M_{nr} & M_{nn} \end{bmatrix} \end{bmatrix} = \begin{bmatrix} 0.3519E4 & 0 & 0.1233E5 & -0.1531E3 & 0.2613E3 & 0.3188E4 & -0.2736E2 & 0.2171E3 \\ & 0.3519E4 & -0.1233E5 & 0 & 0.4823E2 & -0.3162E4 & 0.2822E3 & 0.2882E3 & 0.4618E1 \\ & & 0.3519E4 & 0.1532E3 & -0.4854E2 & 0 & -0.8083E1 & 0.1329E2 & -0.8337E0 & -0.5684E1 \\ & & & 0.4975E5 & -0.1171E2 & -0.1867E3 & 0.1152E5 & -0.1012E4 & -0.6013E3 & -0.5335E1 \\ & & & & 0.4946E5 & -0.3848E3 & 0.8238E3 & 0.1007E5 & -0.1077E3 & -0.1823E4 \\ & & & & & 0.2593E4 & -0.5105E3 & -0.2139E3 & -0.5514E3 & 0.2308E2 \\ \hline & & & & & & 0.3173E4 & 0 & 0 & 0 \\ & & & & & & & 0.3201E4 & 0 & 0 \\ & & & & & & & & 0.2894E3 & 0 \\ & & & & & & & & & 0.2173E3 \end{bmatrix} \quad (19)$$

where the units are kg, kg-m, kg-m²

$$\begin{bmatrix} \begin{bmatrix} 0 & 0 \\ 0 & K_{nn} \end{bmatrix} \end{bmatrix} = \begin{bmatrix} \begin{bmatrix} 0 & 0 \\ 0 & \begin{bmatrix} 0.1779E7 \\ 0.1869E7 \\ 0.3240E6 \\ 0.3333E6 \end{bmatrix} \end{bmatrix} \quad (20)$$

where the units are N/m.

Identification of Eigenvectors

For any structure, the residual mass matrix provides physical insight into the character of the eigenvectors. From Eq. (15),

$$[M_{RES}]^{(i)} = [M_{rr}] - \sum_{j=1}^i [M_{rr}]^{(j)}$$

The terms of the residual mass matrix can be plotted as a function of number of eigenvectors (Fig. 5).

Several characteristics of the residual mass plots are:

- (1) For $n = 0$, the initial value (A) of the curve for each plot represents the original rigid-body mass terms. For instance, the value (A) for $M_{RES}(1,1)$ represents the mass of the system in the 1 direction.

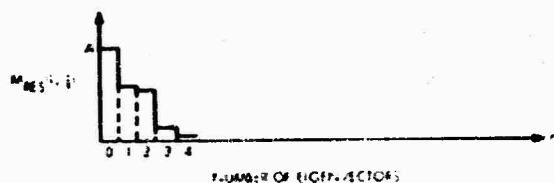


Fig. 5. Residual mass plot vs number of eigenvectors

- 2) For the diagonal terms of $[M_{RES}]^{(i)}$, the plot monotonically decreases to zero.
- (3) When the number of eigenvectors approaches the degrees of freedom of the system, the $M_{RES}(i,j)$ approaches zero.
- (4) A drop between eigenvectors k and $k+1$ indicates the magnitude of inertia reactions for eigenvector $k+1$.
- (5) A local eigenvector is defined as an eigenvector with small reduction in residual mass. A response solution will be dependent on such eigenvectors only if the loads are directly related to the local eigenvectors.

Residual mass plots* of the sample problems for selected elements are shown in Figures 6.

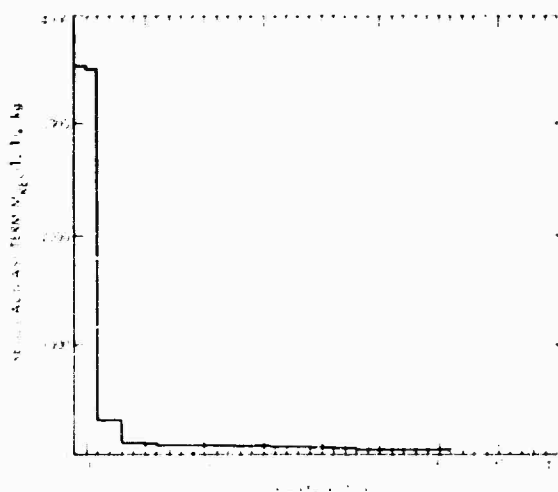


Fig. 6a. $M_{RES}(1,1)$ vs eigenvector

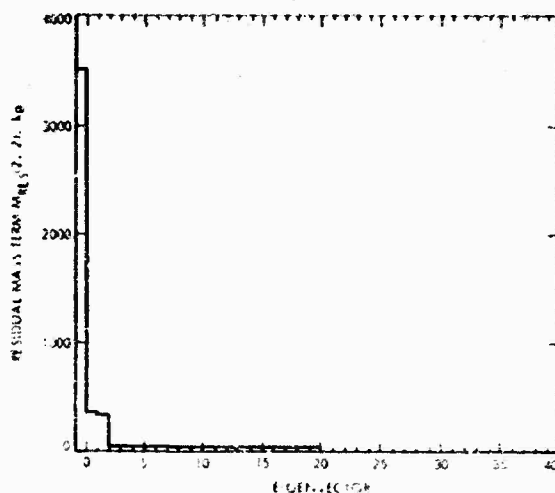


Fig. 6b. $M_{RES}(2,2)$ vs eigenvector

Several features of Figures (6) may be of general interest

- (1) From Figure (6b) and (6d), the first eigenvector has a predominate lateral motion in the 2-direction that results in large inertia shear loads in the 2-direction and large inertia moment about the 1-direction.

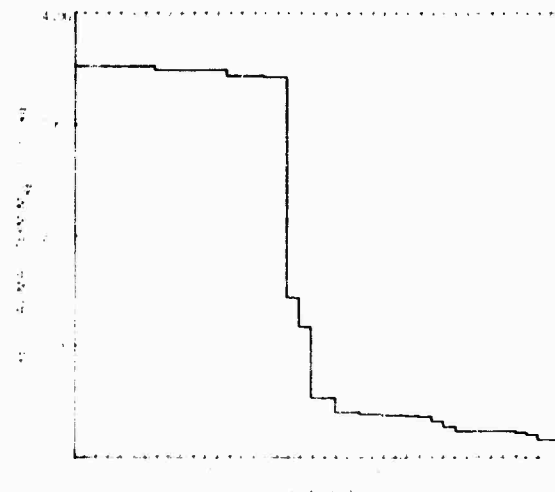


Fig. 6c. $M_{RES}(3,3)$ vs eigenvector

*The terminology is defined as

- | | | |
|-------------|--------------------------|--------------------------|
| 1-direction | \hat{i} direction | = lateral direction |
| 2-direction | \hat{j} direction | = lateral direction |
| 3-direction | \hat{k} direction | = longitudinal direction |
| 4-direction | rotation about \hat{i} | |
| 5-direction | rotation about \hat{j} | |
| 6-direction | rotation about \hat{k} | = torsional direction |

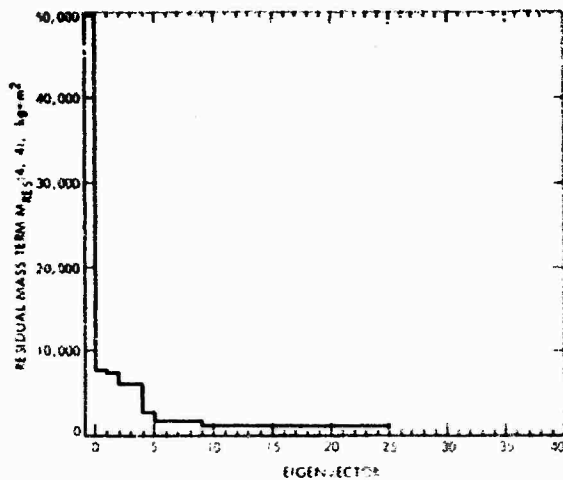


Fig. 6d. $M_{RES}(4,4)$ vs eigenvector

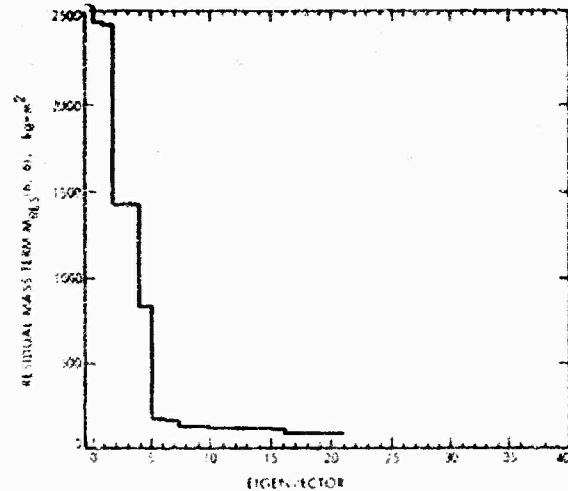


Fig. 6f. $M_{RES}(6,6)$ vs eigenvector

- (2) From Figure (6c), the first predominant longitudinal eigenvector is the 18th eigenvector.
- (3) From Figure (6g), the 18th eigenvector depicts the largest longitudinal-lateral (in 2-direction) coupling.

Other physical interpretations of the data are developed subsequently.

Extraction of Lower-Order Model

Occasionally a general 3-dimensional dynamic model of a structure is available from

which a lower-order model is desired. As an example, if a lateral 2-dimensional model representing translation in the \hat{i} axis is desired, all the terms are retained from the generalized mass matrix of Eqs. (16) or (19) except those of rows and columns 2, 3, 4 and 6. The resulting generalized mass matrix from Eq. (19) is:

$$\begin{bmatrix} 0.1519E1 & 0.1233E5 & 0.2611E1 & 0.3188E4 & 0.2736E2 & 0.0171E3 \\ 0.4446E5 & 0.8238E3 & 0.1007E5 & 0.1677E4 & 0.1873E4 & \\ \text{SYM} & 0.4173E4 & 0 & 0 & 0 & \\ & 0.3201E4 & 0 & 0 & 0 & \\ & 0.2644E4 & 0 & 0 & 0 & \\ & & & & & 0.2173E4 \end{bmatrix}$$

(21)

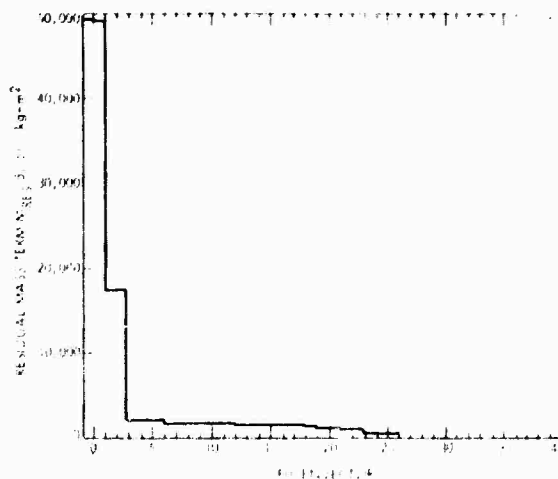


Fig. 6e. $M_{RES}(5,5)$ vs eigenvector

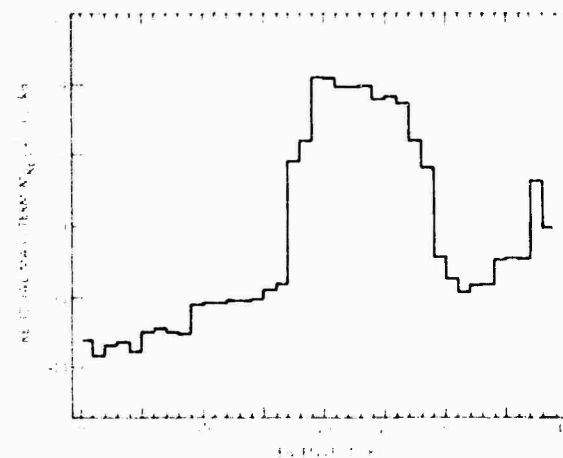


Fig. 6g. $M_{RES}(2,3)$ vs eigenvector

where the units are kg, kg-m, and kg-m². The generalized stiffness matrix is identical to Eq. (20).

Eigenvector, n	Renormalization Factor, q _i
1	0.0824
2	0.996
3	-0.0945
4	0.999

The renormalization factors calculated by Eq. (6) for Eq. (21) are:

The renormalized mass and stiffness matrices for the 2-dimensional structure calculated from Eqs. (7) and (13) are:

$$\begin{bmatrix} [M_{rr}] & [M_{rn}] \\ [M_{nr}] & [M_{nn}] \end{bmatrix} = \begin{bmatrix} 0.3519E4 & 0.1233E5 & 0.2152E2 & 0.3175E4 & 0.2587E1 & 0.2169E3 \\ & 0.4946E5 & 0.6784E2 & 0.1003E5 & 0.1018E2 & 0.1821E4 \\ & & 0.2152E2 & 0 & 0 & 0 \\ & & & 0.3175E4 & 0 & 0 \\ & & & & 0.2587E1 & 0 \\ & & & & & 0.2169E3 \end{bmatrix} \quad (22)$$

where the units are kg, kg-m, and kg-m².

$$\begin{bmatrix} [0] & [0] \\ [0] & [K_{nn}] \end{bmatrix} = \begin{bmatrix} [0] & [0] \\ [0] & \begin{bmatrix} 0.1206E5 \\ 0.1854E7 \\ 0.2896E4 \\ 0.3327E6 \end{bmatrix} \end{bmatrix} \quad (23)$$

where the units are N/m.

Calculations using Eq. (15) for the residual mass matrix as a function of eigenvectors are:

$$[M_{RES}]^{(1)} = \begin{bmatrix} 0.3519E4 & 0.1233E5 \\ \text{SYM} & 0.4946E5 \end{bmatrix} = \begin{bmatrix} 0.2152E2 & 0.6784E2 \\ \text{SYM} & 0.2138E3 \end{bmatrix} = \begin{bmatrix} 0.3497E4 & 0.1226E5 \\ \text{SYM} & 0.4925E5 \end{bmatrix} \quad (24a)$$

$$[M_{RES}]^{(2)} = \begin{bmatrix} 0.3225E3 & 0.2232E4 \\ \text{SYM} & 0.1756E5 \end{bmatrix} \quad (24b)$$

$$[M_{RES}]^{(3)} = \begin{bmatrix} 0.3199E3 & 0.2222E4 \\ \text{SYM} & 0.1752E5 \end{bmatrix} \quad (24c)$$

$$[M_{RES}]^{(4)} = \begin{bmatrix} 0.1030E3 & 0.4010E3 \\ \text{SYM} & 0.2232E4 \end{bmatrix} \quad (24d)$$

where the units are kg, kg-m, and kg-m².

The residual mass matrix terms are identical to those shown on Figures (6a) and (6c). Coefficient matrices (22) and (23) represent the desired 2-dimensional model. Equation (22) is used to illustrate its physical significance.

Figure 7 illustrates the 2-dimensional model. Several features of importance are:

- (1) The distance $1_j = M(5,i)/M(1,i)$ since a unit acceleration of $M(i,i)$ results in a shear reaction $M(1,i)$ and moment reaction $M(5,i)$. Note that if

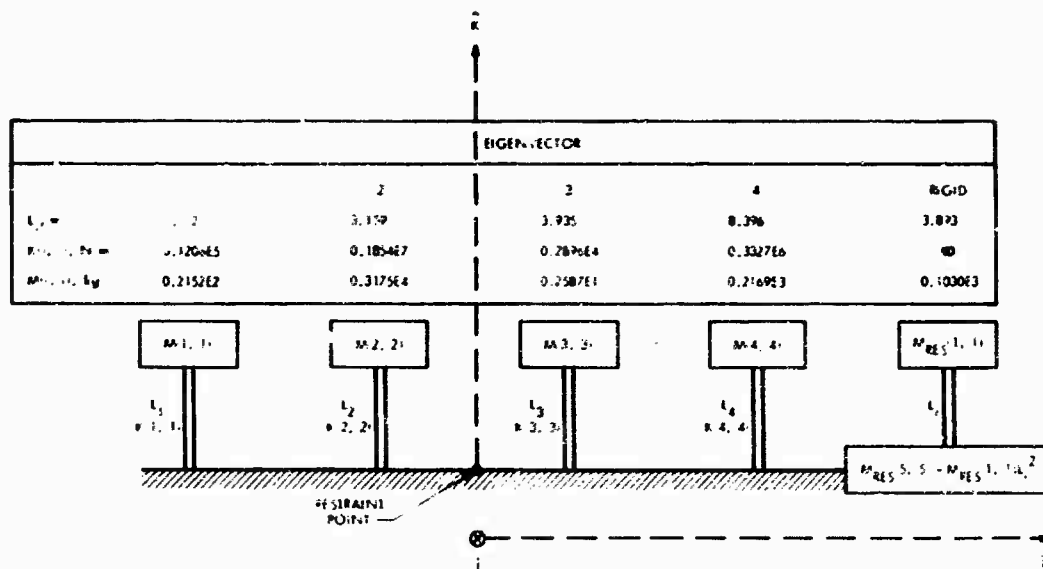


Fig. 7. Two-dimensional model of example problem

the signs of $M(1, i)$ and $M(5, i)$ are not equal, the L_i is negative and the mass is in the negative k -direction.

(2) The eigenvalue $i = \omega_i^2 = K(i, i)/M(i, i)$.

(3) The rigid-body inertia contribution (residual mass matrix) of all truncated eigenvectors greater than 5 is represented by Eq. (24d). A model to represent the residual mass term is shown in Fig. 7, where $L_r = M_{RES}(1, 5)/M_{RES}(1, 1)$ to represent the lateral rotational coupling term. The rotary inertia term $M_{RES}(5, 5)$ is reduced by $M_{RES}(1, 1) L_r^2$ since the offset of $M_{RES}(1, 1)$ by L_r contributes to the rotary inertia.

Similar models can be generated if longitudinal or torsional models are required.

Usage with Limited Computer Programs

Modal synthesis, modal substructure, or modal combination [3] techniques are valuable in solution of large structures. However, special programs are often required to take advantage of the techniques. The equivalent spring-mass system representation allows the use of eigenvectors as generalized coordinates in computer programs capable of accepting lumped masses and weightless elements. Since the equivalent spring-mass system can be obtained from discrete structures, continuous structures, or test data, the origin of the data is immaterial.

For instance, if a structure is comprised of two subsystems A and B where subsystem A

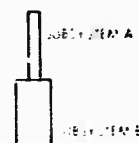


Fig. 8. Structural system comprised of two subsystems

is represented by Fig. 8, modal combination techniques can be used. The dynamic model is pictorially represented as shown in Fig. 9.

For a cantilever beam, the stiffness due to a unit load at the tip is

$$K(i, i) = \frac{3(EI)_i}{L_i^3} \quad (25)$$

Thus $EI_i = L_i^3 K(i, i)/3$, which results in the correct eigenvalue i corresponding to the generalized coordinate Q_i . The EI for the rigid mass is sufficiently large that its eigenvalue is significantly higher than the frequency range of interest.

The use of beams in this fashion automatically transforms the relative displacement modal model into the absolute displacement form required for the finite element model. However, it adds an unnecessary rotational degrees of freedom (without mass) to the problem for each mode. For the more general case of the nonplanar problem or to eliminate the

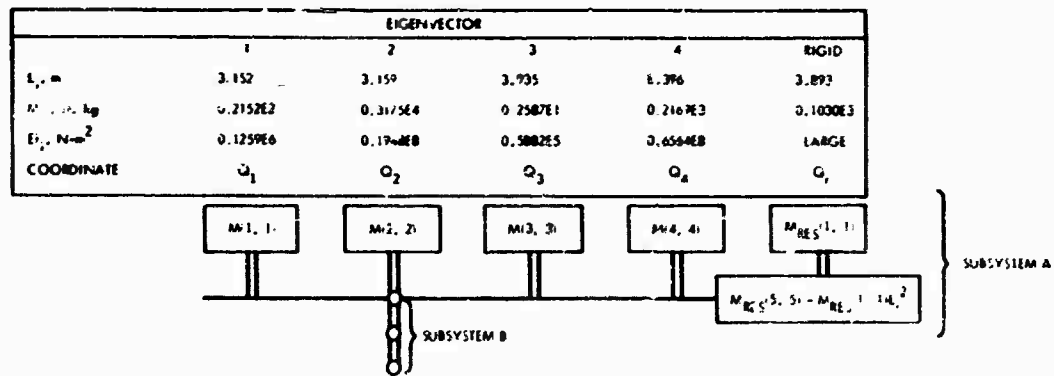


Fig. 9. Modal combination model

unnecessary degree of freedom, the absolute stiffness matrix to be added to the finite element model should be generated by the appropriate transformation [1].

Selection of Significant Eigenvectors

Since one objective of modal combination techniques is to minimize the number of eigenvectors or generalized coordinates, a criterion to select the appropriate eigenvectors is desirable. A criterion that is frequently used is to retain the eigenvectors corresponding to all eigenvalues less than a preselected value.

If information at the intersection of subsystem A and subsystem B of Fig. 9 is required, then the ranking of the first four eigenvectors in order of significance are 2, 4, 1 and 3. A criterion for significance is the magnitude of the effective mass (see Fig. 9) or the decrease in residual mass terms (see Figs. 6a and 6e). If eigenvectors 2 and 4 are retained, then the rigid mass must include the effects of eigenvectors 1 and 3.

Other considerations in the selection of eigenvectors are:

- (1) An eigenvector with small effective mass may result in large loads within the structure if such a local eigenvector is excited.
- (2) Eigenvectors within certain bounds of eigenvalues may be significant because of the anticipated frequency content of the forcing function.
- (3) The accuracy of the loads within a structure may be dependent on the characteristic of the eigenvector that significantly contributes to the loads. For instance, if an eigenvector corresponding to a small effective mass significantly contributes to high loads, then a small error on the model, forcing function, tolerances, or design changes may significantly affect the loads in the structure represented by the effective mass.

Comparison of Similar Models

Occasionally a structural model dynamically similar to another structure is required. For instance, if a dynamic model of subsystem (A) of Fig. 8 is required to assure good dynamic simulation at its interface with subsystem (B), then a criterion for "quality" of the model is the match of the mass coupling calculated at the interface and the corresponding eigenvalues evaluated with the interface restrained.

Figures (10a) and (10b) represent a comparison of the residual mass plots of two structures. A measure of the degree of similarity is the match of the residual mass plots and eigenvalues. The plots indicate that the eigenvector with predominate motion in the i direction switched from the second eigenvector of Model 1 to the first eigenvector of Model 2. The information is also of value in a design process where the loads evaluated from a

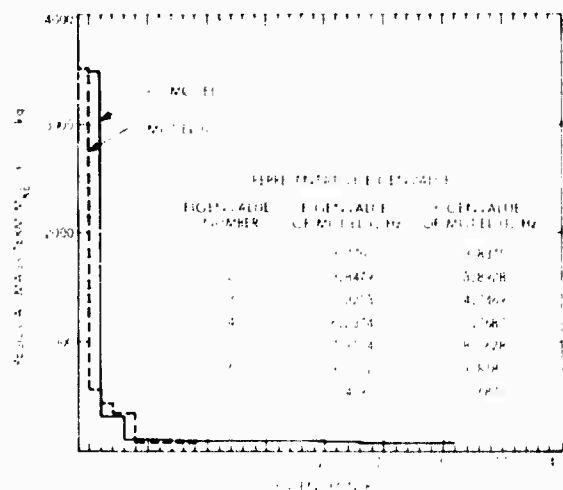


Fig. 10a. $M_{RES}(1, 1)$ vs eigenvector; comparison of two models

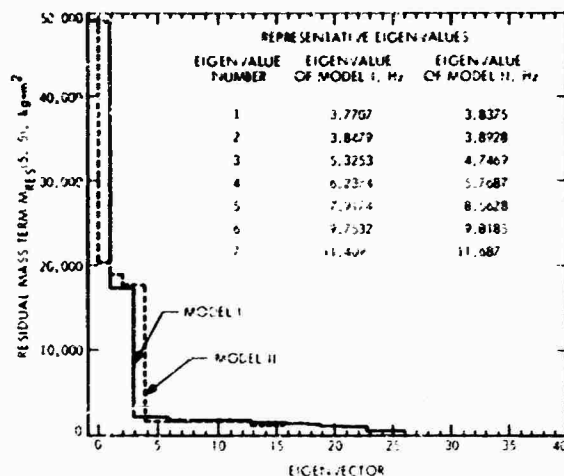


Fig. 10b. $M_{RES}(5,5)$ vs eigenvector; comparison of two models

dynamic model result in design changes, which in turn are reflected in the dynamic model.

A frequent question is whether the design changes significantly influenced the design loads. The residual mass and eigenvalue comparison of two versions of a structure may provide an answer to the question.

Application to Modal Tests

Modal tests are somewhat different from other tests because a measure of the accuracy of the test results exists. The accuracy of the eigenvectors can be evaluated from their orthogonality with respect to each other. A measure of the quantity of eigenvectors required is often neglected.

Current modal test systems include computer terminals at the test site that can compute residual mass plots as the experimental eigenvectors are measured. The magnitude of the residual mass terms is a measure of the unmeasured eigenvectors that contributes to inertial loading at the interface. For instance if torsional eigenvectors are significant, then a plot similar to Fig. 6f generated during a test can be helpful as follows:

- (1) If only five eigenvectors and eigenvalues are measured, Fig. 6f reveals that eigenvectors accounting for about 30% of the inertial reaction of the base have not been measured.
- (2) Eigenvectors 1, 2 and 4 do not have significant torsional inertial reactions at the restraint point.

Consistency of Data

Generalized mass, stiffness, and damping matrices including rigid-body coupling are often calculated and transmitted between organizations as data that characterize the dynamics of the structural system. The data are convenient for transfer because the quantity of the data is minimized, the computer and program compatibility requirements between organization are minimized, and the data provide physical insight into the dynamic characteristics of the structure.

Techniques to check the validity of the data are valuable in minimizing errors. Characteristics that can be checked are described as follows:

- (1) Residual mass plots of the diagonal terms must monotonically converge to zero as the number of eigenvectors approaches the total degrees of freedom of the structure. Negative diagonal terms which can create problems are caused by erroneous data of truncation errors when significant numbers of eigenvectors are used.
- (2) All the terms of the residual mass matrix should equal zero when the number of eigenvectors equal the total degrees of freedom of the structure.

CONCLUSION

The reformulation of the dynamic description of structures as equivalent spring-mass systems results in data that have physical significance to the engineer. The physical interpretation is valuable in minimizing misuse of the information as well as in providing a means to verify the validity of the data.

The equivalent spring-mass system has minimized the analyses effort by providing a means of engineering judgment as the amount of computer data is reduced to a series of single-degree-of-freedom systems.

REFERENCES

1. Bamford, R. M., Wada, B. K., and Gayman, W. H., Equivalent Spring-Mass System for Normal Modes, Technical Memorandum 33-380, Jet Propulsion Laboratory, Pasadena, California, Feb. 15, 1971.
2. Bisplinghoff, R., Ashley, H., and Hoffman, R., Aeroelasticity, Addison-Wesley Publishing Co., Inc., Mass., 1955.
3. Hurty, W., Dynamic Analysis of Structural Systems by Component Mode Synthesis, Technical Report 32-350, Jet Propulsion Laboratory, Pasadena, California, Jan. 15, 1964.

LONGITUDINAL VIBRATION OF COMPOSITE BODIES OF VARYING AREA

D.J. Guzy*, J.C.S. Yang†, W.H. Walston, Jr.‡
Mechanical Engineering Department
University of Maryland
College Park, Maryland

The natural frequencies and corresponding mode shapes for composite, axisymmetric bodies of varying area undergoing longitudinal vibrations are determined both experimentally and theoretically. Composite rods, cones and conical shells of Lucite, Nylon, Polycarbonate and Polyethylene are investigated. Strain measurements are taken from strain gages mounted on the surface of the models which are excited at varying frequencies by a shaker table. Lumped parameter approximations of the continuous bodies are solved numerically on the digital computer for both fixed-free and free-free boundaries in order to determine the natural frequencies, mode shapes and relative strains. The method of characteristics is utilized in a wave propagation approach to obtain the response of a point in the model to a random input. The random input selected is white noise. The natural frequencies are obtained by performing a Fast Fourier Transform Analysis on the response.

LIST OF SYMBOLS

- A cross-sectional area
- a Lagrangian coordinate
- a_{ij} influence coefficients
- c shift rate
- E modulus of elasticity
- f_1 fundamental frequency
- g gravitational constant
- K spring constant
- L length
- t time
- u particle velocity
- x distance from base
- ϵ engineering strain
- ρ density
- σ engineering stress
- φ impact function

* Graduate Assistant
† Associate Professor
‡ Associate Professor

INTRODUCTION

In recent years engineers have been required to design ballistic range models which are capable of being launched at hypersonic velocities for aerodynamic tests of ballistic missiles and space craft. At such velocities the designer is confronted with the dual problem of using materials which are structurally strong enough to withstand the severe loading conditions and materials which minimize the ablation of the missile nose due to aerodynamic heating. These models are frequently used to study boundary layer transition which could be influenced by modal vibration. The purpose of this paper is to study the vibration characteristics of the model as it is being tested in the range, and to develop an analytical means of predicting the transient response of the model under dynamic loadings.

The problem of vibration in continuous systems such as cylindrical rods has been investigated extensively in various research papers and textbooks [1-4]. However, vehicles are generally made up of conical shells, sections with abrupt changes in area, and laminated sections of different materials. There is a definite lack of experimental and analytical developments concerning vibration

Preceding page blank

and wave propagation in structures of varying area and/or multi-layered with changing impedances.

Experimental tests were performed using a shaker table to excite the models. Models were made from Plexi-glass (Lucite), Nylon, Polycarbonate (Lexan), Polyethylene, and the combination thereof. Strain gages and accelerometers were mounted on various positions on the model to determine the natural frequency, mode shape, and transient responses in the model. Two theoretical approaches, classical and wave propagation, were utilized. Natural modes of vibration and mode shapes were determined by first the classical approach, which constitutes the solution to the boundary value problem and in turn the eigenvalue problem. Numerical solutions were obtained by using a system of spring-masses. In the wave propagation approach the method of characteristics was utilized. A numerical integration of the characteristic equations for the range model, in conjunction with appropriate procedures to ensure that the conditions on the external boundaries as well as the continuity conditions at the sections with the step changes in area and varying impedances are satisfied, will yield the stress, displacement, and the particle velocity anywhere in the model[5]. Since this method is applicable for any type of loading, the natural frequencies can be obtained by applying a random input to the model and then performing a Fourier analysis on the response of some point in the model.

EXPERIMENTAL INVESTIGATIONS

A variety of models including rods, composite rods, composite cones and composite conical shells were fabricated and tested. Sketches of these models are shown in Fig. 1. Plastic materials were utilized rather than metals in order to maintain lower natural frequencies. An upper limit on the frequency of the forcing function was imposed by the shaker which was used - MB Electronics Model PM-50.

All models were constructed from solid plastic rods which were turned on a lathe to their final dimensions. In the case of a composite model, the sections were glued together using an epoxy adhesive. Strain gages were then mounted on the surface and the model was glued to a base plate which was bolted to the shaker table. As the input frequency to the shaker was varied, the output from the strain gages was noted. In this manner the natural frequency of each model was determined.

Since the elastic modulus of many plastic materials varies due to manufacturing inconsistencies, age and environment in addition to the effects of turning on the lathe, experiments were performed in order to determine the proper value of the modulus for the materials being used. Solid rods were used as the test specimen since the fundamental frequency

equation for longitudinal vibration of free-fixed rods is well established.

$$f_1 = \frac{1}{4L} \sqrt{\frac{Eg}{\rho}} \quad (1)$$

The fundamental natural frequency of each rod was determined experimentally as was the density. Using this information and Eq. (1) the value of the modulus for each material was calculated. These experimentally determined values are given in Table 1, and are used in all subsequent calculations.

TABLE 1

Experimentally Determined Values of the Modulus of Elasticity and Density

Material	E (lb/in ²)	ρ (lb/in ³)
Polyethylene	2.8×10^5	0.0348
Lucite	3.3×10^5	0.0429
Nylon	6.0×10^5	0.0430
Lexan	3.9×10^5	0.0447

A series of tests involving composite rods made up of two rods glued end to end were performed. These experimental results, given in Table 2 and Fig. 2, are restricted to the first two natural frequencies due to the upper frequency limit of the shaker. The results of the lumped parameter computer analysis which is explained in the next section is also given there.

The next series of tests involved composite cones made up of a base and a tip glued together. Experiments were performed with the base and tip of the same materials as well as different materials. Table 3 and Fig. 3 illustrate the results of these experiments and also the lumped parameter computer results. This also gave a check on the influence of the epoxy bond between the sections. Based on the results, it was concluded that the influence of the epoxy was negligible.

The final experiments were performed using a conical shell as the base and a conical solid of a different material as the tip. These results are shown in Table 4 and Fig. 4.

LUMPED PARAMETER COMPUTER ANALYSIS

The physical models are approximated by a lumped parameter system consisting of concentrated mass elements and concentrated spring elements. Each model is divided into equal length segments with the mass treated as concentrated at the mid-point of the segment. The rods are divided into 16 segments and the cones into 24 segments. The mass of each segment

varies as its volume in the case of the cones. The mass elements are connected by spring elements with spring constants determined from the properties of the material according to the equation:

$$\frac{1}{K_{i-1}^i} = \frac{1}{E} \int_{x(i-1)}^{x(i)} \frac{dx}{A(x)} \quad (2)$$

where x is measured from the base and:

K_{i-1}^i = spring constant between i th and $(i-1)$ th positions

$x(i)$ = distance at i th position

$x(i-1)$ = distance at $(i-1)$ th position

The computer program utilizes the influence coefficients, a_{ij} , which are determined by

$$a_{ij} = a_{ji} = \sum_{k=1}^i \frac{1}{K(L)} \quad i \leq j \leq n \quad (3)$$

The computer program which is used to analyze the lumped parameter models first determines the eigenvalues by (1) pre-multiplying the mass matrix by the influence coefficients to obtain the dynamic matrix, (2) transforming the dynamic matrix to a Hessenberg matrix. The natural frequencies are then determined from the eigenvalues. The eigenvectors and mode shapes are then calculated

Natural frequencies obtained by this method are compared to the experimental results in Tables 2, 3, and 4 and in Figures 2, 3, and 4. The first and second mode shapes and corresponding material frequencies, for additional composite cones, both solids and shells, are computed by this lumped parameter approach. These results are given in Table 5 and in Figures 5 and 6. The relative values of strain for the first and second modes are also computed and are shown in Figures 7 and 8.

Table 2

Composite Rods, Experimental vs. Lumped Parameter Frequencies
(See Fig. 2 for dimensions)

Material		Frequency (KHz)			
Base	Tip	Experimental		Lumped Parameter	
		1st	2nd	1st	2nd
Polyethylene	Lucite	1.6	5.35	1.64	5.27
Nylon	Lexan	2.0	6.0	2.16	5.98
Nylon	Polyethylene	2.25	5.6	2.28	5.68

Table 3

Composite Cones, Experimental vs. Lumped Parameter Frequencies
(See Fig. 3 for dimensions)

Material		Frequency (KHz)			
Base	Tip	Experimental		Lumped Parameter	
		1st	2nd	1st	2nd
Polyethylene	Nylon	4.45	10.2	4.52	10.17
Polyethylene	Lucite	4.5	----	4.53	9.21
Polyethylene	Polyethylene	4.5	9.2	4.64	9.26

Table 4

Composite Cone, Shell Base with Solid Tip, Experimental vs Lumped Parameter Frequencies.

(See Fig. 4 for dimensions)

Material		Frequency (KHz)			
Base	Tip	Experimental		Lumped Parameter	
		1st	2nd	1st	2nd
Polyethylene	Lucite	3.15	8.1	3.18	8.14

Table 5

Composite Cones, Lumped Parameter Frequencies
(Base 1 in. dia. x 3 in. long, Tip 3 in. long)

Material		Frequency (KHz)		Graph Symbol
Base	Tip	1st	2nd	
Poly. solid	Poly. solid	4.64	9.25	Δ
Poly. solid	Lucite solid	4.45	9.21	*
0.1 in. Poly shell	Lucite solid	3.60	10.06	.
0.1 in. Poly shell	Poly. solid	3.80	10.22	o
0.2 in. Poly shell	Poly. solid	4.38	11.31	□

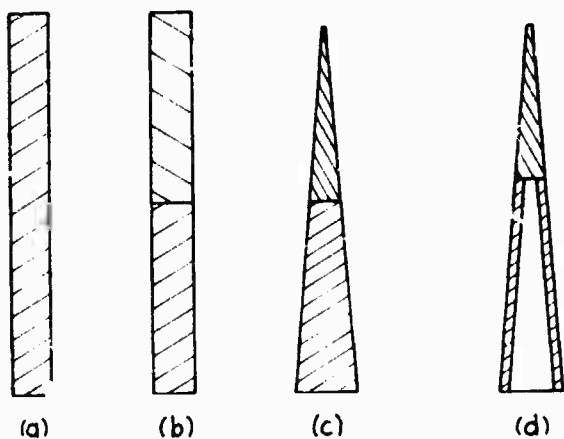


Fig. 1 - Experimental models

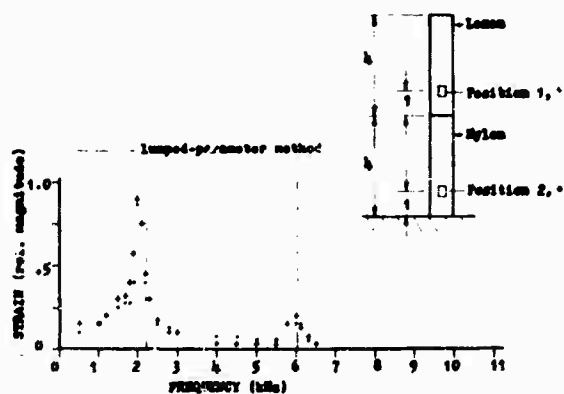


Fig. 2 - Composite rods, experimental vs. lumped parameter frequencies

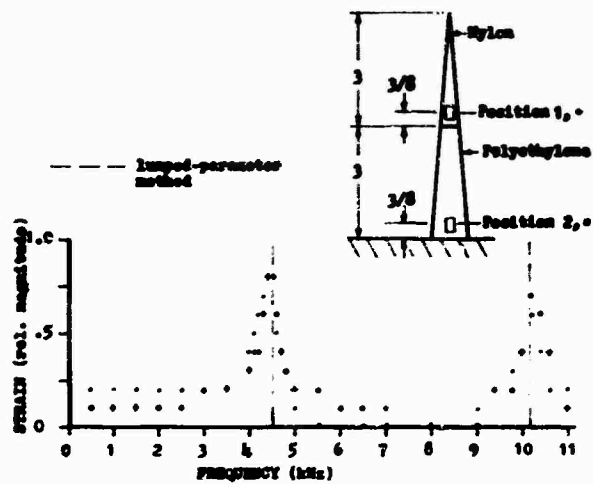


Fig. 3 - Composite cones, experimental vs. lumped parameter frequencies

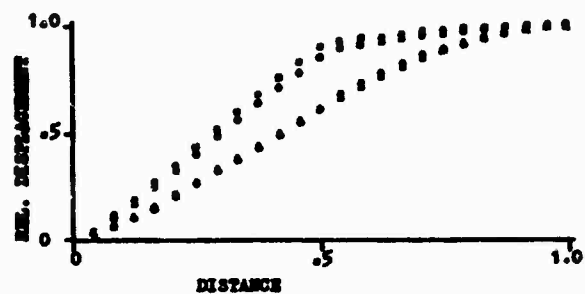


Fig. 5 - Composite cones, first mode shapes (see Table 5 for symbols)

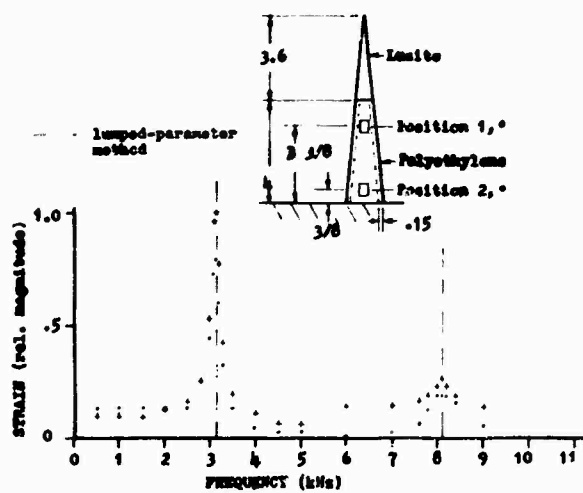


Fig. 4 - Composite cones, shell base with solid tip, experimental vs. lumped parameter frequencies

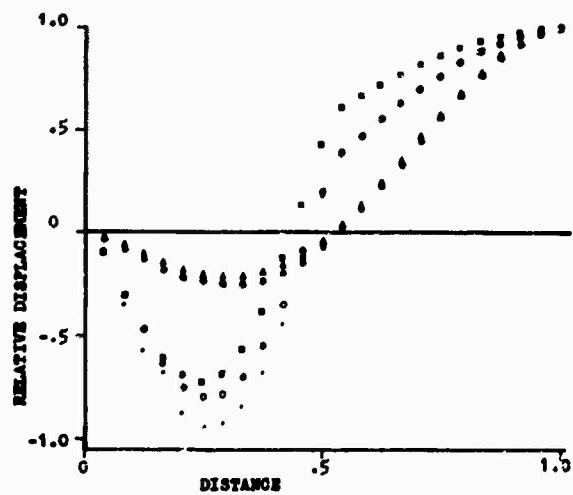


Fig. 6 - Composite cones, second mode shapes (see Table 5 for symbols)

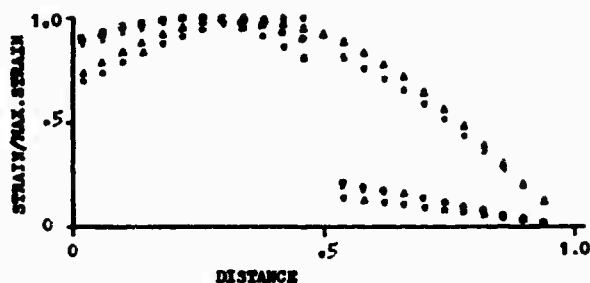


Fig. 7 - Composite cones - first mode strain
(see Table 5 for symbols)

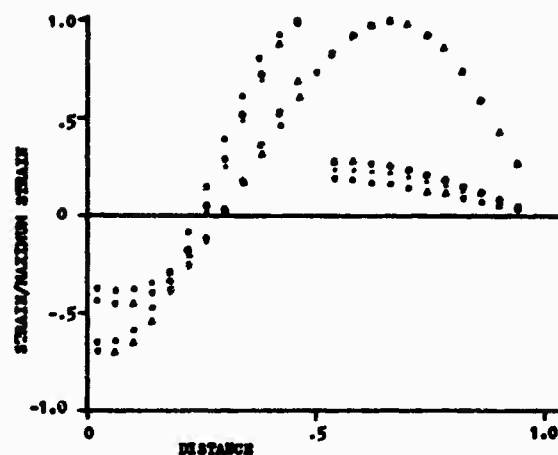


Fig. 8 - Composite cones - second mode strain
(see Table 5 for symbols)

WAVE PROPAGATION ANALYSIS

The stress wave propagation theory used in this analysis was developed independently by T. Von Karman [6] and G. I. Taylor [7] in 1942 and used by many investigators in various forms since that time. It is a one dimensional elastic-plastic theory used to determine the transient properties of solid materials under dynamic loading.

The response of materials is governed by the equations of continuity and momentum which are given in the Lagrangian coordinate system as follows:

$$\frac{\partial u}{\partial a} = \frac{\partial \epsilon}{\partial t} \quad (4)$$

$$\frac{\partial u}{\partial t} = \frac{1}{\rho A} \frac{\partial(\sigma A)}{\partial a} \quad (5)$$

From the above equations the characteristic equations may be obtained:

$$\frac{\partial(u \pm \varphi)}{\partial t} \pm c \frac{\partial(u \pm \varphi)}{\partial a} = \frac{\sigma}{\rho A} \frac{\partial A}{\partial a} \quad (6)$$

where

$$c^2 = \frac{1}{\rho} \frac{\partial \sigma}{\partial \epsilon} \quad (7)$$

and

$$d\varphi = c d\epsilon \quad (8)$$

A numerical integration of the characteristic equations in the range model, in conjunction with appropriate procedures to ensure that the conditions on the external boundaries as well as the continuity conditions at the sections with the step changes in area and varying impedances are satisfied, will yield the stress, displacement, and the particle velocity anywhere in the model [5]. Since this method is applicable for any type of loading a random input was applied to the model. The random input signal selected is white noise which has a delta function as its autocorrelation function. The transient response at a point on the model was obtained numerically on the IBM 7094 computer. A Fast Fourier Transform method was performed on the response to obtain the natural frequencies of the structure. The advantages of the Fast Fourier Transform are two-fold. The number of actual arithmetic operations is reduced drastically, causing increases in speed of several orders of magnitude for reasonable record lengths. Also, because of the fewer operations performed, truncation and roundoff errors are reduced, producing a more accurate result. The results of the wave propagation analysis are compared to the lumped parameter analysis for free-free boundaries in Figures 9, 10 and 11 for various models.

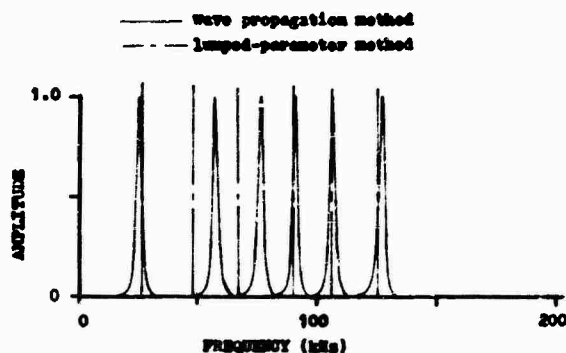


Fig. 9 - Composite cone, natural frequencies, polyethylene base, lucite tip

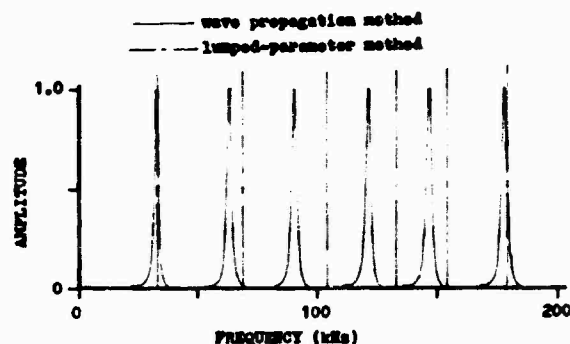


Fig. 11 - Composite cone, natural frequencies, polyethylene shell base, polyethylene tip

DISCUSSION OF RESULTS

The natural frequencies for various composite rods, cones and conical shells obtained experimentally and by the lumped parameter approach compare favorably. The maximum deviation is less than 3% for the composite cones and conical shells. The second natural frequency for the polyethylene-lucite cone was not obtained experimentally because of difficulties in the experimental set-up (Table 3). Subsequent modifications eliminated the difficulties, however the data was not retaken.

Unfortunately the material properties of the different plastic materials do not vary greatly. The use of materials having a wider range of properties should give more significant results for composite bodies. Metals offer certain advantages over plastics such as a wider range of properties, more stable properties, and easier machining—particularly for conical shells. The use of metals is recommended if a higher frequency input is available.

The mode shapes and relative strains are presented from the lumped parameter approach only. Since strain gages were employed at only two locations on each model, comparison was possible only at those points. Therefore these results were not considered significant and are not presented.

Comparison of the two theoretical predictions, lumped parameter and wave propagation for the free-free boundary was very erratic and poor. The fundamental natural frequencies for the various composite cones and conical shells

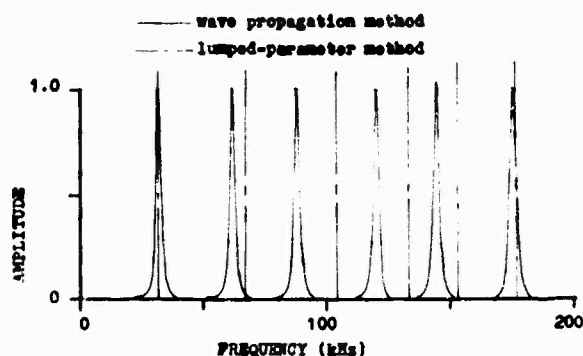


Fig. 10 - Composite cone, natural frequencies, lucite shell base, polyethylene tip

compared reasonably well but not the higher modes. This confirmed the fact that while elastic wave propagation analysis might give good results for problems with a short duration input loading, it does not give very good results for long time input loading. In addition, the wave propagation analysis is a one-dimensional analysis. For conical modes where the area varies, it is dependent on the cone angle and the number of grid points used in representing the model. For one dimensional problems such as longitudinal vibration of composite rods, axially symmetric longitudinal vibration of circular cylinders and spherical shells, good agreements can be expected. (Natural frequencies were obtained for two-layer composite rods, cylindrical and spherical shells using the wave propagation approach. Results compared well with the theoretically computed results. The results for these calculations and comparison are not presented in this paper.)

CONCLUSIONS

The lumped parameter method using a series of mass elements and linear springs can be used to analyze the longitudinal vibration problem of composite axisymmetric bodies of varying area as verified by experimental vibration tests on simple composite rods, cones and conical shells.

The one dimensional elastic wave propagation approach utilized in computing the natural frequencies of the composite models did not give good results, in order to obtain better results using the one dimensional wave propagation analysis for the changing area problem with a long time input loading, much finer grid points must be utilized which require increased running time and storage space on the computer.

More research is needed to determine the effect of cone angle, impedance change, material properties, etc. on the vibration characteristic.

ACKNOWLEDGMENTS

Portions of this paper are part of a thesis presented by D. J. Guzy as a partial requirement for the Master of Science degree at the University of Maryland. Certain segments of this investigation were sponsored by N.A.S.A. Ames Research Center, Moffett Field, California under NASA Grant No. NGR 21-002-292 and under a grant from the Minta Martin Foundation.

REFERENCES

1. J. R. Hutchinson, "Axisymmetric Vibrations of a Solid Elastic Cylinder Encased in a Rigid Container", J. Acoust. Soc. Am., Vol. 42, No. 398, 1967.
2. C. T. Sun and K. C. Valanis, "Axially Symmetric Wave Propagation of a Finite Solid Cylinder", Engineering Res. Inst., Iowa State Univ., 1967.
3. H. D. McNiven and D. C. Perry, "Axially Symmetric Waves in Finite, Elastic Rods", J. Acoust. Soc. Am., Vol. 34, No. 433, 1962.
4. M. Rumerman and S. Raynor, "Natural Frequencies of Finite Circular Cylinders in Axially Symmetric Longitudinal Vibration", J. Sound Vib., Vol. 15, p.529, 1971.
5. J. C. S. Yang and A. Seigel, "Stress Waves in Multi-Layered Cylinders and Conical Frustrums", The Shock and Vibration Bul., No. 40, Part 4, 1969.
6. T. vonKarmon, "On the Propagation of Plastic Deformation in Solids", NORC Report A-29 (OSRD No. 365), Jan., 1942.
7. G. I. Taylor, "The Plastic Wave in a Wire Extended by an Impact Load", R. C. Report No. 329, June 1942.

SIMPLIFIED METHOD FOR THE EVALUATION OF STRUCTUREBORNE VIBRATION TRANSMISSION THROUGH COMPLEX SHIP STRUCTURES

**M. Chernjawski and C. Arcidiacono
Gibbs & Cox, Inc.
New York, New York**

A simplified method for analyzing the transmission of vibration in ship structures is presented. In the first part of the paper, the reflection and transmission of bending and longitudinal elastic waves in plates or beams forming cross-shaped connections is investigated. The second part analyzes the propagation of bending waves through an infinitely long plate which is stiffened by structural elements of arbitrary shape. Finally, a multipath plane structure is investigated for bending wave transmission.

INTRODUCTION

In the analysis of ship structures there is often a need for identifying the path followed by the vibratory energy as it flows from a structural system to another. In any particular configuration, before specific steps toward the effective control of vibration can be taken, it is necessary to investigate the mechanism of structureborne vibration energy propagation and to be able to predict the magnitude of its wave amplitudes.

Snipboard structures, essentially, consist of multiple beam-reinforced plates which are generally reverberant: many natural frequencies are excited and their loss factors are neglected. In the range of plate sizes used in shipbuilding, bending and longitudinal elastic waves carry most of the vibratory energy. The interaction between these two types of waves is considered important and should be taken into account. This paper presents a method of analysis which is not limited to the transmission of vibration waves, but may be also applied in predicting the intensity of elastic stress waves in composite structures. For example, it may be used to evaluate the stress levels developed in a panel by flexural waves reflected off a rivet. These stresses might be considerably higher than the values predicted by the use of static stress concentration factors.

GENERAL

Material related to structureborne vibration can be found in the technical literature. Cremer (1) * was first to investigate the reflection, transmission, and near field effects at beam-plate interconnections. Ungar (2) analyzed an infinite plate attached to a uniform straight beam. Westphal (3) has studied structureborne noise propagation in buildings. The interaction of bending and torsional waves in grillages has been investigated in detail by Heckl (4). The properties of miscellaneous structural joint configurations were discussed by Nikiforov (5) and also jointly by Cremer and Heckl (6). All these investigations, although rigorous and detailed, apply to specific cases only, and the results can not be used directly by practicing engineers.

The object of this paper is to present and formulate a simplified method useful in predicting the transmission of structureborne vibratory waves through ship structures. The procedure developed is amenable to solution by digital computer programming. In order to retain the intrinsic simplicity of the analysis, the derivation is limited to normal wave incidences at the structural discontinuities. The thickness of the plates and beams is assumed to be sufficiently small to justify neglecting the effect of rotatory inertia and transverse shear.

* These numbers refer to the List of References at the end of the paper.

The first part of this paper evaluates the reflection and transmission characteristics of bending and longitudinal waves at the intersection of four semi-infinite plates connected by a rigid mass. In the second part an infinitely long plate, stiffened by structural members, is investigated for transmission of bending waves. The remainder of the paper analyzes a plane structure. The expressions for wave amplitudes are derived at specific locations of the structure.

I. VIBRATIONS OF CROSS-SHAPED RIGID PLATE JOINTS

Most structural joints used in shipbuilding consist of cross, "T" or "L"-shaped connections. It is therefore appropriate to investigate first the general case in which four semi-infinite plates (or beams) of different thicknesses are attached to a rigid structural member as shown in Fig. 1. The plates may be of the same or dissimilar materials. As previously stated, all incident waves are assumed to act normal to the intersection. In accordance with the theory of structural dynamics, as applied to long beams, the following fourth order differential equation is obtained:

$$\frac{d^4 y}{dx^4} - k^4 y = 0$$

where:

$$k^4 = \frac{\omega^2 m}{EI}$$

y is the bending wave deflection, k is defined as the wave number, m represents the mass per unit length of plate, I is the area moment of inertia of face x per unit width of cross-section, and ω is the radial frequency.

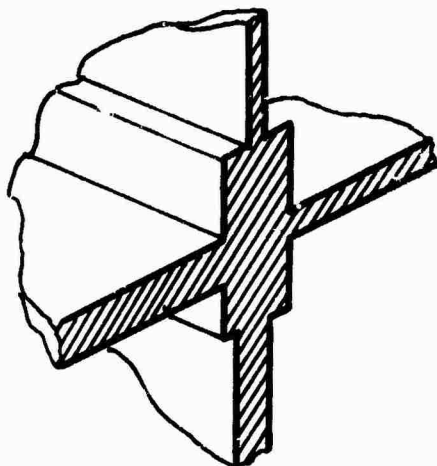


Fig. 1. Cross-section of a rigid plate joint

At any frequency ω the complex amplitude of the bending wave is:

$$y(x, \omega) = B_1(\omega)e^{-jkx} + B_2(\omega)e^{jkx} + C_1(\omega)e^{-kx} + C_2(\omega)e^{kx} \quad (1)$$

where the coefficients B_1 , B_2 , C_1 and C_2 are functions of the boundary conditions. The first two terms in equation (1) correspond to traveling waves in the $+x$ and $-x$ direction, respectively. The last two terms represent the "near field" which exists in the proximity of the boundaries of the plate intersection, or in the vicinity of the noise source. The time factor $e^{j\omega t}$ is neglected throughout this paper.

Referring to Fig. 2, if the plate "1" is excited by a harmonic unit force of angular frequency ω which acts normal to the plate intersection, bending waves are generated. The waves travel to the intersection where they are partially transmitted as bending waves into the other plates. In addition, while passing through the joint, the bending waves generate longitudinal waves. Similarly, when the longitudinal waves propagate through a joint, they are partially transformed into bending waves.

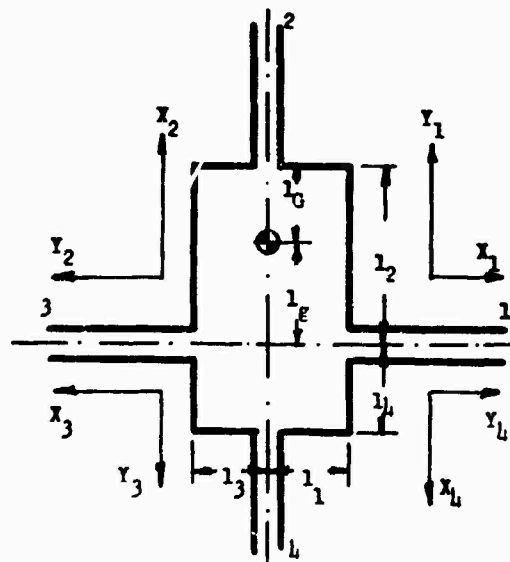


Fig. 2. Dimensions and coordinates of a rigid joint

Since both reflected and transmitted bending waves have near fields and far fields, the bending wave equations for all four plates can be expressed as follows:

For plate "1":

$$y_1 = e^{-jk_1 x_1} + r_1 e^{jk_1 x_1} + C_1 e^{k_1 x_1} \quad (2)$$

where r_1 is the reflection coefficient and C_1 is the near field term.

For plates "2", "3" and "4":

$$y_i = t_i e^{-jk_i x_i} + C_i e^{-k_i x_i} \quad (2a)$$

where i corresponds to the plate number, t_i and c_i represent the transmission and near field coefficients, respectively, and $k_i = \omega/c_{bi}$ is the bending wave number. In the expression for k_i , c_{bi} is the bending wave velocity in plate i and is defined as:

$$c_{bi} = \sqrt[4]{\frac{E_i I_i \omega^2}{m_i}} = \sqrt{1.8 C_{Li} h_i f}$$

C_{Li} is the longitudinal velocity and h_i is the thickness of plate i . The near field terms $C_i e^{-k_i x_i}$ decay very fast and therefore are of minor importance except in the vicinity of an intersection or near a vibration source.

The expressions for longitudinal wave amplitudes in plates "1", "2", "3" and "4" are given by:

$$u_i = D_i e^{-jp_i x_i} \quad (3)$$

where i corresponds to the plate number, and $D_i = D_1$ is the reflection coefficient. $D_i = (D_2, D_3, D_4)$ are the transmission coefficients of the longitudinal waves in plates 2, 3 and 4 and characterize the transition of bending waves to longitudinal waves; p_i is the longitudinal wave number which is expressed as:

$$p_i = \frac{\omega}{C_{Li}}$$

The geometry of the joint and the coordinate systems of each plate are shown in Fig. 2. The four plates, whose thicknesses are not necessarily equal, are connected to a rigid bar of mass M_0 and mass moment of

inertia I_0 . In order to evaluate the coefficients r_1 , t_i , D_i and C_i for the system shown in Fig. 2, the following boundary conditions are used:

$$(a) \quad y_1 - \frac{\partial y_1}{\partial x_1} l_1 - u_4 = 0$$

$$(b) \quad y_4 - \frac{\partial y_4}{\partial x_4} l_4 - u_3 = 0$$

$$(c) \quad y_2 - \frac{\partial y_2}{\partial x_2} l_2 + u_3 = 0$$

$$(d) \quad u_1 + u_2 = 0$$

$$(e) \quad y_3 - \frac{\partial y_3}{\partial x_3} l_3 + u_4 = 0$$

$$(f) \quad u_2 + u_4 = 0$$

$$(g) \quad \frac{\partial y_1}{\partial x_1} - \frac{\partial y_2}{\partial x_2} = 0$$

$$(h) \quad \frac{\partial y_1}{\partial x_1} - \frac{\partial y_3}{\partial x_3} = 0$$

$$(i) \quad \frac{\partial y_1}{\partial x_1} - \frac{\partial y_4}{\partial x_4} = 0$$

$$(j) \quad \Sigma F_{\text{vert}} = E_1 I_1 \frac{\partial^3 y_1}{\partial x_1^3} + E_2 h_2 \frac{\partial u_2}{\partial x_2} - E_3 I_3 \frac{\partial^3 y_3}{\partial x_3^3} - E_4 h_4 \frac{\partial u_4}{\partial x_4} - \omega^2 M_0 u_2 = 0$$

$$(k) \quad \Sigma F_{\text{horiz}} = -E_1 h_1 \frac{\partial u_1}{\partial x_1} + E_2 I_2 \frac{\partial^3 y_2}{\partial x_2^3} + E_3 h_3 \frac{\partial u_3}{\partial x_3} - E_4 I_4 \frac{\partial^3 y_4}{\partial x_4^3} - \omega^2 M_0 \cdot \left(y^2 - \frac{\partial y_2}{\partial x_2} l_G \right) = 0$$

$$\begin{aligned}
 (1) \quad \Sigma M &= - \sum_{i=1}^4 E_i I_i \frac{\partial^2}{\partial x_2^2} \\
 &\left(y_1 - \frac{\partial y_1}{\partial x_1} l_1 \right) + \omega^2 I_0 \frac{\partial y_2}{\partial x_2} \\
 &- \omega^2 M_0 \left(y_2 - \frac{\partial y_2}{\partial x_2} l_G \right) \\
 &\cdot (l_2 - l_G) = 0
 \end{aligned} \quad (4)$$

The substitution of equations (2), (2a) and (3) into equation (4) results in a set of linear equations expressed in terms of the 12 coefficients previously mentioned. The equations may be solved by means of matrix algebra. To illustrate the method, a simple configuration of practical importance will be considered.

it consists of four plate strips connected as shown in Fig. 3. The thickness and Young's modulus of each plate are h_i and E_i respectively. Provided that $l_1 = l_2 = l_3 = l_4 = M_0 = I_0 = 0$ and at $x_1 = 0$ the same boundary conditions given in equation (4) may be used. After substituting the wave equations (2, 2a and 3) into the modified boundary conditions, equation (4), a set of 12 simultaneous linear equations is obtained. The equations may be conveniently expressed in the form:

$$[A] \{C\} = \{F\}$$

$$[A] = \begin{bmatrix}
 1 & 1 & 0 & 0 & 0 & 0 & 0 & 0 & 0 & 0 & 0 & -1 \\
 0 & 0 & 1 & 1 & 0 & 0 & 0 & 0 & 0 & 0 & 1 & 0 \\
 0 & 0 & 0 & 0 & 1 & 1 & 0 & 0 & 0 & 0 & 0 & 1 \\
 0 & 0 & 0 & 0 & 0 & 0 & 1 & 1 & 0 & 0 & -1 & 0 \\
 0 & 0 & 0 & 0 & 0 & 0 & 0 & 0 & 1 & 0 & 1 & 0 \\
 0 & 0 & 0 & 0 & 0 & 0 & 0 & 0 & 0 & 1 & 0 & 1 \\
 -j & -1 & ja_2 & a_2 & 0 & 0 & 0 & 0 & 0 & 0 & 0 & 0 \\
 -j & -1 & 0 & 0 & ja_3 & a_3 & 0 & 0 & 0 & 0 & 0 & 0 \\
 -j & -1 & 0 & 0 & 0 & 0 & ja_4 & a_4 & 0 & 0 & 0 & 0 \\
 j & -1 & 0 & 0 & -ja_3 g_3 & a_3 g_3 & 0 & 0 & 0 & -jd_2 & 0 & jd_4 \\
 0 & 0 & ja_2 g_2 & a_2 g_2 & 0 & 0 & -ja_4 g_4 & a_4 g_4 & jd_1 & 0 & -jd_3 & 0 \\
 -1 & 1 & -g_2 & g_2 & -g_3 & g_3 & -g_4 & g_4 & 0 & 0 & 0 & 0
 \end{bmatrix}$$

$$\{C\} = \begin{bmatrix} r_1 \\ C_1 \\ t_2 \\ C_2 \\ t_3 \\ C_3 \\ t_4 \\ C_4 \\ D_1 \\ D_2 \\ D_3 \\ D_4 \end{bmatrix}$$

$$\{F\} = \begin{bmatrix} -1 \\ 0 \\ 0 \\ 0 \\ 0 \\ 0 \\ -j \\ -j \\ -j \\ j \\ 0 \\ 1 \end{bmatrix}$$

where:

$$\begin{aligned} a_i &= \frac{k_i}{k_1} \\ b_i &= \frac{E_{i1} k_i}{E_1 k_1} \quad (i = 2, 3, 4) \\ g_i &= a_i b_i \\ d_i &= \frac{m_i C_{L,i}}{m_1 C_{b1}} \quad (i = 1, 2, 3, 4) \end{aligned}$$

Using the same equations, the propagation characteristics may also be determined for "L" and "T"-shaped connections, and also for contiguous plates of different thicknesses.

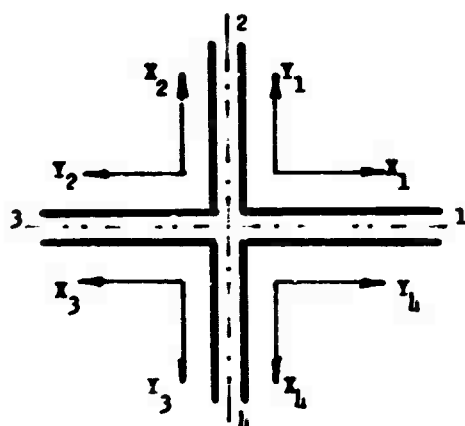


Fig. 3. Coordinate systems of a simplified joint

After inverting the matrix and solving for the coefficients the mechanical power coefficients are calculated. Since the bending wave power flow is:

$$\begin{aligned} P_{bi} &= 2 C_{bi} S_i E_{b, \text{tot}, i} \\ &= 2 C_{bi} m_i \frac{y_i^2 \omega^2}{2} \end{aligned}$$

the longitudinal wave power is given by:

$$\begin{aligned} P_{Li} &= C_{Li} S_i E_{Li, \text{tot}} \\ &= C_{Li} m_i \frac{u_i^2 \omega^2}{2} \end{aligned}$$

where C_{bi} and C_{Li} are the bending and longitudinal wave velocities, y_i is the bending wave deflection, $E_{b, \text{tot}, i}$ is the total bending wave energy, S_i is the cross-sectional area of the plate, u_i is the longitudinal wave deflection, and $E_{L, \text{tot}, i}$ is the total longitudinal energy. The reflection and transmission power coefficients of bending and longitudinal waves are expressed by the following relationships:

$$\begin{aligned} R_{b1} &= |r_1|^2; \quad R_{L1} = |D_1|^2 \frac{m_1 C_{L,1}}{2m_1 C_{b1}} \\ T_{bi} &= |t_i|^2 g_i a_i; \quad T_{Li} = |D_i|^2 \frac{d_i}{2} \\ &\quad (i = 2, 3, 4) \end{aligned}$$

where R_{b1} is the bending wave and R_{L1} is the longitudinal wave power reflection coefficient, respectively. T_{bi} and T_{Li} are the bending and longitudinal wave power transmission coefficients in plates 2, 3 and 4.

The following expression satisfies the conservation of energy law and is useful in verifying the accuracy of the results obtained:

$$R_{b1} + R_{L1} + \sum_{i=2}^4 (T_{bi} + T_{Li}) = 1$$

Since there is transformation of bending waves to longitudinal waves, there must also be transformation in the opposite direction. The derivation of reflection and transmission properties for the normal incident longitudinal waves is similar to that for the incident bending waves and will not be presented in this paper.

II. STIFFENED INFINITELY LONG PLATE

In this section the infinitely long plate shown in Fig. 4, is investigated. The plate is stiffened by structural members. The distances separating the stiffeners are not necessarily equal and each is assumed to be larger than the bending wave length. This assumption permits us to neglect the near field effects except in the vicinity of the members.

The connection between any two sections will be referred to as a discontinuity. In particular the connection between sections $i-1$ and i will be the i^{th} discontinuity. The reflection and transmission coefficients of each individual discontinuity are determined

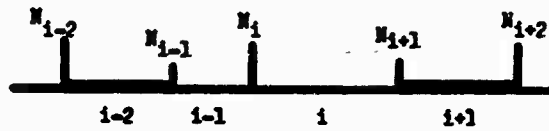


Fig. 4. Stiffened infinite plate strip

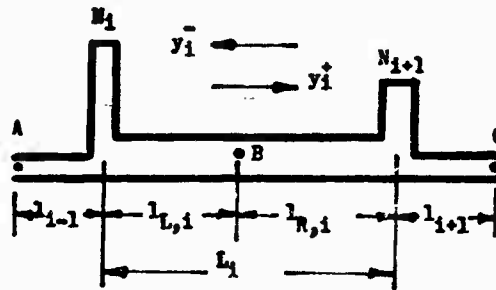


Fig. 5. Section-i of stiffened infinite plate

by the method discussed in the previous section. Although the procedure used here holds for both bending and longitudinal waves acting together, it is assumed that the coupling between these two types of waves is weak and the analysis is therefore restricted to the propagation of bending waves alone. However, the effect of the longitudinal waves could, if desired, be taken into account without major difficulties.

At first the analysis considers a system that has only two discontinuities N_{i-1} and N_i which are separated by a distance L_i (see Fig. 5). Selecting a point "A" at a distance l_{i-1} to the left of the discontinuity N_i as the origin, and assuming that the bending wave is normally incident to the discontinuity, the amplitude of the partially transmitted wave at point "B" is:

$$y_i^+ = y_{i-1}^+ t_{i-1,i} e^{-jk(l_{i-1} + l_{L,i})}$$

where by definition $t_{i-1,i}$ is the transmission coefficient of the bending wave in section $i-1$ propagated into the i^{th} section. After this wave is partially reflected at discontinuity N_{i+1} the wave amplitude at point "B" becomes:

$$y_i^- = y_{i-1}^+ t_{i-1,i} r_{i,i+1} e^{-jk(l_{i-1} + L_i + l_{R,i})} \text{ etc.}$$

where $r_{i,i+1}$ is the reflection coefficient in section i approaching discontinuity $i+1$.

The bending wave originating in the $i+1$ section at point "C" which is at a distance l_{i+1} to the right of discontinuity N_{i+1} is partially transmitted into the i^{th} section. The amplitude at point "B" therefore becomes:

$$y_i^- = y_{i+1}^- t_{i+1,i} e^{-jk(l_{i+1} + l_{R,i})}$$

The amplitude of this wave at point "B" after it is reflected at the discontinuity N_i becomes:

$$y_i^+ = y_{i+1}^- t_{i+1,i} r_{i,i-1} e^{-jk(l_{i+1} + L_i + l_{L,i})} \text{ etc.}$$

It is assumed that standing waves are generated in each section of the structure. Accordingly the amplitude in each section is a function of waves traveling in both the positive and negative direction.

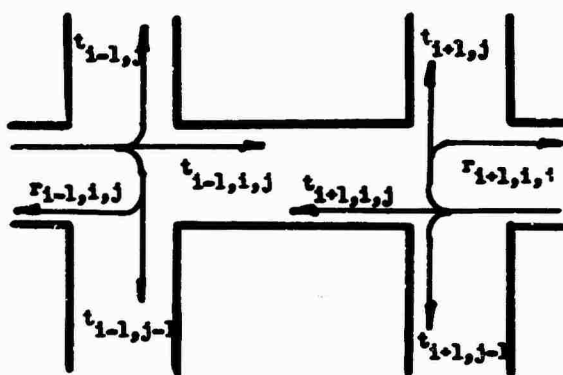


Fig. 7. Directions of reflection and transmission coefficients at section i, j

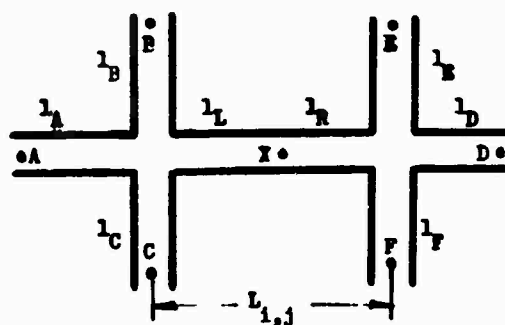


Fig. 8. Section (i, j) of plane structure

The lengths l_A, l_B, \dots, l_F are shown in Fig. 8. The relationship between waves may be derived by utilizing the approach of Section II. The expression for $y_{i,j}^+$ is:

$$y_{i,j} = \left\{ Y_1 e^{-jk_x l_L} + Y_2 e^{-jk_x (L_{i,j} + l_L)} + r_{L,j} \right\} M_{i,j}$$

$$Y_1 = y_{i-1,j}^+ t_{i-1,i,j} e^{-jk_x l_A} + y_{j,i}^- t_{j,i,i} e^{-jk_y l_B}$$

$$+ y_{j-1,i}^+ t_{j-1,i,j} e^{-jk_y l_C}$$

$$Y_2 = y_{i+1,j}^- t_{i+1,i,j} e^{-jk_x l_D}$$

$$+ y_{j,i+1}^- t_{j,i+1,i} e^{-jk_y l_E}$$

$$+ y_{j-1,i+1}^+ t_{j-1,i+1,i} e^{-jk_y l_F}$$

and

$$M_{i,j} = 1 / (1 - r_{L,i} r_{R,i} e^{-2jk_x l_i})$$

which is a measure of the change in the incoming bending waves due to multiple reflections in section (i, j) . Similarly, the wave amplitude $y_{i,j}$ may be expressed by:

The wave represented by y_i^+ will be regarded as the summation of those waves in section i that move in a positive direction, therefore:

$$y_i^+ = \left\{ y_{i-1}^+ t_{i-1,i} e^{-jk(l_{i-1} + l_{L,i})} + y_{i+1}^- t_{i+1,i} r_{i,i-1} e^{-jk(l_{i+1} + l_i + l_{L,i})} \right\} \cdot \left(1 + r_{i,i-1} r_{i,i+1} e^{-j2kl_i} + r_{i,i-1}^2 r_{i,i+1}^2 e^{-j4kl_i} + \dots \right) = \left\{ y_{i-1}^+ t_{i-1,i} e^{-jk(l_{i-1} + l_{L,i})} + y_{i+1}^- t_{i+1,i} r_{i,i-1} e^{-jk(l_{i+1} + l_i + l_{L,i})} \right\} M_i$$

where:

$$M_i = \frac{1}{1 - r_{i,i-1} r_{i,i+1} e^{-j2kl_i}}$$

is the measure of the change in the incoming waves due to multiple reflections at the discontinuities. Similarly, the summation of bending waves that travel in the negative direction is represented by:

$$y_i^- = \left\{ y_{i-1}^+ t_{i-1,i} r_{i,i+1} e^{-jk(l_{i-1} + l_i + l_{L,i})} + y_{i+1}^- t_{i+1,i} e^{-jk(l_{i+1} + l_{L,i})} \right\} M_i$$

Thus in a system consisting of m sections, there are $2m$ algebraic equations, which can be expressed in matrix form. If bending waves are excited in one of the sections, the matrix can be solved for the wave amplitudes in all sections ($i = 1, 2, \dots, n$). Consequently, the attenuation between any two sections may be easily obtained. For example, the attenuation from one section i to another section $i+1$ is expressed in decibels by:

$$TL = 20 \log \left| \frac{y_i}{y_{i+1}} \right|$$

In actual structures, longitudinal waves usually are present together with bending waves. As they are transmitted through the discontinuities, the longitudinal waves are transformed into bending waves, thus reducing appreciably the attenuating effect of the stiffeners.

III. PLANE STRUCTURES

This section considers a complex plane structure consisting of plates (or beams) intersecting at right angles as shown in Fig. 5. The system is generally free to vibrate in the bending and longitudinal modes. Although involved, the configuration can be analyzed in detail without major difficulties. In this particular investigation, however, in order to keep the derivation simple, it is assumed that the coupling between bending and longitudinal waves is small. As before, it is also assumed that the distance between adjacent intersections is larger than the bending wave length. The derivation is similar to that of the system described in Section II. The reflection and transmission coefficients are calculated by the method given in Section I for semi-infinite systems.

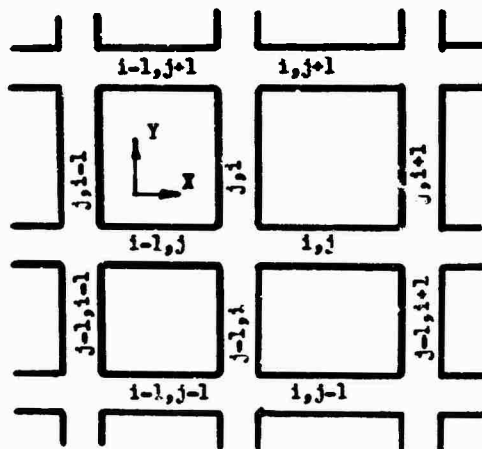


Fig. 6. Plane structure

By definition $r_{L,i}$ and $r_{R,i}$ are the reflection coefficients in section (i, j) approaching N_i and N_{i+1} discontinuities, respectively. The directions of the transmission coefficients $t_{i-1,i,j}$, $t_{i-1,j}$, $t_{i+1,j}$, etc. are defined in Fig. 7. The subscripts define the direction of wave propagation.

We first consider section i, j which has two intersecting plates separated by a distance $L_{i,j}$ (refer to Fig. 8). The wave numbers on horizontal and vertical plates are taken to be k_x and k_y . The standing wave amplitude $y_{i,j}^+$ and $y_{i,j}^-$ is the result of the summation of the bending waves originated at points A, B, C, D, E and F, and transmitted over the discontinuities $N_{i,j}$ and $N_{i+1,j}$.

$$y_{i,j}^- = \left\{ Y_i r_{R,i} e^{-jk_x(L_{i,j} + l_R)} + Y_2 e^{-jk_x l_R} \right\} M_{i,j}$$

For a plane structure having m sections $2m$ equations are derived. They can be solved for traveling wave amplitudes by means of matrix algebra. The attenuation between two sections is evaluated in the same manner as in Section II.

CONCLUSIONS

This paper has presented a method suitable for investigating the behavior of vibratory waves propagating through structural systems. On the basis of the procedure set forth, most of the intrinsic characteristics of the structures can be taken into account. Although the method developed applies primarily to vibration transmission through shipboard structural systems, the procedure is also useful in the study of structureborne noise propagation in all types of structures.

General expressions were obtained for infinitely long plates, stiffened by members of arbitrary shapes, and for plane structures. In order to reduce the complexity of the derivation, only the effect of bending waves was considered. However, in practical problems involving complex structures with a number of discontinuities, it is recommended that the interaction between bending and longitudinal elastic waves be taken into account. The procedure presented is sufficiently broad to permit this treatment.

The analytical derivations of the transmission and reflection properties, expressed in matrix form, are particularly useful in cases requiring the prediction of the filtering action in complex multipath systems. The matrices can be most conveniently solved by means of digital computers.

Time limitations and other overriding considerations limit the scope of any endeavor. This paper is no exception. The authors hope that in the future they will be able to expand the method presented and discuss its application to practical problems.

ACKNOWLEDGMENT

Thanks are due to Mr. E. I. Mohl for support of this paper and to Gibbs & Cox, Inc. for encouraging this study.

REFERENCES

- (1) L. Cremer, "Calculation of Sound Propagation in Structures", *Acustica*, Vol. 3, No. 5, pp 317, 1953
- (2) E. E. Ungar, "Transmission of Plate Flexural Waves Through Reinforcing Beams: Dynamic Stress Concentrations", *J. of Acoustical Soc. of America*, Vol. 33, No. 5, pp 633-39, May 1961
- (3) W. Westphal, "Ausbreitung von Körperschall in Gebäuden" *Acustica*, Vol. 7, pp 335, 1957
- (4) M. A. Heckl, "Investigations on the Vibrations of Grillages and Other Simple Beam Structures", *J. of Acoustical Soc. of America*, Vol. 36, No. 7, pp 1335-43, 1964
- (5) A. S. Nikiforov, et al, "Propagation and Damping of Sound Vibrations on Ships" (Trans.) JPRS:47803, Clearinghouse, 8 April 1969
- (6) L. Cremer and M. Heckl, "Körperschall" pp. 300-430, Springer, New York, 1967